Advanced Grade Control with Multivariate Geostatistics, Blast Movement Modeling, and Optimized Dig Limits

by

Yaroslav Valentynovych Vasylchuk

A thesis submitted in partial fulfillment of the requirements for the degree of

Doctor of Philosophy

in

Mining Engineering

Department of Civil and Environmental Engineering
University of Alberta

ABSTRACT

Grade control in open pit mines establishes the final destination for mined material (e.g., plant, leach pad, stockpile, waste dump, etc.). In contrast to long- and medium-term mine planning, errors at this stage of a mine operation cannot be changed in the future; correct decisions bring a certain amount of profit, while wrong decisions incur a certain amount of loss. In the simplest grade control case, there is only ore and waste. Ore is more profitable to process in the plant than send to the waste dump. More complex cases may involve multiple grades, multiple destinations, locally varying geology, and complex profit calculations. Any flaw in the grade control procedure can lead to significant losses.

This thesis formulates and develops improved theory and practice for grade control procedures in open pit mines. An integrated grade control system called the Advanced Grade Control (AGC) is developed that considers all the relevant data and encodes rules and algorithms to make important decisions automatically. The developed system is a nearly automatic algorithm that seamlessly links all the grade control processes. The main components of the system are: i) spatial prediction of grades or profit, ii) modeling the blast-induced displacement of pre-blast spatial predictions, and iii) optimization of mineable dig limits.

AGC uses the maximum expected profit approach for making grade control decisions. High resolution expected profit is automatically calculated using a new local multivariate simulation algorithm called the Advanced Grade Control-Expected Profit (AGC-EP). The algorithm utilizes a k-fold cross-validation procedure to optimize input parameters. Two case studies based on real data demonstrate that AGC-EP outperforms carefully applied kriging estimation in terms of total profit from a mine bench.

An optimization-based algorithm called the Advanced Grade Control-Blast Movement (AGC-BM) has been developed to model blast-induced displacement of rock in 3-D using gridded pre- and post-blast topography and direct blast movement measurements. The blast movement of rock is considered an optimization assignment problem approximately solved

by a heuristic algorithm. The objective function and optimization details are explained and examples are provided. A method is proposed to calibrate limited blast movement measurements using firing pattern information. Blast movement modeling with approximate topography is considered.

An algorithm for optimizing the classification of surface mine material subject to excavating constraints called the Advanced Grade Control-Dig Limits (AGC-DL) is developed. High resolution expected profit models are input and optimized to classification maps subject to site specific rectangular or non-rectangular excavating constraints. The algorithm is fast and produces classification maps that allow selecting up to 98-99 % of the total maximum expected profit obtained with free selection.

A grade control system should work nearly automatically and be integrated within a mine's short-term planning and processing workflows. It should work in unison with precise location tracking and measuring equipment providing constantly updated information on the position of excavating equipment and ore grade. The Advanced Grade Control system is a step towards intelligent grade control utilizing all available information in real time for maximizing profit from mining operations.

PREFACE

The dissertation is an original work by Yaroslav V. Vasylchuk. Parts of the research documented in the dissertation were previously published.

Chapters 1, 2, 3, 4, 7, and 8 are my original work conducted under the supervision of Dr. Clayton V. Deutsch.

Parts of the research documented in Chapter 5 and summarized in Chapter 8 are published as Y.V. Vasylchuk and C.V. Deutsch (2019) Approximate blast movement modelling for improved grade control, Mining Technology. Parts of the research documented in Chapter 6 and summarized in Chapter 8 are composed as an original research article, Y.V. Vasylchuk and C.V. Deutsch (2019) Optimization of Surface Mining Dig Limits with a Practical Heuristic Algorithm, submitted for publication.

DEDICATION

To my wife and my family

ACKNOWLEDGMENTS

I would like to express my sincere gratitude to my thesis supervisors, Dr. Clayton Deutsch and Dr. Jeffery Boisvert, for their guidance. The invaluable advice, endless enthusiasm, and patience of Dr. Deutsch were essential to this dissertation research.

The financial support of the Centre for Computational Geostatistics (CCG) members is most appreciated.

I would also like to thank my wife, my family, and my dear friends for their moral support and encouragement.

TABLE OF CONTENTS

LIST OF TABLES

LIST OF FIGURES

LIST OF ABBREVIATIONS

Abbreviation	Description
2-D	Two-dimensional
3-D	Three-dimensional
AGC	Advanced Grade Control
AGC-BM	Advanced Grade Control-Blast Movement
AGC-DL	Advanced Grade Control-Dig Limits
AGC-EP	Advanced Grade Control-Expected Profit
BH	Blasthole
BMM	Blast movement monitor
CCG	Centre for Computational Geostatistics
CDF	Cumulative distribution function
DMC	Distinct motion code
FMC	Fraction of maximum correlation
ft	Foot
GMM	Gaussian mixture model
GSLIB	Geostatistical software library
HR	High resolution
HSBM	Hybrid Stress Blast Model
LP	Linear programming
LR	Low resolution
LVA	Locally varying anisotropy
m	Meter
MAF	Minimum/maximum autocorrelation factors
MILP	Mixed integer linear programming

Abbreviation	Description
MOI	Mass moment of inertia
ms	Millisecond
MSE	Mean squared error
NN	Nearest neighbor
NS	Normal scores
OK	Ordinary kriging
PCA	Principal component analysis
PPMT	Projection pursuit multivariate transform
RC	Reverse circulation
RFID	Radio frequency tag ID
SCT	Stepwise conditional transformation
SPGMM	Semi-parametric Gaussian mixture model
UDEC	Universal distinct element code

CHAPTER 1

INTRODUCTION

This chapter motivates the thesis, discusses the current state of grade control practice in open pit mines, and describes limitations. Section 1.1 summarizes the main reasons for the loss of profit in open pit mines and outlines the main objectives of this research. Section 1.2 provides a thesis statement and lists scientific contributions. Section 1.3 provides a thesis outline with a brief description of each chapter.

1.1 Problem Statement and Motivation

Grade control is a set of procedures allowing selective excavation of different ore/waste types with a final goal of maximizing the profit from mining operations. It should start with a comprehensive sampling procedure providing samples from blastholes, trenches, truck dumps, and, maybe, dedicated grade control drilling (J. G. Davis, 1992). In many cases, it is necessary to manage several stockpiles with different ore types and/or grades; they can be used for blending the ore and maintaining specified head grades for the mill.

Typical grade control procedures can be summarized by three main unit operations: i) spatial prediction of grades or profit, ii) modeling the blast-induced displacement of pre-blast spatial predictions, and iii) optimization of mineable dig limits. Grade control practices in open pit mines are moving towards greater automation and using more sophisticated tools in each unit operation. However, there is still no comprehensive framework that combines all these unit operations in a single algorithm and sets the standards for their implementation.

The rules for determining correct destinations for mined material vary in complexity and often depend on the conditions of a particular deposit or a technological process; they usually include spatial information such as grades of metallic or non-metallic elements present in the mined material. Some other information such as rock type may also be used. Since

only a limited number of samples of the pre-blast rock is available, the values of grade variables for any given portion of mined material may be unavailable and should be modeled. Also, it is often necessary to break rocks using explosives prior excavation; a proper selection plan (dig limits) should account for the displacement of the rocks and an increase in their volume caused by the energy of blasted explosives. Stages of a mine's operation related to grade control are schematically illustrated in Figure 1.1.
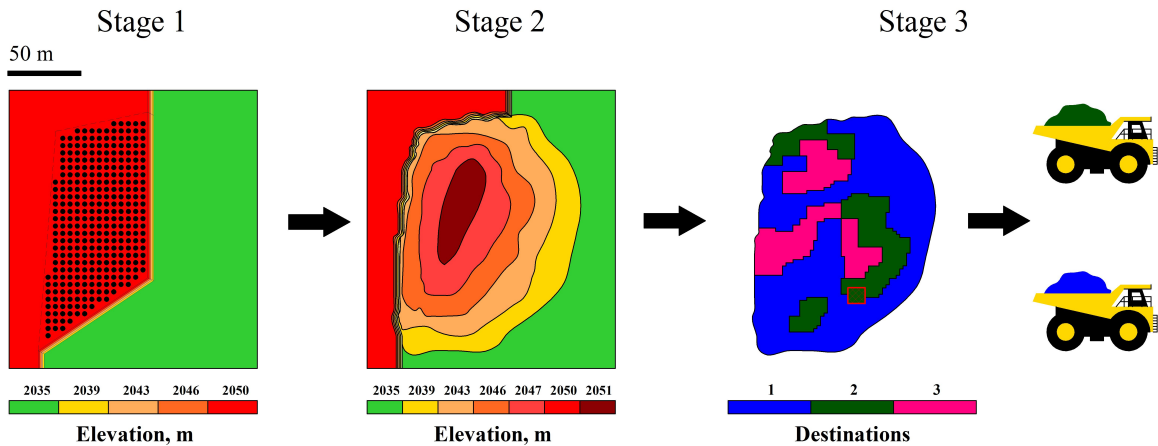
Figure 1.1: Schematic illustration of the stages of grade control

In stage 1, blastholes (illustrated as black dots in Figure 1.1) are bored in rock to prepare it for blasting; rock samples from the blastholes are obtained and analyzed. In stage 2, the rock is blasted to ensure that it can be excavated and loaded. In stage 3, the post-blast rock (mined material) is loaded in trucks and sent to different destinations. The proposed grade control unit operations correspond to the stages of a mine's operation. Each grade control unit operation is characterized by a level of uncertainty in the values of grade variables at a given scale and, therefore, the destination for mined material is also uncertain. The challenge of grade control is to manage the uncertainty at each unit operation using available information and obtain a post-blast excavation plan maximizing profit subject to the limitations of available excavating and hauling equipment.

The uncertainty in the geological composition of a mine bench is usually managed using blasthole (BH) samples; the samples are used to obtain pre-blast predictions of grades for a grid of blocks. If blasting is not performed, there is a direct connection between the spatial predictions and a selection plan; the predicted grades are used to obtain dig limits at

a certain resolution. Vasylchuk and Deutsch (2017) recommend using a block size of 25 % or less of the sample spacing for the spatial predictions to minimize the loss from a mine bench. However, the optimal destinations obtained using the spatial predictions at a high resolution may not be mineable. Therefore, they are usually combined into larger mining units in Stage 3. Ideally, the optimal destination would be determined for each truck load. The implementation of such detailed dig limits would rely on high quality positioning and dispatching systems at the mine.

If blasting is performed, the direct connection between the predictions of grades and a corresponding selection plan is interrupted. This connection can be restored using direct blast movement measurements, which allow mapping the pre-blast predictions onto a post-blast muckpile. The uncertainty in the volume and shape of the post-blast muckpile can be managed using post-blast topography.

Optimizing dig limits using high resolution (HR) spatial predictions and large selection units (e.g., red dashed square in Figure 1.1 (Stage 3)) is another challenge. Each large selection unit can be assigned a destination based on the HR predictions that fall within it; all the units of a selection map have to be placed with respect to each other in such a way that the total profit from a mine bench is as close as possible to the maximum total expected profit possible with free selection at a high resolution.

1.1.1 Grade Control Decision Making Accounting for Economic Benefits

Grade control procedures currently rely primarily on deterministic estimation methods (Dimitrakopoulos & Godoy, 2014; Godoy, Dimitrakopoulos, & Costa, 2001) like inverse distance or kriging that are relatively easy to use by junior mining engineers or geologists. Estimation techniques provide single deterministic predictions at unsampled locations. These predicted grades can be used to assign destinations for mined material based on a cut-off grade or more complex set of rules. Profit functions with asymmetric and non-linear constraints and relationships are sometimes used for determining the correct destinations. Kriging estimates assume equal penalty for underestimation and overestimation (Srivas-

tava, 1987; Isaaks, Treloar, & Elenbaas, 2014). In fact, the actual losses/benefits in grade control decision making are often asymmetric and non-linear. An attempt to obtain best estimates that account for the asymmetry and/or non-linearity in profit would result in bias (Vasylchuk & Deutsch, 2016) and is usually not practical. The concept of the asymmetry in the profit from grade control decisions is illustrated in Figure 1.2.
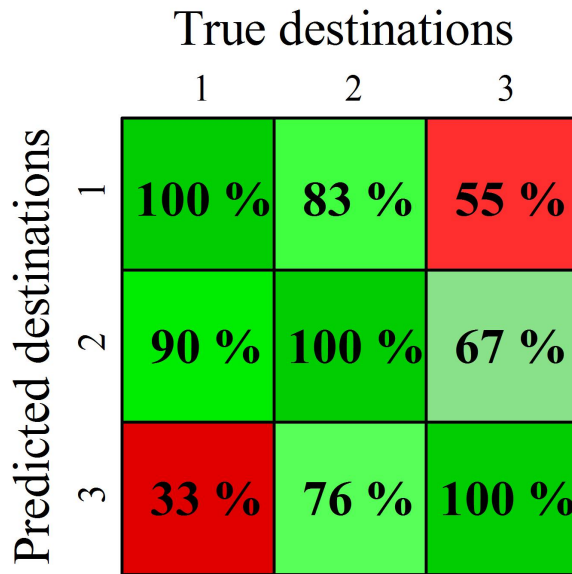
Figure 1.2: An example of a profit map for all possible classification scenarios with 3 destinations for mined material

The matrix in Figure 1.2 shows the percentage of the maximum achievable profit value obtained at a particular location. If a predicted destination is the same as the true destination, 100 % of the profit is achieved; otherwise, the profit is reduced. The benefits from grade control decisions may be asymmetric; for example, the scenarios when the true destination is 1 but a predicted destination is 2 and when the true destination is 2 and a predicted destination is 1 may be not equal. Also, the rules for determining the profit for a particular destination may depend on several grades and variable metal recovery, which means the resulting profit may be non-linear. Ideally, predicted destinations should be equal to the true destinations at all locations, which would maximize the profit. Unfortunately, this is difficult to achieve since the true grades at all locations is unknown.

Geostatistical simulation should be considered as an alternative to estimation for spatial predictions. It provides the uncertainty in grade values, which can be used to assess

the economic benefits of grade control decisions in terms of profit. The profit can be obtained using any type of asymmetric or non-linear profit function; this feature allows more accurate and precise decisions for the grade control cases with asymmetric or non-linear rules for determining correct mined material destinations. Making grade control decisions with simulation using a risk-neutral position on profit allows theoretically maximizing the total expected profit from a mine bench; the maximum expected profit approach (Glacken, 1996) can be used to determine optimal decisions. Theoretically, the more precisely the uncertainty in grade values is estimated, the more often predicted destinations will match the true ones for a grade control model. Mathematically, this principle is expressed in Chapter 3. The quality of the simulated models plays an important role for obtaining the best possible predictions of profit and, therefore, the most correct grade control decisions.

1.1.2   Influence of Locally Varying Geology

Spatial prediction models in grade control are the basis for making classification decisions. Local geological features may contradict a global assumption of stationarity (Journel & Huijbregts, 1978, p. 30) often made for geostatistical models. This can potentially lead to sub-optimal predictions of grades and, consequently, misclassification errors and the loss of profit. Therefore, it is important to have a method for accurate local uncertainty determination for better reproduction of the local geological features.

Simple grade control methods based on estimation do not fully consider the problem of locally varying geology. An advanced grade control system based on geostatistical simulation should have tools for determining the parameters of local anisotropy; this information should be used to obtain better predictions of uncertainty and a final classification of mined material closer to the correct true destination.

1.1.3   Multivariate Relationships Between Grades

In multivariate deposits, the valuation of rock to be sent to different destinations may depend on multiple grades and be subject to constraints. In such cases, it may be important to reproduce multivariate relationships between grade variables in spatial prediction models to

avoid misclassification errors and the loss of profit. The reproduction of the multivariate relationships between grade variables may require specialized tools for their joint simulation. A multivariate simulation workflow should be implemented and simulated values should be considered in a profit function of realistic complexity.

It may be important for a multivariate simulation workflow that all the sample observations are homotopic (without missing collocated grade values). Removing the samples with missing grade values from the modeling procedure may result in a bias (R. J. A. Little & Rubin, 2014) and decrease the quality of the spatial prediction models. A multivariate imputation of the missing grade values should be considered to be a pre-requisite step before simulation to maximize the usage of available data without introducing a bias in grade control models.

1.1.4 Blast Movement of Rock

The ways to account for blast movement in grade control can be summarized into three major categories: i) theoretical modeling of blast movement physics, ii) measuring the blast-induced displacement of rocks, and iii) combining direct measurements and numerical modeling. The theoretical blast movement modeling can be done either in 2-D (Cundall, 1980; R. L. Yang, Kavetsky, & McKenzie, 1989) or 3-D (Hart, Cundall, & Lemos, 1988; Preece & Silling, 2016; R. L. Yang & Kavetsky, 1990); a mine bench can be represented as blocks or circles that are assigned pre-blast rock properties. The theoretical approach allows modeling the trajectory of each block using the physics of blasting and the mechanics of rock breakage. Such modeling algorithms may incorporate information about the properties of blasted rocks, boundary conditions, properties of explosives, and blast design as an input information. However, the quality of final models will always depend on the quality of this input information in addition to the quality of the modeling algorithm (La Rosa & Thornton, 2011). Unfortunately, the unavoidable uncertainty in the input information and parameters may result in misclassification and the loss of profit.

Another approach is to measure the displacement of rocks during blasting using either simple visual markers such as bags or wooden sticks (S. L. Taylor, 1995; Zhang, 1994) or some type of transmitters with remote detecting equipment (Adam & Thornton, 2004;

Gilbride, 1995). Direct measurements provide the most accurate information about blast movement. However, using many transmitters may be unreasonable due to their cost while using inexpensive visual markers may suffer from their low recovery during excavation (S. L. Taylor, 1995; Zhang, 1994) and high labor intensity. Therefore, some method should be developed to use limited blast movement measurements, represented as displacement vectors, for modeling the post-blast distribution of spatial grade control information.

The combination of the direct measurement of blast movement and numerical modeling is a reasonable approach for obtaining post-blast grade control models validated by available information. D. L. Taylor and Firth (2003) interpolate the sparse displacement vectors to correct pre-blast polygons accounting for blast movement. A method to model blast movement using surface topography, historical blast movement measurements, and the blast initiation sequence is described in Isaaks, Barr, and Handayani (2014). Even though historical information about blast movement in a particular mine is a very useful information about a possible behavior of the rock mass during blasting, the conditions of each blast are often unique. This motivates developing a blast movement modeling algorithm incorporating relevant measurements and blast design information and provides the flexibility in input parameters.

A practical modeling algorithm should use all the available information about blast movement including pre- and post-blast topographic surfaces to model the shape of a mine bench before and after blasting and direct measurements to link pre-and post-blast predictions of grades or profit. A practical algorithm should also account for cases when only limited information about a blast is available. The firing pattern configuration can be used as an additional source of information about the direction of rock displacement during blasting. A way to perform blast movement modeling with approximate topography is required if the pre- and post-blast topographies are absent.

1.1.5 Optimal Selection of Mined Material

The post-blast models of grades or profit should be used to delineate areas (dig limits) of a corresponding post-blast mine bench and assign them to optimal destinations. The parameters and characteristics of the excavating and hauling equipment available at a mine

should be taken into account while designing the dig limits (M. Deutsch, 2017; Isaaks, Treloar, & Elenbaas, 2014; Richmond & Beasley, 2004a; Tabesh & Askari-Nasab, 2011). The simplest way to accomplish this task is manually drawing dig limit lines; however, this approach may not be optimal, especially, for the grade control cases with many destinations. Misclassification errors and the loss of profit may occur at the edges of different zones due to marginal ore.

Different zones representing final destinations for mined material should consider the limitations of the excavating equipment to follow the lines. Isaaks, Treloar, and Elenbaas (2014) use the concept of minimum mining width for designing dig limits. The concept of a rectangular selection unit (M. Deutsch, 2017) representing the excavating constraints is appealing due to its straightforward implementation with the maximum expected profit method. The design of dig limits can be expressed as an optimization problem. After the optimization problem is formulated, an algorithm is required to find a solution maximizing the total expected profit from a mine bench subject to meeting the excavating constraints.

1.1.6 Summary

The surface mining industry needs a comprehensive grade control modeling framework linking all the main unit operations and generating all the necessary information to be used directly in the mine. The framework should be automatic and adaptable to site specific conditions. The automation of the grade control modeling ensures that important modeling steps are not omitted and careless errors are not made. Grade control models should be adjusted in real time accounting for new information. Local adaptability in grade control should help maximize the recovery of natural resources and increase the profit from mining operations.

The primary objective of this dissertation research is to develop an integrated grade control modeling framework covering all stages of grade control. There are a number of important aspects that should be considered in the new modeling framework. Simulation should replace estimation to better reflect the uncertainty in profit. Local geological features and multivariate relationships between grade variables should be reproduced in simulated models. High resolution expected profit obtained using the simulated models can be used

as a summary of spatial grade control information; it can be averaged and used to optimize the selection of mined material. The topographic surfaces supplied to the grade control system along with blast movement measurements and the elements of blast design should be used to adjust the pre-blast expected profit for the post-blast muckpile. Finally, optimizing dig limits should be performed with the post-blast expected profit for any number of destinations and accounting for excavating constraints.

1.2 Thesis Statement and Research Contributions

Thesis Statement: *A new comprehensive grade control system based on local multivariate simulation, blast movement modeling, and determination of post-blast optimal dig limits increases profit from mine operations while standardizing and simplifying grade control practice in open pit mines*.

The key contributions of this dissertation research include: i) the development of a robust and flexible algorithm for local multivariate simulation, ii) the modification of the mass moment of inertia (MOI) method for automatic determination of the direction of local anisotropy, iii) the development of a blast movement modeling algorithm based on topography and direct measurements, and iv) the development of a fast heuristic algorithm for the dig limits optimization accounting for excavating constraints. Other developments include a way to incorporate the firing pattern information into blast movement modeling and a way to perform blast movement modeling with approximate topography.

1.2.1 An Automatic Algorithm for Local Multivariate simulation

Estimation methods like kriging or inverse distance provide single deterministic predictions at each unsampled location. Simulation is suggested by many authors (C. V. Deutsch, Magri, & Norrena, 2000; Glacken, 1996; Godoy et al., 2001; Leuangthong, Neufeld, & Deutsch, 2003; Neufeld, Norrena, & Deutsch, 2005; Norrena, 2007; Richmond, 2003; Verly, 2005) as an alternative to estimation in grade control. It allows improving the classification of mined material while accounting for the varied and complex economic consequences of different

grade control decisions. The grade control decisions should be based on the maximum expected profit over many realizations.

A global assumption of stationarity may be unrealistic for some deposits; reproducing local geological features may be important for the correct classification of mined material. Simulation with locally varying anisotropy (LVA) is offered in Leuangthong, Prins, and Deutsch (2006) and Boisvert and Deutsch (2011). Leuangthong et al. (2006) propose a way to change rotation matrices accounting for locally varying directions of anisotropy; the anisotropy ratios are considered stationary. Boisvert and Deutsch (2011) offer representing the data coordinates in higher dimensions using multi-dimensional scaling (MDS) (Torgerson, 1952) with anisotropic distances; the Euclidean distances calculated with these new multi-dimensional coordinates are used to calculate covariances and solve normal equations. Both of the described methods are valuable contributions to the field of computational geostatistics. However, a different approach is implemented in this thesis; the assumption of stationarity is revisited at each location being simulated. A new simulation algorithm performs all modeling steps, including normal score transformation, at modeling locations using nearby samples.

The new simulation algorithm implements a full local multivariate simulation workflow at each location. It is developed as the first part of an integrated grade control system covering all the proposed grade control unit operations. At each modeling location, a simplified simulation workflow includes the following steps for each variable: i) search for closest data, ii) normal score transformation (multivariate if required), iii) local anisotropy determination and variogram modeling, iv) local simulation, and v) the conversion of the simulated values to expected profit. All the modeling steps are performed automatically; the measures of performance and quality checks are incorporated into the modeling workflow to support the automatic operation.

A manual implementation of the proposed local multivariate simulation workflow is challenging. Depending on the resolution of an expected profit model and the number of variables, the number of operations required to perform the modeling locally (e.g., normal score transformation and variogram modeling) can be considerable. Aside from that, the automatic implementation allows incorporating various checks and the measures of perfor-

mance that improve the quality of resulting models. Performing all the modeling and validation operations manually could be overwhelming and prone to errors. This thesis aims to demonstrate that an unsupervised local multivariate simulation algorithm can produce better results than conventional grade control modeling workflow. A detailed workflow of the local multivariate simulation algorithm is provided in Chapters 3 and 4.

1.2.2 Automatic Determination of Local Anisotropy

Within the automatic simulation workflow, a primary consideration for local anisotropy determination algorithm is flexibility. The MOI method (Hassanpour, 2007) is modified for this purpose. The method uses correlation maps for determining the anisotropy angles. Correlation coefficients serve as masses and lag distances serve as the distances to the axes of rotation. A major problem with this method is that the correlation maps often contain artifacts and noise, which may cause errors in the angle determination. An algorithm is implemented to remove the artifacts and leave only the high correlation coefficients pointing in the direction of major geological continuity.

1.2.3 Blast Movement Modeling Algorithm

A reliable approach to model the blast-induced displacement of rock includes direct measurements rather than purely theoretical concepts (La Rosa & Thornton, 2011). Pre- and post-blast topography along with blast movement vectors can be used to predict the post-blast positions of the expected profit units. The pre- and post-blast topographic surfaces and a project bench elevation are the only parameters required to build initial 3-D models. Figure 1.3 shows an example of topographic surfaces created artificially to illustrate the concept.

(a) Pre-blast   **(b)** Post-blast
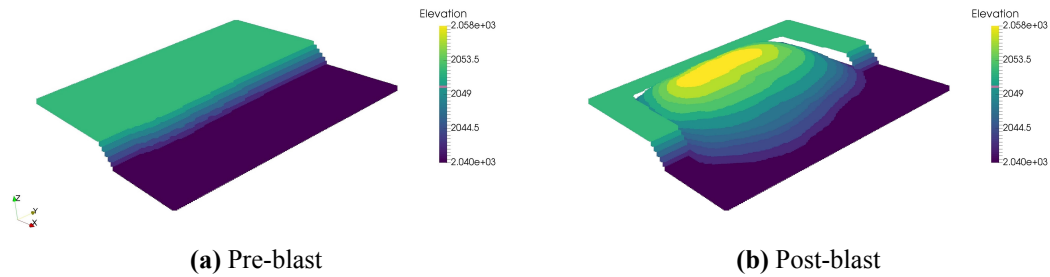
Figure 1.3: Example of pre- and post-blast topographic surfaces

The 3-D models are discretized by blocks; initially, the pre-blast expected profit units are assigned to the blocks of the pre-blast model. The blast movement problem is expressed as a combinatorial assignment problem. A cost function is developed that accounts for the positions of the high resolution blocks of the pre- and post-blast 3-D models with respect to corresponding free faces. Direct blast movement measurements and the elements of blast design may be included into the cost function as well. A stochastic optimization algorithm is developed to minimize the cost function and associate each block of the pre-blast model, along with the expected profit values assigned to it, to a block of the post-blast model. The blast movement algorithm is the second part of the integrated grade control system. More details about the cost function and optimization algorithm are in Chapter 5.

1.2.4   Dig Limits Optimization Algorithm

After a post-blast 3-D model of expected profit is obtained, the displaced expected profit values are used to determine optimal dig limits. The HR blocks of the post-blast 3-D model have the expected profit values for each destination assigned to them. Since the dig limits optimization is done in 2-D, the 3-D expected profit is averaged or accumulated along the vertical direction to obtain a 2-D expected profit map. When the HR expected profit units in 2-D are combined inside a larger selection unit or frame, the total expected profit value of the selection unit in each destination is the total expected profit value of all the HR units falling within it. Small changes in the position of the selection frame may change the most profitable destination. Therefore, an algorithm is required to account for all the possible positions of all selection units with respect to each other.

There are two conditions that an optimized dig limits map should meet: i) every HR block must be assigned to at least one selection frame representing a destination for mined material, and ii) all the HR blocks within a frame must have the same destination.

A fast heuristic optimization algorithm is developed to satisfy the conditions stated above. It is implemented in the third part of the integrated grade control system. Details about the optimization algorithm are in Chapter 6.

1.2.5 Integrated Grade Control System

A comprehensive grade control system called the Advanced Grade Control (AGC) system is developed to define and support the main grade control unit operations: i) spatial prediction of high resolution expected profit, ii) modeling the blast-induced displacement of pre-blast expected profit, and iii) optimization of mineable dig limits accounting for excavating constraints.

The grade control system is implemented as an integrated algorithm that can be incorporated into a mine's short-term planning workflow. The three parts of the system corresponding to the three grade control unit operations are designed to work automatically or nearly automatically in a chained workflow to allow the fast updating of grade control models if new information is available. In order to support the automatic operation of the first part of the system, dedicated checks and measures are used to choose important modeling parameters automatically during a k-fold cross-validation procedure. The system's operation can be classified as partially intelligent; it is designed to assist with high quality grade control modeling in open pit mines.

The AGC system sets the performance standards for each unit operation and aims at increasing the total profit from a mine's operations. The three parts of AGC are designed so that they can be used either altogether or as components of another grade control system.

1.3 Thesis Outline

Chapter 2 contains an overview of the main aspects of grade control in open pit mines. Simulation-based methods for grade control decision making are reviewed. The reproduc-

tion of locally varying geology and multivariate relationships between grade variables for better predictions is discussed. Then, the existing methods to account for blast-induced displacement of rocks are reviewed. The remainder of the chapter is dedicated to reviewing the methods for the optimal classification of mined material for its subsequent excavation.

Chapter 3 describes a simulation-based framework for expected profit calculation used in the spatial prediction part of AGC. The concept of using k-fold cross-validation for optimizing modeling results is explained. Main elements of the k-fold cross-validation procedure are described in detail. A modified MOI method for the determination of local anisotropy directions is described. The choice of important parameters of the expected profit modeling algorithm is justified based on artificial tests.

Chapter 4 describes the main expected profit modeling part of AGC. A detailed simulation workflow is described. A method to post-process high resolution expected profit maps using averaging filters for better modeling results is described. The chapter concludes with a case study partially based on a real multivariate blasthole data set. The performance of the proposed simulation algorithm is compared to the performance of ordinary kriging in terms of total profit from a mine bench.

Chapter 5 describes an optimization-based method for blast movement modeling. Firstly, the optimization problem is defined. Secondly, the steps of a heuristic optimization algorithm are explained. Thirdly, a way to incorporate the firing pattern information into the modeling procedure and a way to perform blast movement modeling with approximate topography are described. The chapter concludes with a series of examples.

Chapter 6 focuses on designing dig limits maximizing total mineable expected profit from a mine bench. A new heuristic algorithm for fast dig limits optimization based on high resolution expected profit for all destinations is described. A way to account for the limitations of excavating and hauling equipment during optimization is explained. A series of examples are provided.

Chapter 7 describes a grade control case study partially based on real data. The performance of AGC is compared to a conventional grade control method based on kriging estimation. Total profit from a mine bench is compared for the two methods. The effect of blast movement on the total profit is investigated. Constraints imposed by excavating and

hauling equipment on the selection of mined material are taken into account. Results of the case study are summarized.

Chapter 8 summarizes the main scholarly contributions of this research. Limitations and possible future work are discussed.

Chapter 2

Literature Review

2.1 Spatial Prediction for Grade Control

Rock samples from rotary percussion or reverse circulation drilling provide relevant information about the composition of a mine bench before blasting and excavation. Although blastholes are relatively closely spaced, most of the volume of a mine bench is not sampled and, therefore, some method should be applied to predict grade values at unsampled locations.

Usually, predictions are made for a grid of nodes or blocks (Vasylchuk & Deutsch, 2017) for the grade variables relevant to short-term planning; the grid of blocks represents the volume of a mine bench. The node spacing of the grid should be chosen accounting for selectivity and misclassification errors (Vasylchuk & Deutsch, 2017). Grade values are obtained at the center of each block without a sample using a numerical modeling method.

In many open pit mines, simple estimation methods like inverse distance (Dimitrakopoulos & Godoy, 2014; Godoy et al., 2001) and the nearest neighbor assignment of grades are used to create grade control models. The nearest neighbor method assigns the closest BH sample value to each unsampled block. The inverse distance interpolation method is used to estimate grade values using a number of nearby BH samples (Shepard, 1968); the nearby samples are used to obtain a weighted average for each block. Although the inverse distance weighting method most likely provides better estimates than local arithmetic averages or the nearest neighbor method, it does not account for the details of the data configuration or varying anisotropy at different scales. Kriging is a popular estimation method for grade control predictions that accounts for these factors and theoretically minimizes the estimation variance under certain assumptions.

Misclassification of mined material occurs due to limited sampling; however, the misclassification errors and financial consequences are often asymmetric (Dimitrakopoulos & Godoy, 2014) and non-linear. If many variables are used for determining the optimal

destinations for mined material, the multivariate relationships and constraints between the variables should be taken into account (Vasylchuk & Deutsch, 2017). Kriging assumes equal penalties for underestimation and overestimation (Isaaks, Treloar, & Elenbaas, 2014; Srivastava, 1987) and, therefore, should be used carefully for grade control. Simulation provides the distribution of uncertainty in grades to permit the asymmetric consequences of grade control decisions to be considered. Vasylchuk and Deutsch (2017) demonstrate that simulation outperforms kriging, inverse distance estimation method, and the nearest neighbor assignment method in terms of minimizing loss when the penalties for underestimation and overestimation are asymmetric.

The following sections will review geostatistical tools for grade control. The influence of locally varying geology, multivariate relationships between grade variables, and non-linear profit on decision making will be discussed.

2.1.1 Regionalized Variables and Stationarity

The concept of a regionalized variable is used to describe continuous geological phenomena such as grades; it is defined at a series of locations $\boldsymbol{u}_i$, $i = 1, ..., n$ over some domain D. The sample values $z(\boldsymbol{u}_i)$, $i = 1, ..., n$ are considered outcomes or realizations of a random function $F(Z(\boldsymbol{u}_i))$, $i = 1, ..., n$ (Journel & Huijbregts, 1978, p. 29). In order to perform statistical inference at an unsampled location $\boldsymbol{u}_0$, a conditional distribution $F(Z(\boldsymbol{u}_0)|\, z_1, ..., z_n)$ must be inferred. An n+1-variate distribution function is needed to estimate this conditional distribution:

$$F(z, z_1, ..., z_n; \boldsymbol{u}_0, \boldsymbol{u}_1, ..., \boldsymbol{u}_n) = Prob\{Z(\boldsymbol{u}_0) < z, Z(\boldsymbol{u}_1) < z_1, ..., Z(\boldsymbol{u}_n) < z_n\}$$

The first two moments of the n+1-variate distribution function are considered to be sufficient for most of the applications in mining (Journel & Huijbregts, 1978, p. 31).

This distribution cannot be obtained having only a single realization of $z(\boldsymbol{u})$ at a particular location. Some generalization must be made. The decision of stationarity is made to provide replicates by considering the samples from the domain D as members of the same population but distributed in space. The assumption of second order stationarity implies two conditions: i) the expectation $E\{Z(\boldsymbol{u})\}$, $\forall\, \boldsymbol{u}$ does not depend on the location $\boldsymbol{u}$, and

ii) the covariance between two random variables $Z(\boldsymbol{u})$ and $Z(\boldsymbol{u} + \boldsymbol{h})$ exists; the separation lag $\boldsymbol{h}$ is the only parameter that determines the covariance, $C(\boldsymbol{h}) = E\{Z(\boldsymbol{u}) \cdot Z(\boldsymbol{u} + \boldsymbol{h})\} - E\{Z(\boldsymbol{u})\}^2$, $\forall$ $\boldsymbol{u}$ (Journel & Huijbregts, 1978, p. 32). The existence of the covariance and stationary mean implies that the variance is finite and that the variogram and covariance are equivalent tools for spatial prediction (Journel & Huijbregts, 1978, p. 32):

$$Var\{Z(\boldsymbol{u})\} = E\{[Z(\boldsymbol{u}) - E\{Z(\boldsymbol{u})\}]^2\} = C(0)$$

$$\gamma(\boldsymbol{h}) = 0.5 \cdot Var\{Z(\boldsymbol{u}) - Z(\boldsymbol{u} + \boldsymbol{h})\} = C(0) - C(\boldsymbol{h}) \tag{2.1}$$

where $\gamma(\boldsymbol{h})$ is a semi-variogram for lag distance $\boldsymbol{h}$.

The assumption of second order stationarity is then used for deriving the theory of kriging. The term variogram will be used throughout this thesis instead of the term semi-variogram for consistency with geostatistical literature (Isaaks & Srivastava, 1989; Journel & Huijbregts, 1978; Matheron, 1963; Rossi & Deutsch, 2014).

2.1.2 Kriging and Simulation

Krige (1951) pioneered the use of statistical methods for the valuation of mineral deposits. Matheron (1963) formulated the theory of best unbiased spatial prediction and named it kriging. The theory of kriging is further explained with respect to its application in mining by other authors (David, 1977; Isaaks & Srivastava, 1989; Journel & Huijbregts, 1978).

Kriging is an estimation method that minimizes the theoretical error variance (quadratic error) between true values and estimates (Journel & Huijbregts, 1978, p. 305). Simple kriging assumes that the mean is known and stationary (Rossi & Deutsch, 2014, p. 138). Ordinary kriging constrains the weights to samples to sum to 1 to remove the need for the global mean (Rossi & Deutsch, 2014, p. 139). Ordinary kriging adapts to local trends in the mean and is more suitable for grade control. Vasylchuk and Deutsch (2017) demonstrate that for a single variable and a symmetric loss/profit function, ordinary kriging provides results close to more advanced simulation-based methods in terms of misclassification. For the cases with asymmetric penalties, the performance of kriging deteriorates significantly compared to simulation.

Multiple variables can be estimated with cokriging (Journel, 1989); if a primary variable is missing at a location, it can be estimated from secondary data. Cokriging also minimizes the error variance of estimation; the cross-correlation between variables helps to reduce the estimation error even more compared to kriging with one variable (Isaaks & Srivastava, 1989, p. 400).

Simulation is a way to model uncertainty in a grade distribution that can be later used for assessing economic consequences of particular decisions (C. V. Deutsch et al., 2000; Glacken, 1996; Isaaks, 1991; Neufeld et al., 2005; Richmond, 2003). Similar to kriging, simulation honors local data but also reproduces the histogram and variogram (Rossi & Deutsch, 2014, p. 167). The use of a multivariate transformation technique permits reproduction of the multivariate relationships between variables. Unlike kriging, simulation better reproduces the distribution of extreme values.

Sequential Gaussian Simulation (SGS) is a popular simulation method (Isaaks, 1991). Like most simulation techniques, it relies on a multivariate Gaussian assumption after normal score transformation of the grades. Turning bands simulation (Matheron, 1973) and LU simulation (Luster, 1986) are other simulation techniques that have seen use in mining.

2.1.3   Economic Functions and Optimal Estimates

The error of estimation can be defined as: $e(\boldsymbol{u}) = z^*(\boldsymbol{u}) - z(\boldsymbol{u})$, where $z^*(\boldsymbol{u})$ is an estimated value and $z(\boldsymbol{u})$ is the true value at a location $\boldsymbol{u}$. Then, the loss from this error can be defined by a loss function (Journel, 1989). The quadratic loss function is well known:

$$L(e(\boldsymbol{u})) = e^2(\boldsymbol{u})$$

where $e(\boldsymbol{u})$ is the variance of estimation at a location $\boldsymbol{u}$.

The mean of a distribution minimizes the quadratic loss function regardless of the distribution shape. Simple kriging computes a conditional mean and theoretically minimizes the quadratic loss function between the true and estimated values. Also, the mean value of multiple realizations (E-type estimate) at a location $\boldsymbol{u}$ minimizes the quadratic loss function (Glacken, 1996, p. 29).

Journel (1984) shows that the median minimizes the absolute error loss function:

$$L(e(\boldsymbol{u})) = |e(\boldsymbol{u})|$$

Another simple loss function type is a constant loss function; some constant value is assigned if the error between truth and estimate is not 0:

$$\begin{cases} L(e(\boldsymbol{u})) = 0, & \text{if } e(\boldsymbol{u}) = 0; \\ \text{Constant}, & \text{if } e(\boldsymbol{u}) \neq 0. \end{cases}$$

The mode of the distribution of values minimizes this loss function (Glacken, 1996, p. 30).

Journel (1984) proves that if the loss function is linear and asymmetric, the optimal estimate decision will be a p quantile of a distribution instead of the median. This can be understood as if, for example, underestimation is penalized more than overestimation, the value minimizing the error of estimation is above the mean. An example of such a loss function is in Figure 2.1.
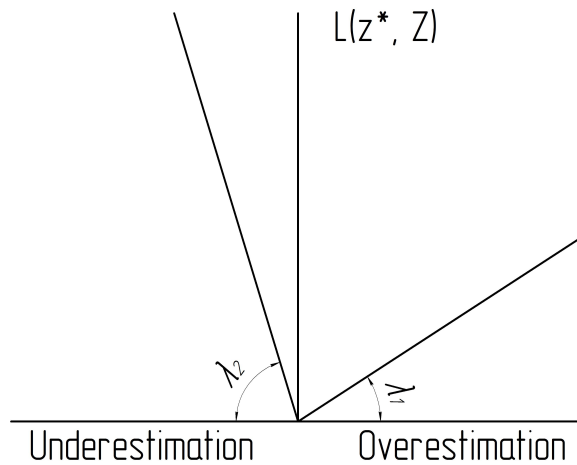
Figure 2.1: An asymmetric loss function

The p quantile can be calculated using the following expression (Journel, 1984):

$$p = \frac{\lambda_1}{\lambda_1 + \lambda_2}$$

where λ_1 and λ_2 represent that angles determining the rates for the overestimation and underestimation errors, respectively.

Loss functions may be asymmetric non-linear and have multiple constraints. In such cases, an analytical solution is impossible (Glacken, 1996) and a numerical approach should be used. If the distribution of uncertainty at a location $\boldsymbol{u}$ for n conditioning data, $F(\boldsymbol{u}; z|(n)) = Prob\{Z(\boldsymbol{u}) \leq z|(n)\}$, is available, a general optimal estimate or L-optimal estimate can be derived using the expression below (Glacken, 1996, p. 28; Journel, 1989, p. 27):

$$E\{L(z^*(\boldsymbol{u}), Z(\boldsymbol{u}))|(n)\} = \int_{-\infty}^{\infty} L(z^*(\boldsymbol{u}), z(\boldsymbol{u})) \cdot dF(z; \boldsymbol{u}|(n))$$

where $L(z^*(\boldsymbol{u}), Z(\boldsymbol{u}))|(n)$ is a loss function; $z^*(\boldsymbol{u})$ is an estimate value; $Z(\boldsymbol{u})$ is a random variable representing the true value.

In practice, the integral can be solved by a discrete sum over all the realizations of simulation (Glacken, 1996, p. 28):

$$E\{L(z^*(\boldsymbol{u}), Z(\boldsymbol{u}))|(n)\} = \frac{1}{S} \sum_{s=1}^{S} L(z^*(\boldsymbol{u}), z^s(\boldsymbol{u})) \tag{2.2}$$

where $z^s(\boldsymbol{u})$ are the simulated values at a location $\boldsymbol{u}$ over the realizations $s = 1, ..., S$.

It is required to find such $z^*(\boldsymbol{u})$ that minimizes the expected loss; one would need to check a range of values of $z^*(\boldsymbol{u})$ using Equation (2.2) to find the one that brings the smallest expected loss. This principle can be used to determine an optimal destination for mined material at each location instead of a grade value. In real life, there is asymmetry in the profit calculation for each destination, but loss functions are not really applicable given the repeated nature of grade control decisions. A neutral position on risk maximizes the expected profit. Therefore, using the most applicable profit functions and maximizing the expected profit is more reasonable for this task.

In Vasylchuk and Deutsch (2016), the authors attempt to directly obtain the optimal estimates for non-linear loss functions using training images and iterative optimization of kriging weights. Tests show that the method tends to overestimate or underestimate grades in order to minimize the specified error of estimation.

2.1.4 Grade Control Decision Making with Simulation

Minimum expected loss (Isaaks, 1991) and maximum expected profit (Glacken, 1996) are sometimes considered two separate methods but they are the same in principle; both of

them should yield the same classification of mined material in a risk neutral situation. A brief description of simulation methods for grade control is in Verly (2005) and Vasylchuk (2016).

In Verly (2005), only a simple grade control case with one cutoff grade is considered; the cutoff grade allows distinguishing between two destinations: ore and waste. This defines four scenarios for a location being estimated: i) correct acceptance (both estimate and true value are above the cutoff), ii) correct rejection (both estimate and true value are below the cutoff), iii) false acceptance (estimate is above the cutoff but true value is below the cutoff), iv) and false rejection (estimate is below the cutoff but true value is above the cutoff). The false acceptance and false rejection errors may also be interpreted as Type 1 and Type 2 errors, respectively. More information about hypothesis testing is in Sheskin (2003). Figure 2.2 illustrates the four scenarios.
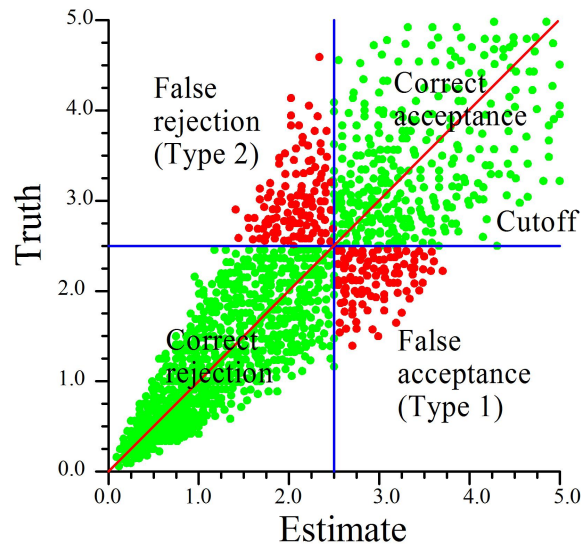
Figure 2.2: Four scenarios for ore and waste decisions

The expected loss method (Isaaks, 1991; Srivastava, 1987) is based on two simple utility functions:

$$
\begin{cases}
U_{ore}(z) = z \cdot r \cdot p - c_m - c_p; \\
U_{waste}(z) = -c_m.
\end{cases}
\tag{2.3}
$$

where $U_{ore}(z)$ is the utility obtained from mined material of a certain grade z; $U_{waste}(z)$ is the loss incurred when the waste material is mined; r is the recovery of grade; p is the

price of commodity; c_m and c_p are the costs for mining and processing, respectively. The cutoff grade is calculated using the following expression:

$$z_c = \frac{c_p}{r \cdot p}$$

According to this method, the expected loss for the ore decision is calculated as follows:

$$L(\boldsymbol{u}; \text{ore}) = \begin{cases} 0, & \text{correct acceptance;} \\ -p \cdot r \cdot Z(\boldsymbol{u}) + c_p, & \text{false acceptance (Type 1 error).} \end{cases} \quad (2.4)$$

$$EL(\boldsymbol{u}; \text{ore}) = E\{L(\boldsymbol{u}; \text{ore})\}$$

where $L(\boldsymbol{u}; \text{ore})$ is the loss at a location $\boldsymbol{u}$ given the ore decision; $EL(\boldsymbol{u}; \text{ore})$ is the expected loss at a location $\boldsymbol{u}$ given the ore decision.

The expected loss for the waste decision is calculated as follows:

$$L(\boldsymbol{u}; \text{waste}) = \begin{cases} 0, & \text{correct rejection;} \\ p \cdot r \cdot Z(\boldsymbol{u}) - c_p, & \text{false rejection (Type 2 error).} \end{cases} \quad (2.5)$$

$$EL(\boldsymbol{u}; \text{waste}) = E\{L(\boldsymbol{u}; \text{waste})\}$$

where $L(\boldsymbol{u}; \text{waste})$ is the loss at a location $\boldsymbol{u}$ given the waste decision; $EL(\boldsymbol{u}; \text{waste})$ is the expected loss at the location $\boldsymbol{u}$ given the waste decision.

The correct decision at the location $\boldsymbol{u}$ has the smallest corresponding expected loss.

Glacken (1996) offers another approach to the optimal classification problem. The same utility function parameters as in the ore utility function from Equation 2.3 are used. If the ore decision is correct, the grade value is at least high enough to cover a processing cost. If the ore decision is incorrect, there is overestimation and the profit turns negative because the grade value does not fully pay for the processing cost. If the waste decision is correct, then profit is equal to 0, while an incorrect waste decision implies underestimation and a negative profit associated with lost ore. Glacken (1996) introduced the coefficients for the underestimation and overestimation decisions (false rejection and false acceptance) that are supposed to reflect a mine operator's attitude to treating the waste material as ore and to losing ore by directing it to a waste dump. According to this method, the expected profit

for the ore decision can be calculated as follows:

$$P(\boldsymbol{u}; \text{ore}) = \begin{cases} p \cdot r \cdot Z(\boldsymbol{u}) - c_p, & \text{correct acceptance;} \\ w_1 \cdot (p \cdot r \cdot Z(\boldsymbol{u}) - c_p), & \text{false acceptance (Type 1 error).} \end{cases} \tag{2.6}$$

$$EP(\boldsymbol{u}; \text{ore}) = E\{P(\boldsymbol{u}; \text{ore})\}$$

where $P(\boldsymbol{u}; \text{ore})$ is the profit at a location $\boldsymbol{u}$ given the ore decision; $EP(\boldsymbol{u}; \text{ore})$ is the expected loss at the location $\boldsymbol{u}$ given the ore decision; w_1 is the false acceptance coefficient.

The expected profit for the waste decision can be calculated as follows:

$$P(\boldsymbol{u}; \text{waste}) = \begin{cases} 0, & \text{correct rejection;} \\ -w_2 \cdot (p \cdot r \cdot Z(\boldsymbol{u}) - c_p), & \text{false rejection (Type 2 error).} \end{cases} \tag{2.7}$$

$$EP(\boldsymbol{u}; \text{waste}) = E\{P(\boldsymbol{u}; \text{waste})\}$$

where $P(\boldsymbol{u}; \text{waste})$ is the profit at the location $\boldsymbol{u}$ given the waste decision; $EP(\boldsymbol{u}; \text{waste})$ is the expected loss at the location $\boldsymbol{u}$ given the waste decision; w_2 is the false rejection coefficient.

For this method, the correct decision at the location $\boldsymbol{u}$ has the largest corresponding expected profit.

C. V. Deutsch et al. (2000) propose a modification of the expected profit method. Unlike in Glacken (1996), the cost of mining is considered here. There is a lost opportunity cost included in the case the waste decision is incorrect. The cutoff grade accounts for the difference in mining waste and ore:

$$z_c = \frac{c_p + (c_o - c_w)}{p \cdot r}$$

where c_o is the cost of mining ore; c_w is the cost of mining waste.

The expected profit for the ore decision can be expressed as follows:

$$P(\boldsymbol{u}; \text{ore}) = \begin{cases} p \cdot r \cdot Z(\boldsymbol{u}) - c_o - c_p, & \text{correct acceptance;} \\ p \cdot r \cdot Z(\boldsymbol{u}) - c_o - c_p, & \text{false acceptance (Type 1 error).} \end{cases} \tag{2.8}$$

$$EP(\boldsymbol{u}; \text{ore}) = E\{P(\boldsymbol{u}; \text{ore})\}$$

In the case of a false acceptance, the profit for the ore decision will be less than $-c_w$. The expected profit for the waste decision can be calculated as follows:

$$P(\boldsymbol{u}; \text{waste}) = \begin{cases} -c_w - c_{lo}, & \text{correct rejection;} \\ -c_w - c_{lo}, & \text{false rejection (Type 2 error).} \end{cases} \quad (2.9)$$

$$EP(\boldsymbol{u}; \text{waste}) = E\{P(\boldsymbol{u}; \text{waste})\}$$

where $c_{lo} = i(Z(\boldsymbol{u}), z_c) \cdot (-p \cdot r \cdot Z(\boldsymbol{u}) + c_o + c_p - c_w)$ is the lost opportunity cost; $i(Z(\boldsymbol{u}), z_c)$ is equal to 1 if a grade is greater than z_c and it is equal to 0 otherwise.

Neufeld et al. (2005) also use the expected profit approach with a profit function that accounts for a difference in the costs of mining ore and waste. The function converts simulated grades to negative or positive profit values depending on whether a grade exceeds a cutoff grade; a 'cost of processing waste' coefficient is used to scale negative profit values:

$$c_{pr} = \frac{p \cdot r(z_c) \cdot z_c - c_o + c_w}{p \cdot r(z_c) \cdot z_c}$$

where c_{pr} is the cost of processing waste coefficient; $r(z_c)$ is the recovery at the cutoff grade.

Grades are converted to profit as follows:

$$P(\boldsymbol{u}) = \begin{cases} (Z(\boldsymbol{u}) \cdot r(Z(\boldsymbol{u})) - z_c \cdot r(z_c)) \cdot p, & \text{if} \quad Z(\boldsymbol{u}) > z_c; \\ (Z(\boldsymbol{u}) \cdot r(Z(\boldsymbol{u})) - z_c \cdot r(z_c)) \cdot p \cdot c_{pr}, & \text{if} \quad Z(\boldsymbol{u}) < z_c. \end{cases} \quad (2.10)$$

$$EP(\boldsymbol{u}) = E\{P(\boldsymbol{u})\}$$

If the expected profit value calculated using Equation 2.10 is greater than 0, the decision is ore; the decision is waste otherwise.

Vasylchuk and Deutsch (2017) offer a simpler implementation of the minimum expected loss method: if either the ore or the waste decision is correct, the loss is 0; otherwise, the loss is calculated as the difference between the cutoff grade and a grade variable value. The underestimation and overestimation decisions could be scaled by coefficients similar to Glacken (1996).

The expected loss for the ore decision is calculated as follows:

$$L(\boldsymbol{u}; \text{ore}) = \begin{cases} 0, & \text{correct acceptance;} \\ (z_c - Z(\boldsymbol{u})) \cdot w_1, & \text{false acceptance (Type 1 error).} \end{cases} \quad (2.11)$$

$$EL(\boldsymbol{u}; \text{ore}) = E\{L(\boldsymbol{u}; \text{ore})\}$$

The expected loss for the waste decision is calculated as follows:

$$L(\boldsymbol{u}; \text{waste}) = \begin{cases} 0, & \text{correct rejection;} \\ (Z(\boldsymbol{u}) - z_c) \cdot w_2, & \text{false rejection (Type 2 error).} \end{cases} \tag{2.12}$$

$$EL(\boldsymbol{u}; \text{waste}) = E\{L(\boldsymbol{u}; \text{waste})\}$$

All the reviewed methods are similar in nature; they all account for a single cutoff grade and assume linear profit or loss. Simulation is used to calculate multiple realizations of grade and calculate the expected profit or loss. In real life, grade control cases are rarely so simple. Mined material can be routed to multiple destinations; asymmetric or non-linear profit/loss for a particular destination can be calculated using multiple variables. A more flexible method is required.

2.1.5 Multivariate Normal Score Transformation

Grade control may depend on multiple variables. A multi-Gaussian distribution of grades is assumed for Gaussian simulation; unfortunately, the univariate normal score transformation does not ensure multi-Gaussianity and complex multivariate features such as heteroscedasticity, non-linearity, and constraints will remain (Barnett, Manchuk, & Deutsch, 2014). Therefore, common cosimulation techniques assuming multi-Gaussianity will not be able to reproduce the complex features in the simulated realizations (Almeida & Journel, 1994; Verly, 1993). Another approach assumes independent simulation of multiple variables. There are advanced methods for decorrelation/normal score transformation of multiple variables such as principal component analysis (PCA) (B. M. Davis & Greenes, 1983; Hotelling, 1933), minimum/maximum auto-correlation factors (MAF) (Desbarats & Dimitrakopoulos, 2000; Switzer, 1985), stepwise conditional transformation (SCT) (Leuangthong & Deutsch, 2003; Rosenblatt, 1952), and projection pursuit multivariate transform (PPMT) (Barnett et al., 2014; Friedman, 1987).

PCA is a classic dimension reduction and decorrelation technique. A multivariate distribution of data is decorrelated using spectral decomposition of a corresponding covariance matrix at $\boldsymbol{h} = 0$ lag distance (Barnett & Deutsch, 2015a, p. 38).

The application of PCA implicitly assumes that if the correlation between multivariate data is removed at the $h = 0$ lag distance, it is also removed for all other $h > 0$ lag distances; this assumption makes PCA less effective for complex multivariate data (Barnett & Deutsch, 2015a, p. 39). MAF performs the spectral decomposition of covariance matrix at $h = 0$ and $h > 0$ lag distances. The covariance matrix at $h > 0$ is also corrected to have no cross-correlation between the factors (Barnett & Deutsch, 2015a, p. 39).

Stepwise conditional transformation is performed in a sequential manner. A primary variable is normal score transformed. The second variable is transformed conditional to the first variable. Subsequent variables are transformed with respect to all previous variables. The method is influenced by the curse of dimentionality with increasing the number of variables, that is, there are too few data to define the conditional distributions in a non-parametric manner with multiple previous variables. (Rossi & Deutsch, 2014, p. 184). The details of the theory and implementation of this method can be found in Leuangthong (2003).

A multivariate transformation algorithm is useful for an automatic grade control system; it should not require extensive tuning and supervision. PPMT appears to be a suitable algorithm. The method is based on aspects of the Projection Pursuit Density Estimation algorithm (PPDE) (Friedman, 1987). PCA is used to decorrelate the normal score transformed variables. Then, projection pursuit can be performed on the processed data (Barnett & Deutsch, 2015a). The idea is to find vectors that if the input data are projected on them the resultant projections are the most non-Gaussian; a projection index is used to measure the degree of the Gaussianity of the projection. Once such a vector is found, the input data are transformed so that the values on this projection become Gaussian. Then, this process is repeated until a pre-defined number of iterations is completed or when a stopping criterion is achieved. The details of the theory and implementation of this method can be found in Barnett et al. (2014) or Barnett and Deutsch (2015a).

2.1.6   Multivariate Imputation of Heterotopic Observations

Multivariate grade control cases benefit from the PPMT workflow described above. Isotopic observations, that is, all variables are available at all data locations, are required for

most of the methods described in Section 2.1.5. Due to various reasons, some variables may be missing, which creates heterotopic observations; removing the heterotopic observations may lead to omitting valuable information and producing biased results (R. J. A. Little & Rubin, 2014). A solution to the problem of heterotopic observations is to impute the missing variables using spatial and multivariate relationships between variables.

Missing samples may or may not follow a specific pattern; for example, the high grade areas of a domain are usually sampled more densely. Depending on this pattern, different imputation techniques may be used. Barnett and Deutsch (2015b) indicate that a suitable method for geostatistical modeling should reproduce the variability of observed data and do not introduce a bias; multiple imputation (Rubin, 1978) and maximum likelihood estimation (Dempster, Laird, & Rubin, 1977) methods satisfy these conditions.

Consider K regionalized random variables $Z_1, ..., Z_K$; the variables are sampled at n locations. The observations can be represented as a data matrix Z with $z_{ij}, i = 1, ..., n, j = 1, ..., K$ entries. The observed and missing values of Z are denoted Z_{obs} and Z_{mis}, respectively. A multiple imputation method implies constructing a conditional distribution $f(Z_{mis}|Z_{obs})$ and then sampling it to obtain L realizations of imputed missing values, Z^l, $l = 1, ..., L$ consisting of the observed values and imputed values (Barnett & Deutsch, 2015b). This workflow is suitable for performing geostatistical simulation; a realization of imputed values Z^l can be used with a realization of simulation l.

Barnett and Deutsch (2015b) propose two multiple imputation methodologies adapted for geological data: i) the parametric merged method, and ii) the non-parametric merged method. The parametric merged method is based on the assumption of multivariate Gaussianity of the data. The non-parametric merged method is recommended if input variables exhibit complex multivariate relationships. This method is based on multivariate kernel density estimation for better reproducing complex multivariate features and Gibbs sampling (Geman & Geman, 1984; Metropolis, Rosenbluth, Rosenbluth, Teller, & Teller, 1953).

Silva and Deutsch (2016) propose a semi-parametric method using Gaussian mixture models (SPGMM). The method is similar to the non-parametric merged method from Barnett and Deutsch (2015b) but it uses Gaussian mixture model (GMM) for calculating marginal and conditional probabilities. SPGMM is faster than the non-parametric merged method

(Silva & Deutsch, 2016) but requires the number of kernels for GMM specified. SPGMM is the most suitable when the data are missing independent of the missing data; however, the data may still be missing dependently on the observed values (Silva & Deutsch, 2016).

2.1.7 Local Anisotropy and Variography

Mineral deposits often exhibit different non-linear and anisotropic features in different directions. In such cases, the major direction of geological continuity, as well as the parameters of an underlying variogram function, could be different for different regions of a mine bench. In other words, the assumption of stationarity (constant mean and variogram) might be unrealistic. The idea of incorporating locally varying anisotropy into geostatistical modeling is not new. Te Stroet and Snepvangers (2005) propose Local Anisotropy Kriging (LAK), which is based on gradient calculations for local orientations and subsequent kriging with local anisotropy; the two above operations are repeated iteratively until some optimization criterion is satisfied. Boisvert, Manchuk, and Deutsch (2009) consider non-Euclidian distances for calculating covariances and incorporating locally varying anisotropy into kriging models. Magneron, Jeannee, Le Moine, and Bourillet (2010) offer the local optimizing of the variogram model parameters using moving windows and cross-validation. The idea to use the mass moment of inertia tensors for determining major directions of local geological continuity was described by Hassanpour (2007). Machuca-Mory and Deutsch (2013) offer adjusting local cumulative distribution functions and variograms based on weighting by the distance to some anchor points. Feng and Milanfar (2002) present a method for finding the local orientation of geological features called multiscale PCA; the method uses the singular value decomposition (SVD) of gradient matrices at different resolutions (gradient pyramid layers) to determine a dominant orientation using resulting singular vectors and singular values. Estimated orientation vectors are then propagated from the coarsest to the finest resolution using the Kalman filter (Kalman, 1960). The 2-D method from Feng and Milanfar (2002) was further extended to a 3-D version in Martin (2017). Lillah and Boisvert (2015) discuss techniques for determining locally varying anisotropy (LVA) fields for different types of data.

In order to fully implement a local simulation algorithm, it is necessary to obtain local

anisotropy ratios in addition to the orientation of the anisotropy. For multiscale PCA and the mass moment of inertia methods, it can be done directly from the singular values and eigenvalues, respectively. Nevertheless, the ratios can be more reliably estimated from local variogram models. The concept of variograms and fitting variogram models is extensively described in geostatistical literature (David, 1977; Journel & Huijbregts, 1978, p.148-303; Matheron, 1963). Cressie (1985) and Cressie (1992) discuss different types of variogram estimators and least squares fitting algorithms; the weighted least squares fitting method in a combination with a robust estimator is compared to the generalized least squares and the ordinary least squares methods. Brunell (1992) offers an algorithm for an automatic fitting of variogram models with the weighted least squares method from Cressie (1985). Larrondo, Neufeld, and Deutsch (2003) describe an iterative algorithm for automatic variogram fitting. Desassis and Renard (2013) present a modification of the Gauss-Newton minimization algorithm to fit variogram models to experimental variograms or variogram maps. The algorithm is implemented in univariate and multivariate cases. J. L. Deutsch (2015) presents a modified iterative algorithm that offers an increase in speed and reliability. Another modification of the Gauss-Newton algorithm for fitting variogram models is in Manchuk and Deutsch (2017).

After the local anisotropy information is obtained, it can be used within a kriging or simulation workflow. The implementation of *sgsim* (C. V. Deutsch & Journel, 1998) that uses locally changing rotation matrices for calculating covariances and solving normal equations is described in Leuangthong et al. (2006). Another method to perform SGS and kriging using locally varying anisotropy, non-Euclidian distances and multi-dimensional scaling fields is offered in Boisvert and Deutsch (2011).

2.2 Modeling Blast Movement

2.2.1 Background

In many open pit mines, rock blasting is a necessary step before excavation. It is performed by means of explosives that are placed in dedicated blastholes. The chemical reaction following the initiation of explosives induces a fast release of detonation gases that creates an

initial impulse on the walls of the blastholes; the gases also perform the subsequent moving and breaking of the rock. Persson, Holmberg, and Lee (1993, p. 87-143) provide more information on the detonation theory and the mechanics of the rocks breakage. Blasting engineers are usually concerned with the harmonic and reasonable distribution of blast energy inside the mine bench. This design considers a number of constraints imposed by geology, the configuration of the free face, available explosives and firing systems, environmental and safety regulations, desired degree of fragmentation among other considerations.

Blasting rocks causes their movement depending on the configuration of a blast. A post-blast muckpile is also characterized by a swell factor, that is, an increase in the volume after blasting. Grade control is concerned with decreasing dilution and ore loss due to incorrect classification of the mined rock. Therefore, the blast-induced displacement of rocks and the swell factor should be accounted for in grade control models (Dimitrakopoulos & Godoy, 2014; Vasylchuk & Deutsch, 2017).

There are two main approaches to model blast movement for grade control: i) modeling based on the physics of rocks breaking, and ii) modeling based on direct measurements of the blast-induced displacement of rocks.

2.2.2 Overview of Existing Blast Movement Models

Early attempts to theoretically model the blast movement of rocks were limited by computational capability. A classification of early blast movement models is in Gilbride (1995, p. 14-24). Cundall (1980) presents a sophisticated Universal Distinct Element Code (UDEC) that allows modeling the post-blast displacement of rocks represented as discrete blocks. UDEC was later implemented in a 3-D commercial code, 3DEC (Hart et al., 1988); the method accounts for the displacement and rotation of individual blocks. Schamaun (1984) describes two models named BLOCKS and BUMP, where blast movement is represented by discrete blocks or circles, respectively; the dynamic behavior of the discrete particles for both models is governed by the geological characteristics of mine benches, shapes and sizes of the particles, and the parameters regulating the interactions between the particles. Preece and Taylor (1989) present a Distinct Motion Code (DMC) that allows incorporating the properties of explosives for modeling the motion of rocks; DMC also uses the principle

of moving sphere objects. Some developments in the field of blast modeling are described in Tordoir, Weatherley, Onederra, and Bye (2009). A 3-D version of the DMC algorithm is presented in Preece and Silling (2016); it now utilizes parallel processing for modeling millions of discrete parcels. The modern version of DMC is able to predict the influence of different initiation schemes on blast movement. Furtney, Andrieux, and Hall (2016) describe the application of a new numerical model for modeling the blasting process. The model is developed as a part of the Hybrid Stress Blast Model (HSBM) project implemented in a software called Blo-Up (Onederra, Furtney, Sellers, & Iverson, 2013). The program aims to predict the detonation process, fragmentation, blast movement, and a final muckpile. P. Yang et al. (2017) present a new model simulating the entire process occurring in rocks during blasting including an initial impulse from waves propagation, rock movement, and fragmentation. It is reported that the simulation results are in good agreement with blasting cylinder and projectile fire tests (P. Yang et al., 2017).

Modeling the entire blasting process is an interesting approach for predicting blast movement. However, incomplete knowledge of the geological characteristics, fracture locations and orientation, and mechanical properties of the rocks together with uncertainty in blast parameters such as timing, stemming ejection, and the influence of free faces undermines these modeling results. La Rosa and Thornton (2011) discuss the possible economic consequences of having discrepancies between theoretically modeled blast movement and measured blast movement; for two test blasts, the error between a physics-based model and real measurements was from 1 to 7 m, which was estimated to be equivalent to a total loss of from 2.2 to 4.8 million dollars, respectively. La Rosa and Thornton (2011) argue that even a 0.5 m error may make the theoretical modeling less economically effective than actually measuring the blast-induced displacement of rock. Therefore, any theoretical blast models should be calibrated with real pre- and post-blast configurations of a mine bench.

2.2.3   Direct Measurement of Blast-induced Displacement of Rock

There are two major ways that have been used to measure blast movement: i) using simple visual markers, and ii) using remote detecting equipment. Zhang (1994) and S. L. Taylor (1995) investigate the displacement of rocks during blasting using sand bags and wooden

stakes as markers. Gilbride (1995) offers to use remote sensing magnetic target markers put inside a mine bench with magnetic radiometers. La Rosa and Thornton (2011) describe the use of radio frequency tags ID (RFID) for measuring blast movement. Adam and Thornton (2004) present a new method of remote blast movement measuring using Blast Movement Monitors (BMM), transmitters placed in a protective shell. The BMMs are put in dedicated drill holes to different depths and detected after blasting using a specialized receiver. The blast movement vectors are calculated using the pre-blast surveyed locations of the dedicated drillholes and the post-blast positions of the BMMs. Thornton, Sprott, and Brunton (2005) report the error of measurement of the system of about 0.1-0.5 m (increasing with depth). Thornton (2009b) provides a summary of a 6 years long monitoring the blast movement displacement of rocks with BMM; the most important conclusions are as follows: i) the bottom and middle parts of the bench move more than the upper part; a classical D-shaped profile is created, ii) swell is approximately uniform throughout the bench, iii) the movement of the central part of the mine bench during buffered and free-faced blast are similar, and iv) the echelon blast is preferred because it creates the most predictable blast movement. Vasylchuk (2016) indicates that there is a lack of methods to reconcile the pre- and post-blast 3-D models with complex configurations of free faces using sparse displacement vectors.

D. L. Taylor and Firth (2003) model separately the directional components of the sparse measurement vectors with any interpolation method (e.g., kriging) to get displacement vectors at all the grid points and later model the post-blast dig limits. Isaaks, Barr, and Handayani (2014) use the pre- and post-blast topographic surfaces to create the pre- and post-blast 3-D models of mine benches. The directions of displacement are determined perpendicular to the timing contours. The horizontal displacements are drawn from the distributions of horizontal displacements based on historical data.

2.3   Classification of Rocks for Short-term Planning

A traditional way to determine mined material destinations is hand contouring using rock types or a cutoff grade (Norrena & Deutsch, 2001). This method is prone to errors with

marginal ore and at the boundaries of different rock types. There are two major require-
ments for dig limits: i) maximizing profit, and ii) honoring selection constraints including
equipment maneuverability, the direction of excavation, and other factors. Gershon (1983)
discusses using linear programming (LP) and mixed integer linear programming (MILP)
approaches for solving mine planning and scheduling problems. Tabesh and Askari-Nasab
(2011) offer to optimize long-term planing using a two-stage clustering algorithm based on
hierarchical clustering and tabu search. Tabesh and Askari-Nasab (2013) use hierarchical
clustering for determining dig limit polygons; first, similar block-units are merged accord-
ing to a similarity index and then post-processed to remove small clusters and smooth the
shapes of the polygons. A way to account for the direction of mining during the clustering is
described; however, it is not clear how to determine the ultimate optimal number of clusters
as a stopping criterion. Norrena and Deutsch (2001) present an algorithm that optimizes
the dig limit boundaries by maximizing profit and accounting for 'digability' (a measure of
difficulty to follow dig limit lines for mining equipment) using simulated annealing (Kirk-
patrick, Gelatt, & Vecchi, 1983); initial dig limits are determined automatically. Neufeld,
Norrena, and Deutsch (2003) offer a semi-automatic algorithm for the dig limit determina-
tion using simulated annealing and initial polygons supplied by the user; an algorithm is pro-
posed to account for multiple destinations. Richmond and Beasley (2004b) use 'demolition
and reconstruction' heuristics to find an optimal solution to the grade control problem with
different processing options expressed as a mixed integer non-linear problem. In Richmond
and Beasley (2004a), a discrete efficient frontier is built using the output of an optimization
function with different weights to utility and risk penalty. A floating circle algorithm is
applied to account for equipment constraints during selection. Wilde and Deutsch (2007)
optimize selection using expected profit maps and accounting for pre-defined shapes of
selection units and the direction of mining. Isaaks, Treloar, and Elenbaas (2014) use the
minimum loss principle and simulated annealing to find optimal dig limit lines constrained
by a minimum mining width. Ruiseco (2016) solves the selection problem using a genetic
optimization algorithm that starts from random dig limits and iterates using the concept
of evolving through breeding, mutation, and survival. An idea of a clustering penalty is
incorporated in an objective function to account for selecting equipment constraints. Sari

and Kumral (2018) formulate the selection problem as a MILP; only a simple case with one variable and a linear utility function is considered. M. Deutsch (2017) demonstrates an algorithm for dig limits optimization partially based on a branch-and-bound algorithm (Land & Doig, 1960; J. D. C. Little, Murty, Sweeney, & Karel, 1963). Dig limits are often optimized on a block basis; the dimensions of the blocks account for a mining width. The optimized boundaries are then contoured to generate mineable polygons.

2.4   Conclusion

This literature review covers the topics that are necessary for understanding this thesis. It also demonstrates that the grade control procedure is still not perceived by the scientific community as an integrated process with all its aspects and unit operations interdependent. Many of the improvements in the field of grade control target a specific area of the short-term mine planning, which is unlikely an optimal approach.

This review is by no means comprehensive but it rather provides a useful guidance for finding more information on a particular topic.

CHAPTER 3

AUTOMATIC CALCULATION OF EXPECTED PROFIT

Chapter 2 discusses the minimum expected loss (Isaaks, 1991) and maximum expected profit (Glacken, 1996) methods for grade control; the two methods are expected to make identical grade control decisions in a risk neutral situation. Since the main purpose of a mine is maximizing profit, the maximum expected profit method may be considered more intuitive and, therefore, is advocated in this thesis. All the reviewed simulation-based grade control methods assume only two destinations for mined material: ore and waste. However, real grade control cases often involve multiple destinations depending on a particular technological process and mine plan. A flexible maximum expected profit method should allow incorporating complex rules for defining profit.

This chapter describes a new maximum expected profit method based on local multivariate simulation. The method is implemented as the first part of the Advanced Grade Control (AGC) system. The simulation workflow and its main components are described in detail.

3.1   Problem Formulation

Consider a stationary domain A (usually a mine bench) chosen based on geological and statistical characteristics that conform to site specific considerations. There are $g = 1, ..., G$ true grade values associated with each location $\boldsymbol{u} \in A$.

$$z_{true}(\boldsymbol{u}; g), \ g = 1, ..., G, \ \boldsymbol{u} \in A$$

The true grades permit calculating true profit for every destination $k = 1, ..., K$ through a profit function P:

$$P_{true}(\boldsymbol{u}; k) = P(z_{true}(\boldsymbol{u}; g), g = 1, ..., G; k), \ k = 1, ..., K, \ \boldsymbol{u} \in A$$

The true optimal destination at each location is the one that maximizes the true profit:

$$d_{true}(\boldsymbol{u}) = \max k \text{ of } (P_{true}(\boldsymbol{u}; k), \ k = 1, ..., K), \ \boldsymbol{u} \in A$$

The true cumulative profit over the domain is written as:

$$CP_{true} = \sum_{\boldsymbol{u} \in A} P_{true}(\boldsymbol{u}; d_{true}(\boldsymbol{u}))$$

This is the global maximum cumulative profit since it is a sum of maximum local profit values. Of course, the true grades and true profit values are inaccessible. A carefully applied geostatistical framework would provide L realizations of grades that accurately and precisely represent uncertainty in the true values.

$$z^l(\boldsymbol{u}; g), \ \boldsymbol{u} \in A, \ g = 1, ..., G, \ l = 1, ..., L \tag{3.1}$$

The expected profit for each destination at each location could be calculated as follows:

$$EP(\boldsymbol{u}; k) = \frac{1}{L} \sum_{l=1}^{L} P(z^l(\boldsymbol{u}; g), \ g = 1, ..., G; \ k) \tag{3.2}$$

The optimal destination for each location could be calculated from the expected profit:

$$d_{opt}(\boldsymbol{u}) = \max k \text{ of } (EP(\boldsymbol{u}; k), \ k = 1, ..., K), \ \boldsymbol{u} \in A \tag{3.3}$$

The cumulative profit based on these optimal destinations maximizes the expected profit, that is, a sum of maximum values is the maximum of the sum.

$$CP_{opt} = \sum_{\boldsymbol{u} \in A} EP(\boldsymbol{u}; d_{opt}(\boldsymbol{u})) \tag{3.4}$$

Given unavoidable uncertainty and differences between $d_{opt}(\boldsymbol{u})$ and $d_{true}(\boldsymbol{u})$ at some locations, the optimized cumulative profit must be less than the true cumulative profit:

$$CP_{opt} < CP_{true}$$

Nevertheless, the optimal decisions $d_{opt}(\boldsymbol{u})$ are the best possible without additional information that would make the uncertainty more precise and the predicted expected profit values converge to the truth. A risk neutral position implies that the destination corresponding to the highest expected profit value at a certain location should be chosen even if the

difference in the expected profit values for different destinations is marginal. This strategy allows maximizing the expected profit.

The profit function regulates how much profit is expected with each grade control decision. Provided the geostatistical realizations are truly accurate and precise, the expected profit should be close to the true profit over multiple locations. There will be differences due to incomplete sampling and short scale variability. A measure of error could be written as:

$$MSE_{profit} = E\{(EP(\boldsymbol{u}; k) - P_{true}(\boldsymbol{u}; k))^2\} > 0, \ \boldsymbol{u} \in A, \ k = 1, ..., K \qquad (3.5)$$

As written, this MSE is across all locations and destinations. The mean squared error would represent the amount of local data and the quality of the geostatistical approach. Of course, it could only be calculated when the true values are known in cross-validation mode or with a synthetic true model.

3.2 Profit Functions

Similar to the reviewed maximum expected profit/minimum expected loss methods, simulated grades $z^l(\boldsymbol{u}; g)$, $g = 1, ..., G$, $l = 1, ..., L$ are used to estimate the uncertainty in profit through a profit function P. Optimal destinations for mined material are then determined using Equations (3.2) - (3.3). Multiple constraints and relationships between any number of relevant grade variables may be considered. Two types of profit functions are proposed for AGC: a cutoff-based and a user-defined.

3.2.1 Cutoff-based Profit Function

The cutoff-based profit function can be used to calculate the expected profit values for the ore and waste destinations similar to the minimum expected loss/maximum expected profit methods reviewed in Chapter 2. A risk neutral position on profit allows maximizing total expected profit from a mine bench, which is reasonable considering the short-term nature of grade control and the fact that grade control decisions are irreversible. Therefore, the proposed profit function assumes that correct decisions bring a certain amount of profit and

incorrect decisions bring neither profit nor loss. It also assumes that all the mined material must be removed, and it should at least cover the processing cost if classified as ore. If a simulated value $z^l(\boldsymbol{u})$ at a location $\boldsymbol{u}$ is greater than or equal to a cutoff grade z_c, the expected profit for the ore decision is calculated as follows:

$$P(z^l(\boldsymbol{u}); \text{ore}) = \begin{cases} (z^l(\boldsymbol{u}) - z_c) \cdot b_1, & \text{if } z^l(\boldsymbol{u}) \geq z_c, \text{ (correct acceptance);} \\ 0, & \text{if } z^l(\boldsymbol{u}) < z_c, \text{ (false acceptance).} \end{cases} \tag{3.6}$$

$$EP(\boldsymbol{u}; \text{ore}) = \frac{1}{L} \sum_{l=1}^{L} P(z^l(\boldsymbol{u}); \text{ore})$$

where $P(z^l(\boldsymbol{u}); \text{ore})$ is the profit at the location $\boldsymbol{u}$ given the ore decision; $EP(\boldsymbol{u}; \text{ore})$ is the expected profit at the location $\boldsymbol{u}$ given the ore decision; b_1 is a scaling coefficient for correct acceptance.

If $z^l(\boldsymbol{u})$ is below than z_c, the expected profit for the waste decision is calculated as follows:

$$P(z^l(\boldsymbol{u}); \text{waste}) = \begin{cases} (z_c - z^l(\boldsymbol{u})) \cdot b_2, & \text{if } z^l(\boldsymbol{u}) < z_c, \text{ (correct rejection);} \\ 0, & \text{if } z^l(\boldsymbol{u}) \geq z_c, \text{ (false rejection).} \end{cases} \tag{3.7}$$

$$EP(\boldsymbol{u}; \text{waste}) = \frac{1}{L} \sum_{l=1}^{L} P(z^l(\boldsymbol{u}); \text{waste})$$

where $P(z^l(\boldsymbol{u}); \text{waste})$ is the profit at the location $\boldsymbol{u}$ given the waste decision; $EP(\boldsymbol{u}; \text{waste})$ is the expected profit at the location $\boldsymbol{u}$ given the waste decision; b_2 is a scaling coefficient for correct rejection.

The scaling coefficients b_1 and b_2 are included as an option to add asymmetry in the profit calculations. The cutoff-based function can be applied only to the simplest grade control cases assuming ore and waste destinations for mined material only.

3.2.2　User-defined Profit Functions

The proposed cutoff-based profit function does not incorporate complex multivariate or non-linear relationships between grades. Complex grade control cases may include multiple grade variables, multiple destinations, and multiple rules for defining profit for the destinations. Multiple grade variables may be associated with multiple cutoff grades and/or

recovery functions as well as various constraints. The recovery functions, in turn, may involve linear and non-linear relationships between grades (Dimitrakopoulos & Godoy, 2014). A user-defined profit function should be based on information related to a particular mine's plan and technological process. In order to define a dedicated profit function for AGC, the following general suggestions may be used:

- Information related to metallurgical recovery from a mine should be used as a basis for the profit function such as recovery functions, stockpile blending criteria, geological information, and others.

- A risk neutral position should be used; profit should be defined for correct decisions, while classification errors should not be penalized.

- A strategic mine plan should be taken into account (e.g., cutoff grade, scheduling).

- A profit function's design should be reasonable and balanced; dividing by zero or very small numbers should be avoided.

An example of an arbitrary user-defined profit function with non-stationary recoveries is provided below. There are three destinations for mined material: i) plant, ii) leach (pad), and iii) waste (dump). There are three simulated grade variables, $z^l(\boldsymbol{u}; g)$, $g = 1, ..., 3$, $l = 1, ..., L$, $\forall \boldsymbol{u} \in A$, and two recovery functions, $R_1(z^l(\boldsymbol{u}; 1), z^l(\boldsymbol{u}; 3))$, $l = 1, ..., L$, $\forall \boldsymbol{u} \in A$ and $R_2(z^l(\boldsymbol{u}; 2))$, $l = 1, ..., L$, $\forall \boldsymbol{u} \in A$. As written, the recovery of the first grade variable depends on the values of the first and third grade variables at each location $\boldsymbol{u}$. The recovery of the second grade variable depends on the value of the second grade variable only at each location $\boldsymbol{u}$. The expected profit for the plant decision is determined as follows:

$$
P(z^l(\boldsymbol{u}; 1), z^l(\boldsymbol{u}; 3); \text{plant}) =
$$

$$
\begin{cases} p_1 \cdot R_1(z^l(\boldsymbol{u}; 1), z^l(\boldsymbol{u}; 3)) \cdot z^l(\boldsymbol{u}; 1) - c_p^1, & \text{if profit} \geq \text{cost}; \\ 0, & \text{otherwise}. \end{cases}
\tag{3.8}
$$

$$
EP(\boldsymbol{u}; \text{plant}) = \frac{1}{L} \sum_{l=1}^{L} P(z^l(\boldsymbol{u}; 1), z^l(\boldsymbol{u}; 3); \text{plant})
$$

where p_1 is the price for metal/mineral per unit of mined material represented by the first grade variable; c_p^1 is the cost associated with processing the mined material at the plant.

The expected profit for the leach decision is determined as follows:

$$P(z^l(\boldsymbol{u}; 2); \text{leach}) =$$

$$\begin{cases} p_2 \cdot R_2(z^l(\boldsymbol{u}; 2)) \cdot z^l(\boldsymbol{u}; 2) - c_p^2, & \text{if profit} \geq \text{cost}; \\ 0, & \text{otherwise.} \end{cases} \tag{3.9}$$

$$EP(\boldsymbol{u}; \text{leach}) = \frac{1}{L} \sum_{l=1}^{L} P(z^l(\boldsymbol{u}; 2); \text{leach})$$

where p_2 is the price for metal/mineral per unit of mined material represented by the second grade variable ; c_p^2 is the cost associated with processing the mined material at the leach pad.

The expected profit for the waste decision is determined as follows:

$$P(z^l(\boldsymbol{u}; 1), z^l(\boldsymbol{u}; 2), z^l(\boldsymbol{u}; 3); \text{waste}) =$$

$$\begin{cases} -p_1 \cdot R_1(z^l(\boldsymbol{u}; 1), z^l(\boldsymbol{u}; 3)) \cdot z^l(\boldsymbol{u}; 1) - \\ p_2 \cdot R_2(z^l(\boldsymbol{u}; 2)) \cdot z^l(\boldsymbol{u}; 2) + c_p^1 + c_p^2, & \text{if cost} > \text{profit}; \\ 0, & \text{otherwise.} \end{cases} \tag{3.10}$$

$$EP(\boldsymbol{u}; \text{waste}) = \frac{1}{L} \sum_{l=1}^{L} P(z^l(\boldsymbol{u}, 1), z^l(\boldsymbol{u}; 2), z^l(\boldsymbol{u}; 3); \text{waste})$$

Even though the arbitrary function described by Equations (3.8) - (3.10) is more complex than the cutoff-based profit function described in Section 3.2.1, real life profit calculations may be more complex and changing frequently. The profit calculations are not limited to grade variables. Some constraints may be added based on geology, the capacities of final destinations, and other considerations. Also, it may be important to address stockpile blending criteria (since they may influence recovery) and mine planning in the profit calculations.

3.3 Modeling Framework

The expected profit calculation part of the Advanced Grade Control system is abbreviated as AGC-EP. The number of nearby samples used locally in the main modeling part of AGC-EP

is the most important parameter of the entire system. This number affects the local normal score data transformation, anisotropy determination, and variogram calculation. An unsupervised modeling approach requires that this parameter is determined automatically. A k-fold (5-fold is considered by default) cross-validation procedure at blasthole (BH) sample locations is used as a basis for decision making within AGC-EP.

The original data set is divided into 5 validation data sets V_i, $i = 1, .., 5$ (20 % of data in each); the validation data sets are extracted at random without overlapping. The training data set for each validation data set is the data in the other four folds. Necessary calculations are performed for each fold $i = 1, .., 5$, and the results are assembled.

The modeling decisions made in the cross-validation mode are transferred to the main modeling mode. It is assumed that minimizing the mean squared error in profit (Equation (3.5)) in the cross-validation mode allows maximizing the expected profit from a mine bench for final models.

Before the cross-validation starts, some pre-processing steps are carried out: i) multivariate imputation (if required), ii) the division of the original data to training and validation data sets, iii) the calculation of the average lag distance for anisotropy and variogram calculations, and iv) the definition of the parameters of a coarser super grid for faster parameter inference.

3.3.1 Multiple Imputation

Multivariate grade control cases are common in open pit mines. If the rules for determining correct destinations for mined material are non-linear and include multivariate conditions, the reproduction of multivariate relationships between grade variables in simulated models may be important for modeling local uncertainty. Advanced multivariate transformation methods like Projection Pursuit Multivariate Transform (PPMT) (Barnett et al., 2014) require homotopic observations. Excluding heterotopic observations (with missing grade values) may negatively impact the quality of grade control models and result in a bias (R. J. A. Little & Rubin, 2014).

Imputation should be performed prior to the start of expected profit modeling if missing samples are detected. If the rock type information is available, the imputation procedure

should be performed for each rock type independently. Methods from Silva and Deutsch (2016) and Barnett and Deutsch (2015b) should be considered for multivariate grade control cases.

3.3.2 Average Lag Distance

As a part of the local multivariate modeling workflow, local anisotropy directions are determined using correlation maps and the mass moment of inertia tensor (MOI) method (Hassanpour, 2007). The correlation maps summarize correlation coefficients in different directions. Since the BH samples are relatively densely spaced (spacing is usually in the range from 3 m to 8 m), the average distance from a BH location to the closest BH samples may be used as the lag distance for the calculation of the correlation coefficients.

Usually, blastholes do not provide enough information about the geological variability in 3-D and, therefore, are not used for modeling 3-D variograms; the lag distances are calculated only in the horizontal plane using N BH samples. Let $C = \{c_1, ..., c_N\} \in R^3$ be a set of vectors. Each vector $c_i = (c_1^i, c_2^i, c_3^i)$, $i = 1, ..., N$ has the Euclidean distances from a BH location i to three closest BH samples as its elements. The average lag distance is calculated as follows:

$$h_{xy} = \frac{1}{N} \sum_{i=1}^{N} \frac{c_1^i + c_2^i + c_3^i}{3} \tag{3.11}$$

Each location i might have a different number of locations situated at approximately the same distance from it depending on a drilling pattern and its position within a mine bench. Locations on the edges and in the corners of a mine bench are likely to have fewer close neighbors than the ones in the middle of the bench. Also, blastholes may be missing and bored with positioning errors. Selecting three closest BH samples for calculating the average lag distance provides a reasonable and unbiased estimate based on many test cases.

3.3.3 Super Grid Parameters

The concept of a super grid is implemented to decrease the operation time of the local multivariate simulation workflow. It is based on an assumption that local anisotropy parameters and variogram models are similar at nearby locations. A set of pre-blast coordinate vectors

$B = \{\boldsymbol{b}_1, ..., \boldsymbol{b}_N\} \in R^3$, where $\boldsymbol{b}_i = (b_x^i, b_y^i, b_z^i)$, $i = 1, ..., N$ is used to define the super grid. The elements of B with the largest and the smallest x and y components are extracted. The numbers of super grid nodes in the x and y directions are calculated as follows:

$$n_{sx} = (b_x^{largest} - b_x^{smallest} - h_{xy})/(h_{xy} \cdot v_{const});$$
$$n_{sy} = (b_y^{largest} - b_y^{smallest} - h_{xy})/(h_{xy} \cdot v_{const}). \tag{3.12}$$

where n_{sx} and n_{sy} are the numbers of super grid nodes in the x and y directions rounded up to the nearest integers, respectively; $b_x^{smallest}$ and $b_x^{largest}$ are the smallest and largest coordinate components in the x direction among all the elements in B; $b_y^{smallest}$ and $b_y^{largest}$ are the smallest and largest coordinate components in the y direction among all the elements in B; v_{const} is a constant value used to scale the average lag distance h_{xy}.

Locations of super grid nodes $\boldsymbol{x} \in A$ are defined using the minimum coordinates in the x and y directions ($b_x^{smallest}$ and $b_y^{smallest}$), a grid size (calculated as $h_{xy} \cdot v_{const}$), and the number of nodes in each direction. The concept of defining grid parameters is explained in C. V. Deutsch and Journel (1998). The constant value v_{const} is used to increase the super grid size relative to the average lag distance for faster parameter inference; guidance for choosing this value is provided later in this chapter. A super grid node location is clipped if there is no a coordinate location $\boldsymbol{b}_i$ closer to it than $h_{xy} \cdot 2$; this is done to account for complex boundaries of a mine bench.

3.3.4 K-fold Cross-validation Workflow

The estimated profit values are compared to the true profit values obtained from the data left out. All the modeling steps required for the expected profit calculation are performed using the nearby data and statistics from a super grid location $\boldsymbol{x}$ of domain A (representing a mine bench). A primary performance measure for selecting the number of samples is the mean squared difference between the true profit and the expected profit over all the BH locations of a validation data set and all destinations for mined material (Equation (3.5)). The workflow of the cross-validation part of AGC-EP is shown in Figure 3.1 and explained in detail below.

Cross-validation

1 Start with a fold $i = 1,...,5$
2 Associate each BH sample of a validation data set V_i with the nearest super grid node location $\boldsymbol{x}$
3 Start with the minimum number of nearby data of a training data set T_i
4 Go to a super grid node location $\boldsymbol{x}$
    4.1 Search for n_d BH samples and store them in a set D
    4.2 NS transform grade values in D (PPMT for multivariate)
    4.3 Save the NS and PPMT back-transformation information for $\boldsymbol{x}$
       4.3.1 Select a variable g
          4.3.1.1 Determine a major direction of anisotropy
          4.3.1.2 Calculate, model, and save a 2-D variogram model $\gamma(\boldsymbol{h})$ using BH samples from D
       4.3.2 Repeat for all variables $g = 1,...,G$
    4.4 Select a location $\boldsymbol{u} \in V_i$ associated with $\boldsymbol{x}$
    4.5 Use the statistics and data saved for $\boldsymbol{x}$
       4.5.1 Select a variable g
       4.5.2 Use the BH samples in D and $\gamma(\boldsymbol{h})$
          4.5.2.1 Solve normal equations
          4.5.2.2 Simulate $z^l(\boldsymbol{u})$, $l = 1,...,L$ values
       4.5.3 Repeat for all variables $g = 1,...,G$
       4.5.4 Obtain a nearest neighbor estimate $z_{NN}(\boldsymbol{u})$
       4.5.5 Back-transform $z^l(\boldsymbol{u})$, $l = 1,...,L$ using corresponding NS and PPMT
            back-transformation information
    4.6 Start with a destination for mined material k
       4.6.1 Calculate P_{true} using true variable values $z_{true}(\boldsymbol{u};g)$, $g = 1,...,G$
       4.6.2 Calculate EP using the simulated values $z^l(\boldsymbol{u})$, $l = 1,...,L$
       4.6.3 Calculate $SE_{profit} = (P_{true} - EP)^2$
       4.6.4 Calculate P_{NN} using $z_{NN}(\boldsymbol{u})$
       4.6.5 Calculate $SE^{NN}_{profit} = (P_{true} - P_{NN})^2$
       4.6.6 Increment SE_{profit} and SE^{NN}_{profit}
    4.7 Repeat for all destinations $k = 1,...,K$
    4.8 Repeat for all locations $\boldsymbol{u} \in V_i$ associated with $\boldsymbol{x}$
5 Repeat for all super grid node locations $\boldsymbol{x} \in A$
6 Calculate and save $MSE_{profit} = E\{SE_{profit}\}$, $\forall \boldsymbol{u} \in V_i$ and $MSE^{NN}_{profit} = E\{SE^{NN}_{profit}\}$, $\forall \boldsymbol{u} \in V_i$
7 Increase n_d and repeat all the above steps
8 Save minimum values of MSE_{profit} and MSE^{NN}_{profit} for fold i
9 Save n_d corresponding to the minimum MSE_{profit} value
10 Increment MSE_{profit} and MSE^{NN}_{profit}
11 Repeat for all folds $i = 1,...,5$
12 Average n_d corresponding to the minimum MSE_{profit} values across $i = 1,...,5$
13 Calculate $E_{avg} = (MSE^{NN}_{profit} - MSE_{profit})/5$; normally, E_{avg} should be positive

Figure 3.1: K-fold cross-validation workflow

Step 1

The cross-validation procedure starts with selecting validation and training data sets from V_i, $i = 1,...,5$ and T_i, $i = 1,...,5$, respectively; all the modeling steps are carried out using the samples from T_i.

Step 2

Each BH sample location $\boldsymbol{u} \in A$ of the validation data set V_i is associated with the closest super grid node location $\boldsymbol{x} \in A$. Since the number of super grid nodes is often smaller than the number of BH samples in V_i, each super grid node location will likely have several BH samples assigned to it.

Step 3

The cross-validation procedure is performed with different numbers of nearby BH samples associated with the super grid nodes, starting with some specified number of BH samples.

Step 4

The cross-validation algorithm starts at a super grid node location $x \in A$.

Step 4.1

A number of BH samples n_d situated nearby x are retrieved from the bench and stored in a set D. A simple search algorithm based on the shortest Euclidean distance between x and the nearby data locations is used.

Step 4.2

The normal score (NS) transformation of the grade values in D corresponding to $g = 1, ..., G$ grade variables is performed. If there are multiple grade variables in each BH sample, the PPMT multivariate normal score transformation is performed. The PPMT algorithm requires relatively few input parameters specified, which makes it suitable for automation; some other multivariate transformation algorithms may be considered (including MAF (Desbarats & Dimitrakopoulos, 2000; Switzer, 1985)). PPMT is intended to reproduce the non-linear relationships between grades in simulated models, which may be beneficial for multivariate grade control cases with complex profit calculations. Some parameters required for the PPMT algorithm are fixed according to recommendations from Barnett and Deutsch (2015a).

Fixed parameters for PPMT:

- The minimum and maximum numbers of iterations are 25 and 50, respectively.

- Targeted Gaussian percentile (Barnett & Deutsch, 2015a; Barnett et al., 2014) is 50.

Step 4.3

The NS and PPMT back-transformation information is saved for this super grid location x. It is used for back-transforming the simulated values at each location $u \in A$ associated with x.

Step 4.3.1

If there are multiple variables $g = 1, ..., G$, the following operations start with a variable g.

Step 4.3.1.1

The principal direction of anisotropy is calculated using a modified MOI method described in Section 3.4.1. If the number of nearby data nd is insufficient for the MOI method, the initial specified number of nearby samples should be increased and the k-fold cross-validation procedure should be repeated starting from Step 1.

Step 4.3.1.2

Experimental variogram values are calculated using grade values in D; then, a 2-D variogram model $\gamma(\boldsymbol{h})$ is fitted to the experimental points. Average lag distance h_{xy} (Section 3.3.2) is used for the variogram calculations. Details about the automatic variogram modeling are provided in Section 3.4.2. If the number of nearby samples nd is insufficient for calculating the experimental variogram values, the initial specified number of nearby samples should be increased and the k-fold cross-validation procedure should be repeated starting from Step 1.

Step 4.3.2

Steps 4.3.1.1 - 4.3.1.2 are repeated for all variables $g = 1, ..., G$.

Steps 4.4 - 4.5

The cross-validation algorithm continues at a location $\boldsymbol{u} \in V_i$; previously saved variogram models and anisotropy directions for each variable associated with $\boldsymbol{x}$ are retrieved.

Step 4.5.1

The simulation part of the algorithm starts with a grade variable g.

Step 4.5.2

The BH samples from D and a variogram model $\gamma(\boldsymbol{h})$ are used to solve normal equations for this variable.

Steps 4.5.2.1 - 4.5.2.2

Normal equations are solved and a conditional mean and standard deviation are obtained. A number of values $z^l(\boldsymbol{u})$, $l = 1, ..., L$ are drawn from a cumulative distribution function defined by the mean and standard deviation. The higher the number of simulated values L, the better local uncertainty is estimated. However, selecting a large value for L will

significantly decrease the operation time of AGC-EP. Guidance on selecting a reasonable value for L is provided later in Section 3.5.

Step 4.5.3

Steps 4.5.2.1 - 4.5.2.2 are repeated for all variables $g = 1, ..., G$.

Step 4.5.4

In order to test the performance of AGC-EP, an alternative estimate is obtained. A nearest neighbor (NN) estimate $z_{NN}(\boldsymbol{u})$ is obtained with the BH samples from D and used to estimate profit at location $\boldsymbol{u}$. The performance of AGC-EP and NN is compared with respect to true profit across all locations $\boldsymbol{u} \in A$ in the end of the workflow.

Step 4.5.5

The back-transformation information saved for $\boldsymbol{x}$ is used to back-transform the simulated values from Step 4.5.2.2 to original units.

Step 4.6

In this step, the profit and expected profit values are calculated for mined material destinations $k = 1, ..., K$ using a profit function. The profit function may involve any number of variables. The calculations start with a destination k.

Step 4.6.1

A true local profit value P_{true} for k is calculated using the true values of all the grade variables involved in the profit calculation $z_{true}(\boldsymbol{u}; g)$, $g = 1, ..., G$. The true values are known in the cross-validation mode.

Steps 4.6.2 - 4.6.3

A local expected profit value EP for this destination is calculated using the simulated values $z^l(\boldsymbol{u})$, $l = 1, ..., L$. Then, a squared error SE_{profit} is calculated between the true profit value P_{true} and the expected profit value EP.

Steps 4.6.4 - 4.6.5

Calculate a local profit value P_{NN} using the NN estimates for all the variables involved in the profit calculation. Then, calculate a squared error SE_{profit}^{NN} between the true profit value P_{true} and the NN profit value P_{NN} for this destination.

Step 4.6.6

The squared errors SE_{profit} and SE_{profit}^{NN} are incremented.

Step 4.7

Steps 4.6.1 - 4.6.6 are repeated for all destinations for mined material $k = 1, ..., K$.

Step 4.8

Steps 4.5 - 4.7 are repeated for each location $\boldsymbol{u} \in V_i$ associated with the super grid node location $\boldsymbol{x}$.

Step 5

Steps 4.1 - 4.8 are repeated for all super grid nodes $\boldsymbol{x} \in A$.

Step 6

Squared errors SE_{profit} and SE_{profit}^{NN} are averaged across all the BH locations $\boldsymbol{u} \in V_i$ to obtain the mean squared errors in profit MSE_{profit} and MSE_{profit}^{NN}, respectively. The averaging of the squared error values is not essential for the cross-validation workflow; it is done for consistency with the mathematical notation in Section 3.1.

Step 7

The number of samples n_d is increased by a certain increment (10 samples is a default values). Steps 4 - 6 are repeated a certain number of times or until n_d cannot be increased anymore.

Steps 8 - 9

The minimum values of MSE_{profit} and MSE_{profit}^{NN} for the current fold i are saved. Also, the number of samples n_d corresponding to the smallest MSE_{profit} value is saved.

Step 10

The values of MSE_{profit} and MSE_{profit}^{NN} are incremented and saved.

Step 11

Steps 2 - 10 are repeated for all $i = 1, ..., 5$ folds.

Step 12

The optimal numbers of nearby samples is chosen as the average values of n_d corresponding to the smallest MSE_{profit} values across all the folds.

Step 13

The expected value of the difference between MSE_{profit}^{NN} and MSE_{profit} is calculated. This measure (E_{avg}) indicates the difference in performance between simulation and the

nearest neighbor estimation. Normally, E_{avg} is positive; a negative value would indicate a problem with the input data or parameters.

The 13 major steps explained above summarize the cross-validation part of the expected profit calculation algorithm used in AGC-EP. All the operations are performed automatically. Some parameters for local anisotropy determination and variogram modeling are fixed based on synthetic tests with different true values.

3.4 Local Anisotropy Modeling

Chapter 2 emphasizes the importance of modeling local geological anisotropy for some deposits to make better predictions of grade or profit. For geostatistical modeling in 2-D, local anisotropy parameters can be fully defined by the first angle of rotation (azimuth correction) and the first anisotropy ratio (C. V. Deutsch & Journel, 1998). This information is used within estimation and simulation workflows to make correct local predictions of grade values or uncertainty, respectively.

Within a local multivariate simulation workflow, it is necessary to have tools for local anisotropy modeling that operate fully automatically. This section describes a modification of the MOI algorithm for determining locally varying angles of anisotropy; the algorithm is described in detail with examples. The first anisotropy ratio is determined using the ranges of local variogram models. Automatic variogram modeling is performed using a stochastic optimization algorithm based on weighted least squares described by Larrondo et al. (2003) and J. L. Deutsch (2015).

3.4.1 Determination of the Direction of Local Anisotropy

Variogram maps plotted for lags in different directions and for different distances (Rossi & Deutsch, 2014, p. 102) or smooth kriging estimates can be used to determine the principal direction of geological continuity; another option is to use expert judgment based on available geological information. This approach is usually robust in case of stationary deposits. Determining the principal direction of continuity for deposits with many non-stationary features can be challenging and prone to errors. Models of local anisotropy, expressed

as locally varying anisotropy (LVA) fields, can be used (e.g., by the kriging method from Boisvert et al. (2009)) to better model local geological features as opposed to using stationary anisotropy parameters for such deposits. The idea to use the mass moment of inertia tensors for obtaining local directions of anisotropy was described earlier by Hassanpour (2007). Moment of inertia or rotational inertia can be understood as the inertia of a rigid body rotated around one of the axes of rotation.

$$I = \int r^2 dm$$

where m is the mass and r is the perpendicular distance from the point mass to the axis of rotation.

Moment of inertia can be expressed as a scalar, when the axis of rotation is known, and as a tensor, summarizing the moments and products of inertia for all the axes. The correlation coefficients from a correlation map can be considered as masses m; while the lag distances, for which the correlations are calculated, can be considered as distances to the axes of rotation r. The inertia tensor for a 2-D is expressed as follows:

$$M = \begin{bmatrix} I_{xx} & I_{xy} \\ I_{yx} & I_{yy} \end{bmatrix}$$

The directional moments and products of inertia are calculated according to the following equations:

$$I_{xx} = \sum_{x=-nx}^{nx} \sum_{y=-ny}^{ny} d_y^2 \cdot p_{xy} \tag{3.13}$$

$$I_{yy} = \sum_{x=-nx}^{nx} \sum_{y=-ny}^{ny} d_x^2 \cdot p_{xy} \tag{3.14}$$

$$I_{xy} = I_{yx} = -\sum_{x=-nx}^{nx} \sum_{y=-ny}^{ny} d_x \cdot d_y \cdot p_{xy} \tag{3.15}$$

where I_{xx} is the moment of inertia around the x axis; I_{yy} is the moment of inertia around the y axis; I_{xy} and I_{yx} are the products of inertia; nx and ny are the total numbers of cells of a correlation map in the x and y directions, respectively; ρ_{xy} is the correlation coefficient corresponding to a particular cell of the correlation map.

The correlation coefficient is calculated as follows:

$$\rho_{xy}(\boldsymbol{h}) = \frac{C\{Z(\boldsymbol{u}), Z(\boldsymbol{u+h})\}}{\sqrt{Var\{Z(\boldsymbol{u})\} \cdot Var\{Z(\boldsymbol{u}+\boldsymbol{h})\}}}$$

The inertia tensor describes a current state of an anisotropic property (correlation) in a given coordinates system. It is possible to find such an angle θ that would rotate the initial coordinates system such that the off-diagonal elements of the tensor are equal to 0; this means the new coordinate axes would be aligned with the principal directions of geological continuity.

Hassanpour (2007) indicates that the eigenvectors and eigenvalues of the inertia tensor can be used to determine the principal directions of anisotropy. In this case, the eigenvalue decomposition of the inertia tensor should be performed. The eigenvector corresponding to the largest eigenvalue should be used to find the principal angle of rotation between the coordinate axes and the current principal direction of continuity.

There are a number of algorithms for finding eigenvalues and eigenvectors of a symmetric matrix. For a 2-D tensor, one would need to find a solution to a classical eigenvalue problem (Wierzbicki, 2013):

$$(M - \lambda_i I)n_i = 0 \tag{3.16}$$

where M is the moment of inertia tensor (2×2), I is an identity matrix; λ_i are the eigenvalues of M and n_i are their corresponding eigenvectors.

Then, the determinant of the matrix $(M - \lambda_i I)$ has to be zero for a solution $n_i \neq 0$ to exist. If this condition is satisfied, the determinant $\det(M - \lambda_i I) = 0$ has to be solved for λ_i to obtain a characteristic polynomial. Then, the roots λ_i of the characteristic polynomial are substituted into Equation (3.16) to obtain eigenvectors.

3.4.1.1   A Simple Example of Finding Anisotropy Directions with the MOI method

An artificial reference model is simulated using $sgsim$ (C. V. Deutsch & Journel, 1998) for an area of 100×100 m^2 with a grid size of 1×1 m^2. The variogram model used for simulation has one spherical nested structure with the nugget effect contribution of 0.1. The major direction of continuity is set at $25°$ from North. The major and minor ranges of continuity are 25 m and 5 m, respectively. The reference model is sampled at the resolution of 5×5 m^2 with a random error in coordinates of up to 1 m; this is done for making the example more realistic. There are 400 artificial BH samples. In order to demonstrate the work of the MOI method, the anisotropy direction is determined globally for the entire map

using the BH samples. The reference realization and BH samples are illustrated in Figure 3.2.

(a) Reference realization
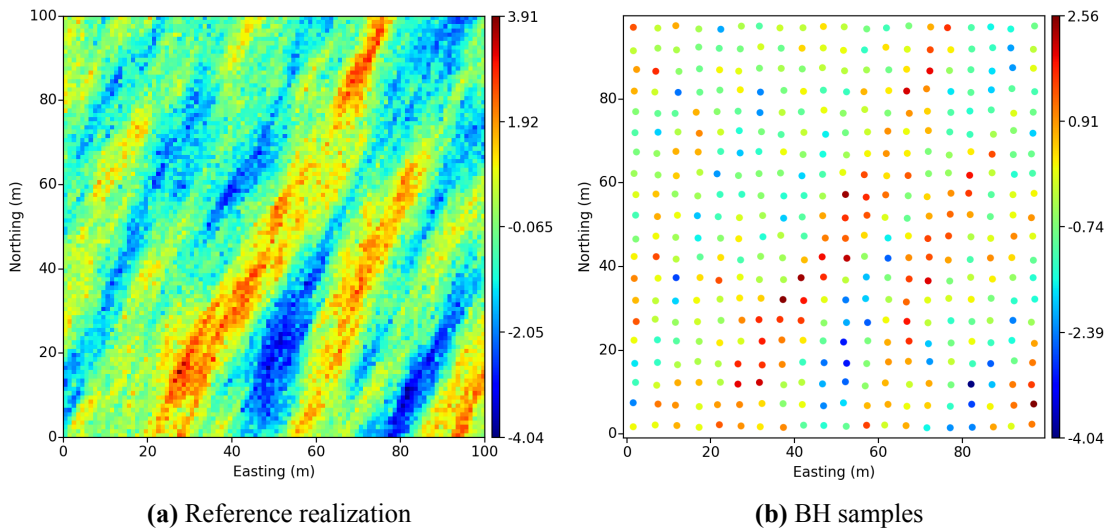
(b) BH samples

Figure 3.2: Artificial reference realization and BH samples (simple example)

A correlation map is calculated using all 400 BH samples. Correlation coefficients are calculated for the lags in the ranges from $-nx = 5$ to $nx = 5$ and from $-ny = 5$ to $ny = 5$. The lag distance is 5 m with the lag tolerance of 2.5 m. The correlation map is illustrated in Figure 3.3.
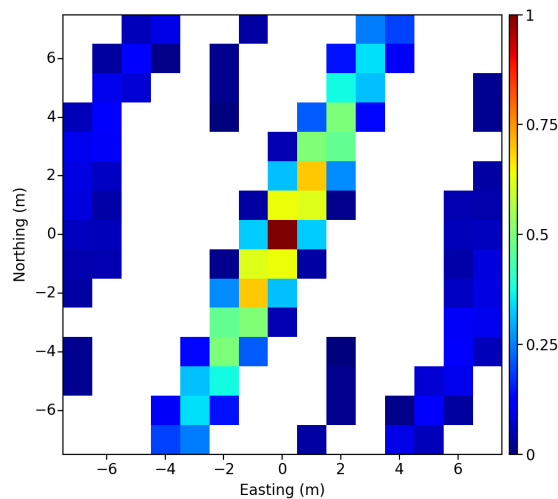
Figure 3.3: A global correlation map (simple example)

Negative correlations are not used for the calculation of the moments and products of inertia and, therefore, not shown in the correlation map.

Equations (3.13) - (3.15) are used to calculate the moments and products of inertia for tensor M:

$$M = \begin{bmatrix} 229.755 & -40.366 \\ -40.366 & 149.839 \end{bmatrix}$$

The determinant of $(M - \lambda_i I)$ is calculated as follows:

$$\det \begin{bmatrix} 229.755 - \lambda & -40.366 \\ -40.366 & 149.839 - \lambda \end{bmatrix}$$

$$\det(M - \lambda_i I) = (229.755 - \lambda)(149.839 - \lambda) - (-40.366^2) = \lambda^2 - 379.594\lambda + 32796.845$$

$$\lambda_1 = 246.595; \ \lambda_2 = 132.999$$

The largest eigenvalue $\lambda_1 = 246.595$ is substituted into Equation (3.16) to obtain a corresponding eigenvector (Wierzbicki, 2013):

$$\begin{bmatrix} 229.755 - 246.595 & -40.366 \\ -40.366 & 149.839 - 246.595 \end{bmatrix} \begin{bmatrix} e_x \\ e_y \end{bmatrix} = \begin{bmatrix} 0 \\ 0 \end{bmatrix}$$

Next, the following equation with two unknown values can be derived:

$$(229.755 - 246.595)e_x - 40.366e_y = 0$$

Any e_x and e_y satisfying the equation above are the components of an eigenvector; therefore, it is possible to set e_y to 1 and then solve for e_x:

$$e_x = \frac{40.366}{-16.84} = -2.397$$

Then, the eigenvector is normalized as follows:

$$n_1 = \frac{1}{\sqrt{(-2.397)^2 + 1^2}} \begin{bmatrix} -2.397 \\ 1 \end{bmatrix} = \begin{bmatrix} -0.923 \\ 0.385 \end{bmatrix}$$

Eigenvector n_1 points in the direction of the principal moment of inertia, which is the minor direction of anisotropy. The angle of rotation defined by eigenvector n_1 and an

initial axis is 90 °apart from the first anisotropy angle, defined according to the GSLIB conventions (C. V. Deutsch & Journel, 1998). The first anisotropy angle can be determined as follows:

$$\alpha_{major} = \arctan\left(\frac{-0.923}{0.385}\right) + 90\,° = 22.64\,°$$

The calculated angle of anisotropy α_{major} equals to 22.64 °, which is a 9.44 % difference from the theoretical angle of 25 °. Even though the calculated angle is unlikely to be exactly 25 °due to the relatively small size of the artificial reference model and, as a result, the lack of stationarity, it is possible to increase the accuracy and reliability of the MOI method. The anisotropy angle can also be determined using a method based on Mohr's circle, which is described in Hassanpour (2007). More information about Mohr's circle can be found, for example, in Beer, Johnston, Mazurek, Cornwell, and Self (2015, p. 523-528).

3.4.1.2 Fixing Algorithm for Correlation Maps

The determination of the direction of anisotropy with the MOI method is based solely on correlation maps. Therefore, the quality of the correlation maps is the most important factor for the reliability of the method. This is especially important for deposits with complex locally varying geology and/or sparse data. The correlation map in Figure 3.3 shows a cluster of cells with high correlation coefficients directed at approximately 25° from North. However, there are obvious artifacts at the sides of the correlation map that may potentially decrease the accuracy of the MOI method.

An algorithm is developed for removing cells that are not relevant for determining the correct principal direction of anisotropy. There are two conditions for a cell of the correlation map to be considered valid and left in the correlation map: i) its correlation coefficient value has to be above some minimum threshold value, and ii) it has to be connected to at least one cell previously considered valid. The central cell of the correlation map with the correlation coefficient value of 1 is considered valid by default. The minimum threshold value is determined as the fraction of the maximum correlation value of the correlation map; the central cell of the map is not taken into account. A cell under consideration can be connected to a valid cell in four directions measured from the current cell: i) one cell to the right, ii) one cell to the left, iii) one cell up, and iv) one cell down. Valid cells connected

to the cell under consideration diagonally are not considered to avoid artifacts in a final correlation map.

At each pass of the algorithm, cells of the correlation map under consideration are all the cells defined in the range from $-n_x$ to n_x and from $-n_y$ to n_y. At the first pass, the range is defined from $-n_x = -1$ to $n_x = 1$ and from $-n_y = -1$ to $n_y = 1$; at the second pass the range is defined from $-n_x = -2$ to $n_x = 2$ and from $-n_y = -2$ to $n_y = 2$. At each subsequent pass, the range is increased by one cell in each direction until it reaches a maximum number of cells; it is assumed that using large correlation maps with many cells is better in terms of the precision of the angle calculation (provided the fixing algorithm is used) than using small correlation maps. The maximum number of cells is adjusted automatically depending on the dimensions of a mine bench and the maximum number of lags that can be calculated; this number is limited (7 is a default number) to avoid excessive computational time for large benches.

The fixing algorithm consists of the following steps:

Step 1

Check all the cells of the correlation map in the range from $-n_x$ to n_x and from $-n_y$ to n_y.

Step 2

Save all cells in the range that satisfy the conditions of validity.

Step 3

Increase the range by one cell in each direction and repeat Steps 1 - 2.

Step 4

Reset the range to one cell in each direction and repeat steps 1 - 3.

Step 4 is performed to account for the cells not considered in the first iteration of the algorithm. Figures 3.4 - 3.5 illustrate all the passes of the two iterations of the algorithm using the correlation map from the simple example in Section 3.4.1.1; the fraction of maximum correlation of 0.3 is chosen for this example.
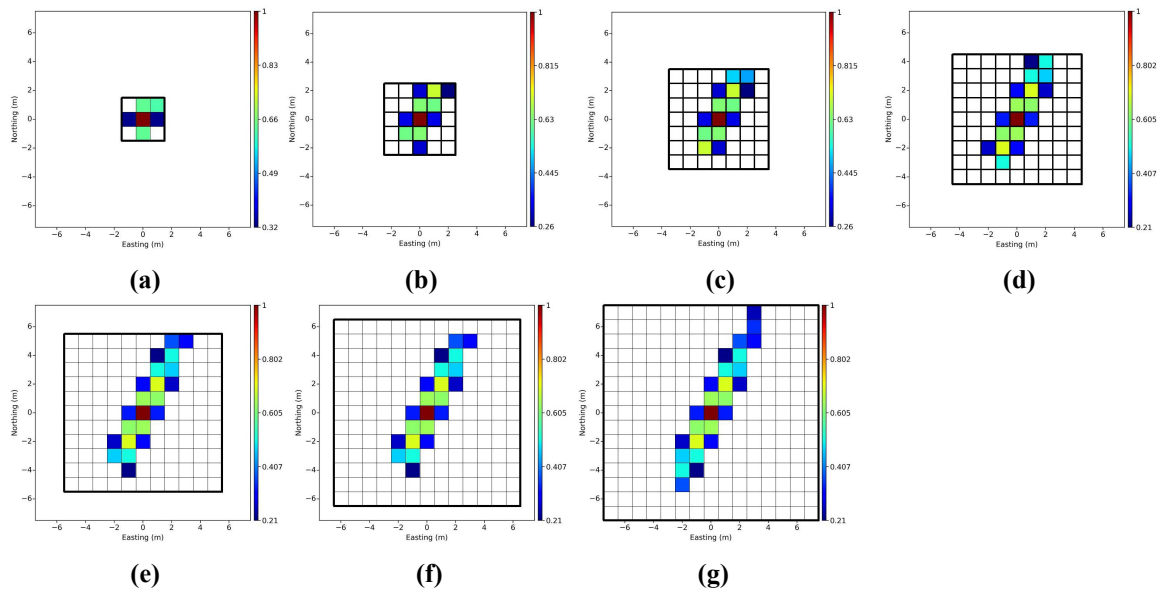
Figure 3.4: First iteration of the fixing algorithm

Figure 3.4g illustrates that not all the valid cells are found after the last pass of the first iteration of the algorithm; this is because the algorithm visits all the cells in a neighborhood (black colored grid in Figure 3.4) starting from the bottom left cell, which results in some valid cell not having a valid neighbor. The second pass of the algorithm detects the rest of valid cells, which results in a symmetrical map (Figure 3.5).
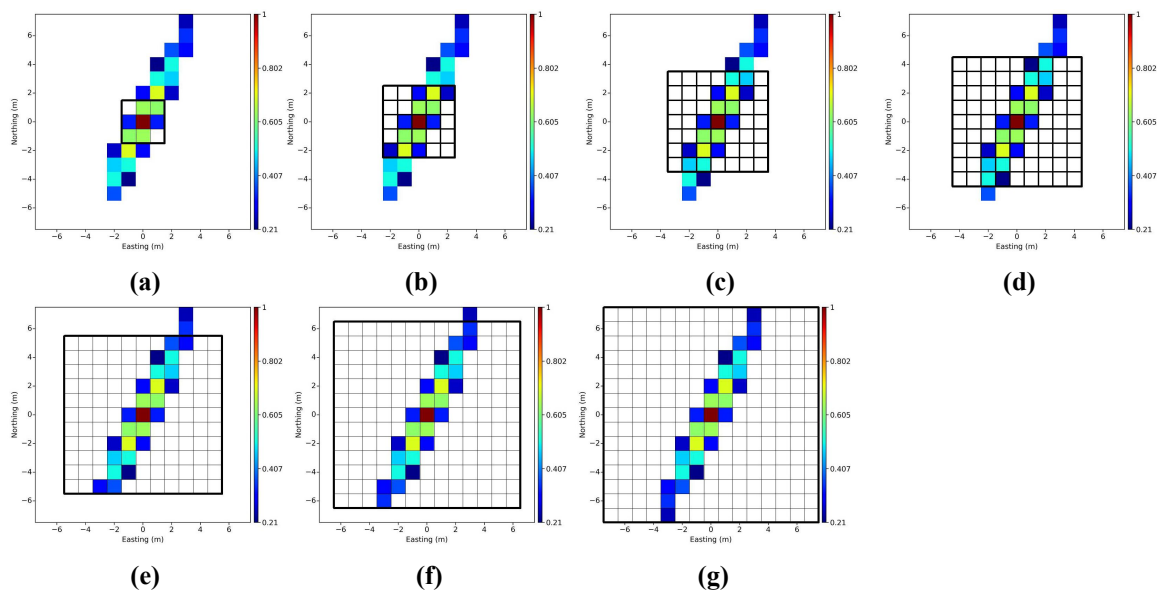
Figure 3.5: Second iteration of the fixing algorithm

Figure 3.5g demonstrates that all the valid cells are found and the fixed correlation map is symmetrical. The MOI algorithm from Section 3.4.1.1, performed with the fixed correlation map from Figure 3.5g, determines the first anisotropy angle to be 25.67°; this is a 2.68 % difference from the theoretical angle of 25°. The use of the fixed correlation map from Figure 3.5g with the MOI method resulted in significantly more accurate detection of the principal direction of anisotropy for this artificial example.

3.4.1.3 Selection of the Fraction of Maximum Correlation

Unsupervised use of the MOI method coupled with the new fixing algorithm for correlation maps (Section 3.4.1.2) requires specifying the fraction of maximum correlation (FMC) value. This process is largely automated inside AGC-EP. All the elements of the tensor calculated in Equations (3.13) - (3.15) must be non-zero. If M has a zero entry, it indicates that there is likely not enough data for calculations. Therefore, the minimum FMC specified by default is automatically decreased by a small number (allowing more cells of the map to be considered valid) until all the entries of the tensor M are greater than zero. FMC can be set as large as 1.0 since the algorithm will automatically reduce it until the moment of inertia calculations are possible. An artificial experiment is designed to define a reasonable range for FMC

Reference realizations of *sgsim* (C. V. Deutsch & Journel, 1998) are obtained for an area of 100×100 m^2 (representing domain A). The realizations are then sampled at a grid of 5×5 m^2 with a random error of up to 1 m in coordinates. The variogram model used for simulation has one spherical nested structure; other parameters of the variogram model change depending on a particular reference realization. The MOI method is used to determine major anisotropy directions at all locations of the domain A. The major directions of anisotropy, measured with MOI, are checked against theoretical directions of anisotropy used to simulate the reference realizations. The directions are represented by the first anisotropy angles (azimuths) measured from North (C. V. Deutsch & Journel, 1998). Let $\alpha_1, ..., \alpha_N$ and $\beta_1, ..., \beta_N$ be the theoretical and measured angles of anisotropy at N locations of A, respectively. A mean squared error between the measured and theoretical

angles is calculated using the following expression:

$$MSE_{ang} = \frac{1}{N} \sum_{i=1}^{N} \left(\frac{(\alpha_i - \beta_i)^2}{90^2} \right) \cdot 100\% \qquad (3.17)$$

where MSE_{ang} is the mean squared error between the theoretical and measured angles standardized by the maximum possible error of 90^2.

The mean squared error from Equation (3.17) is used as a performance measure for the MOI method to select a reasonable fraction of maximum correlation in the range from 0.0 to 1.0. A series of influencing factors are taken into account when simulating artificial reference realizations to avoid a bias in results: i) theoretical angles of anisotropy change in the range from 0° to 150° with a step of 30°, ii) the ratios between the major and minor ranges of continuity change from 2:1 to 10:1, iii) the nugget effect contribution change from 0.0 to 0.6 with a step of 0.1, and iii) the numbers of local data used by the MOI method change from 20 to 100 samples with a step of 10 samples. Reference models are simulated for each of the factors in its corresponding range and for 10 realizations, which results in 3780 reference realizations in total. Finally, MSE_{ang} is averaged across all the 3780 reference realizations for each instance of FMC. The theoretical angles of anisotropy and the ranges of geological continuity are specified through the variogram model used for simulating the reference realizations. Table 3.1 and Figure 3.6 summarize the experiment results.
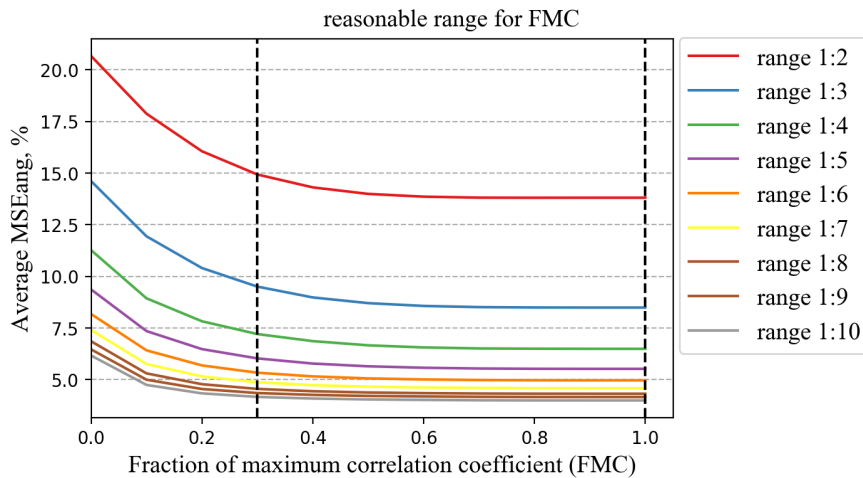
Figure 3.6: Fraction of maximum correlation versus the average mean squared error between the theoretical and measured angles of anisotropy

Table 3.1: Average mean squared error between the theoretical and measured angles of anisotropy for different FMC values

FMC	Range 1:2	Range 1:3	Range 1:4	Range 1:5	Range 1:6	Range 1:7	Range 1:8	Range 1:9	Range 1:10
0	20.664	14.611	11.269	9.368	8.177	7.404	6.860	6.468	6.170
0.1	17.872	11.939	8.939	7.353	6.421	5.757	5.306	5.001	4.748
0.2	16.056	10.405	7.829	6.481	5.692	5.160	4.783	**4.550**	**4.340**
0.3	**14.931**	9.506	7.209	**6.032**	**5.340**	**4.877**	**4.556**	4.356	4.169
0.4	14.308	**8.982**	**6.868**	5.782	5.161	4.738	4.442	4.266	4.089
0.5	13.992	8.706	6.665	5.649	5.064	4.663	4.383	4.216	4.046
0.6	13.858	8.570	6.562	5.579	5.013	4.624	4.351	4.189	4.023
0.7	13.811	8.514	6.514	5.544	4.985	4.603	4.332	4.171	4.005
0.8	13.806	8.495	6.501	5.529	4.974	4.593	4.324	4.164	3.999
0.9	13.808	8.491	6.496	5.526	4.971	4.590	4.323	4.163	3.998
1.0	13.808	8.491	6.495	5.526	4.971	4.590	4.323	4.163	3.998

Black dashed lines on the graph in Figure 3.6 indicate a reasonable range for FMC. A lower boundary for FMC for each of the anisotropy ratios corresponds to an MSE_{ang} value that is not higher than a minimum MSE_{ang} value for this case by more than 10 % (bolded values in Table 3.1); the average of all the lower boundaries for the FMC values (0.3) is a lower limit of the reasonable range for FMC. An upper limit for the reasonable range is 1.0. The results of the artificial experiment confirm the assumption that FMC can be set as high as 1.0 to ensure low MSE_{ang}. The FMC of 1.0 is a default value for the fraction of maximum correlation inside AGC-EP.

3.4.1.4   Example with Complex Local Anisotropy

Two complex artificial examples are created to test the modified MOI algorithm. Locally varying directions of anisotropy are determined at each sample location and compared to theoretical local angles of anisotropy. Different numbers of nearby samples are used for determining directions; optimal ranges for the numbers of nearby samples are determined for each example

Example 1

The first complex example is represented by realizations of grade, with incorporated arti-

ficial LVA information, simulated for an area of 300×200 m^2 at a grid of 1×1 m^2. A modified version of $sgsim$ (C. V. Deutsch & Journel, 1998) is used to simulate the reference realizations with pre-determined local anisotropy parameters; the modified program takes local anisotropy parameters (angles and ratios) as an input at each simulated location to reproduce complex non-stationary geological features in simulated models. The example represents a case that may be challenging for an estimation or simulation algorithm not accounting for LVA; major direction of geological continuity, represented by the first anisotropy angle, changes from 135° on the left side of the area to 90° in the center of the area and 45° from North on the right side of the area. A variogram model used for simulation has one spherical nested structure and the nugget effect of 0.1. Major and minor ranges of continuity are 50 m and 10 m at the sides of the area and 100 m and 10 m in the center. The mine bench is sampled at a grid of 5×5 m^2 with a random error in coordinates of up to 1 m. A reference realization and sampled locations for this example are illustrated in Figure 3.7.

(a) Reference realization

(b) BH samples
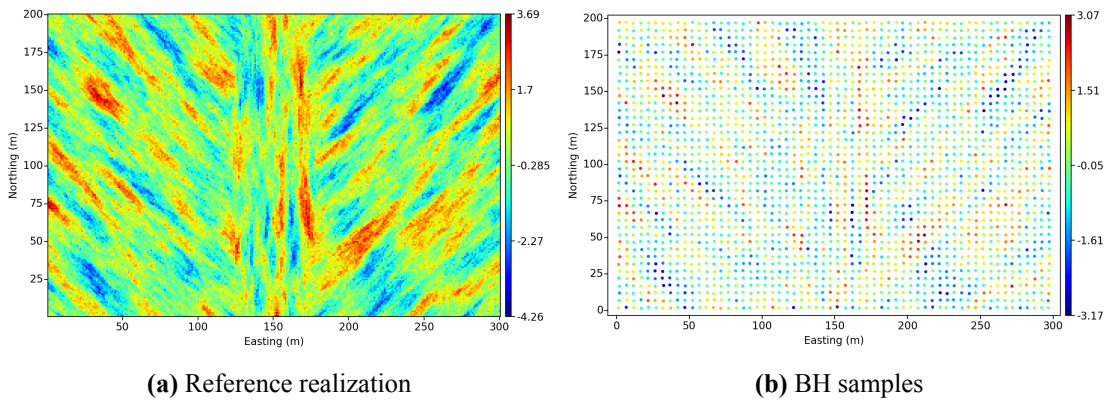
Figure 3.7: Reference realization and samples (example 1)

The fraction of maximum correlation is set to 1.0 according to the conclusion from Section 3.4.1.3. There are 2400 samples in total; different numbers of local samples are used with the modified MOI method to determine locally varying angles of anisotropy in 2-D; results are averaged over 10 reference realizations for stability. For this example, the true angles of anisotropy at each location are known since they were used to obtain the reference realization with $sgsim$. Therefore, Equation (3.17) is used to calculate the mean squared error MSE_{ang} between the true and measured angles. A graph in Figure 3.8 summarizes

the performance of the modified MOI method with the numbers of nearby samples in the range from 20 to 200 with a step of 5 samples.
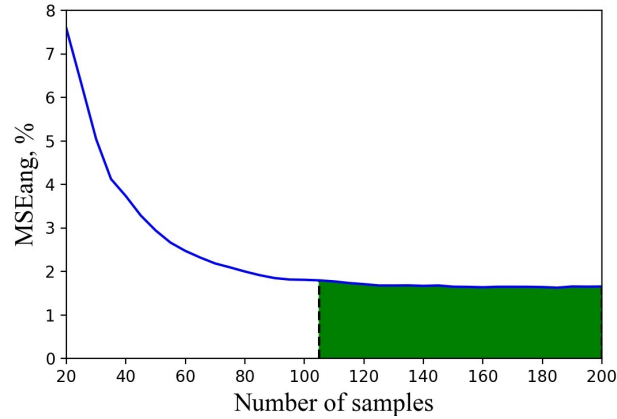
Figure 3.8: Number of nearby samples used at each location with the modified MOI method versus mean squared error between the theoretical and measured angles of anisotropy (example 1)

According to the graph in Figure 3.8, the performance of MOI improves with the increase in the number of samples used locally. The green area under the graph indicates the range where MSE_{ang} does not exceed 10 % of the lowest MSE_{ang} value of 1.625 % (achieved with 185 nearby samples). Figure 3.9 displays local anisotropy angles estimated by the modified MOI method with 50, 100, 150, and 200 samples used locally; the reference map for the first example is shown with the anisotropy angles, depicted as vectors, superimposed on it.

(a) 50 samples

(b) 100 samples

(c) 150 samples

(d) 200 samples
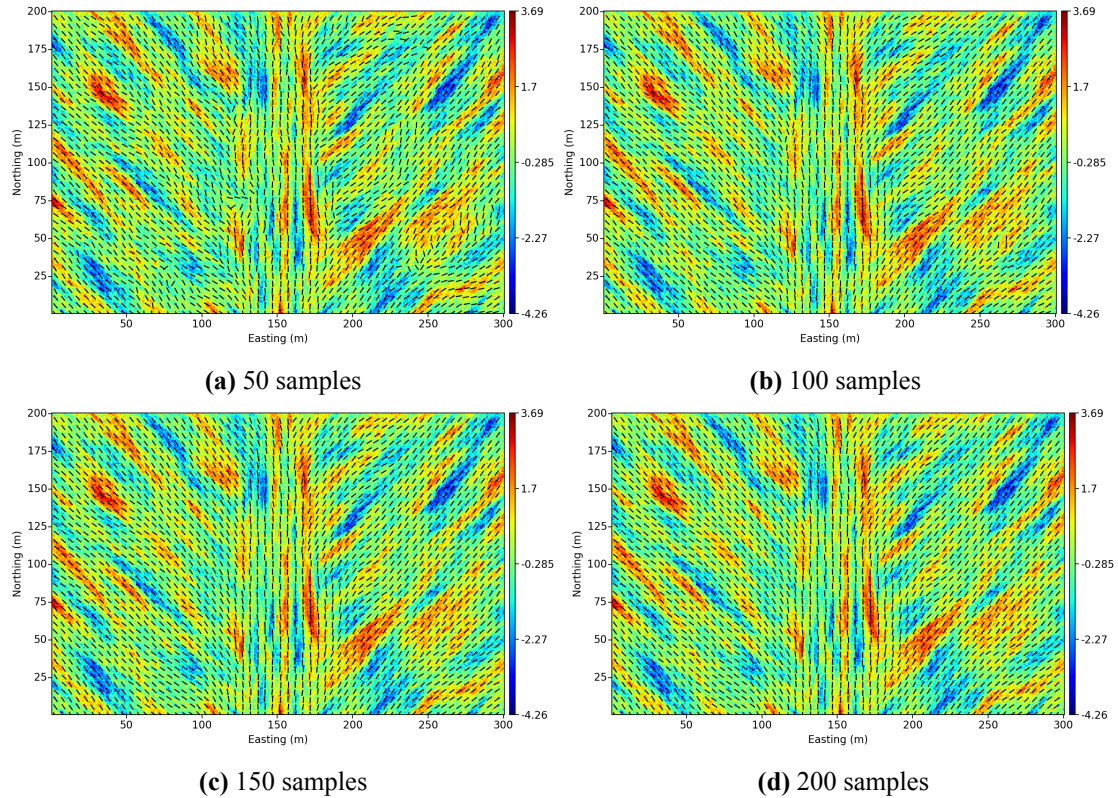
Figure 3.9: Local anisotropy angles obtained with the modified MOI method (example 1)

Figure 3.9 illustrates that using the modified MOI method with 50 and 100 local samples results in overfitting to local geological features, which results in higher MSE_{ang} values compared to using the MOI method with 150 and 200 local samples.

Example 2

The second complex case represents even more challenges for correct anisotropy estimation. Reference realizations are simulated for an area of 300×200 m^2 at a grid of 1×1 m^2 and sampled at a grid of 5×5 m^2 with a random error in coordinates of up to 1 m. For most of this reference realization, major direction of anisotropy is at 0 degrees from North; major and minor ranges of geological continuity are 75 and 15 m, respectively. There is an annulus area in the center of the realization, inside which the major anisotropy direction changes in a circular manner; the minor and major ranges are 25 and 5 m, respectively. A variogram model used for simulation has one spherical nested structure with the nugget effect of 0.1. A reference realization and samples for this example are illustrated in Figure 3.10.

(a) Reference realization

(b) BH samples
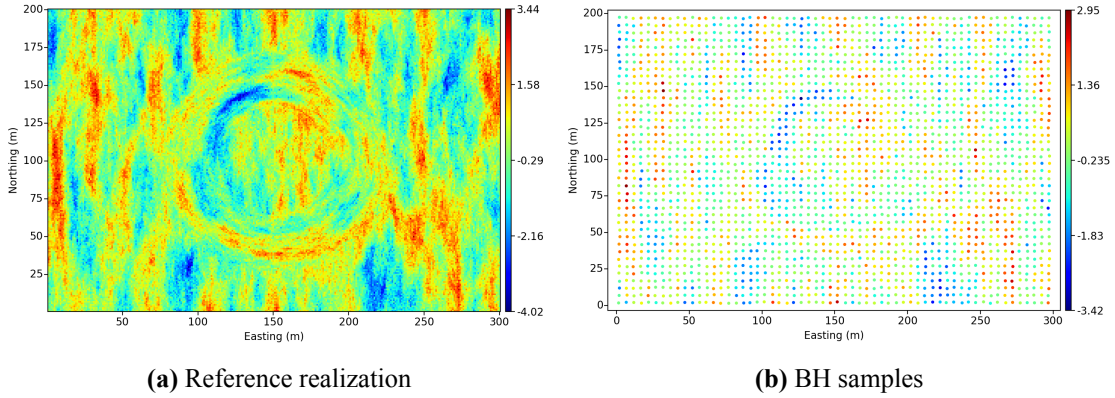
Figure 3.10: Reference realization and samples (example 2)

The performance of the modified MOI method with different numbers of samples used locally is performed similarly to the first example; theoretical angles of anisotropy are compared to measured ones at each sample location. Results are averaged over 10 reference realizations. A graph in Figure 3.11 summarizes the performance of the modified MOI method for the second example with the numbers of samples in the range from 20 to 200 with a step of 5 samples.
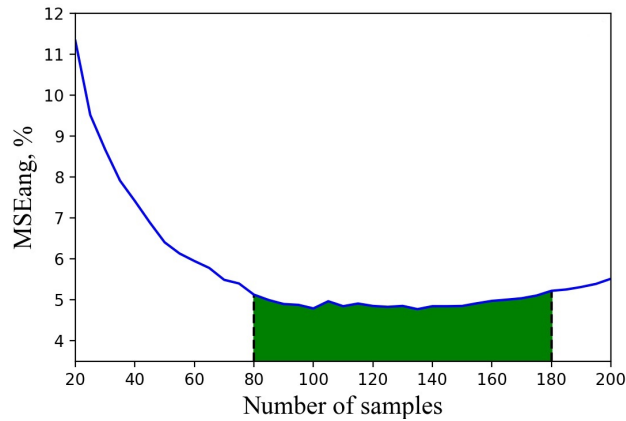
Figure 3.11: Number of samples used locally with the modified MOI method versus mean squared error between the theoretical and measured angles of anisotropy (example 2)

The graph in Figure 3.11 indicates an optimal range for the numbers of nearby samples (green area under the curve) from 80 to 180 samples; in this range, MSE_{ang} does not exceed the minimum MSE_{ang} of 4.78 (achieved with 135 samples) by more than 10 %, whereas using more than 180 samples results in an increase of MSE_{ang}. Since using more samples

64

results in determining more global directions of anisotropy at each location, the annulus feature in the center may be disregarded; this results in higher MSE_{ang} values. Figure 3.12 displays local anisotropy angles estimated by the modified MOI with 50, 100, 150, and 200 samples used locally for example 2.

(a) 50 samples   **(b)** 100 samples

(c) 150 samples   **(d)** 200 samples
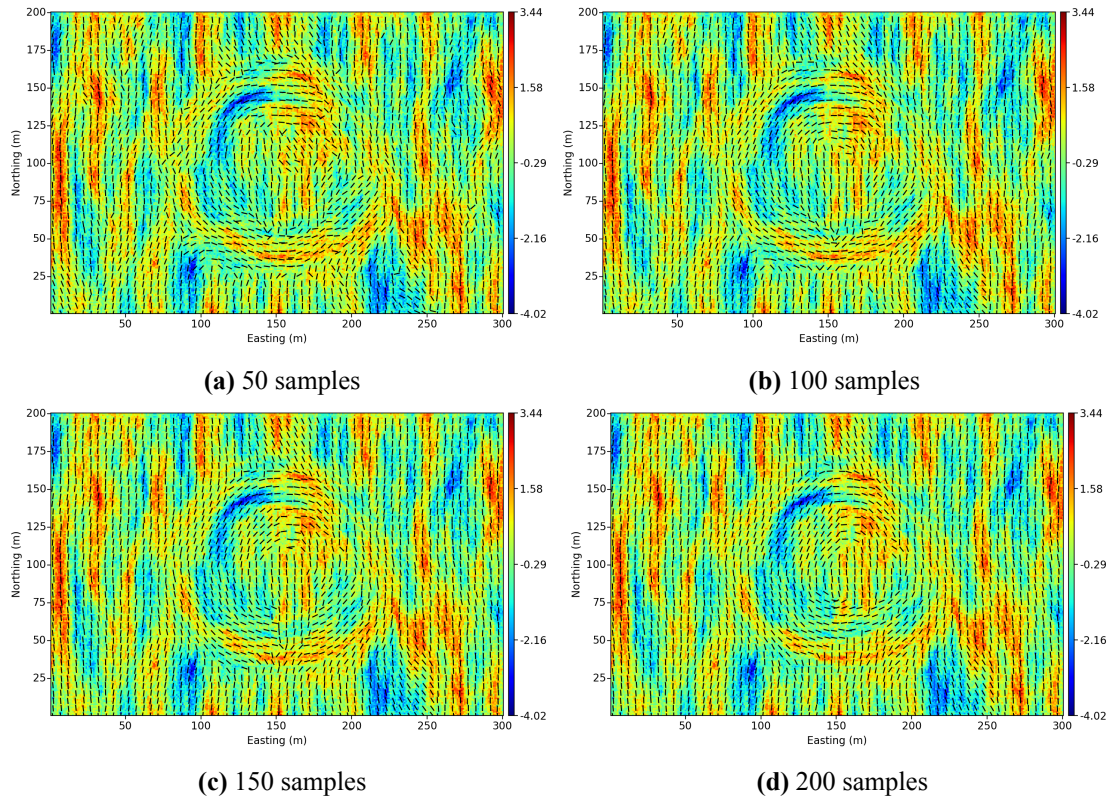
Figure 3.12: Local anisotropy angles obtained with the modified MOI method (example 2)

Similar to the previous example, the number of samples used locally determines how well local geological features are captured. Overall, the modified MOI method works relatively well with any number of samples due to the ability to change its sensitivity automatically (tuning FMC). Since the true angles of anisotropy are unknown with real grade control data and MSE_{ang} cannot be used as a performance measure, an optimal number of samples should be selected based on a different performance measure. When incorporated into the AGC-EP modeling workflow, the performance of the modified MOI method is measured indirectly by the mean squared error between the true and estimated profit values during the k-fold cross-validation procedure. Parameters of local anisotropy corresponding to the best profit predictions are selected.

3.4.2 Automatic Variogram Modeling

Automatic variogram modeling is relatively simple in grade control due to the following reasons: i) the number of BH samples is usually sufficient; regular blasts in open pits often have anywhere between 100 and 400 blastholes, ii) the distances between BH samples are relatively short, and iii) the BH samples are situated in a regular pattern.

The average lag distance h_{xy} is calculated beforehand using Equation (3.11). A variogram value for a lag distance $\boldsymbol{h}$ is calculated using Equation (2.1). If the Euclidean distance between a BH sample at a location $\boldsymbol{u}$ and a BH sample at a location $\boldsymbol{u} + \boldsymbol{h}$ in a particular direction is greater than or equal to $h_{xy} \times j - h_{tol}$, $j = 0, ..., n_h$ and is less than or equal to $h_{xy} \times j + h_{tol}$, $j = 0, ..., n_h$, these two locations, separated by $\boldsymbol{h}$, are accepted for the variogram calculations; the number of lags j scales the average lag distance h_{xy} accounting for some lag tolerance h_{tol}. The number of lags should depend on the dimensions of a mine bench. The maximum lag distance should not be more than a half of deposit A (Rossi & Deutsch, 2014, p. 101). Dimensions of deposit A are measured in the x and y directions; the largest dimension $d_{largest}$ is used to calculate the maximum number of lags as follows:

$$n_h = \frac{d_{largest}}{2 \cdot h_{xy}}$$

The maximum number of lags n_h is rounded up to the nearest integer. The maximum number of lags in any direction cannot exceed 10 by default to limit calculations for large domains. Variogram modeling is performed at each super grid node location $\boldsymbol{x}$ using nearby BH samples associated with it. Grade values in the BH samples are normal score transformed (using the quantile-to-quantile method) prior to the experimental variogram calculations.

Local anisotropy directions are calculated using the modified MOI method. For each grade variable, experimental variogram values are calculated for major and minor directions of continuity using the algorithm from J. L. Deutsch (2015). Some input parameters for the variogram calculation and modeling are fixed during tests or with respect to the spatial configuration of data to support automatic operation. The fixed parameters for the variogram calculation can be summarized as follows:

- Lag tolerance is calculated as $h_{xy} \times 0.5$. Calculating the lag tolerance as a half of the lag distance is a common practice (Rossi & Deutsch, 2014, p. 101; Pyrcz & Deutsch, 2014, p. 83). The lag tolerance can be reduced since blastholes are usually bored on a regular grid. The significant tolerance is used to account for data with positioning errors.

- Azimuth is calculated beforehand using the MOI method; azimuth tolerance is set to 22.5°. The azimuth tolerance should be selected as small as possible to better estimate directional anisotropy (C. V. Deutsch & Journel, 1998, p. 59). The value of 22.5° is mentioned by Pyrcz and Deutsch (2014, p. 84) as a reasonable tolerance parameter, which should be iteratively refined. The relatively large azimuth tolerance is used inside AGC-EP to account for data with positioning errors.

- Horizontal bandwidth is calculated as $h_{xy} \times 1.5$. Pyrcz and Deutsch (2014, p. 84) recommend to use a relatively small horizontal bandwidth if there are sufficient data; the values between 1 to 3 lag distances are recommended.

- Dip and tilt are set to 0 °.

The tolerance parameters used inside AGC-EP assume densely spaced data at a regular pattern; they should be refined for other data configurations. Experimental variogram values and directions of continuity determined with the modified MOI method are used with a stochastic optimization algorithm described in Larrondo et al. (2003) and J. L. Deutsch (2015) to fit a variogram model. The algorithm starts by determining an initial guess variogram model; an initial objective value is a weighted mean squared error between the experimental variogram points and variogram points obtained using the variogram model. Then, the initial values of some parameters of the variogram model (e.g., ranges, the contributions of the nugget effect and nested structures, etc.) are randomly changed by adding to or subtracting from them small values; changes to the model bringing improvement to the objective function are accepted. The algorithm performs a certain number of iterations (this parameter is explained below) to decrease the objective function.

Within AGC-EP, the majority of parameters for variogram modeling, including the variogram ranges, the nugget effect contribution (optimization boundaries are from 0 to 1.0),

the types of variogram nested structures (spherical, exponential, or Gaussian), and the contributions of nested structures are unconstrained during optimization for a higher flexibility and decreasing the number of input parameters. In order to obtain an initial variogram model, reasonable parameters are chosen within the algorithm; for instance, the variogram ranges are calculated by diving the maximum experimental lag distance in a corresponding direction to the number of nested variogram structures used to fit the model. Experimental variogram values are standardized by the variance of all data; the variogram model sill value is fixed at 1. Experimental variogram values calculated using as few as 1 pair accepted for optimization; the weighting of the experimental variogram points by the number of pairs is used for better fitting to the variogram points calculated using more information. In addition, weighting the variogram points by the inverse distance is used for better fitting to the variogram points at short lag distances (Larrondo et al., 2003). Other crucial parameters such as the number of variogram nested structures being fit and the total number iterations of the optimization algorithm are fixed. Ideally, the k-fold cross-validation should be used to optimize these parameters along with optimizing the number of nearby samples. Unfortunately, the k-fold cross-validation operation time would increase significantly in this case, since the number of times the cross-validation procedure is repeated would grow significantly with the addition of each new parameter being optimized.

Selecting Parameters for the Optimization Algorithm

In order to select the number of iterations of the optimization algorithm to be used within AGC-EP, the results of experiments with artificial data sets are used. The minimum mean squared error in profit MSE_{profit} averaged across 5 folds is used as a performance measure. The cross-validation procedure is repeated with different numbers of iterations of the optimization algorithm (from 200 to 10000). The average minimum MSE_{profit} is saved for each case; the results are averaged over a range of nugget effect values and over 50 realizations (obtained using different seed numbers of a random number generator) for stability.

Realizations of $sgsim$ (C. V. Deutsch & Journel, 1998) are obtained for an area of 100×60 m^2. A variogram model required for simulation has a single spherical nested structure with the nugget effect contribution changing form 0.0 to 0.3 with a step of 0.1. Major direction of anisotropy as well as major and minor ranges of anisotropy change throughout

the area. Most of the first half of the area (from 0 m to 50 m in the West-East direction) is simulated with the major direction of anisotropy at 0° from North and the major and minor ranges of anisotropy of 50 m and 5 m, respectively. Most of the second half of the area (from 50 m to 100 m in the West-East direction) is simulated with the major direction of anisotropy at 0° from North and the major and minor ranges of anisotropy of 25 m and 5 m, respectively. There is a tortuous streak going through the entire area in the West-East direction simulated using different anisotropy parameters. The section of the streak from 0 m to around 27 m in the West-East direction is simulated with the major direction of anisotropy at 12° from North. The section of the streak from around 27 m to around 54 m in the West-East direction is simulated with the major direction of anisotropy at 131.5° from North. The section of the streak from around 54 m to around 100 m in the West-East direction is simulated with the major direction of anisotropy at 51.2° from North. The major and minor ranges of anisotropy within the streak are 50 m and 10 m, respectively. The simulated realizations are converted to be lognormal with the mean and standard deviation of 1.0. The reference realizations are then sampled at a grid of 4×4 m^2 (which results in 375 samples) with a random error of up to 1 m in coordinates. The cutoff-based profit function from Section 3.2.1 is used to calculate expected profit for ore and waste mined material destinations; a cutoff grade of 1.0 is used to distinguish between the two destinations. The scaling coefficients for correct acceptance and correct rejection are set to 1.0. Cross-validation is repeated using the number of nearby data for simulation in the range from 60 to 150 with a step of 10 samples. The super-grid multiplier v_{const} of 3 is used to decrease the cross-validation operation time. One thousand simulated values is used for expected profit calculation. An example of a simulated realization and sampled data are in Figure 3.13.

(a) Reference realization **(b)** Sampled data
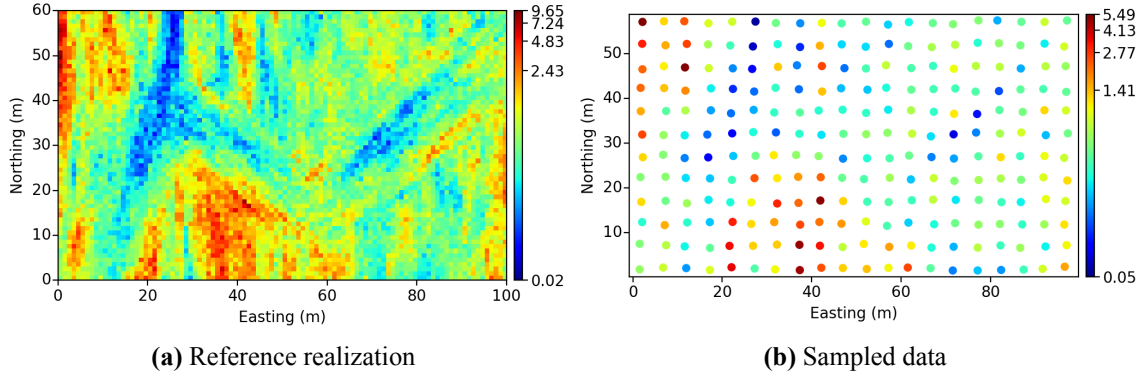
Figure 3.13: Example of an $sgsim$ realization used for selecting variogram modeling parameters

Figure 3.14 summarizes the performance of k-fold cross-validation with different numbers of iterations of the optimization algorithm; the calculations are also repeated for different numbers of variogram nested structures of the variogram model being fit. The average minimum MSE_{profit} and operation time are recorded for each case.

(a) Average minimum MSE_{profit} **(b)** Average cross-validation time
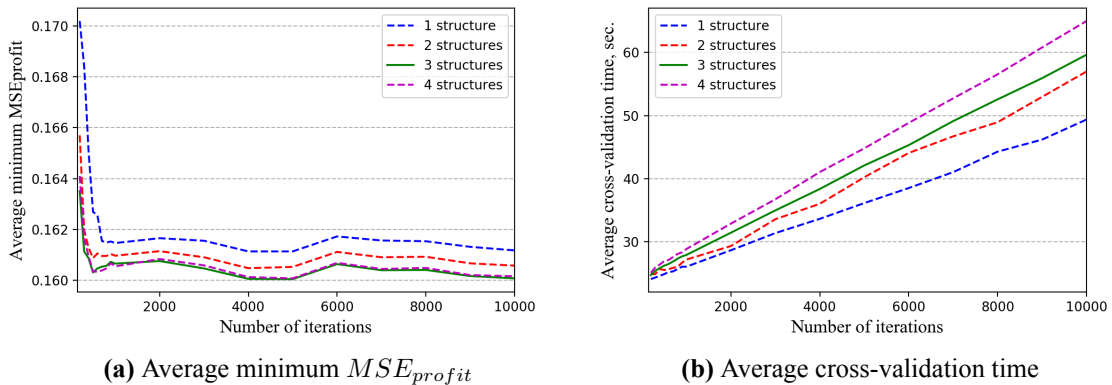
Figure 3.14: Number of iterations of the variogram modeling algorithm versus the average minimum MSE_{profit} and cross-validation time

Analysis of the graph in Figure 3.14 indicates that increasing the number of iterations of the optimization algorithm after a certain limit does not significantly improve the value of the average minimum MSE_{profit}. For each nested structure, an optimal range for the number of iterations is defined where the average minimum MSE_{profit} does not exceed 0.5 % of a corresponding minimum value. The lower boundaries for each nested structure are defined as follows: i) 700 iterations with 1 nested structure, ii) 400 iterations with 2 nested structures, iii) 500 iterations with 3 nested structures, and iv) 500 iterations with 4 nested

structures. An upper boundary is 10000 iterations for each case. Figure 3.14a indicates that the optimization algorithm with 3 and 4 nested variogram structures perform slightly better than the other options; the option with 3 structures is chosen for AGC-EP due to faster operation. Figure 3.14b shows that the operation time grows linearly with the increase in the number of iterations of the optimization algorithm. As few as 500 iterations can be used with 3 nested structures to minimize the operation time; however, 2000 of iterations are selected for AGC-EP to account for more complex cases of variogram modeling that may occur with real data. The two selected parameters should be changed if the k-fold cross-validation procedure indicates problems with expected profit models.

3.5   Selecting the Number of Simulated Realizations and Super Grid Parameters

The quality of expected profit calculation with AGC-EP is measured by the average minimum MSE_{profit} during the k-fold cross-validation procedure. Important input parameters for simulation such as the number of simulated realizations L and super grid size may have an impact on the value of MSE_{profit} and, consequently, an optimal number of data used for the final expected profit calculation on a grid.

Pyrcz and Deutsch (2014, p.377-379) discuss selecting an optimal number of simulated realizations based on the confidence level for a reported quantile; for example, 6600 realizations is suggested to achieve the 99 % confidence level with the tolerance of +/-1 %. Theoretically, using many realizations is better for grade control decision making, since the entire distribution of a simulated grade is used to estimate profit; the higher precision is required, the more realizations should be used. From the practical point of view, a very high number of simulated realizations may not bring additional benefits for grade control decision making with AGC-EP. Even though simulating realizations is relatively fast within AGC-EP, additional time will be required for back-transforming the simulated values from normal score to original units before expected profit calculation.

Results of an artificial test are used to define a reasonable range for the number of realizations used with AGC-EP. The average minimum MSE_{profit}, obtained with cross-

validation, is used as a performance measure. Reference realizations are simulated with *sgsim* for an area of $120 \times 120 \ m^2$. The variogram model required for simulation has one spherical nested structure. Geological continuity is directed at $45°$ from North with the major and minor ranges of 100 and 20 m, respectively. Realizations are converted to be lognormal with the mean and standard deviation of 1.0 and then sampled at a grid size of $8 \times 8 \ m^2$ with a random error in coordinates of up to 1 m. The cutoff-based profit function (Section 3.2.1) is used to convert simulated grade values to expected profit; the cutoff grade of 1.0 is used. The k-fold cross-validation procedure is run with the numbers of data in the range from 50 to 170 samples with a step of 10 samples. Calculations are repeated for the nugget effect contribution varying between 0.0 and 0.3 with a step of 0.1 and 20 reference realizations; overall, results are averaged over 80 realizations. The test procedure is repeated for different numbers of simulated realizations at each location and for different super grids. The super grid sizes are defined based on the average sample spacing and a scaling coefficient v_{const} (Section 3.3.3). The results of the artificial test are summarized in Figure 3.15.

(a) Average minimum MSE_{profit} **(b)** Average cross-validation time
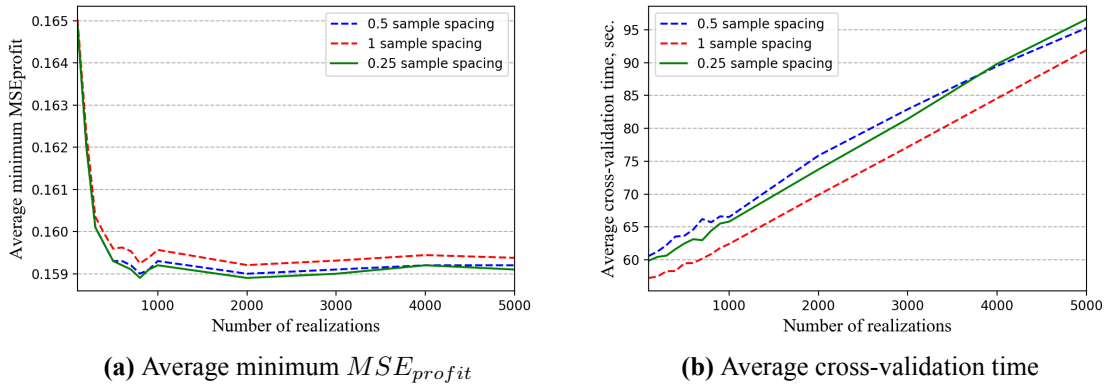
Figure 3.15: Number of local simulated realizations versus the average minimum MSE_{profit}

Analysis of the graph in Figure 3.15a indicates that increasing the number of realizations used locally after a certain limit does not significantly improve the value of the average minimum MSE_{profit}. For each super grid size (represented by the average sample spacing multiplier, v_{const}), an optimal range for the number of realizations is defined where the average minimum MSE_{profit} does not exceed 0.5 % of a corresponding minimum value. The optimal range across all three super grids is between 400 and 5000 realizations.

Considering the rapid increase in the operation time with the increase in the number of realizations used, the number of realizations for AGC-EP is chosen to be 1000. The graph in Figure 3.15a also shows that the super grids with sizes of 0.25 and 0.5 sample spacing perform better than the super grid with the size of 1 sample spacing. The super grid size multiplier, v_{const}, is chosen to be 0.25 for the k-fold cross-validation part of AGC-EP.

3.6 Summary

This chapter describes a new workflow for automatic local multivariate simulation implemented in the first part of the AGC system. Main operations of the workflow include: i) normal score data transformation (multivariate for multiple variables), ii) determination of local anisotropy directions, iii) modeling local variograms, iv) modeling local uncertainty, and v) expected profit calculation. The algorithms used to perform each operation are described. The choice of specific parameters used for the algorithms is explained.

The current version of AGC-EP demonstrates the concept of unsupervised spatial modeling for grade control. All the main elements of the workflow are replaceable. K-fold cross-validation is proposed as a tool for optimizing the number of local data used for performing the modeling operations. Other parameters of the system could also be optimized in a similar manner. The workflow of the main modeling part and comparison to another grade control method are provided in Chapter 4.

CHAPTER 4

GRADE CONTROL DECISION MAKING

Chapter 3 describes the local multivariate simulation algorithm including expected profit calculation and k-fold validation called the Advanced Grade Control-Expected Profit (AGC-EP). The main part of AGC-EP is used to model expected profit for a grid of blocks. The number of nearby samples used for modeling is either predicted by the k-fold cross-validation or specified by the user. Elements of the workflow of the main modeling part of AGC-EP include: i) normal score transformation, ii) determination of local anisotropy angles, iii) modeling local variograms, iv) modeling local uncertainty, v) expected profit calculation, and vi) post-processing of expected profit estimates. The expected profit estimates generated by AGC-EP at a high resolution can be used for determining optimal pre-blast destinations for mined material and as input information for blast movement modeling.

This chapters describes final expected profit calculation with AGC-EP at a high resolution. Main steps of the modeling workflow are described in detail. A method to improve local anisotropy determination is described. A method to post-process high resolution expected profit maps for improved grade control predictions is proposed. A multivariate grade control study based on real data is described. Grade control decisions made by AGC-EP and kriging are compared in terms of total misclassification (type 1 and type 2 errors) and profit gained from mining operations.

4.1 Main Modeling Part of the Expected Profit Calculation Workflow

In AGC-EP, local uncertainty is modeled at a high resolution approximately one quarter of sample spacing as recommended in Vasylchuk and Deutsch (2017). This could be achieved by performing all modeling operations at all high resolution grid locations. A coarser super grid can could also be used to decrease the modeling time for large domains (e.g., when

several mine benches are modeled simultaneously). If a coarse super grid is used, final expected profit estimates (maps) may contain visual artifacts potentially causing misclassification and a loss of profit. A method is proposed for post-processing the final expected profit maps to remove the artifacts and improve the expected profit predictions. The steps of the main modeling part of the local multivariate simulation workflow are provided in Figure 4.1.

Main Modeling

1 Associate each BH sample with the nearest super grid node location x
2 Go to the first super grid node location x
    2.1 Search for a number of BH samples n_d and store them in a set D
    2.2 NS transform variable values in D (PPMT for multivariate)
    2.3 Save the NS and PPMT back-transformation information for x
        2.3.1 Select a variable g
            2.3.1.1 Determine major direction of anisotropy using MOI
                2.3.1.1.1 If n_d is insufficient for MOI, increase n_d and go to Step 2.1
            2.3.1.2 Calculate, model, and save variogram model $\gamma(h)$ using BH samples from D
                2.3.1.2.1 If n_d is insufficient to model $\gamma(h)$, increase n_d and go to Step 2.1
        2.3.2 Repeat for all variables $g = 1,...,G$
    2.4 Go to the first main grid location u associated with the super grid node location x
    2.5 Retrieve the statistics and data saved for x
        2.5.1 Select a variable g
            2.5.1.1 Solve normal equations
            2.5.1.2 Simulate $z^l(u)$, $l = 1,...,L$ values
        2.5.2 Repeat for all variables $g = 1,...,G$
    2.6 Back-transform $z^l(u)$, $l = 1,...,L$ using corresponding NS and PPMT back-transformation information
    2.7 Start with a destination for mined material k
        2.7.1 Calculate $EP(u;k)$ using the back-transformed $z^l(u)$, $l = 1,...,L$
    2.8 Repeat for all destinations $k = 1,...,K$
    2.9 Repeat for each main grid location u associated with x
3 Repeat for each super grid node location $x \in A$
4 Smooth the expected profit estimates using an averaging filter

Figure 4.1: Main modeling workflow

Step 1

Each blasthole (BH) sample is associated with the closest super grid node location $x \in A$. The super grid node locations are placed in the centers of the blocks of the main modeling grid for the highest precision of uncertainty modeling; however, a coarser super grid can be user to decrease the operation time of the modeling algorithm.

Step 2

The modeling algorithm starts at a super grid node location x.

Steps 2.1-2.3

A simple search based on the shortest Euclidean distance between the super grid location x and BH sample locations is used. The number of nearby BH samples n_d used for

calculations is retrieved and placed in a set D. Then, the BH samples from D are normal score (NS) transformed. The Projection Pursuit Multivariate Transform (PPMT) method (Barnett et al., 2014) is used if there are more than one variable; the input parameters for PPMT are set according to recommendations from Barnett and Deutsch (2015a). The NS and PPMT back-transformation information is saved for the location $\boldsymbol{x}$ for later use.

Step 2.3.1

The following operations are performed with samples of a variable g in normal scores.

Step 2.3.1.1

Major direction of anisotropy is determined using the modified mass moment of inertia tensors (MOI) method (explained in Chapter 3).

Step 2.3.1.1.1

If the number of nearby BH samples n_d is insufficient for the mass moment of inertia tensor calculation, n_d is increased by a certain number (10 % is a default value) and Steps 2.1-2.3 are repeated until an anisotropy angle is calculated with MOI or until n_d cannot be increased anymore. If n_d cannot be increased anymore (the direction of anisotropy cannot be determined even globally with all BH samples), anisotropy parameters are specified through a default variogram model.

Step 2.3.1.2

A variogram is modeled using BH samples from D. The algorithms for calculating experimental variograms and fitting variogram models are described in J. L. Deutsch (2015), Larrondo et al. (2003), and Chapter 3. A default variogram model should be specified to use when the local direction of anisotropy cannot be determined in Step 2.3.1.1.

Step 2.3.1.2.1

If the number of nearby BH samples n_d is insufficient to model the variogram, n_d is increased by a certain number (10 % is a default value), and Steps 2.1-2.3 are repeated until a local variogram model $\gamma(\boldsymbol{h})$ is obtained. If n_d cannot be increased anymore (a variogram cannot be modeled even globally with all BH samples), the default variogram model is used.

Step 2.3.2

Steps 2.3.1.1-2.3.1.2 are repeated for all variables $g = 1, ..., G$.

Step 2.4

The expected profit calculation part of the modeling workflow starts at a location $\boldsymbol{u}$ of the main modeling grid associated with the super grid node location $\boldsymbol{x}$. If a coarse super grid is not used, the coordinates of super grid node locations, $\boldsymbol{x} \in A$, coincide with the coordinates of block centers of the main modeling grid, $\boldsymbol{u} \in A$.

Step 2.5

Variogram models for each variable and back-transformation information are retrieved for the super grid location $\boldsymbol{x}$.

Step 2.5.1

If there are multiple variables $g = 1, ..., G$, the following operations start with a variable g.

Steps 2.5.1.1 - 2.5.1.2

Normal equations are solved using the variogram model $\gamma(\boldsymbol{h})$ and BH samples from D; a conditional mean and a standard deviation are obtained. A number of values $z^l(\boldsymbol{u}), l = 1, ..., L$ are drawn from a cumulative density function defined by the mean and standard deviation; the number of realizations can be chosen based on k-fold cross-validation or artificial tests with known true values. The default number of realizations for AGC-EP is 1000 (this choice is explained in Chapter 3).

Step 2.5.2

Repeat Steps 2.5.1.1 - 2.5.1.2 for all variables $g = 1, ..., G$.

Step 2.6

Back-transform the simulated values $z^l(\boldsymbol{u}), l = 1, ..., L$ for all the variables $g = 1, ..., G$ using the previously retrieved back-transformation information associated with the location $\boldsymbol{x}$.

Step 2.7

The following step is performed for different destinations for mined material $k = 1, ..., K$ defined by a profit function P. Calculations start for a destination k.

Step 2.7.1

Calculate expected profit $EP(\boldsymbol{u}; k)$ for the destination k using the back-transformed values $z^l(\boldsymbol{u}), l = 1, ..., L$.

Step 2.8

Step 2.7 is repeated for all the destinations $k = 1, ..., K$.

Step 2.9

Steps 2.5-2.8 are repeated for all locations $\boldsymbol{u} \in A$ associated with the super grid node location $\boldsymbol{x}$.

Step 3

Steps 2.1 - 2.9 are repeated for all the super grid node locations $\boldsymbol{x} \in A$. If the super grid is not used, Steps 2.1-2.9 are performed for all the main grid locations $\boldsymbol{u} \in A$.

Step 4

Expected profit estimates are post-processed using an averaging filter to remove artifacts and/or improve expected profit predictions. This steps is explained in detail in Section 4.1.1.

The four major steps explained above are used to generate high resolution expected profit maps for any number of destinations for mined material. AGC-EP is intended to work automatically or nearly automatically. AGC-EP generates locally varying anisotropy (LVA) fields, local variogram models, and local normal score transformed data as text ASCII files to validate modeling results; any type of tools can be used to visualize and inspect the generated information. It is important to validate local modeling parameters, especially if modeling is performed with a small number of nearby samples. Final expected profit maps can be used to find optimal pre-blast destinations for mined material or used with a blast movement modeling algorithm to predict the post-blast distribution of expected profit.

4.1.1 Post-processing of Expected Profit Maps

Due to the local nature of expected profit calculation with AGC-EP, final expected profit maps may contain visual artifacts, which may be transferred to corresponding selection plans. This is particularly noticeable if a coarse super grid is used for faster calculations. A method is proposed for smoothing expected profit maps and mitigating the effect of the artifacts on grade control decision making.

An image enhancing method based on neighborhood averaging (a moving averaging filter) (Russ, 2016, p. 208) is used for post-processing expected profit maps. This operation

can be explained as a convolution operation of an image (expected profit map) and a filter (kernel). Mathematically, this operations can be expressed as follows (Russ, 2016, p. 372):

$$g(x, y) * f(x, y) = \int \int f(s, t) \cdot g(x - s, y - t) ds dt \qquad (4.1)$$

where $f(x, y)$ is a function representing an expected profit map; $g(x, y)$ is a function representing a filter; s and t are the variables for integration with the ranges encompassing the entire image $f(x, y)$.

Equation (4.1) can be expressed as a matrix operation. A matrix $\boldsymbol{G}$ represents a filter, which usually has dimensions 3×3, 5×5, 7×7, etc. (Russ, 2016, p. 209), while a matrix $\boldsymbol{F}$ represents the blocks of an expected profit map (spatial domain A), which are covered by $\boldsymbol{G}$. For example, the filter matrix with the dimensions of 3×3 is chosen for post-processing the expected profit map. Using the matrix notation, expected profit value $EP(\boldsymbol{u}; k)$ for mined material destinations $k = 1, ..., K$ is calculated as follows:

$$EP(\boldsymbol{u}; k) = \begin{bmatrix} f_{11} & f_{12} & f_{13} \\ f_{21} & f_{22} & f_{23} \\ f_{31} & f_{32} & f_{33} \end{bmatrix} * \begin{bmatrix} g_{11} & g_{12} & g_{13} \\ g_{21} & g_{22} & g_{23} \\ g_{31} & g_{32} & g_{33} \end{bmatrix}, k = 1, ..., K, \forall \boldsymbol{u} \in A \qquad (4.2)$$

where $g_{11}, ..., g_{33}$ are the weights applied to the entries $f_{11}, ..., f_{33}$ of $\boldsymbol{F}$.

An expected profit value $EP(\boldsymbol{u}; k)$ corresponds to the central entry of $\boldsymbol{F}$, f_{22}, and is a linear combination of all its elements $f_{11}, ..., f_{33}$ and corresponding weights $g_{11}, ..., g_{33}$. Other operations can be performed with $f_{11}, ..., f_{33}$ to obtain an estimate for f_{22}; for example, minimum, maximum, or median values in the neighborhood can be used (Russ, 2016). Using estimates for f_{22} other than a linear combination of non-negative weights and blocks of an expected profit map (e.g., in Jensen (2016, p. 296)) can be beneficial for improving the visual quality of the map in certain cases. However, this may cause the loss of important spatial information or introduce artifacts, which, in turn, may cause misclassification and a loss of profit.

Handling the edges and corners of expected profit maps is another aspect of the filtering. Some specific rules may be applied to handle the problematic locations including mirroring the blocks at the edges, extrapolating the edge and corner blocks, or wrapping the expected profit maps (Russ, 2016, p. 210). Another straightforward approach is implemented inside

AGC-EP; the main modeling grid is increased by a certain number of blocks (e.g. 1 block for a 3×3 block^2 filter) at each side of the map in the x and y directions during modeling. The extra expected profit blocks are used for smoothing with the filter.

4.1.1.1 Averaging Filters

In order to demonstrate the post-processing of expected profit maps and compare different types of averaging filters, an artificial example is created. Reference realizations are simulated with $sgsim$ (C. V. Deutsch & Journel, 1998) for an area of 100×100 m^2 with a grid size of 1×1 m^2; the simulated values in Gaussian units are converted to be lognormal with both mean and standard deviation of 1.0 for more realistic results. A variogram model used for simulation has one spherical nested structure and the nugget effect contribution of 0.1. Major direction of continuity is at $135°$ from North. Major and minor ranges of continuity are 50 and 10 m, respectively. The reference realizations are then sampled at a grid size of 8×8 m^2 with a random error in coordinates of up to 1 m. An example of a reference realization and samples are in Figure 4.2.

(a) Reference realization   (b) Samples
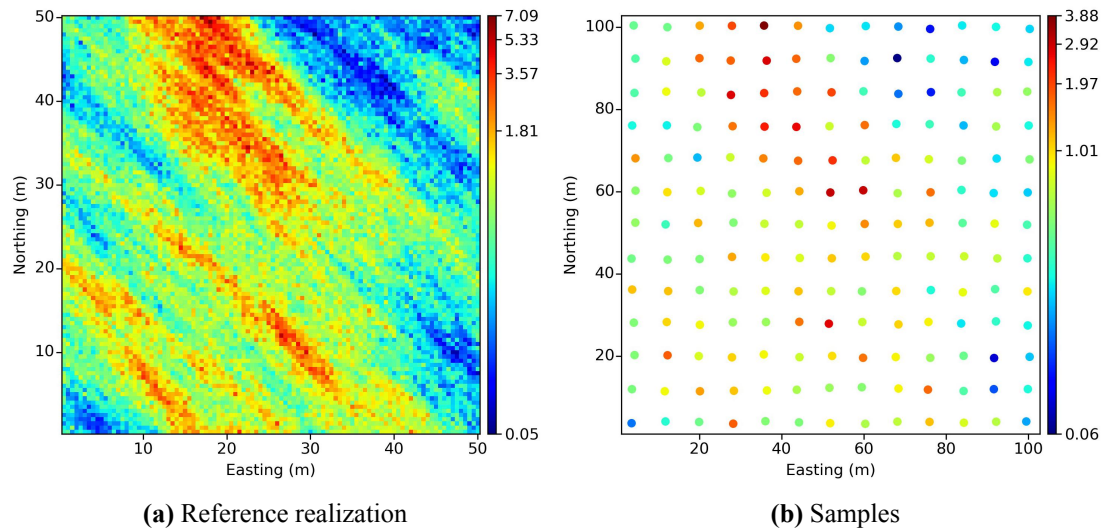
Figure 4.2: Reference realization and samples

The samples are used to generate expected profit maps for the entire area of 100×100 m^2 with the grid size of the reference model (1×1 m^2). A cutoff-based profit function (described in Chapter 3) is used to convert simulated values to expected profit; a cutoff grade

of 1.0 is used. The k-fold cross validation procedure is not performed since optimizing the number of nearby samples is not essential for this example; 100 nearby samples are used locally to calculate expected profit.

Expected profit for ore and waste destinations is generated using AGC-EP. A super grid is defined by the average lag distance h_{xy} and a constant value $v_{const} = 3$ (details are in Chapter 3); general rules for defining grid parameters are described in C. V. Deutsch and Journel (1998). The super grid, used to infer local anisotropy parameters, is coarser than the main modeling grid, used to calculate expected profit; this causes some visual artifacts in final expected profit maps. In order to mitigate or remove the artifacts, the expected profit maps are post-processed using different averaging filters; the post-processed expected profit maps are compared to the original ones with no filter used. For all the expected profit maps, cumulative profit gained from correct decisions, CP_{gained}, mean squared error in profit, MSE_{profit}, and total misclassification (calculated as a fraction of misclassified locations out of all modeling locations in percent) are recorded. The results are averaged over 10 realizations for stability. The cumulative gained profit is the true profit gained at the locations $\boldsymbol{u} \in A$, where estimated destinations are equal to the true destinations; this measure can be calculated when the true destinations are known for artificial reference realizations at a high resolution. Following the notation from Chapter 3, the cumulative gained profit is expressed mathematically as follows:

$$CP_{gained} = \sum_{\boldsymbol{u} \in A} P_{true}(\boldsymbol{u}; d_{est}(\boldsymbol{u})), \ \forall \boldsymbol{u} \in A, \text{ where } d_{true}(\boldsymbol{u}) = d_{est}(\boldsymbol{u}) \qquad (4.3)$$

where $d_{true}(\boldsymbol{u})$ and $d_{est}(\boldsymbol{u})$ are the true and estimated best destinations for mined material at a location $\boldsymbol{u}$; $P_{true}(\boldsymbol{u}; d_{est}(\boldsymbol{u}))$ is the true profit gained at the location $\boldsymbol{u}$ if mined material is sent in the true best destination $d_{true}(\boldsymbol{u})$.

Figure 4.3 illustrates examples of original expected profit maps for the ore and waste destinations with no filter applied; estimated best destinations, obtained using the expected profit maps, and corresponding true destination are also provided.

(a) Ore destination

(b) Waste destination

(c) True optimal destinations

(d) Estimated optimal destinations
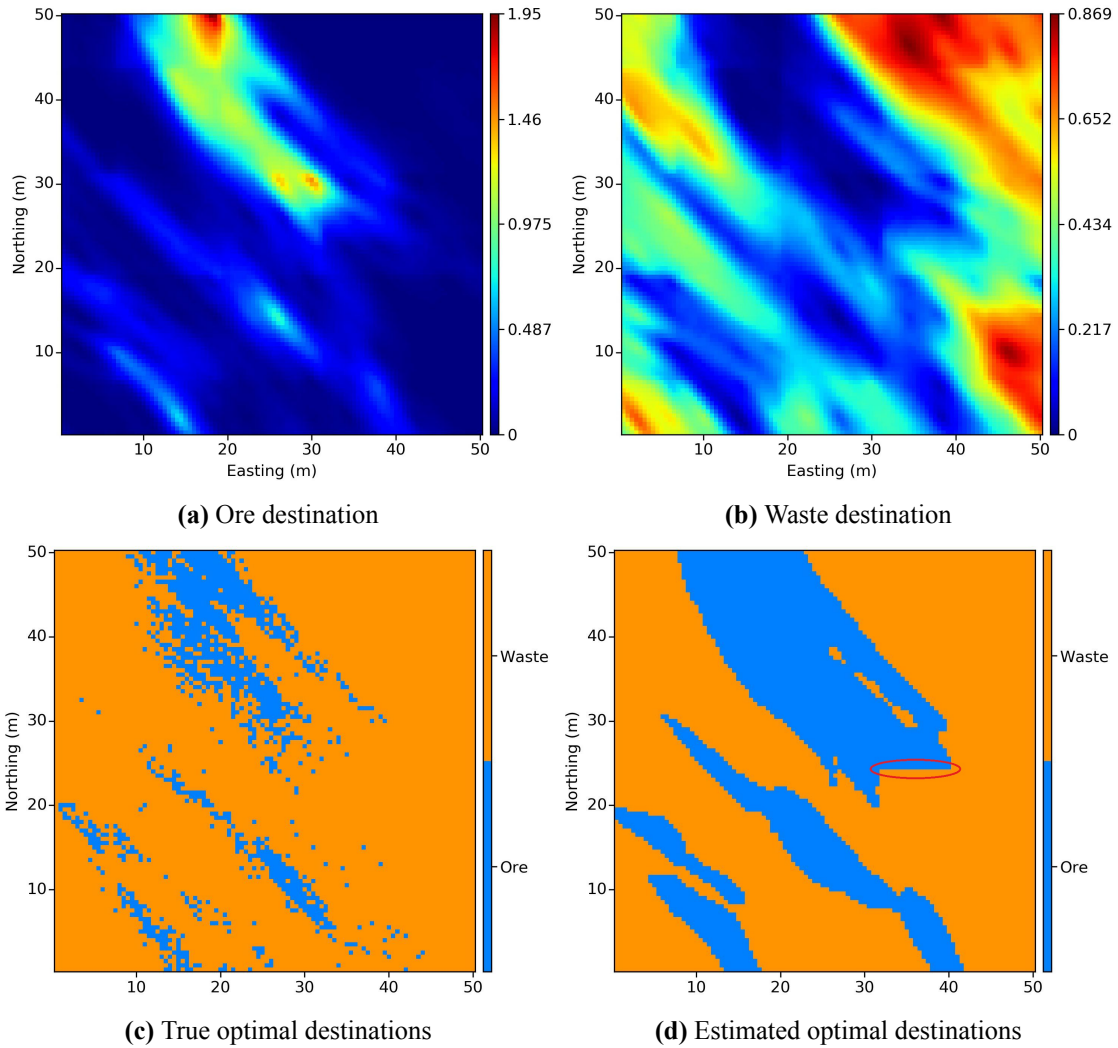
Figure 4.3: Expected profit maps before applying an averaging filter and corresponding estimated best destinations and the true best destinations; the red ellipse indicates artifacts caused by using a super grid.

The expected profit maps in Figure 4.3 demonstrate minor still visible artifacts (especially, for the waste destination expected profit) caused by using the coarse super grid. The artifacts from the expected profit maps are transferred to the selection ore/waste map; an example of a problematic zone caused by the artifacts is indicated by a red ellipse in Figure 4.3d. Analysis of the expected profit and selection maps provides the following results:

- Average CP_{gained}: 110.08

- Average MSE_{profit}: 0.7

- Average total misclassification: 22.408 %

It is assumed that the post-processing of the expected profit maps with averaging filters may mitigate the artifacts and result in improving the performance indicators described above. Summary of the performance of AGC-EP with different filters is provided below.

Simple Averaging Filter with Equal Weights

The first type of filters has equal weights applied to each expected profit unit falling within it; the weights should sum up to 1. Filters with dimensions of 3×3 block^2, 5×5 block^2, and 7×7 blocks^2 are considered. The 3×3 block^2 filter is expressed in the matrix notation as follows:

$$
G = \frac{1}{9} \begin{bmatrix} 1 & 1 & 1 \\ 1 & 1 & 1 \\ 1 & 1 & 1 \end{bmatrix}
$$

The 5×5 block^2, and 7×7 block^2 filters can be expressed in a similar manner. Figure 4.4 demonstrates expected profit maps for the ore and waste destinations after applying the 3×3 block^2 filter with equal weights; estimated best destinations, obtained using the post-processed expected profit maps, and the true best destinations are also shown.

(a) Ore destination

(b) Waste destination

(c) True optimal destinations

(d) Estimated optimal destinations

Figure 4.4: Expected profit maps after applying the 3×3 block^2 averaging filter with equal weights and corresponding estimated best destinations and the true best destinations

Figure 4.4 demonstrates that the artifacts present in the expected profit maps and the selection ore/waste map before applying the filter are mitigated, while the general structure of geological continuity is preserved. Analysis of the expected profit and selection ore/waste maps after applying the 3×3 block^2 filter provides the following results:

- Average CP_{gained}: 113.606

- Average MSE_{profit}: 0.657

- Average total misclassification: 18.145 %

The post-processing of the expected profit maps with the 3×3 block^2 filter improved all the three performance indicators. Average CP_{gained}, average total misclassification, and average MSE_{profit} are improved by 3.203 %, 6.143 %, and 19.024 %, respectively.

Filters Based on a Gaussian Kernel Function

The weights of the second type of filters are calculated using a Gaussian kernel function and then normalized to ensure that they sum up to 1.0. The Gaussian kernel-based filters are further referred to as Gaussian for brevity. Similar to the previous type of filters, Gaussian filters can be implemented with the dimensions of 3×3 block^2, 5×5 block^2, and 7×7 block^2. Non-normalized weights for a Gaussian filter are calculated using the following equation (Russ, 2016, p. 212):

$$G(x, y, \sigma) = \frac{1}{2 \cdot \pi \cdot \sigma^2} e^{-\left(\frac{x^2+y^2}{2 \cdot \sigma^2}\right)} \tag{4.4}$$

where x and y are measured in expected profit blocks from the central block; σ is a standard deviation expressed in terms of the expected profit blocks.

Weights calculated using Equation (4.4) are non-zero for any filter size and any σ value. However, with the increase in the filter size and the value of σ staying constant, the weights that are farther away from the central entry of the filter become negligibly small. In general, large Gaussian filters require large σ values. The σ value of 1 is used by default for the 3×3 block^2, 5×5 block^2, and 7×7 block^2 Gaussian filters. The weights produced by the Gaussian kernel function are normalized; each weight is divided by the sum of all the weights. It should be noted that the sum of weights for the 5×5 block^2, and 7×7 block^2 Gaussian filters are very close to 1.0 with the σ parameter of 1 block; therefore, the normalization of weights does not significantly alter them.

Figure 4.5 demonstrates the expected profit maps for the ore and waste destinations after applying the 3×3 block^2 Gaussian filter; estimated best destinations obtained using the post-processed expected profit maps and the true best destinations are also shown for comparison.

(a) Ore destination

(b) Waste destination

(c) True optimal destinations

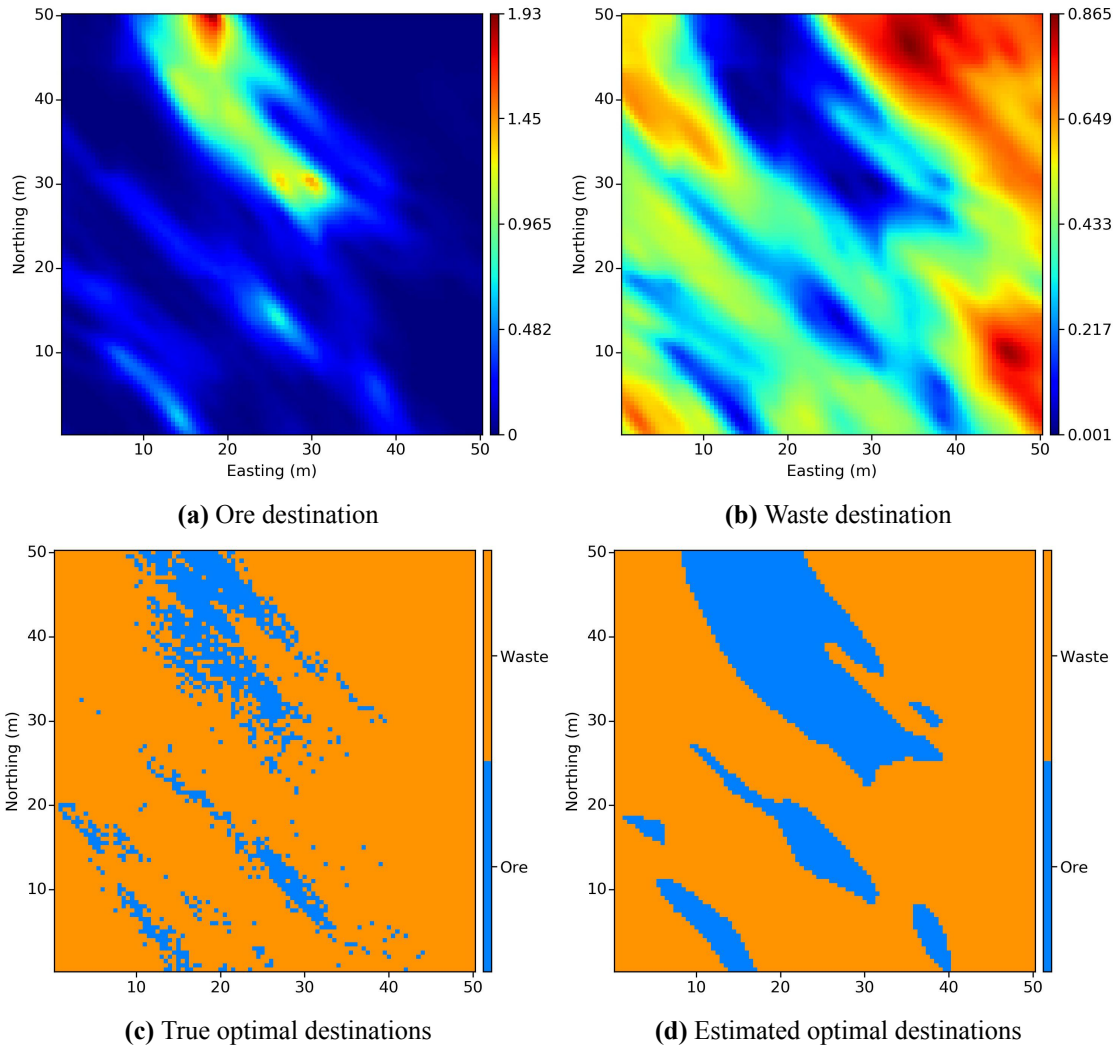**(d)** Estimated optimal destinations
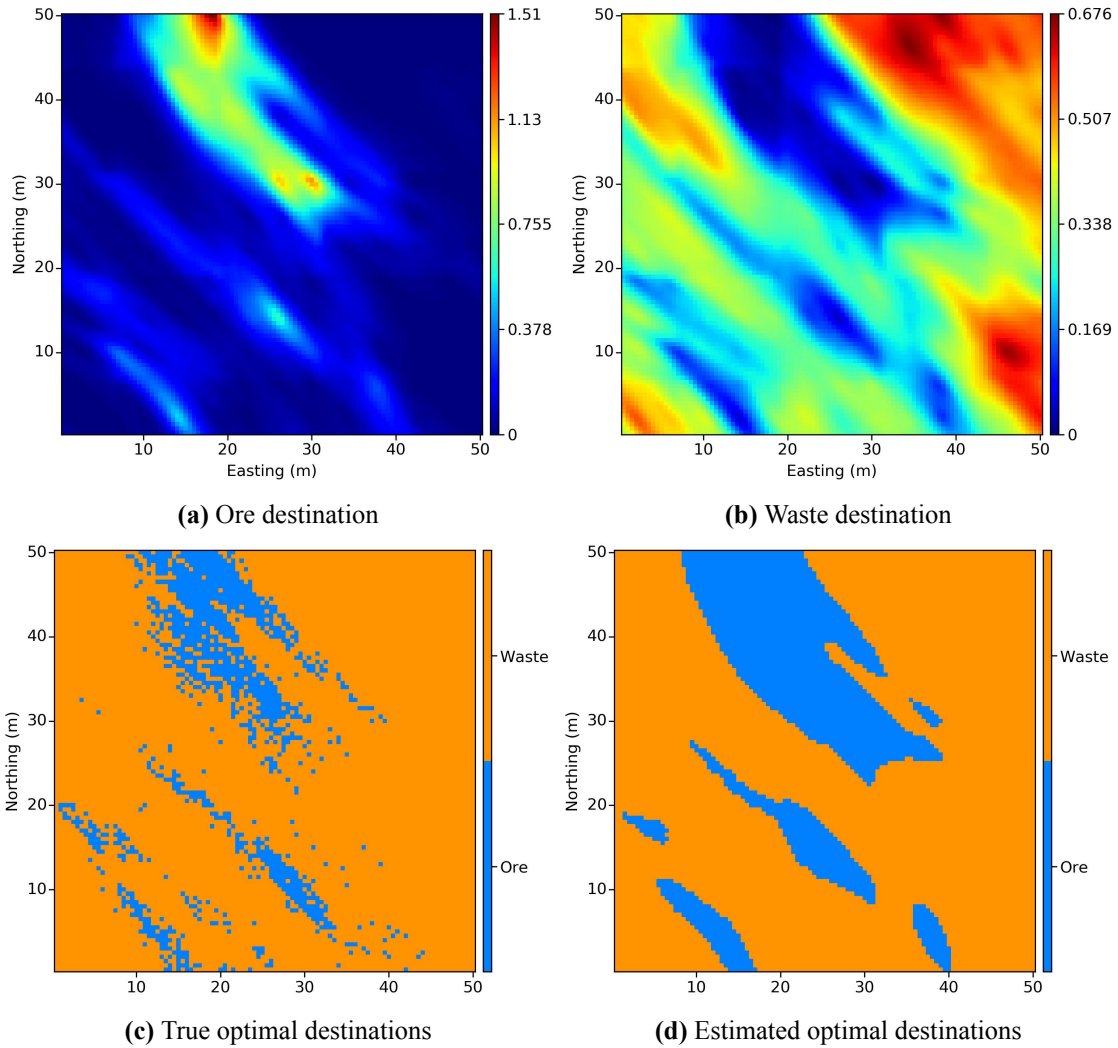
Figure 4.5: Expected profit maps after applying the 3×3 block^2 Gaussian filter and corresponding estimated best destinations and the true best destinations

The post-processing of the expected profit maps with the 3×3 block^2 Gaussian filter improves average CP_{gained}, average MSE_{profit}, and average total misclassification by 3.203 %, 6.169 %, and 18.998 %, respectively.

Table 4.1 summarizes the performance indicators for all the 6 filters.

Table 4.1: Performance summary for 6 averaging filters

Filter	CP_{gained}	MSE_{profit}	Type 1 and 2 errors, %
No filter	110.080	0.700	22.408
Simple (3×3 block^2)	113.606	0.657	18.145
Simple (5×5 block^2)	113.430	0.654	18.396
Simple (7×7 block^2)	112.311	0.663	19.124
Gaussian (3×3 block^2)	113.606	0.657	18.151
Gaussian (5×5 block^2)	113.476	0.656	18.359
Gaussian (7×7 block^2)	112.371	0.668	19.142

Table 4.1 shows that the post-processing of the expected profit maps for this example improves the performance of AGC-EP. The simple filters with equal weights and Gaussian filters demonstrate similar performance. Generally, the performance of the two types of filters deteriorates with the increase in the size of the filters from 3×3 block^2 to 7×7 block^2, according to all the performance indicators.

It is reasonable to include the post-processing of expected profit maps by either the simple or Gaussian filter with the dimensions of 3×3 block^2 as a final step in the local multivariate simulation workflow. However, the performance of the filters may vary for different grade control situations. The expected profit modeling on a high resolution grid (not using a super grid) and without the filtering may produce better results for sharp ore/waste boundaries. It is recommended to construct artificial tests mimicking grade control conditions at a particular mine and calibrate filters for specific grade control situations. Even though rectangular averaging filters are useful and straightforward to implement, filters with different shapes and/or different ranking strategies can be used to address specific artifacts. More research could be done in this direction.

4.2   Case Study: Grade Control at the Red Dog Mine

Grade control modeling in open pit mines is a multistage procedure. Such modeling operations as declustering, normal score transformation, variogram modeling, among others, can be performed by various tools. An industry professional responsible for grade control

at a mine selects the best tool for each particular modeling operation, defines optimal input parameters, and validates modeling results. Relatively simple estimation tools like inverse distance or ordinary kriging (OK) are traditionally used for grade control modeling in open pit mines (Dimitrakopoulos & Godoy, 2014) due to their robustness. This choice is often reasonable for grade control cases with one grade variable, only ore and waste destinations for mined material, and a simple cutoff-based profit function. However, grade control cases involving multiple grade variables and/or locally varying geology may be more complex. For such cases, the reproduction of local anisotropy and multivariate relationships between grade variables in grade control models may improve the predictions of optimal destinations for mined material and, as a result, increase profit from mining operations.

This case study is designed to demonstrate that a carefully applied traditional grade control method based on OK can be outperformed by an unsupervised spatial prediction algorithm based on local multivariate simulation. A real blasthole data set from the Red Dog mine in Alaska is used to simulate a multivariate reference realization of truth at a high resolution. The AGC-EP modeling algorithm and OK are used to predict profit at unsampled locations and estimate optimal destinations for mined material. A profit function is designed based on stockpile blending criteria that were used to improve plant recovery at the Red Dog mine. Performance measures such as cumulative gained profit, mean squared error in profit, and total misclassification (type 1 and type 2 errors) are compared.

4.2.1 Background

The Red Dog mine is located approximately 150 km north from Kotzebue, Alaska, USA. The mine is owned by a Canadian metals and mining company Teck Resources Limited previously known as Teck Cominco Limited. The Red Dog mine is one of the world's largest producers of zinc. It also produces significant amounts of lead and silver (Teck Cominco Alaska Inc., 2009).

There are seven deposits comprising the Red Dog mine: Main, Aqqaluk, Qanaiyak, Paalaaq, Aŋarraaq, Su, and Aktigiruq. Production in the Main deposit completed in 2012. The Aqqaluk deposit is being mined since 2010, while pre-stripping at the Qanaiyak deposit started in 2016 (Krolak, Palmer, Lacouture, & Paley, 2017). The deposits of the Red

Dog mine area are of sedimentary exhalite and replacement origin. The Main, Aqqaluk, Qanaiyak, Paalaaq deposits are believed to be the parts of a single formation faulted by tectonic forces (Teck Cominco Alaska Inc., 2009). There are three main rock types: i) silica rock, ii) barite rock, and iii) sulfide rock. All the rock types can contain ore (Teck Cominco Alaska Inc., 2009). More detailed information about deposits of the Red Dog district can be found in Kelley and Jennings (2004) and Moore, Young, Modene, and Plahuta (1986)

4.2.1.1 Available Data and Information for Grade Control

Blasthole data are available from the Main deposit only. The data is released by Teck Resources Limited to the Centre for Computational Geostatistics (CCG) for PhD research. BH samples inform on the grade of five variables: Zn, Pb, Fe, Ba, and SPb (soluble lead). There were three metallurgical rock types distinguished for the Main deposit (Teck Cominco Alaska Inc., 2009): i) siliceous, ii) veined, and iii) baritic. Siliceous ore was the most abundant; its metallurgical recovery depended on the grade of Fe. High grade of Fe caused low Zn recovery (Teck Cominco Alaska Inc., 2009). Baritic ore, defined where the grade of Ba is more than 7 % and the grade of Fe is less than 8 %, had a variable recovery depending on the grade of Zn; higher Zn grade resulted in higher recovery of baritic ore. Veined ore had a constant Zn recovery of 89 % (Teck Cominco Alaska Inc., 2009).

Stockpile blending criteria were used at the Red Dog mine to optimize plant recovery and honor grinding/flotation capacity; they are used as a basis for developing a user-defined profit function for this case study. The stockpile blending criteria are expressed by the following constraints (Teck Cominco Alaska Inc., 2009):

1. Zn/Fe ratio ≥ 2.5

2. Zn/Pb ratio ≥ 3.65

3. Baritic ore ≤ 10 %

4. Total organic carbon ≤ 0.65

5. Weathered ore ≤ 5 %

Only the first three criteria are used for this case study. The content of total organic carbon is unavailable for blasthole samples. The rules for defining weathered ore are unknown. The third criteria is modified based on the rules for defining baritic ore. Additionally, the constraint for Zn to be greater than or equal to 5 % is included. Details are provided in Section 4.2.2.3.

4.2.2 Methodology

Short-term modeling for the Main deposit was performed using OK with data from reverse circulation (RC) drilling, diamond drilling, and blastholes. Long-term modeling was performed using RC and diamond drilling only (Teck Cominco Alaska Inc., 2009). Planning at the Main Pit combined the long- and short-term models. The original long- and short-term models are not available for this study.

According to Teck Cominco Alaska Inc. (2009), a multi-pass OK approach was used to construct both the long- and short-term models. The first pass was done using a $100\text{ft} \times 100\text{ft} \times 60\text{ft}$ ellipse search and from 3 to 7 composites as conditioning data. The second pass was done using a $50\text{ft} \times 50\text{ft} \times 20\text{ft}$ ellipse search and from 4 to 7 composites. Geological models at the Main Pit were constructed with a grid size of $25 \times 25 \times 25 \text{ ft}^3$. The multi-pass approach was used with BH samples as well to construct short-term models; however, exact input parameters of corresponding kriging plans are unknown and, therefore, not used for this case study.

Since it is impossible to reproduce the short-term grade control models used at the Main Pit exactly due to the limited information and data, a different methodology is implemented for this study. OK is performed with different numbers of nearby BH samples and compared to AGC-EP. The grid size of the grade control models approximately equals to 25 % of the average BH spacing according to the recommendations from Vasylchuk and Deutsch (2017). General workflow of the case study consists of the following steps:

- Grades of Zn, Pb, and Fe are obtained from the BH samples taken in the Main Pit during its operations. A reference model is obtained for each grade variable at a high resolution. A full multivariate simulation workflow based on the PPMT method is

used. The reference model is used to determine the true profit and optimal destinations at the high resolution.

- The reference model is validated in terms of reproducing important univariate and multivariate statistics and other measures of performance.

- A dedicated profit function is developed based on the stockpile blending criteria used at the Red Dog mine.

- The reference model is sampled with positioning errors in coordinates to better reproduce a real grade control situation.

- The artificial BH samples are used to perform grade control modeling at the resolution of the reference model using OK and AGC-EP. Grade control models produced by the two methods are used to predict optimal destinations based on the dedicated profit function.

- Cumulative gained profit (CP_{gained}) (calculated using Equation (4.3)), mean squared error in profit (MSE_{profit}) (calculated using Equation (3.5)), and total misclassification are compared for the two methods.

The following section describes the construction of the reference model and its validation in detail. Also, the dedicated profit function is described. Finally, a performance summary for the two methods is provided along with concluding remarks.

4.2.2.1 Construction of a Reference Model

Original BH samples from bench '18243' of the Main Pit are used as conditioning data for multivariate simulation. A single realization of the multivariate simulation is the 'true' reference model, which is used as a basis for comparing the OK-based grade control method and AGC-EP. Figure 4.6 and Figures 4.7 show location maps for original Zn, Pb, Fe, and Ba sampled grades and corresponding histograms.
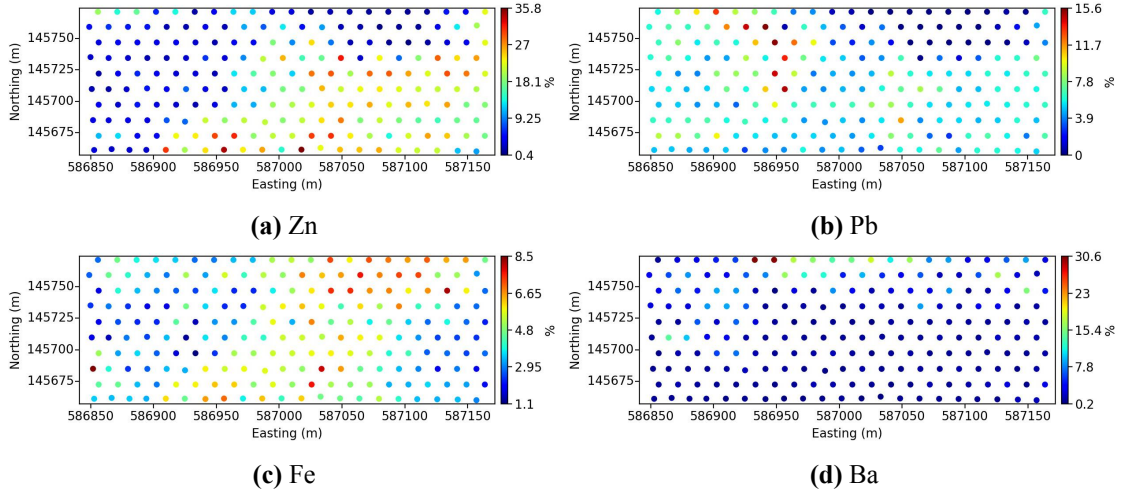
Figure 4.6: Location maps for grade variables sampled at '18243' mine bench
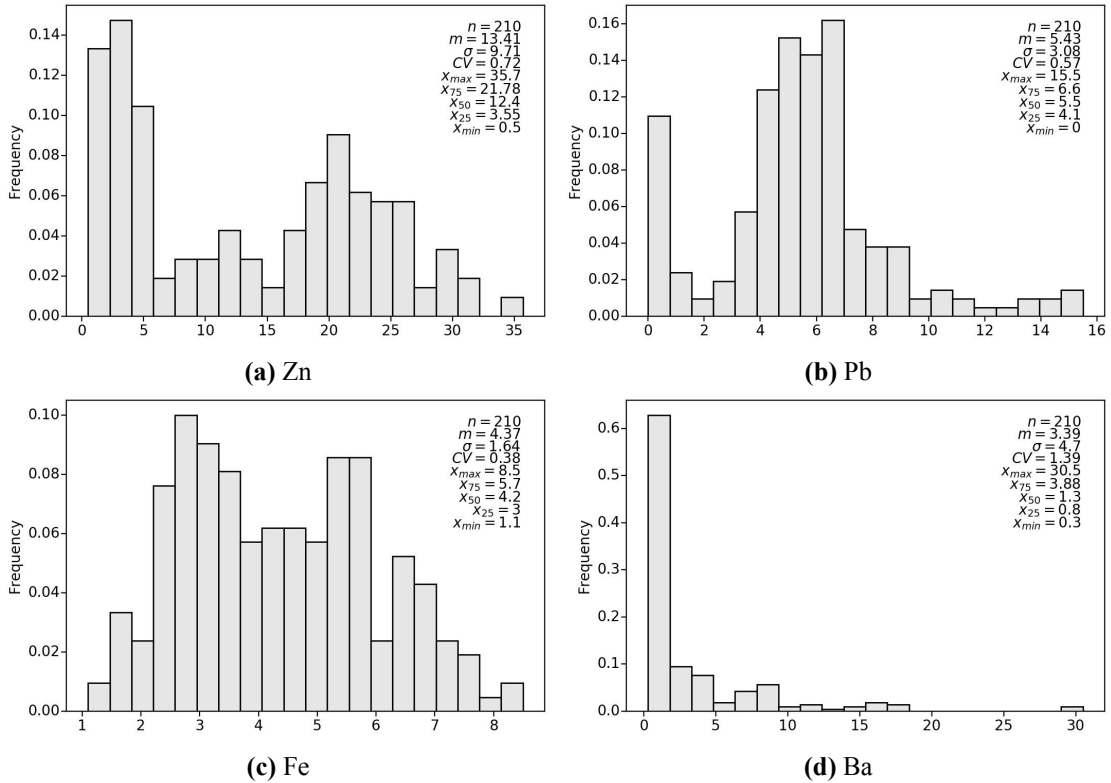
Figure 4.7: Histograms for grade variables sampled at '18243' mine bench

There are 210 BH samples situated at a staggered pattern with the average distance between BHs, h_{xy}, of 14.38 ft (calculated using Equation (3.11)). The reference model is simulated in 2-D, since BH samples do not provide information on vertical geological variability, using the following steps:

- Collocated grades of Zn, Pb, Fe, and Ba from '18243' mine bench are NS transformed using the quantile to quantile method (Rossi & Deutsch, 2014, p. 22). Declustering is not required because blastholes are situated on the regular grid.

- Variograms for Zn, Pb, Fe, and Ba are modeled using corresponding normal scored grades. This is done to improve the variogram reproduction in the reference simulated model according to recommendations from Barnett and Deutsch (2015a). Figure 4.8 demonstrates the variograms for each grade variable.

(a) Zn (calculated at 90° from North)

(b) Pb (calculated at 96.5° from North)

(c) Fe (calculated at 42.5° from North)

(d) Ba (calculated at 90° from North)
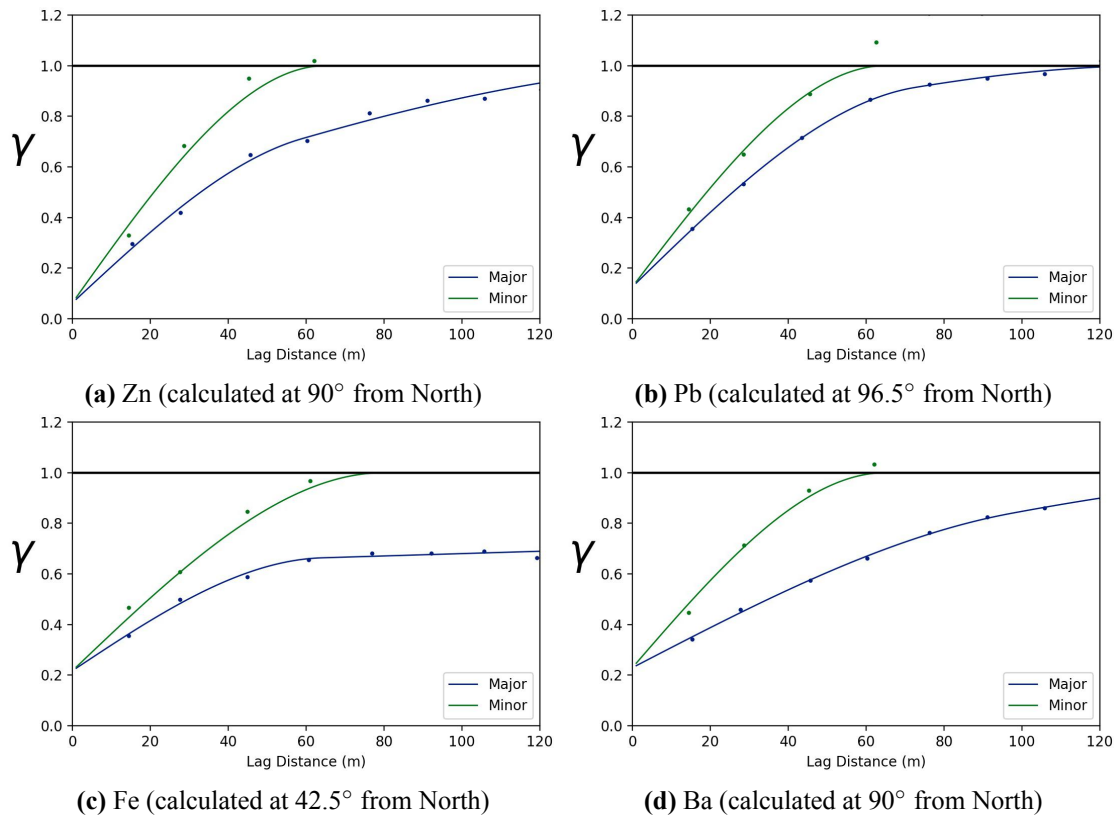
Figure 4.8: Variograms of grade variables sampled at '18243' mine bench

- The original grades of Zn, Pb, Fe, and Ba are PPMT forward-transformed using $ppmt$ program described in Barnett and Deutsch (2015a).

- The PPMT transformed grades of Zn, Pb, Fe, and Ba are modeled separately for an area of 326.25×116.25 ft^2 with a grid size of 3.75×3.75 ft^2 using $sgsim$ (C. V. Deutsch & Journel, 1998).

- The simulated grades are back-transformed altogether using *ppmt_b* program described in Barnett and Deutsch (2015a).

The back-transformed simulated realization is sampled at a grid size of 15×15 ft^2 with a random error in coordinates of up to 1 ft. The samples are then used with both OK and AGC-EP to predict optimal destinations at the resolution of the reference model (326.25×116.25 ft^2 with the grid size of 3.75×3.75 ft^2).

Reference Model Validation

The reference models for Zn, Pb, Fe, and Ba and corresponding location maps for artificial BH samples are shown in Figures 4.9 and 4.10.

(a) Zn

(b) Pb

(c) Fe

(d) Ba
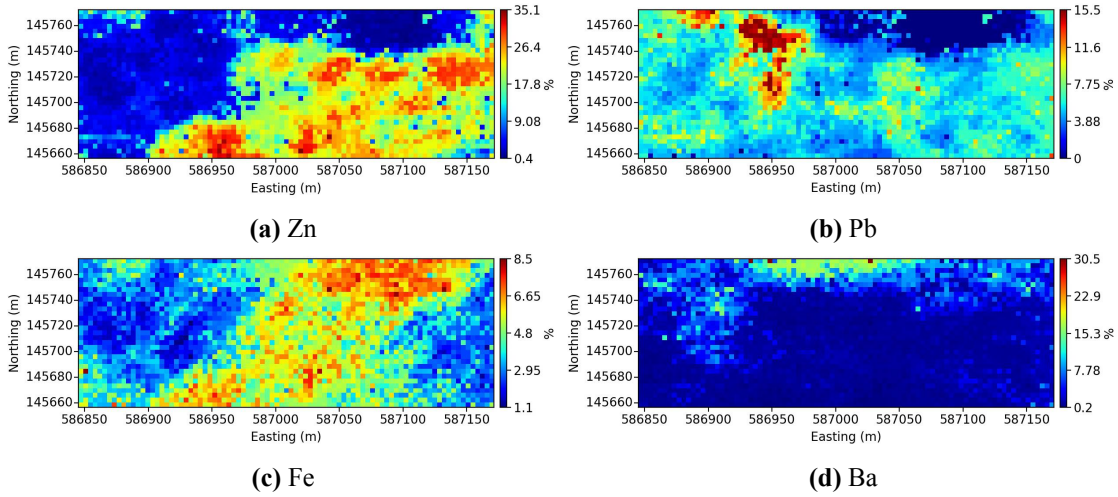
Figure 4.9: Reference models for all four grade variables

(a) Zn

(b) Pb

(c) Fe

(d) Ba
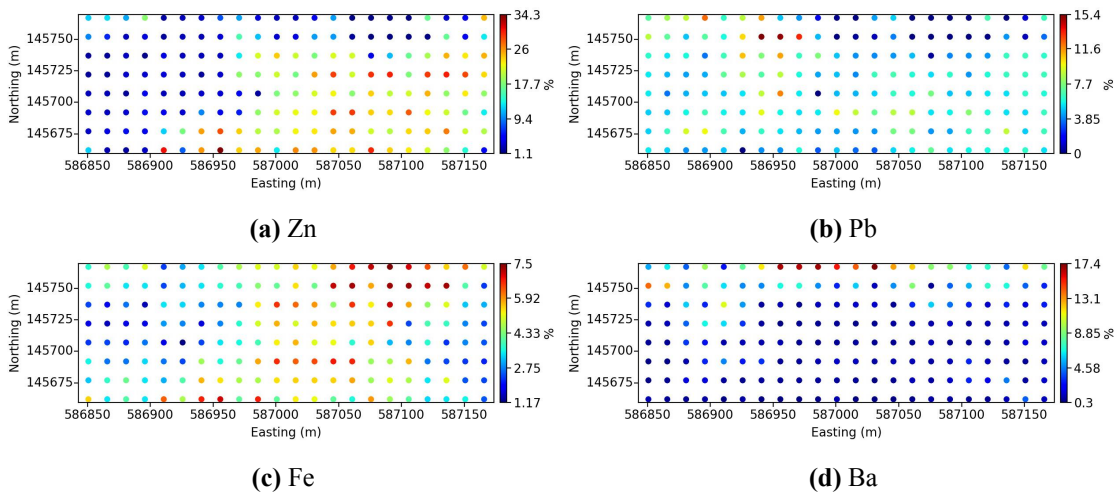
Figure 4.10: Artificial BH samples for all four grade variables

Histogram Reproduction

Histogram reproduction is an important validation check. Means and standard deviations of the reference and simulated realizations should be close as well as the shapes of corresponding cumulative distribution functions (CDFs). For '18243' mine bench, this check is performed using 20 simulated realizations. Figure 4.11 demonstrates the CDFs of the original (red color) and simulated (black color) distributions and important statistics.

(a) Zn

(b) Pb

(c) Fe

(d) Ba
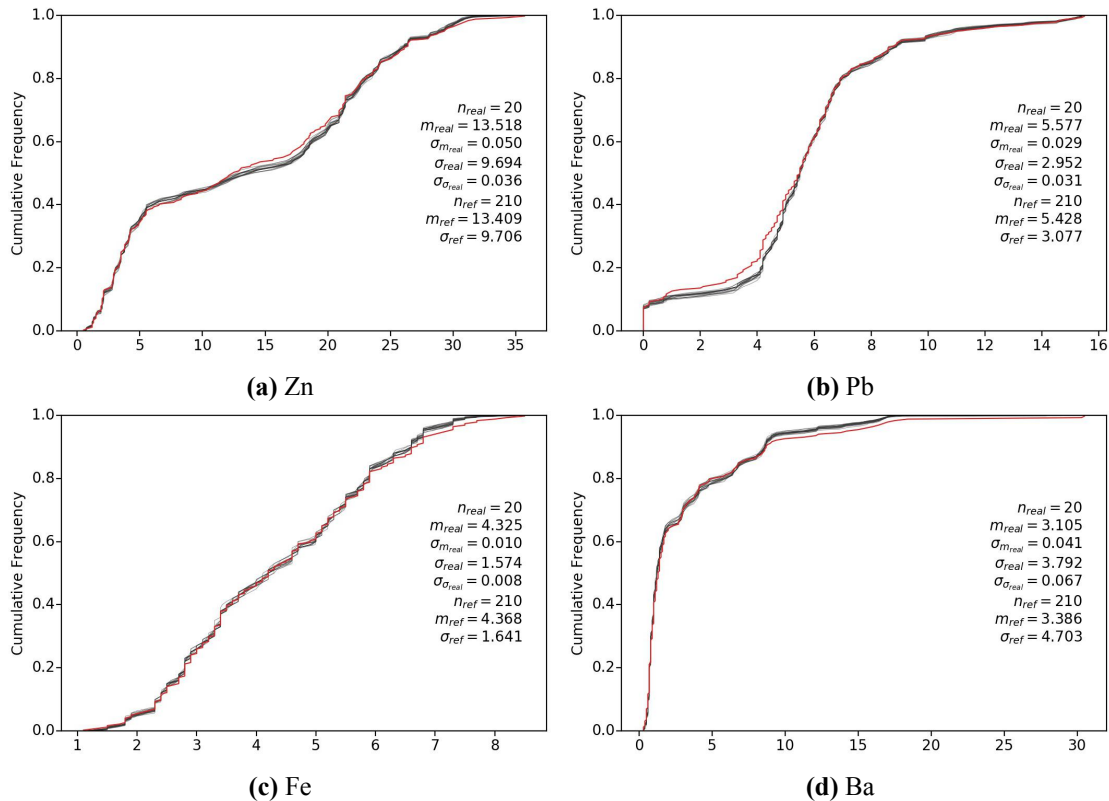
Figure 4.11: Histogram reproduction for all four grade variables sampled at '18243' mine bench

According to Figure 4.11, the CDFs of the four grade variables and corresponding univariate statistics are close to the CDFs and univariate statistics of original grade variables.

Variogram Reproduction

The reference models are simulated using the variograms of normal scored grades. Therefore, the reproduction of variogram models is checked for the simulated grades in normal scores (before the PPMT back-transformation). Figure 4.12 illustrates the reproduction of variograms for all four grade variables.

(a) Zn

(b) Pb

(c) Fe

(d) Ba
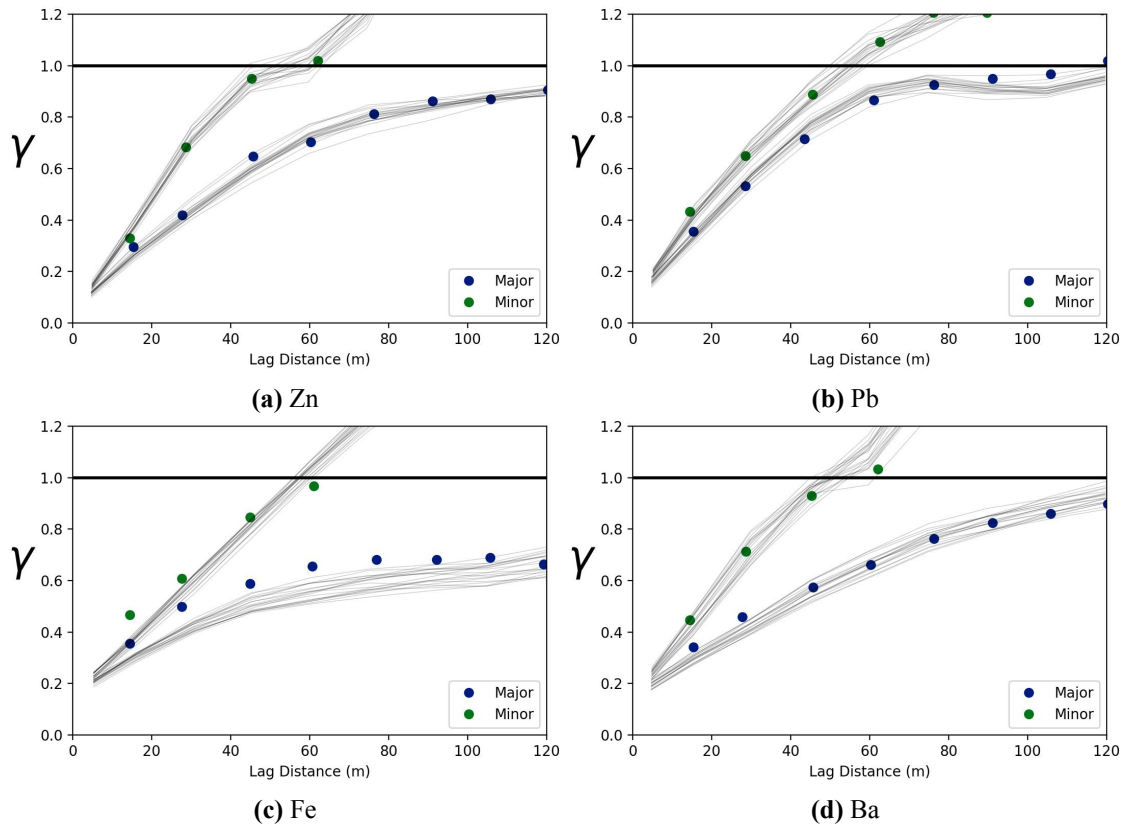
Figure 4.12: Variogram reproduction for all four grade variables sampled at '18243' mine bench

In Figure 4.12, blue and green dots represent experimental variogram values for the major and minor directions, respectively, while continuous grey lines represent corresponding variograms of simulated models. The variograms of the simulated models are calculated in the same directions as the variograms of original grade variables in normal scores. Some statistical fluctuations are expected and desired. Overall, the variogram reproduction is reasonable.

Reproduction of Bivariate Relationships between Grade Variables

The Red Dog mine stockpile blending criteria used to design a dedicated profit function for this case study involve multivariate relationships between grade variables. These bivariate relationships may influence profit calculations and, therefore, should be reproduced in the simulated reference model. The PPMT multivariate normal transformation method decorrelates variables and removes multivariate relationships between them. Figures 4.13 and 4.14 demonstrate the bivariate relationships between the four grade variables before and after the PPMT transformation, respectively.
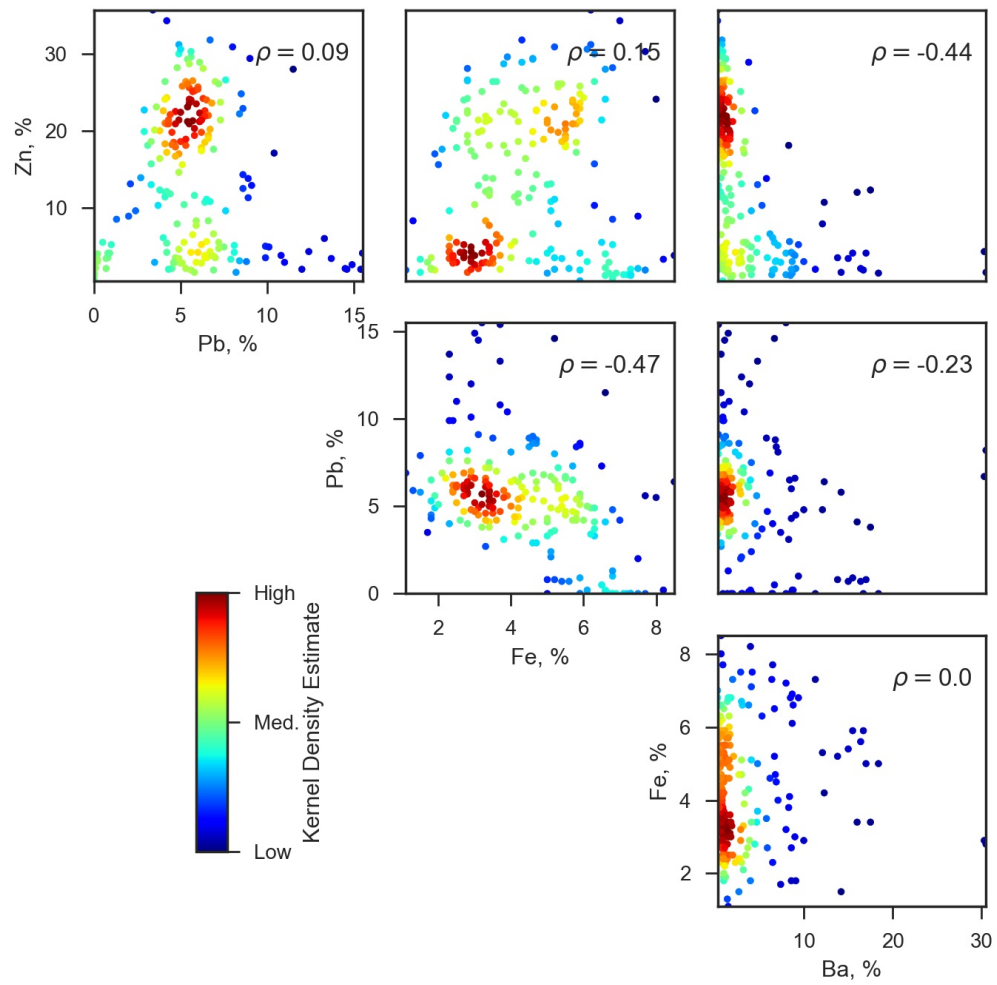
Figure 4.13: Bivariate relationships between grades variables before the PPMT transformation
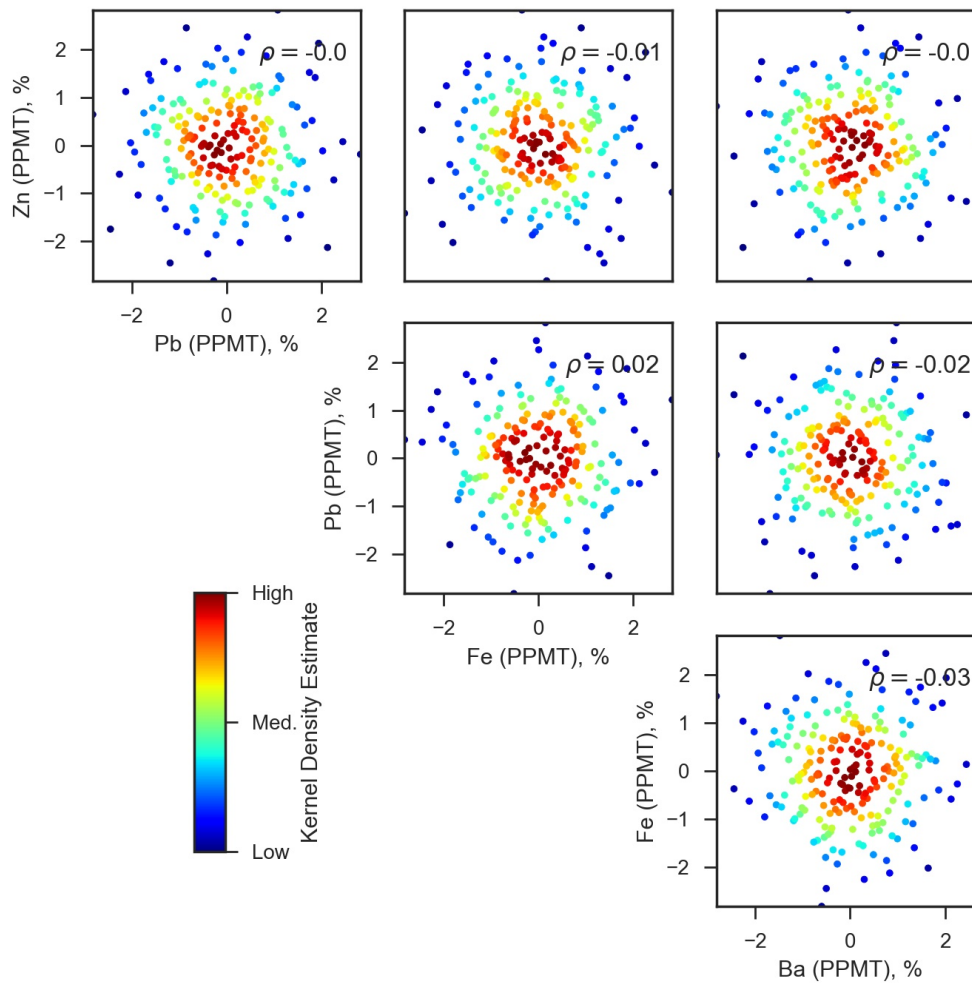
Figure 4.14: Bivariate relationships between grades variables after the PPMT transformation

Figure 4.14 demonstrates that correlation and complex non-linear relationships between all pairs of grade variables are removed. The multivariate relationships are then reintroduced in the simulated models during back-transformation. Figure 4.15 shows the bivariate plots for the simulated PPMT back-transformed variables.
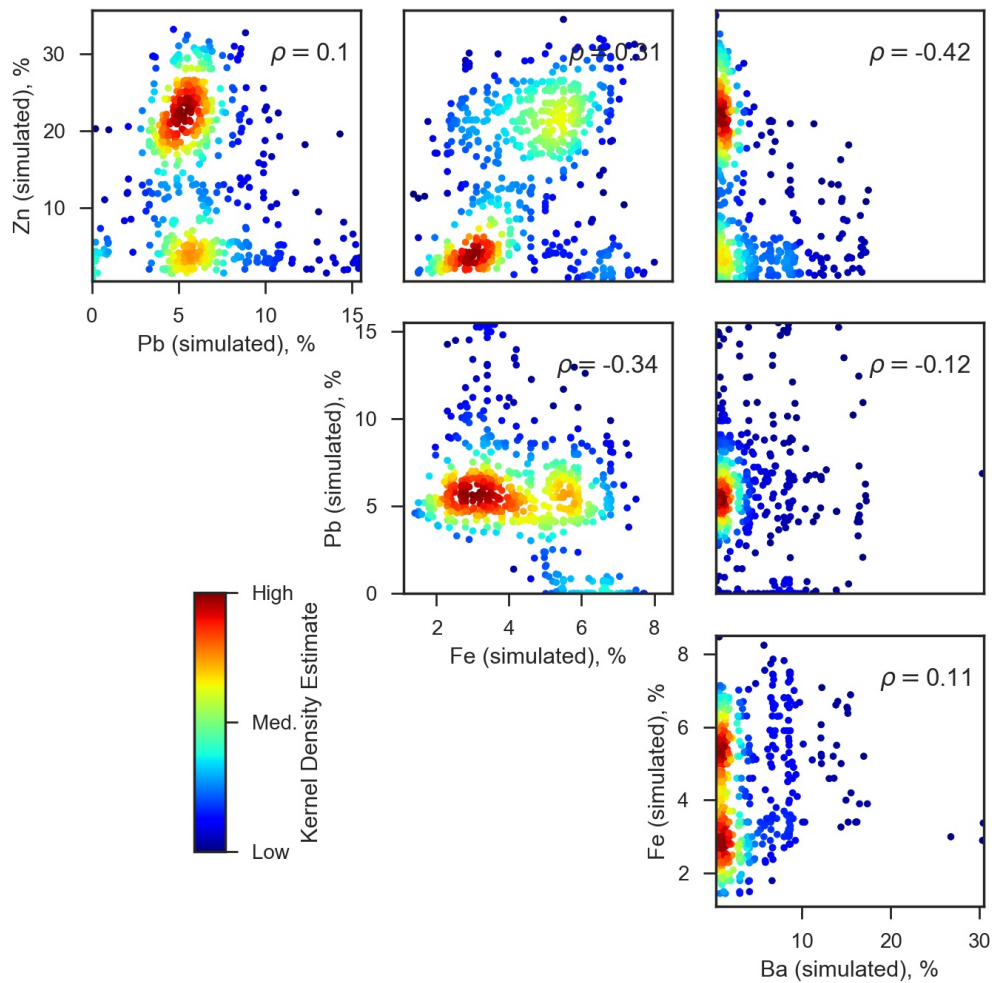
Figure 4.15: Bivariate relationships between simulated grade variables after the PPMT back-transformation

Figures 4.13 and 4.15 demonstrate that the complex bivariate relationships between original grade variables are reintroduced for the simulated grade variables.

4.2.2.2   Grade Control Decision Making with AGC-EP and OK

The BH samples from mine bench '18243' (domain A) are used to obtain reference models for Zn, Pb, Fe, and Ba grade variables. The reference models are then used to measure and compare the performance of AGC-EP and OK with respect to known true values. Two destinations for mined material $k = 1, ..., 2$ (ore and waste, respectively) are considered. The grade control modeling procedure is performed using the following steps:

1. For each grade variable, a corresponding reference model is sampled at a grid size of 15×15 ft^2 with a random error in coordinates of up to 1 ft; the error in coordinates is the same for all the grade variables since they are collocated.

2. Sampled grade variables $g = 1, ..., 4$ (Zn, Pb, Fe, and Ba, respectively) are modeled with OK for an area of 326.25×116.25 ft^2 with a grid size of 3.75×3.75 ft^2. A dedicated profit function P is used to convert ordinary kriging estimates $z_{ok}(\boldsymbol{u}; g)$, $g = 1, ..., 4$ to profit values $P(z_{ok}(\boldsymbol{u}; g), \ g = 1, ..., 4; k)$ for destinations $k = 1, ..., 2$ at all locations $\boldsymbol{u} \in A$, representing blocks of the modeling grid. Then, the OK-based profit estimates $P(z_{ok}(\boldsymbol{u}; g), \ g = 1, ..., 4; k), \ k = 1, ..., 2$ are used to define optimal destinations $d_{opt}^{ok}(\boldsymbol{u})$ at all locations $\boldsymbol{u} \in A$.

3. The sampled grade variables $g = 1, ..., 4$ are used to model expected profit with AGC-EP for the area of 326.25×116.25 ft^2 with the grid size of 3.75×3.75 ft^2. The dedicated profit function P is used with local uncertainty estimates $z^l(\boldsymbol{u}; g)$, $g = 1, ..., 4$, $l = 1, ..., L$ to calculate expected profit $EP(\boldsymbol{u}, k)$, $k = 1, ..., 2$ at all locations $\boldsymbol{u} \in A$ (more details are in Chapter 3). Then, the expected profit $EP(\boldsymbol{u}, k)$, $k = 1, ..., 2$ is used to determine the best AGC-EP destinations $d_{opt}(\boldsymbol{u})$ at all the locations $\boldsymbol{u} \in A$.

4. True grades $z_{true}(\boldsymbol{u}; g)$, $g = 1, ..., 4$ are used to obtain true profit values $P_{true}(z_{true}(\boldsymbol{u}; g), \ g = 1, ..., 4; k)$, $k = 1, ..., 2$ at all the locations $\boldsymbol{u} \in A$. The true profit $P_{true}(z_{true}(\boldsymbol{u}; g), \ g = 1, ..., 4; k)$, $k = 1, ..., 2$ is then used to obtain true optimal destinations $d_{true}(\boldsymbol{u})$ at all the locations $\boldsymbol{u} \in A$.

5. The optimal OK destinations $d_{opt}^{ok}(\boldsymbol{u})$ and the best AGC-EP destinations $d_{opt}(\boldsymbol{u})$ are compared to the true optimal destinations $d_{true}(\boldsymbol{u})$ at all the locations $\boldsymbol{u} \in A$. Cumulative gained profit CP_{gained}, mean squared error in profit MSE_{profit}, and total misclassification are calculated. Mean squared error in profit MSE_{profit} for the AGC-EP expected profit estimates is calculated using Equation 3.5. A modified version of Equation 3.5 is used to calculate MSE_{profit} for the OK profit estimates:

$$MSE_{profit} = E\{(P(z_{ok}(\boldsymbol{u}; g), \ g = 1, ..., 4; k) - P_{true}(\boldsymbol{u}; k))^2\}, \ k = 1, ..., 2, \ \boldsymbol{u} \in A$$

After steps 1-5 of the workflow are completed, the performance measures are recorded and analyzed for both grade control methods.

4.2.2.3 Profit Function

The stockpile blending criteria described in Section 4.2.1.1 are used to design the dedicated profit function P for this case study. The function governs how much profit is assigned to the ore and waste decisions based on the true or estimated Zn, Pb, Fe, and Ba grades. Profit for the ore decision is calculated as follows:

$$P(z(\boldsymbol{u}; Zn), z(\boldsymbol{u}; Pb), z(\boldsymbol{u}; Fe), z(\boldsymbol{u}; Ba); \text{ore}) =$$
$$\begin{cases} (z(\boldsymbol{u}; Zn) - 5) \cdot s(z(\boldsymbol{u}; Zn), z(\boldsymbol{u}; Pb), z(\boldsymbol{u}; Fe), z(\boldsymbol{u}; Ba)), & \text{if } z(\boldsymbol{u}; Zn) \geq 5; \\ 0, & \text{otherwise.} \end{cases}$$

$$(4.5)$$

where $z(\boldsymbol{u}; Zn)$, $z(\boldsymbol{u}; Pb)$, $z(\boldsymbol{u}; Fe)$, and $z(\boldsymbol{u}; Ba)$ are either true or estimated grade values at a location $\boldsymbol{u}$; $s(z(\boldsymbol{u}; Zn), z(\boldsymbol{u}; Pb), z(\boldsymbol{u}; Fe), z(\boldsymbol{u}; Ba))$ is a function depending on the compliance with the stockpile blending criteria at the location $\boldsymbol{u}$.

Profit for the waste decision is calculated as follows:

$$P(z(\boldsymbol{u}; Zn); \text{waste}) = \begin{cases} 5 - z(\boldsymbol{u}; Zn), & \text{if } z(\boldsymbol{u}; Zn) < 5; \\ 0, & \text{otherwise.} \end{cases} \qquad (4.6)$$

Function $s(z(\boldsymbol{u}; Zn), z(\boldsymbol{u}; Pb), z(\boldsymbol{u}; Fe), z(\boldsymbol{u}; Ba))$ in Equation (4.5) is defined by the outcome of three bivariate functions: $s_1(z(\boldsymbol{u}; Ba), z(\boldsymbol{u}; Fe))$, $s_2(z(\boldsymbol{u}; Zn), z(\boldsymbol{u}; Fe))$, and $s_3(z(\boldsymbol{u}; Zn), z(\boldsymbol{u}; Pb))$. The first function is defined as follows:

$$s_1(z(\boldsymbol{u}; Ba), z(\boldsymbol{u}; Fe); ore) = \begin{cases} 0.5, & \text{if } z(\boldsymbol{u}; Ba) > 7 \text{ and } z(\boldsymbol{u}; Fe) < 8; \\ 0.9, & \text{otherwise.} \end{cases} \qquad (4.7)$$

The second function is defined as follows:

$$s_2(z(\boldsymbol{u}; Zn), z(\boldsymbol{u}; Fe)) =$$
$$\begin{cases} \exp(-(2.5 - z(\boldsymbol{u}; Zn)/z(\boldsymbol{u}; Fe))), & \text{if } z(\boldsymbol{u}; Zn)/z(\boldsymbol{u}; Fe) < 2.5; \\ 1, & \text{otherwise.} \end{cases} \qquad (4.8)$$

The third function is defined as follows:

$$s_3(z(\boldsymbol{u}; Zn), z(\boldsymbol{u}; Pb)) =$$

$$\begin{cases} \exp(-(3.65 - z(\boldsymbol{u}; Zn)/z(\boldsymbol{u}; Pb))), & \text{if } z(\boldsymbol{u}; Zn)/z(\boldsymbol{u}; Pb) < 3.65; \\ 1, & \text{otherwise.} \end{cases} \quad (4.9)$$

Function $s(z(\boldsymbol{u}; Zn), z(\boldsymbol{u}; Pb), z(\boldsymbol{u}; Fe), z(\boldsymbol{u}; Ba))$ is expressed as follows:

$$s(z(\boldsymbol{u}; Zn), z(\boldsymbol{u}; Pb), z(\boldsymbol{u}; Fe), z(\boldsymbol{u}; Ba)) =$$

$$s_1(z(\boldsymbol{u}; Ba), z(\boldsymbol{u}; Fe)) \cdot s_2(z(\boldsymbol{u}; Zn), z(\boldsymbol{u}; Fe)) \cdot s_3(z(\boldsymbol{u}; Zn), z(\boldsymbol{u}; Pb)) \quad (4.10)$$

The first function $s_1(z(\boldsymbol{u}; Ba), z(\boldsymbol{u}; Fe))$ defines a coefficient, which can be viewed as an equivalent of a recovery factor. Grades of Ba and Fe determine whether mined material at a location $\boldsymbol{u}$ can be classified as baritic ore. The function returns the value of 0.5 if the mined material is baritic ore and 0.9 otherwise. Other two functions are used to penalize the profit for the ore decision if the first and/or second blending criteria are not satisfied. If $z(\boldsymbol{u}; Zn)/z(\boldsymbol{u}; Fe) \geq 2.5$ and $z(\boldsymbol{u}; Zn)/z(\boldsymbol{u}; Pb)) \geq 3.65$, then $s(z(\boldsymbol{u}; Zn), z(\boldsymbol{u}; Pb), z(\boldsymbol{u}; Fe), z(\boldsymbol{u}; Ba))$ is equal to either 0.5 or 0.9 and the full amount of profit $P(z(\boldsymbol{u}; Zn); \text{ore})$ is achieved at the location $\boldsymbol{u}$. If either of the stockpile blending criteria is not satisfied, the profit is reduced. If the stockpile blending ratios are close to 0 at the location $\boldsymbol{u}$, so is the value of $s(z(\boldsymbol{u}; Zn), z(\boldsymbol{u}; Pb), z(\boldsymbol{u}; Fe), z(\boldsymbol{u}; Ba))$ and corresponding profit.

4.2.3 Results

OK is performed separately for each grade variable. The OK estimates $z_{ok}(\boldsymbol{u}; g)$, $g = 1, ..., 4$ are used with the profit function P described in Section 4.2.2.3 to obtain estimates of profit $P(z_{ok}(\boldsymbol{u}; g), g = 1, ..., 4; k)$, $k = 1, ..., 2$ and corresponding optimal destinations $d_{opt}^{ok}(\boldsymbol{u})$ at all locations $\boldsymbol{u} \in A$. OK is performed with the variograms modeled using the artificial samples for each variable. Calculations are repeated for OK with the number of nearby conditioning samples varying from 15 to 155 with a step of 5 samples. AGC-EP is performed with all the grade variables at once. Similarly to OK, calculations are repeated with nearby samples in the range from 15 to 155 with a step of 5. Expected profit estimates

$EP(\boldsymbol{u}, k), \ k = 1, ..., 2$ are used to obtain corresponding optimal destinations $d_{opt}(\boldsymbol{u})$ at all the locations $\boldsymbol{u} \in A$. The 3×3 block^2 Gaussian filter is used to smooth the expected profit estimates. Figures 4.16, 4.17, and 4.18 show cumulative gained profit CP_{gained}, mean squared error in profit MSE_{profit}, and total percent of misclassification plotted versus the number of nearby samples used with OK and AGC-EP, respectively.
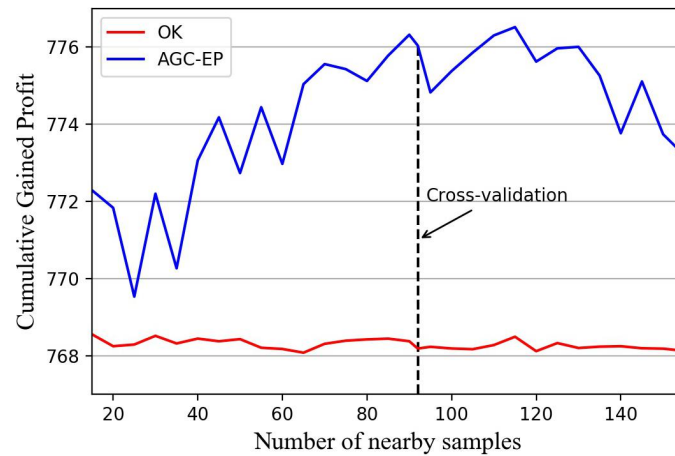
Figure 4.16: Cumulative gained profit CP_{gained} versus the number of nearby samples

The highest CP_{gained} for OK is achieved with 15 nearby samples; this measure, however, is almost constant for the range from 15 to 155 nearby samples. The highest CP_{gained} for AGC-EP is achieved with 115 nearby samples used. K-fold cross-validation is performed using the range from 65 to 140 (80 % of all 176 samples) nearby samples with a step of 5 samples; 65 is the minimum number of samples, for which angles of anisotropy are determined with the MOI method for all the locations. K-fold cross-validation predicts the optimal number of nearby samples to be 92, which falls into the optimal region between approximately 85 to 130 nearby samples.
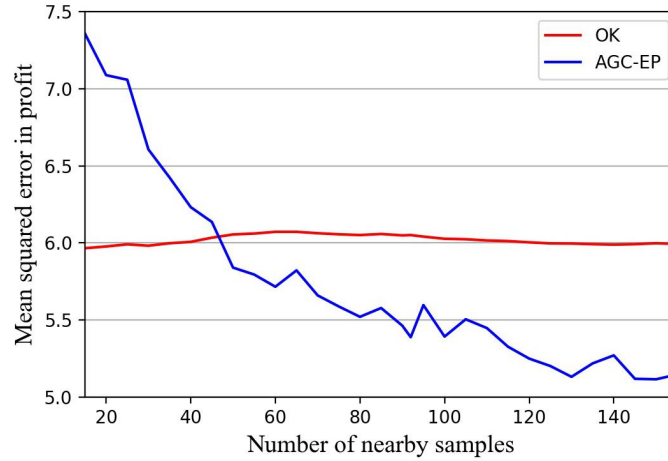
Figure 4.17: Mean squared error in profit versus the number of nearby samples

For OK, mean squared error in profit MSE_{profit} also remains nearly constant for all the considered numbers of nearby samples. For AGC-EP, MSE_{profit} rapidly decreases with the increase in the number of nearby samples used. The highest and lowest values are achieved with 15 and 150 nearby samples, respectively.
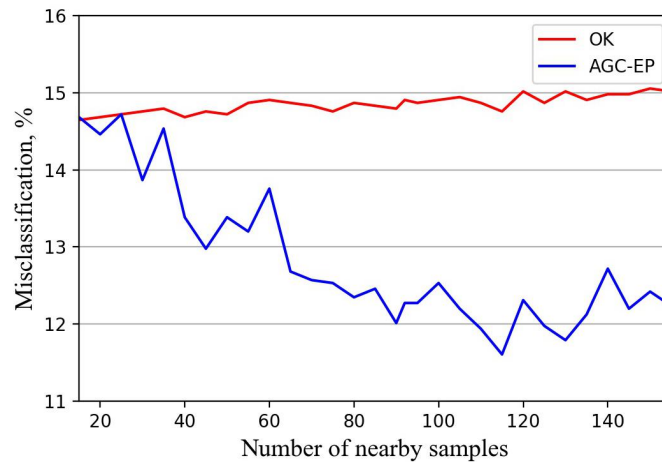
Figure 4.18: Total misclassification versus the number of nearby samples

For OK, the lowest total misclassification value is achieved with 15 nearby samples. Then, it slowly grows for the range from 15 to 155 nearby samples. For AGC-EP, the highest total misclassification is achieved with 25 nearby samples. Then, it rapidly decreases for the range from 30 to 90 nearby samples, remains nearly constant for the range from 90 to 130 nearby samples, and slightly increases for the range from 135 to 155 nearby samples. The lowest misclassification is achieved for AGC-EP used with 155 nearby samples.

The graphs in Figures 4.16 and 4.17 support the assumption stated in Chapter 3 that decreasing mean squared error in profit increases profit from mining operations. AGC-EP performs much better in terms of minimizing MSE_{profit} than OK, which results in a higher corresponding CP_{gained} value.

Figures 4.19 and 4.20 show OK estimates obtained with the optimal number of nearby samples and corresponding optimal ore/waste and the true optimal destinations.

(a) Zn

(b) Pb

(c) Fe

(d) Ba
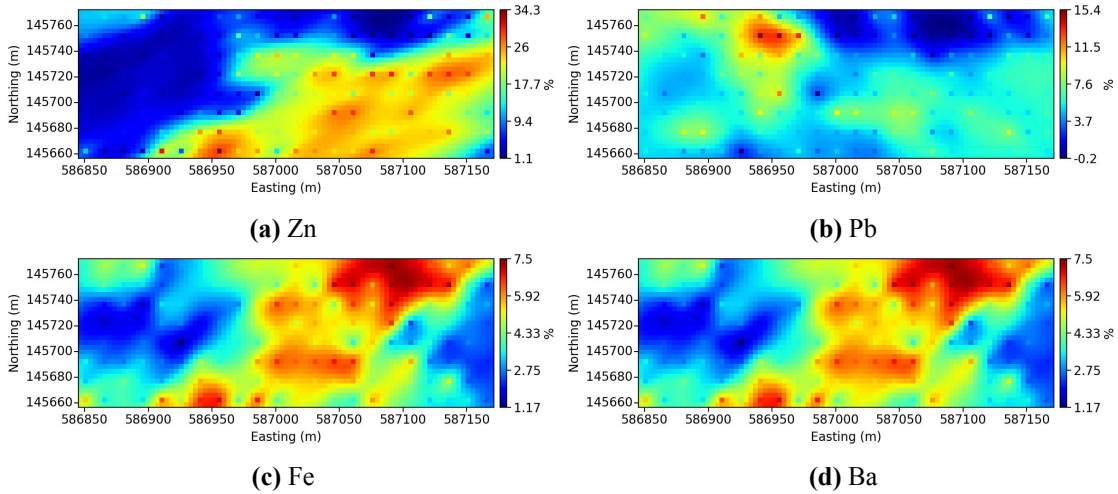
Figure 4.19: OK estimates for Zn, Pb, Fe, and Ba grade variables

(a) Estimated destinations

(b) True destinations
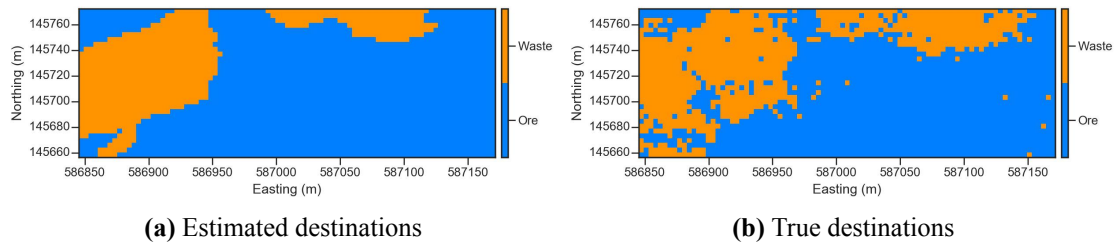
Figure 4.20: Optimal destinations for mined material determined with OK and the true optimal destinations

Figure 4.21 shows the variograms used for OK.

(a) Zn   **(b)** Pb

(c) Fe   **(d)** Ba
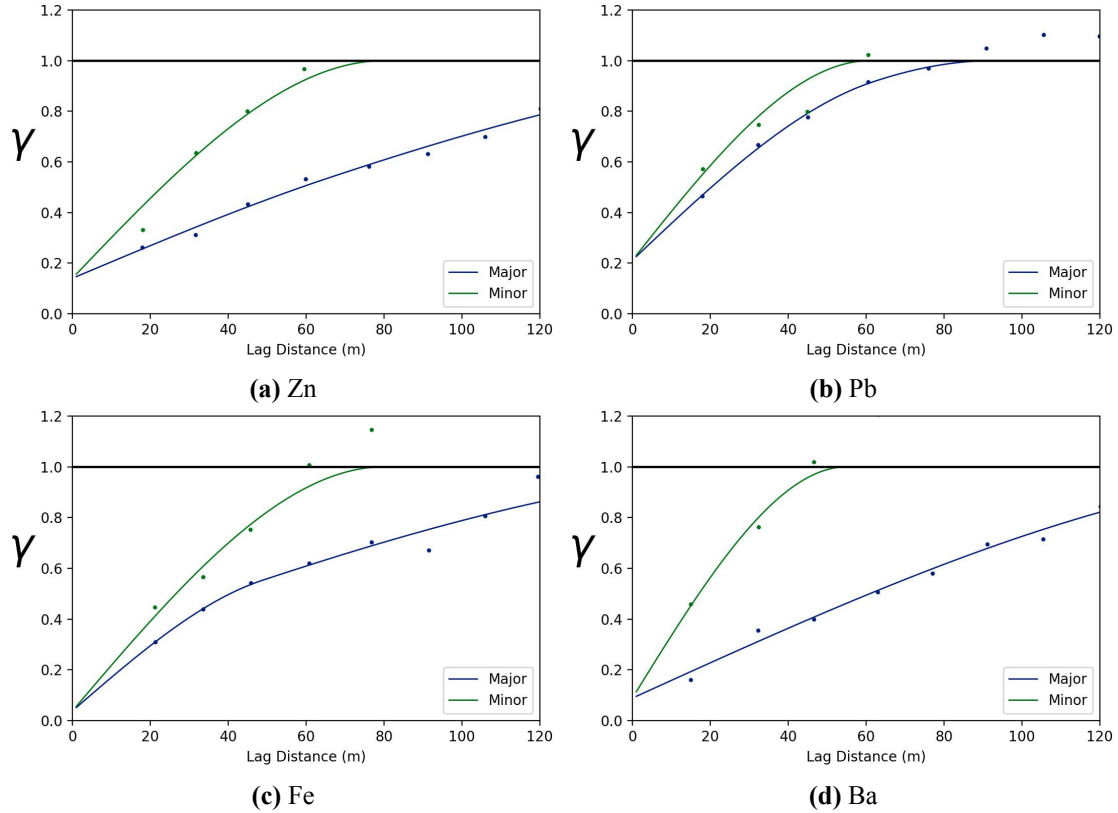
Figure 4.21: Variograms of all four grade variables used for OK

Figure 4.22 shows optimal ore/waste destinations determined by AGC-EP with 92 nearby samples and the true optimal ore/waste destinations.

(a) Estimated destinations   **(b)** True destinations
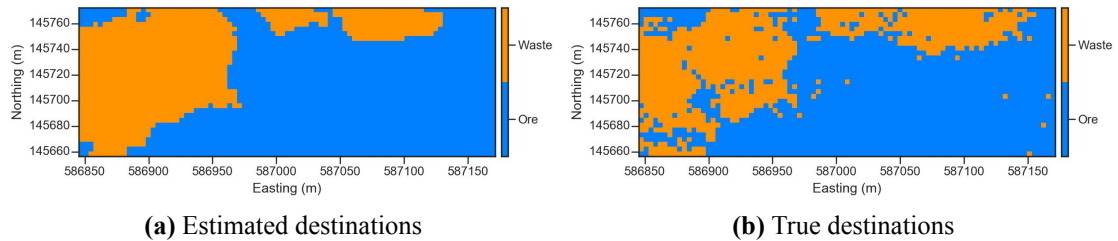
Figure 4.22: Optimal destinations for mined material determined with AGC-EP and the true optimal destinations

Overall, both methods show a good performance for this grade control case study. Nonetheless, AGC-EP outperforms the OK-based method by around 1.0 % in terms of cumulative gained profit CP_{gained}, 9.7 % in terms of mean squared error in profit MSE_{profit}, and 16.2 % in terms of total misclassification.

4.3 Summary

The workflow of the main part of AGC-EP is explained in detail. The post-processing of expected profit estimates produced by AGC-EP for better predicting correct mined material destinations is discussed. A practical method based on averaging filters is proposed.

A multivariate grade control case study based on real data from the Red Dog mine in Alaska is described. A carefully applied grade control modeling method based on OK is compared to the automatic AGC-EP algorithm. AGC-EP outperforms OK in terms of cumulative gained profit, mean squared error in profit, and total misclassification (type 1 and type 2 errors). The k-fold cross-validation algorithm (explained in Chapter 3) accurately predicts the number of nearby samples to use with AGC-EP.

The expected profit predictions obtained with AGC-EP can be used to determine optimal destinations for mined material directly if blasting is not performed. If blasting is performed, the pre-blast positions of high resolution expected profit should be corrected accounting for the shape and volume of the post-blast muckpile.

Chapter 5

Optimization Approach for Modeling Blast Movement

Final selection of mined material is performed on the post-blast muckpile. However, all grade control information (e.g., samples from blastholes, trenches, dedicated drillholes, etc.) is inherently pre-blast. If blasting is performed, mineable dig limits should be obtained for the post-blast muckpile to minimize misclassification. Blast movement modeling is a procedure that makes pre-blast predictions of grades or profit relevant for dig limits optimization and post-blast selection.

Pre-blast topography is necessary to estimate the pre-blast volume of rocks. The post-blast volume of rocks can be determined by discretizing the pre-blast volume into units or blocks and then transforming or moving them to define a post-blast shape. The size of the pre-blast blocks should correspond to pre-blast spatial prediction models. Modeling the trajectories of all blocks allows predicting the post-blast positions of all the pre-blast blocks along with the information assigned to them; post-blast topography is not necessary in this case but may be used for defining the post-blast muckpile (Isaaks, Barr, & Handayani, 2014). This approach also allows modeling the collisions and mixing of blocks. The physics of the breakage of rocks during blasting is very complex, which makes it difficult to predict the exact effect of blasting on the pre-blast rocks. Uncertainly in the geological composition and fractures of a mine bench as well as variations in the properties and characteristics of explosives and initiation systems will likely compromise even very good models and lead to significant positioning errors (La Rosa & Thornton, 2011).

Precise information about blast movement is obtained from blast movement measurements and detailed post-blast topography. By using measured blast movement vectors, it is possible to approximately estimate the post-blast positions of dig limits. A common approach is the translation of each pre-blast block to its post-blast position and fixing pre-blast polygons based on interpolated blast movement vectors (Thornton et al., 2005). This ap-

proach is unlikely to be accurate due to the difference of the pre- and post-blast shapes of a mine bench. A method will be developed to overcome this issue.

In this chapter, an optimization-based algorithm for modeling blast-induced displacement of rock in 3-D using gridded pre- and post-blast topography and direct blast movement measurements is described; the algorithm is called Advanced Grade Control-Blast Movement (AGC-BM). The blast movement problem is expressed as an optimization assignment problem. The optimization assignment problem is solved by a heuristic algorithm offering an approximate solution in a reasonable time. The objective function and optimization details are explained. The modeling algorithm can be used to map the pre-blast positions of expected profit blocks to the post-blast muckpile in 3-D. The post-blast profit can then be used to define optimal post-blast dig limits. Specific grade control cases with limited information about the direction of blast movement and the shape of post-blast muckpile are discussed. Relevant examples are provided.

5.1   Sources of Information about Blast Movement

Detailed topography allows creating accurate pre- and post-blast 3-D models. The pre- and post-blast models should be discretized such that the swell (an increase in the volume of rocks during blasting) is taken into account but the number of blocks is the same for both models. An assumption is made that the material in each pre-blast block is kept together and mapped to a post-blast block. If topography is absent, it can be approximately estimated using the major direction of rock displacement, the locations of free faces, and the swell factor.

After the pre- and post-blast models are created and discretized, some criteria should be used to map the blocks of the pre-blast model to the blocks of the post-blast model. Direct blast movements is a valuable source of information that may be used to improve the mapping and avoid modeling the complex physics of blasting. Simple visual markers like sands bags and wooden stakes (S. L. Taylor, 1995; Zhang, 1994) may be placed in drill-holes before blasting and used to determine the displacement vectors for some zones of a mine bench. S. L. Taylor (1995) indicates that only 35 % of stakes and bags were recov-

ered over 5 blasts. Zhang (1994) also reports low bag recovery for some blasts. Another drawback of this method is its labor intensiveness; the visual markers have to be recovered manually during excavation. Remote sensing equipment like magnetic radiometers (Gilbride, 1995), radio frequency ID tags (La Rosa & Thornton, 2011), or other specialized transmitters (Adam & Thornton, 2004) may be used for a more reliable blast movement measurement. Usually, only sparse measurements are available; some tools are necessary to use this limited information to improve the understanding of blast movement for often complex configurations of post-blast muckpiles.

Thornton (2009a) confirms that the firing sequence of a blast has a significant impact on the direction of blast movement; rocks move preferentially perpendicular to the timing contours. Programmable electronic detonators (Lusk, Silva, & Eltschlager, 2013) offer a high level of control over the timing and initiation sequence of a blast. Therefore, the firing pattern configuration may be used to calibrate sparse blast movement measurements.

To summarize, there are three primary sources information about blast movement: i) detailed topography, ii) direct blast movement measurements, and iii) the elements of blast design. A practical blast movement modeling algorithm should allow incorporating this information for obtaining better blast movement models.

5.2 Problem Formulation

The movement of rock due to blasting could be considered to be a combinatorial assignment problem. A pre-blast mine bench and a post-blast muckpile can be discretized by a set of blocks; the coordinate location of the centre of each pre- and post-blast block is known. It is assumed that the numbers of pre- and post-blast blocks are the same. A set of post-blast coordinate vectors $A = \{\boldsymbol{a}_1, ..., \boldsymbol{a}_N\} \in R^3$, where $\boldsymbol{a}_i = (a_x^i, a_y^i, a_z^i)$, $i = 1, ..., N$ should be assigned to a set of pre-blast coordinate vectors $B = \{\boldsymbol{b}_1, ..., \boldsymbol{b}_N\} \in R^3$, where $\boldsymbol{b}_i = (b_x^i, b_y^i, b_z^i)$, $i = 1, ..., N$ using a bijective mapping (or permutation) $\varphi : A \mapsto B$ (Burkard & Derigs, 2013). Each post-blast block should be assigned to a pre-blast block based on some cost function $c(\varphi)$, where φ is one permutation out of the set of all possible permutations P. Given that $\boldsymbol{C}$ is the matrix of cost elements $c_{i,j}$, the cost for every permutation is associated

as follows (Burkard & Derigs, 2013, p. 1):

$$c(\varphi) := \sum_{i=1}^{N} c_{i,\varphi(i)}$$

The objective is to find a mapping $\varphi \in P$ such that the cost is minimized:

$$\min_{\varphi \in P} \sum_{i=1}^{N} c_{i,\varphi(i)}$$

This problem can also be expressed as a bipartite graph in Figure 5.1.
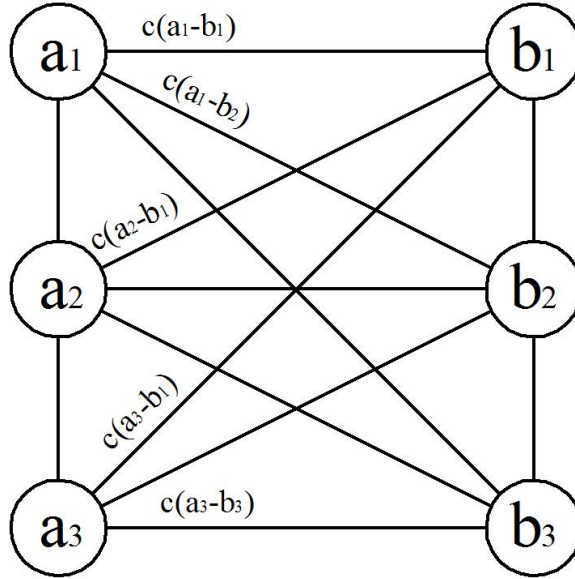
Figure 5.1: A bipartite graph illustrating the linear sum assignment problem

Due to the nature of complex geological and grade control boundaries, it is desirable to have a high resolution. The resolution of the grade control models is recommended to be around 25 % of the sample spacing (Vasylchuk & Deutsch, 2017); for example, a $2 \times 2 \, \text{m}^2$ grid is recommended for a blasthole pattern with an average spacing of $8 \, \text{m}$. The 3-D models of mine benches built according to these recommendations would consist of approximately 10 000 to 25 000 blocks.

The Kuhn-Munkres or 'Hungarian' algorithm (Kuhn, 1955) is a popular algorithm for solving linear sum assignment problems in polynomial time if the size of the cost matrix is reasonable. Unfortunately, the current blast movement problem cannot be solved by such an algorithm because some elements $c_{i,j}$ of matrix C change at each permutation; this is due to one element of the cost function explained below. Therefore, a heuristic algorithm is applied to find an approximate solution in a reasonable time.

5.2.1 Cost Function

It is necessary to make assumptions about the blast movement including i) there is no mixing and collision of particles inside the mine bench during blasting, and ii) the swell factor is uniform throughout the entire muckpile. Although the rocks mix and collide during blasting, it is currently infeasible to model blast movement with correct physics due to computational considerations and uncertainty in initial and boundary conditions. Fortunately, the direct blast movement measurements made by the systems such as described by Adam and Thornton (2004) allow creating 3-D blast movement vectors that can be used to constrain pre- and post-blast blocks. Topography is a primary source for creating detailed 3-D models. Gridded topographic surfaces of a mine bench before and after blasting may be created using laser scanners (Isaaks, Barr, & Handayani, 2014) or scanning drone systems.

The proposed cost function consists of four aspects: i) the distance between the pre-and post-blast blocks, ii) the distance between each pre- and post-blast block to neighboring blocks within a corresponding 3-D model, iii) distance from each pre- and post-blast block to the boundaries of a corresponding model in three orthogonal directions, and iv) the closeness of optimized displacement vectors to real displacement vectors measured with specialized equipment.

Mathematically, the proposed cost function is expressed as follows:

$$c(\varphi) \;=\; \sum_{i=1}^{4} w_i\Big(c_i(\varphi)/c_i(\varphi_{init})\Big) \tag{5.1}$$

where $c_i(\varphi)$, $i = 1, 2, 3, 4$ are components (elements) of the cost function $c(\varphi)$ dependent on a current permutation $\varphi \in P$; $c_i(\varphi_{init})$ are from the initial permutation $\varphi_{init} \in P$ corresponding to an initial guess model; w_i, $i = 1, 2, 3, 4$ are weights corresponding to the components of the cost function $c(\varphi)$.

Note that the units of all the components are similar, that is, the units of distance. Also, the initial costs are checked to ensure that they are not close to zero. Since the initial permutation φ_{init} is obtained using a simple algorithm based on search and sorting (explained below), the initial costs are unlikely to be close to 0; if they are, in fact, close to 0, then the initial solution is very close to an optimal one and no or very few iterations are required to

reach it. A tolerance parameter is used to ensure that optimization terminates if the initial cost is close to 0.

First Element of the Cost Function

The purpose of this element is to assign each post-blast block to the closest pre-blast block based on their corresponding x, y, and z coordinates. Even though the difference in coordinates for the associated blocks of the pre- and post-blast models is expected to be smaller at the back of the mine bench and larger closer to its free face, the general principle is the same. This idea is illustrated in Figure 5.2 and described mathematically as follows:

$$c_1(\varphi) \;=\; 1/N \sum_{i=1}^{N} \| \, \boldsymbol{a}_{\varphi(i)} - \boldsymbol{b}_i \, \| \tag{5.2}$$

where $c_1(\varphi)$ is the first element of $c(\varphi)$; $\boldsymbol{b}_i$ is the coordinate vector of a pre-blast block; $\boldsymbol{a}_{\varphi(i)}$ is the coordinate vector of a post-blast block corresponding to the current permutation $\varphi \in P$.

Figure 5.2: A graph illustrating the idea behind the first element of the cost function

Second Element of the Cost Function

This element of the cost function is calculated as the average quadratic difference between the corresponding off-diagonal elements of pre- and post-blast distance matrices, $\boldsymbol{D}^B$ and $\boldsymbol{D}^A$, respectively. This element of the cost function represents the assumption that the post-blast blocks do not significantly change their position relative to surrounding blocks if compared to the assigned blocks of the pre-blast model; it accounts for the coherency of

the post-blast model. This is the part of the cost function that prohibits using an exact linear sum assignment algorithm; it is expressed mathematically as follows:

$$d_{ij}^B = \| \boldsymbol{b}_i - \boldsymbol{b}_j \|, \; i = 1, ..., N, \; j = 1, ..., N$$

$$d_{ij}^A = \| \boldsymbol{a}_{\varphi(i)} - \boldsymbol{a}_{\varphi(j)} \|, \; i = 1, ..., N, \; j = 1, ..., N$$

$$c_2(\varphi) = \frac{1}{N^2 - N} \sum_{i=1}^{N} \sum_{j=1}^{N} (d_{ij}^B - d_{ij}^A)^2, \; \forall \, i \neq j \tag{5.3}$$

where $c_2(\varphi)$ is the second element of $c(\varphi)$; d_{ij}^B are the elements of the matrix of distances between all pre-blast blocks, $\boldsymbol{D^B}$; d_{ij}^A are the elements of the matrix of distances between all post-blast blocks, $\boldsymbol{D^A}$.

Third Element of the Cost Function

The next element of the cost function accounts for relative positions of each pre- and post-blast block with respect to the boundaries of a corresponding 3-D model. A set of N vectors $K = \{\boldsymbol{k}_1, ..., \boldsymbol{k}_N\} \in R^3$ corresponds to each block of a pre-blast model. Each vector $\boldsymbol{k}_i = (k_x^i, k_y^i, k_z^i), \; i = 1, ..., N$ has the distances to the boundaries of the pre-blast model as its elements. Similarly, a set of N vectors $L = \{\boldsymbol{l}_1, ..., \boldsymbol{l}_N\} \in R^3$, where $\boldsymbol{l}_i = (l_x^i, l_y^i, l_z^i), \; i = 1, ..., N$ corresponds to each block of a post-blast model. The idea behind this element of the cost function is illustrated in Figure 5.3.

Figure 5.3: A graph illustrating the idea behind the third element of the cost function

The third element of the cost function is calculated using the following equation:

$$c_3(\varphi) = \frac{1}{N} \sum_{i=1}^{N} \| \boldsymbol{l}_{\varphi(i)} - \boldsymbol{k}_i \| \tag{5.4}$$

where $c_3(\varphi)$ is the third element of $c(\varphi)$; $\boldsymbol{l}_{\varphi(i)}$ is the confinement coordinate vector of a post-blast block corresponding to the current permutation $\varphi \in P$.
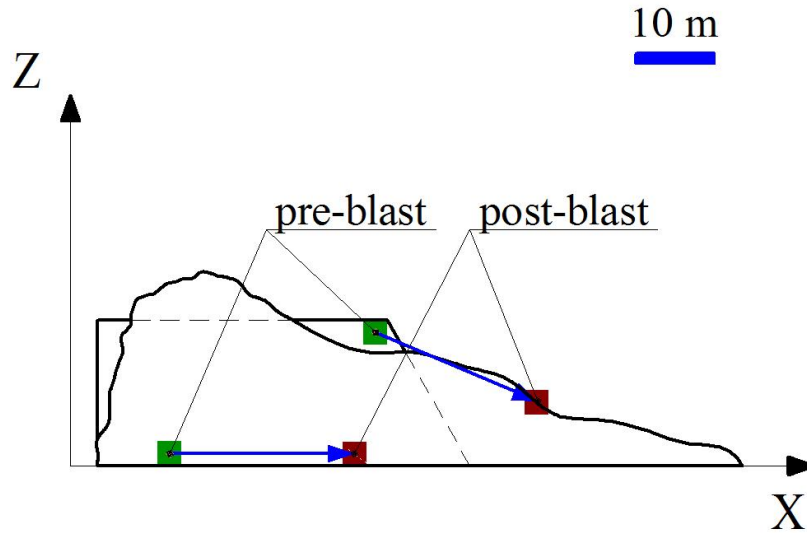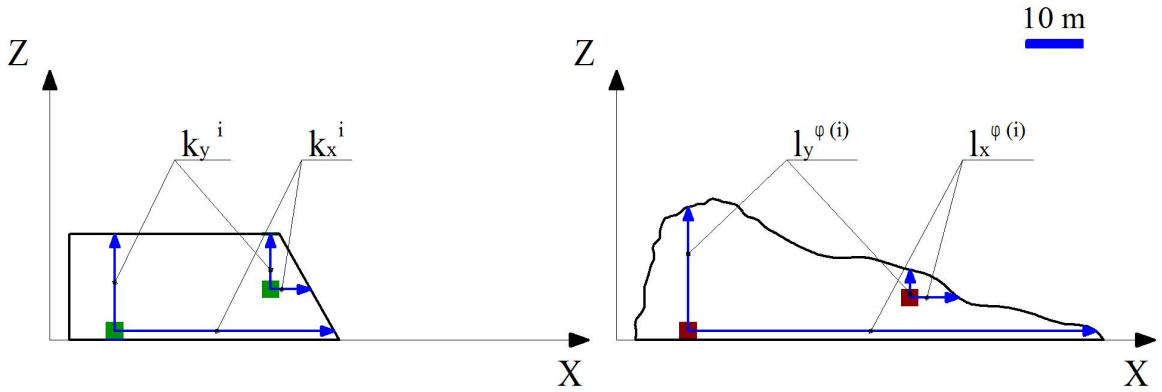
Fourth Element of the Cost Function

The specialized equipment for measuring blast movement usually consists of some type of transmitters and detecting equipment (a receiver). The pre- and post-blast positions of the transmitters are used to calculate the directions and magnitudes of displacement for each assigned pair of pre- and post-blast blocks. Unfortunately, it is not economically viable to use many transmitters for a blast. Some researchers report using around 5 transmitters on average for 38 blasts (Yennamani, 2010, p. 73-74). The components of the measured pre- and post-blast coordinate vectors of the transmitters should be interpolated and assigned to the closest pre-blast block. After interpolation, the pre- and post-blast positions of the transmitter can be expressed as two sets of vectors $P = \{\boldsymbol{p}_1, ..., \boldsymbol{p}_N\} \in R^3$ and $S = \{\boldsymbol{s}_1, ..., \boldsymbol{s}_N\} \in R^3$, respectively. The set of measured displacement vectors assigned to each pre-blast block, $M = \{\boldsymbol{m}_1, ..., \boldsymbol{m}_N\} \in R^3$, is obtained as follows:

$$\boldsymbol{m}_i = \boldsymbol{s}_i - \boldsymbol{p}_i, \ i = 1, ..., N$$

The set of optimized displacement vectors for the assigned pairs of pre- and post-blast blocks, $O = \{\boldsymbol{o}_1, ..., \boldsymbol{o}_N\} \in R^3$, is calculated as follows:

$$\boldsymbol{o}_i = \boldsymbol{a}_{\varphi(i)} - \boldsymbol{b}_i, \ i = 1, ..., N$$

The fourth element of the cost function accounts for minimizing the average difference between the measured and optimized displacement vectors. This is the element of the cost function that allows calibrating the theoretical blast movement modeling with real measurements without the need for modeling mixing and colliding blocks (Figure 5.4).
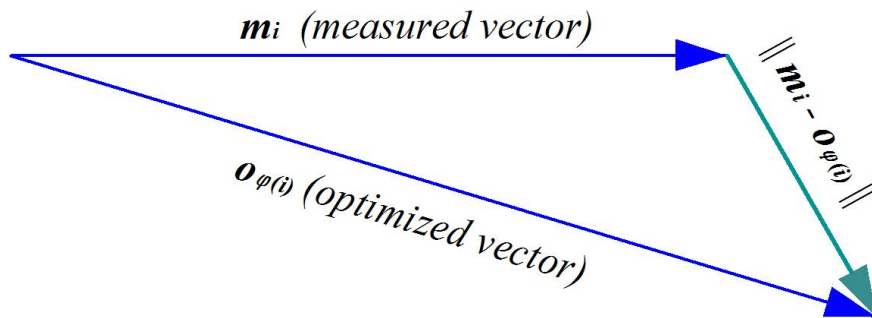
Figure 5.4: The magnitude of the difference between measured and optimized displacement vectors

Mathematically, the fourth element of the cost function is expressed as follows:

$$c_4(\varphi) = \frac{1}{N} \sum_{i=1}^{N} \| \boldsymbol{m}_i - \boldsymbol{o}_{\varphi(i)} \| \tag{5.5}$$

where $c_4(\varphi)$ is the fourth element of $c(\varphi)$; $\boldsymbol{o}_{\varphi(i)}$ is an ith optimized displacement vector corresponding to the current permutation $\varphi \in P$.

The firing sequence information of a blast can be used to calibrate sparse blast movement vectors. Details about this procedure are provide later in this chapter.

The cost function $c(\varphi)$ is minimized using a stochastic algorithm based on random restarts. A detailed description of the algorithm with an example is provided below.

5.3 Optimization Algorithm

The primary idea of the optimization algorithm is to find a permutation φ that approximately minimizes the cost function using random changes to the permutation vector. Each element of the cost function is standardized and has a weight. The algorithm is first implemented on low-resolution (LR) pre- and post-blast models to reduce the number of required permutations; a fine-tuning optimization is then used on high-resolution (HR) models (e.g., one quarter of sample spacing). A detailed workflow is provided below:

1. Build pre- and post-blast 3-D models using topography and polygons.

2. Determine the grid size for the LR models; there should be at least 4 blocks in the vertical direction for an adequate representation of the muckpile shape. The grid size is calculated using the following equation:

$$g^{LR} = (h_{pre} + h_{post})/8$$

where h_{pre} and h_{post} are the average heights of the pre- and post-blast topographic surfaces above the bottom elevation, respectively; g^{LR} is the grid size for the LR 3-D models.

The LR grid size defines a new grid definition. The pre-blast gridded topography is re-gridded according to the new definition; the re-gridded topography and the bottom

116

elevation are sufficient for creating the pre- and post-blast LR 3-D models. Due to the swell factor, the post-blast 3-D model has more blocks than the pre-blast one.

3. Change the grid sizes of the LR post-blast model in the x, y, and z directions such that the numbers of blocks for the LR pre- and post-blast models are the same accounting for the swell factor. A derivative free adaptively controlled random search optimization algorithm (ACRS) (Brachetti, Ciccoli, Di Pillo, & Lucidi, 1997; Cirio, Lucidi, Parasiliti, & Villani, 2002; Liuzzi & Lucidi, n.d.; Liuzzi, Lucidi, Parasiliti, & Villani, 2003) is used. It is based on a global optimization algorithm from Price (1977).

4. After the numbers of blocks for the two models are equal, the pre-blast blocks A should be assigned to the post-blast blocks B using an initial bijective mapping $\varphi_{init} : A \mapsto B$. The objective for each pair of assigned blocks is formulated separately:

$$\min_{\varphi_{init} \in P} \left((a_x^{\varphi_{init}(i)} - b_x^i)^2 + (a_y^{\varphi_{init}(i)} - b_y^i)^2 + (a_z^{\varphi_{init}(i)} - b_z^i)^2 + \right.$$
$$\left. (l_x^{\varphi_{init}(i)} - k_x^i)^2 + (l_y^{\varphi_{init}(i)} - k_y^i)^2 + (l_z^{\varphi_{init}(i)} - k_z^i)^2 \right)^{(1/2)}, \ 1, ..., N \qquad (5.6)$$

After a post-blast block $\varphi_{init}(i)$, is assigned to a pre-blast block i, this pair is removed from the queue. The procedure above is implemented using a simple search based on sorting.

5. Calculate an initial value of the cost function $c(\varphi_{init})$ for the LR model corresponding to the initial guess mapping φ_{init} using Equation (5.1); then, optimize the LR initial guess model by minimizing the cost function using an algorithm based on random restarts and permutations (described below).

6. In order to build the second initial guess HR model, the blocks of the optimized LR post-blast model are associated with the blocks of the HR post-blast model. The grid definition for the HR pre- and post-blast 3-D models is obtained using a grid size provided by the user; similar to the LR models, the pre- and post-blast topography is re-gridded using the new definition and then used to create the HR 3-D models. The grid sizes in the x, y, and z directions of the HR post-blast model are changed to match the number of blocks in the HR models similar to the LR models. Each block of the

HR post-blast model is associated with the closest block of the LR post-blast model; naturally, each LR block will have several HR blocks associated with it. Then, each block of the LR pre-blast model is associated with the blocks of the HR pre-blast model in a similar fashion. After Steps 1-5, each block of the LR post-blast model is assigned to a block of the LR pre-blast model; this mapping can be used to assign each block of the HR pre-blast model to a block of the HR post-blast model. It is not known exactly in which order the HR blocks from each of the pre- and post-blast pulls should be assigned to each other; therefore, they are assigned by the closeness to their respective LR blocks in Euclidian space. The main idea behind this step is illustrated in Figure 5.5.
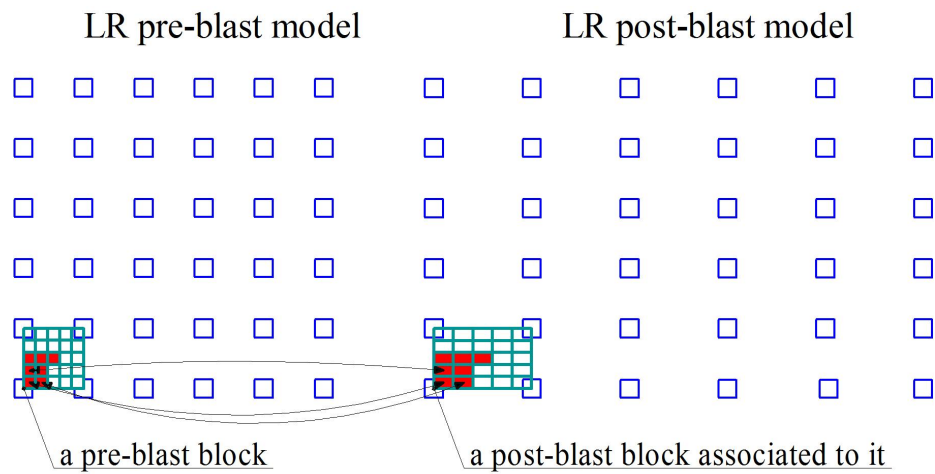
Figure 5.5: Schematic illustration of associating blocks of high resolution pre- and post-blast models using low resolution pre- and post-blast models

7. Calculate an initial value of the cost function $c(\varphi_{init2})$ for the HR model corresponding to the second initial guess mapping φ_{init2} using Equation (5.1); then, optimize the HR second initial guess model by minimizing the cost function. Start from a random location of the post-blast model; search for a user-specified number of nearby blocks.

8. Switch the first starting block with a block in its neighbourhood, calculate a difference in the total cost and save this permutation if the cost is decreased; continue until all the blocks in the neighbourhood are used in a random order and go to the next start location. This allows randomly permuting the blocks of the HR post-blast model assigned to the blocks of the HR pre-blast model.

9. Perform the number of random restarts specified by the user.

10. Output the optimized model for further processing and obtaining mineable dig limits.

The numbers of restarts for the LR and HR 3-D models could be selected automatically. The algorithm iterates until the improvement to the cost function of a model is less than a tolerance parameter. The improvement to the cost function is calculated and saved as the percentage of the initial cost function value, Improvement $= ((c(\varphi_{init} - c(\varphi))/c(\varphi_{init})) \cdot 100\%$. The number of neighbours for the LR and HR models should be selected by the user. It is recommended using no less than 20 and 40 neighbours for the LR and HR models, respectively. The user can also specify the numbers of restarts for the two models manually.

5.4 Example with Topography and Blast Movement Vectors

The optimization algorithm described in Section 5.3 is implemented in Fortran according to the GSLIB conventions (C. V. Deutsch & Journel, 1998). A synthetic example is developed to demonstrate the steps for blast movement modeling.

A realization of grade is simulated using sequential Gaussian simulation algorithm (Isaaks, 1991) implemented in $sgsim$ (C. V. Deutsch & Journel, 1998) for an area of 70×110 m^2 with a grid size of 1×1 m^2. The reference realization is then sampled at a grid size of 8×8 m^2 with a random error of up to 1 m in coordinates. The variogram model required for the simulation has one spherical nested structure with a nugget effect of 0.2 and the major direction of continuity at $30°$ from North. The major and minor ranges of continuity are 100 m and 35 m, accordingly. Simulated grades in Gaussian units are converted to be lognormal to appear more realistic. Then, the simulated grades are converted to expected profit for three destinations using two cutoff grades; the expected profit is generated for the same area with a grid size of 2×2 m^2 to match the resolution of 3-D models. Figure 5.6 illustrates the reference simulated model and samples.

(a) Reference model
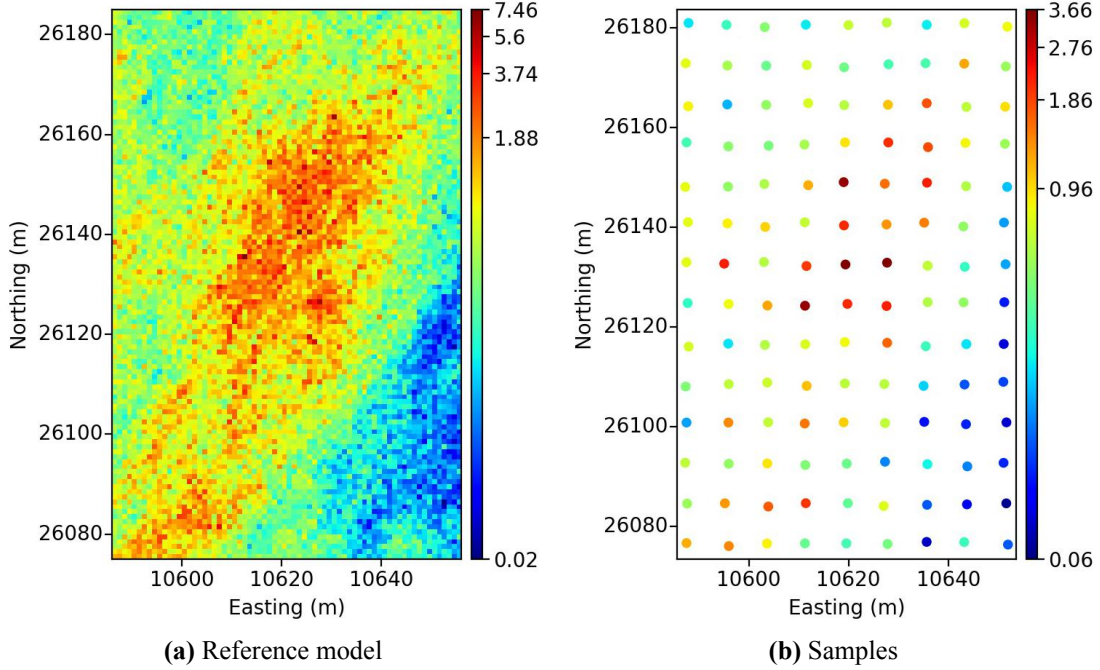
(b) Samples

Figure 5.6: Artificial reference realization and samples

Profit Function

The Advanced Grade Control-Expected Profit (AGC-EP) algorithm (more details about the algorithm are in Chapters 3 and 4) is used to perform local multivariate simulation and expected profit calculation. Simulated values $z^l(\boldsymbol{u}), l = 1, ..., L$ at all locations $\boldsymbol{u} \in A$ are converted to expected profit using a profit function designed for this example. The profit function uses a single grade variable and two cutoff grades, $z_c^1 = 1.0$ and $z_c^2 = 0.5$, to distinguish between three destinations for mined material: ore, stockpile, and waste. If a simulated value $z^l(\boldsymbol{u})$ at a location $\boldsymbol{u}$ is greater than or equal to the cutoff grade z_c^1, the expected profit for the ore decision is calculated as follows:

$$P(z^l(\boldsymbol{u}); \text{ore}) = \begin{cases} z^l(\boldsymbol{u}) - z_c^1, & \text{if } z^l(\boldsymbol{u}) \geq z_c^1; \\ 0, & \text{otherwise.} \end{cases} \tag{5.7}$$

$$EP(\boldsymbol{u}; \text{ore}) = \frac{1}{L} \sum_{l=1}^{L} P(z^l(\boldsymbol{u}); \text{ore})$$

where $P(z^l(\boldsymbol{u}); \text{ore})$ is the profit at the location $\boldsymbol{u}$ given the ore decision; $EP(\boldsymbol{u}; \text{ore})$ is the expected profit at the location $\boldsymbol{u}$ given the ore decision.

If $z^l(\boldsymbol{u})$ is below than z_c^1 and $z^l(\boldsymbol{u})$ is greater than or equal to z_c^2, the expected profit for the stockpile decision is calculated as follows:

$$P(z^l(\boldsymbol{u}); \text{stockpile}) = \begin{cases} z^l(\boldsymbol{u}) - z_c^2, & \text{if } z^l(\boldsymbol{u}) < z_c^1 \text{ and } z^l(\boldsymbol{u}) \geq z_c^2; \\ 0, & \text{otherwise.} \end{cases} \tag{5.8}$$

$$EP(\boldsymbol{u}; \text{stockpile}) = \frac{1}{L} \sum_{l=1}^{L} P(z^l(\boldsymbol{u}); \text{stockpile})$$

where $P(z^l(\boldsymbol{u}); \text{stockpile})$ is the profit at the location $\boldsymbol{u}$ given the stockpile decision; $EP(\boldsymbol{u}; \text{stockpile})$ is the expected profit at the location $\boldsymbol{u}$ given the stockpile decision.

If $z^l(\boldsymbol{u})$ is below than z_c^2, the expected profit for the waste decision is calculated as follows:

$$P(z^l(\boldsymbol{u}); \text{waste}) = \begin{cases} z_c^2 - z^l(\boldsymbol{u}), & \text{if } z^l(\boldsymbol{u}) < z_c^2; \\ 0, & \text{otherwise.} \end{cases} \tag{5.9}$$

$$EP(\boldsymbol{u}; \text{waste}) = \frac{1}{L} \sum_{l=1}^{L} P(z^l(\boldsymbol{u}); \text{waste})$$

where $P(z^l(\boldsymbol{u}); \text{waste})$ is the profit at the location $\boldsymbol{u}$ given the waste decision; $EP(\boldsymbol{u}; \text{waste})$ is the expected profit at the location $\boldsymbol{u}$ given the waste decision.

Equations (5.7)-(5.9) define the profit function for this example. Figure 5.7 demonstrates high resolution expected profit obtained with AGC-EP.

(a) Ore   **(b)** Stockpile   **(c)** Waste
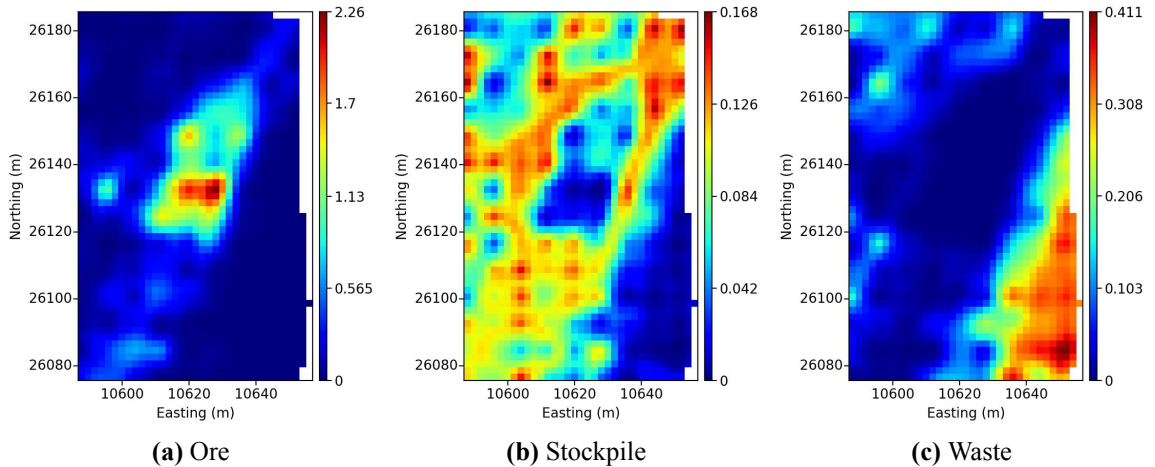
Figure 5.7: Expected profit maps for three mined material destinations

Pre- and post-blast topographic surfaces are required to build 3-D models. Also, pre- and post-blast polygons are required for better defining the limits of the models. The arti-

ficial pre- and post-blast topographic surfaces illustrating probable blast movement are in Figure 5.8 .

(a) Pre-blast   **(b)** Post-blast
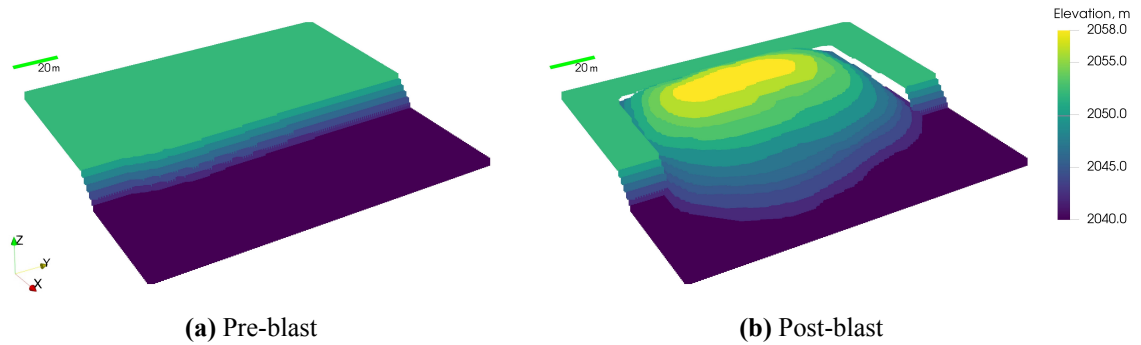
Figure 5.8: Artificial pre- and post-blast topographic surfaces

Measured displacement vectors are used for calibrating theoretical blast modeling. In Figure 5.9, a set of artificial blast movement vectors created for this example is illustrated.
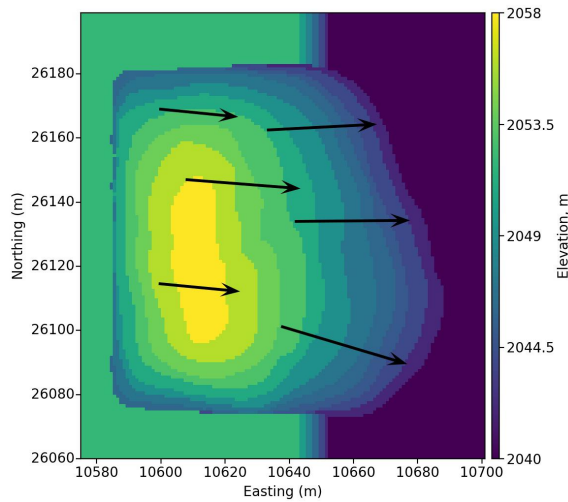
Figure 5.9: Artificial blast movement vectors

After the LR model is optimized (steps 1-5 of the algorithm), it is used to obtain a HR initial guess model (Figures 5.10d-5.10f) with a corresponding permutation φ_{init2}.

(a) Ore   **(b)** Stockpile   **(c)** Waste

(d) Ore   **(e)** Stockpile   **(f)** Waste
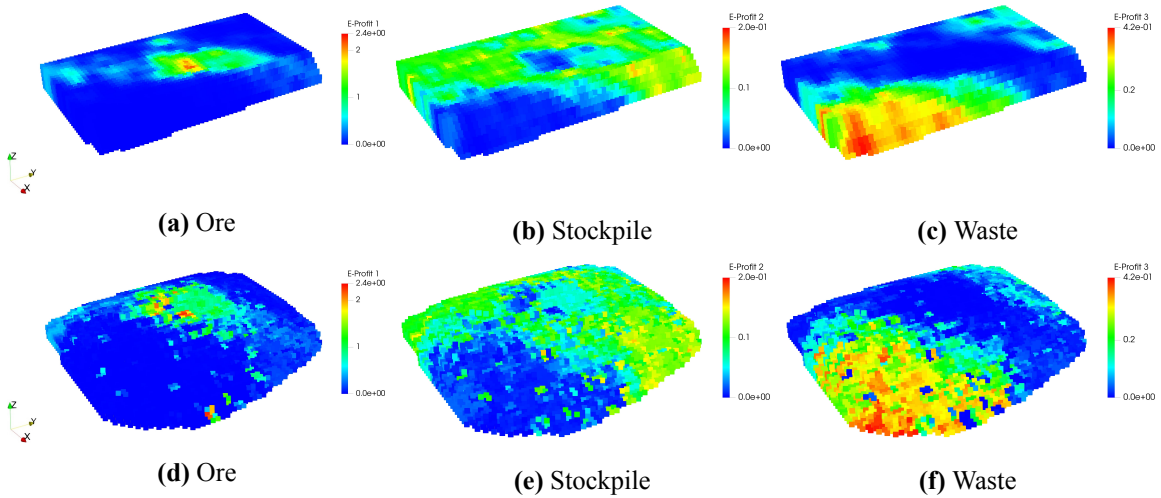
Figure 5.10: Initial guess post-blast 3-D models compared to pre-blast 3-D models of expected profit

Equation (5.1) is used to calculate the initial value of the cost function corresponding to the permutation. After the initial guess permutation for the HR model φ_{init2} is obtained and the corresponding cost is calculated, the final part the optimization algorithm starts; each new permutation φ is accepted if it brings an improvement to the cost function. The tolerance parameter was set to 0.005 % of improvement. The LR and HR neighbors were set to 20 and 40, respectively. The algorithm performed 58 000 and 100 000 iterations to minimize the cost functions for the LR and HR models, respectively. The post-blast 3-D models after 30 % and 100 % of the performed number of random restarts for the HR model are illustrated in Figures 5.11 and 5.12.

(a) Ore   **(b)** Stockpile   **(c)** Waste
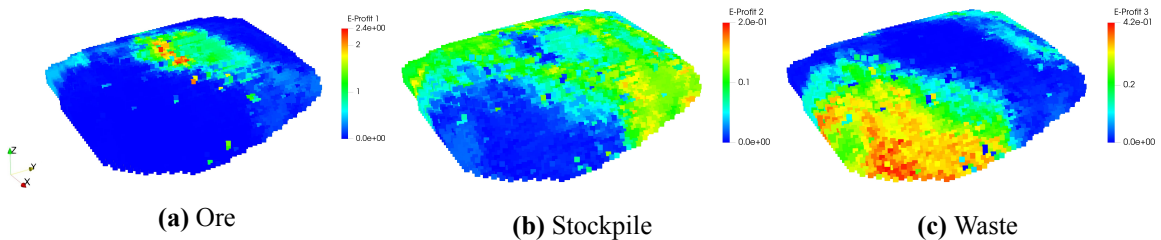
Figure 5.11: Expected profit units for three destinations mapped on the post-blast 3-D models (30 % of random restarts)

(a) Ore **(b)** Stockpile **(c)** Waste
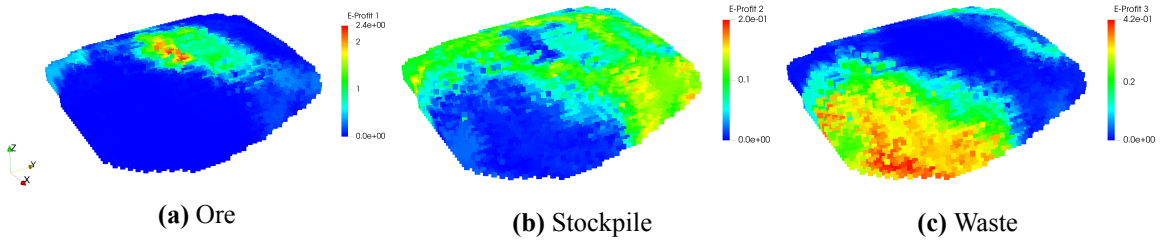
Figure 5.12: Expected profit units for three destinations mapped on the post-blast 3-D models (100 % of random restarts)

After the optimized post-blast expected profit in 3-D is obtained, it can be used to optimize dig limit boundaries. Figure 5.13 shows HR pre- and post-blast expected profit maps converted to 2-D HR classification maps. It can be seen that spatial structures of the HR pre- and post-blast classification maps are similar despite apparent differences in the shapes of the underlying 3-D models.

(a) Pre-blast **(b)** Post-blast
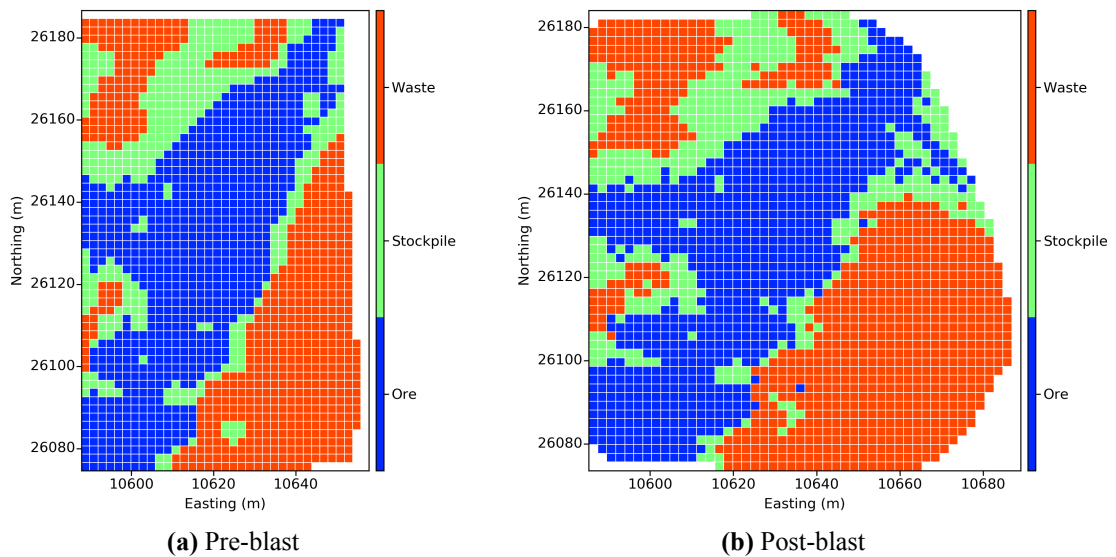
Figure 5.13: Pre-blast classification of mined material versus post-blast classification of mined material

The current example is performed with the third element of the cost function receiving half the weight of the rest of the elements; this reduces the amount of visual artifacts that occur due to the artificial nature of the pre- and post-blast topographic surfaces. Giving more or less weight to one of the elements does not necessarily mean it will drastically change the mapping since all the elements are related. However, it might be reasonable

to give more weight to the fourth element of the cost function if many transmitters are available to measure blast movement directly. Having very good and detailed pre- and post-blast topography would justify weighting the third elements of the cost function more than the others. Figure 5.14 shows the improvement in the cost function versus the number of random restarts performed.
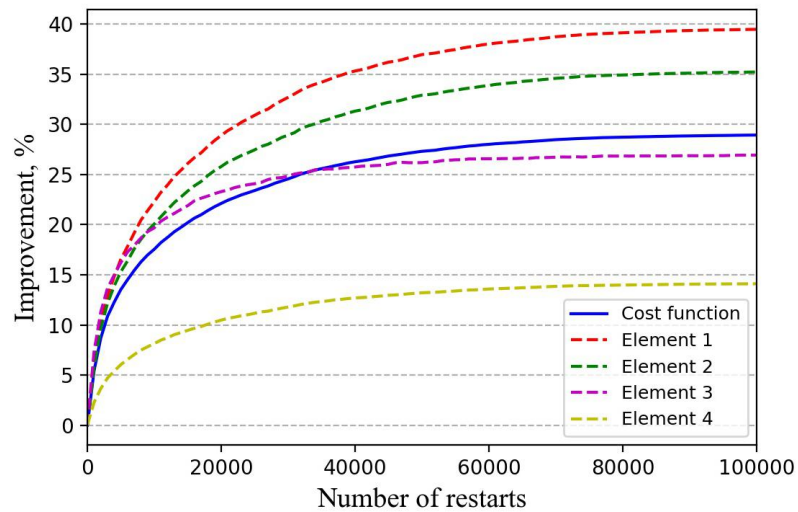
Figure 5.14: Improvement to the cost function and all its elements versus the number of random restarts

The improvement to the cost function increases quickly up to around 30 % of the random restarts and then gradually flattens out; this trend is observed for all the elements of the cost function irrespective of the improvement each element brings. A case with more weight to the fourth element of the cost function would be interesting to analyze; unfortunately, only artificial data are available, which may not represent blast movement accurately.

The run-time for this example was 36.4 minutes for 10149 blocks on an older PC. In the majority of cases, it can be decreased to 10-15 minutes by reducing the number of random restarts or neighbors; this may introduce some minor visual artifacts in the 3-D models, which, nevertheless, should not significantly impact final results.

5.5 Blast Movement Modeling with Limited Information

Blast movement modeling with AGC-BM should always be performed with detailed topography and accurate blast movement measurements for obtaining the best results. However, there are situations when only limited information about the configuration of a muckpile and blast movement is available for short-term planning. This may happen due to equipment malfunction, harsh weather conditions, and human error, among other reasons.

In this section, two cases are reviewed: i) blast movement modeling with sparse blast movement vectors, and ii) blast movement modeling with approximate topography. Algorithms for inferring approximate blast movement vectors and topography based on blast design are proposed.

5.5.1 Modeling with Approximate Displacement Vectors

For some blasts, the pre- and post-blast positions of only a few transmitters (e.g., the transmitters described in Adam and Thornton (2004)) are available due to their damage during blasting or economical considerations. In such situations, blast movement modeling can be performed using only detailed pre- and post-blast topography or with the topography and approximate blast movement vectors. Sparse blast movement vectors can be interpolated using estimation methods like inverse distance (Shepard, 1968) or kriging (Matheron, 1963); this procedure is performed by default within AGC-BM. Some practitioners may consider using local directions of blast movement obtained based on the firing sequence of a blast, especially, if available blast movement measurements are limited or deemed unreliable. Thornton (2009a) indicates that the direction of blast movement at a particular location of a mine bench is usually perpendicular to the timing contours of a firing pattern. However, different factors may have an impact on the directions such as the proximity of free faces, stemming ejection, the firing pattern configuration (e.g., diagonal or v-shaped) and delays, the blasthole design, etc.. Initiating different parts of a column charge with different delays or separating the column charge by air decks or inert material may also have an effect on the local blast movement directions. For complex cases involving some or all of the described factors, blast movement should be measured with a sufficient number

of specialized transmitters. Determining a minimum sufficient number of transmitters is a separate issue and is not addressed in this thesis.

Approximate blast movement vectors may be inferred using the firing sequence of a blast. The firing sequence may provide information on the theoretical direction of rock displacement but not on its magnitude unlike real blast movement vectors obtained with specialized transmitters. Limited blast movement vectors can be used to estimate the magnitude of displacement locally.

A practical method for inferring approximate blast movement vectors using theoretical directions and sparse blast movement vectors is described below with examples. The method should be used for simple blasting cases with one or two free faces, solid column charge (with a single initiation point), and a reasonable blast design (e.g., reasonable burden, spacing, sub-drill, stemming length, etc.). Figure 5.15 schematically illustrates a simple diagonal firing pattern; the pre-blast topography created for the example in Section 5.4 is used.
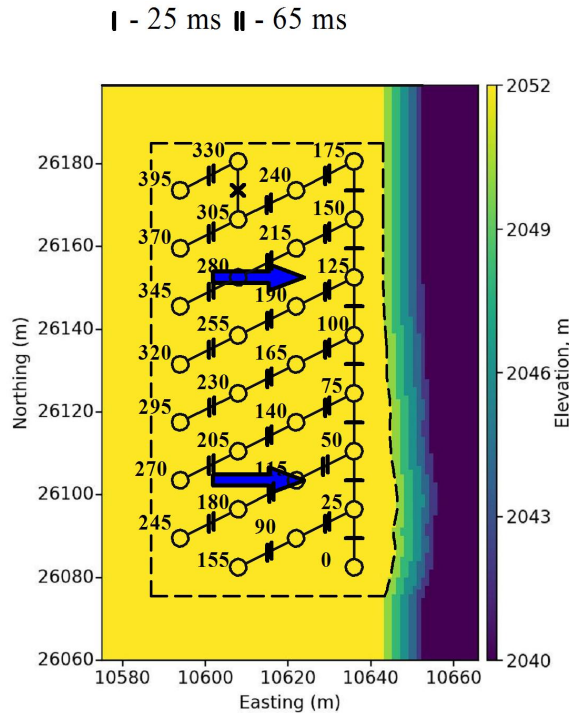
Figure 5.15: Schematic illustration of the major blast movement direction (diagonal firing pattern); the numbers are the firing times in milliseconds.

In Figure 5.15, blastholes in a row are connected with 25 millisecond delays while

the rows are connected with 65 millisecond delays. Blastholes in each row are blasted almost instantaneously creating a new free face for the subsequent row. The large blue arrows indicate the theoretical major direction of displacement of the rock mass, which is perpendicular to timing contours. Different firing patterns may result in a different direction of displacement; also, the blasted rock mass can move in several directions.

Optimization Algorithm for Blast Movement Vectors

A simple a stochastic optimization algorithm is developed to obtain approximate blast movement vectors at N_{loc} arbitrary locations of a mine bench. Local directions of displacement are expressed as azimuths α_i, $i = 1, ..., N_{loc}$ in degrees from North (from $0°$ to $360°$ measured clockwise) perpendicular to timing contours. Measured displacement vectors are calculated by subtracting pre-blast coordinates of the transmitters from the post-blast coordinates of transmitters. Then, the measured displacement vectors are interpolated using inverse distance (Shepard, 1968) and stored in a set $D = \{d_1, ..., d_{N_{loc}}\} \in R^3$, where $d_i = (d_x^i, d_y^i, d_z^i)$, $i = 1, ..., N_{loc}$. Initial magnitudes of displacement vectors $\| d_i \|$, $i = 1, ..., N_{loc}$ are calculated and saved. The components of pre-blast coordinate vectors at all locations N_{loc} are obtained and stored in a set $H = \{h_1, ..., h_{N_{loc}}\} \in R^3$, where $h_i = (h_x^i, h_y^i, h_z^i)$, $i = 1, ..., N_{loc}$. Components h_x^i and h_y^i for each element h_i are known for each location where α_i is determined and, therefore, are not interpolated. Component h_z^i, in turn, is not known and is interpolated using the corresponding components of the measured pre-blast coordinate vectors of the transmitters. A set of post-blast vectors $G = \{g_1, ..., g_{N_{loc}}\} \in R^3$ is obtained as follows:

$$g_i = h_i + d_i, \ i = 1, ..., N_{loc} \tag{5.10}$$

The following expression is used to re-calculate the displacement vectors in $D = \{d_1, ..., d_{N_{loc}}\} \in R^3$ during optimization:

$$d_i = g_i - h_i, \ i = 1, ..., N_{loc} \tag{5.11}$$

Angles β_i, $i = 1, ..., N_{loc}$ between displacement vectors in D and the West-East direction are determined as follows:

$$\beta_i = \arctan\left(\frac{d_y^i}{d_x^i}\right), \ i = 1, ..., N_{loc} \tag{5.12}$$

The angles β_i, $i = 1, ..., N_{loc}$ are then converted to be in the range from $0°$ to $360°$. Average absolute error between angles β_i, $i = 1, ..., N_{loc}$ and α_i, $i = 1, ..., N_{loc}$ is calculated as follows:

$$E_{ang} = \frac{1}{N_{loc}} \sum_{i=1}^{N_{loc}} |\beta_i - \alpha_i| \qquad (5.13)$$

The optimization algorithm is performed using the following steps:

1. Coordinate components of a randomly chosen element in G are changed by adding or subtracting small values.

2. Equation 5.11 is used to recalculate coordinate components of a displacement vector in D affected by the change in Step 1 and a corresponding new vector magnitude.

3. If the difference between the new magnitude of the changed displacement vector and the initial magnitude exceeds a tolerance parameter tol_{magn}, the change in Step 1 is not accepted, and the optimization algorithm returns to Step 1.

4. If the change in Step 1 is accepted, the angle β_i corresponding to the changed displacement vector is re-calculated using Equation (5.12).

5. Average absolute error E_{ang} is re-calculated using Equation (5.13). If the new E_{ang} is smaller than the initial one, the initial value is replaced with the new one, and the change in Step 1 is accepted; otherwise, it is revered, and the algorithm returns to Step 1.

6. If the new value E_{ang} is smaller than a tolerance parameter tol_{ang}, the optimization algorithm terminates.

7. Steps 1-6 are repeated a user-specified number of iterations.

Tolerance parameters tol_{magn} and tol_{ang} should be set as small as possible. Smaller tolerance parameters usually require more iterations. Figure 5.16 illustrates post-blast topography for the artificial example from Section 5.4 but with only 4 measured displacement vectors.
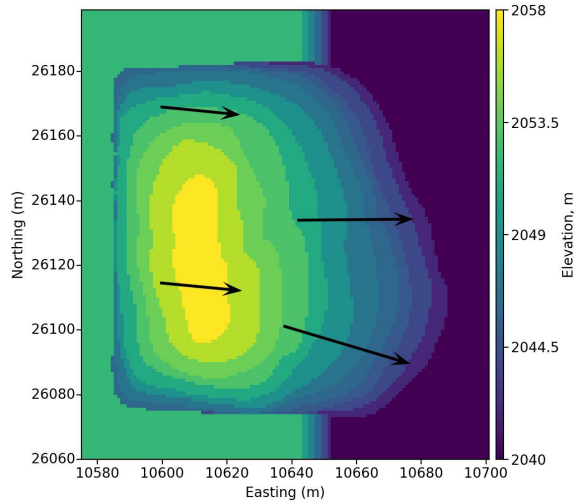
Figure 5.16: Artificial post-blast topography with limited vectors

Figure 5.16 illustrates the locations at which approximate displacement vectors are inferred (black dots) using the described optimization algorithm versus a final set of optimized vectors.

(a) Locations

(b) Optimized vectors
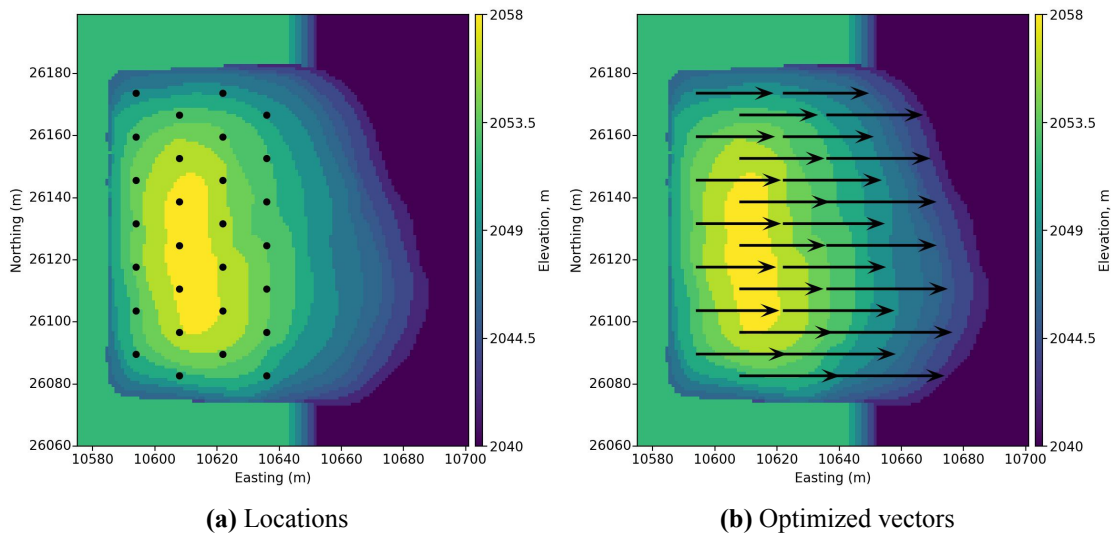
Figure 5.17: Approximate blast movement vectors (diagonal firing pattern)

The theoretical angles are directed at $90°$ from North. Also, the artificial 'measured' vectors are in 3-D even though they are depicted in 2-D; this has an influence on the final optimized vectors. The optimization algorithm was performed with 1×10^7 iterations. Both tol_{ang} and tol_{magn} were set to 1×10^{-2}. The algorithm terminated based on tol_{ang} in 1.24

130

seconds. The optimized vectors have the directions obtained from the firing sequence and the magnitudes estimated using the limited measured vectors.

Figure 5.18 shows a schematic illustration of a v-shaped pattern. The large blue arrows illustrate possible directions of rock displacement.
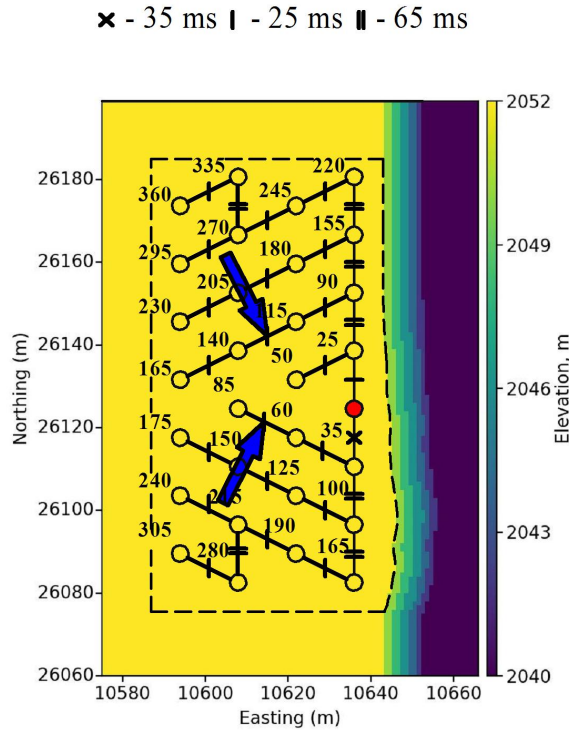
Figure 5.18: Schematic illustration of a v-shaped firing pattern

Thornton (2009a) indicates that muckpiles formed from blasts initiated via v-shaped patterns are often characterized by a distinct centerline of the blast initiation. During blasting, rocks are moving towards the centerline and upwards creating a ridge. Blast movement is often unpredictable in the centerline region (Thornton, 2009a); therefore, measured blast movement vectors close to this region should be used carefully. Figure 5.19 illustrates artificial blast movement vectors created for this example plotted on the top of an artificial post-blast topographic surface.
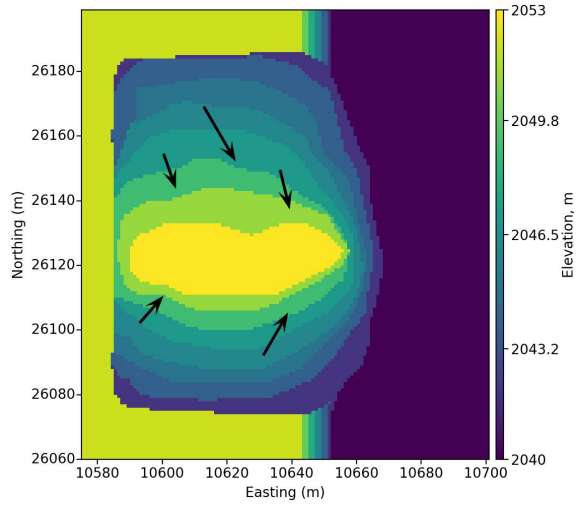
Figure 5.19: Artificial blast movement vectors (v-shaped firing pattern)

Figure 5.20 illustrates the locations at which approximate blast movement vectors are inferred for this example using the optimization algorithm versus a final set of optimized vectors.

(a) Locations

(b) Optimized vectors
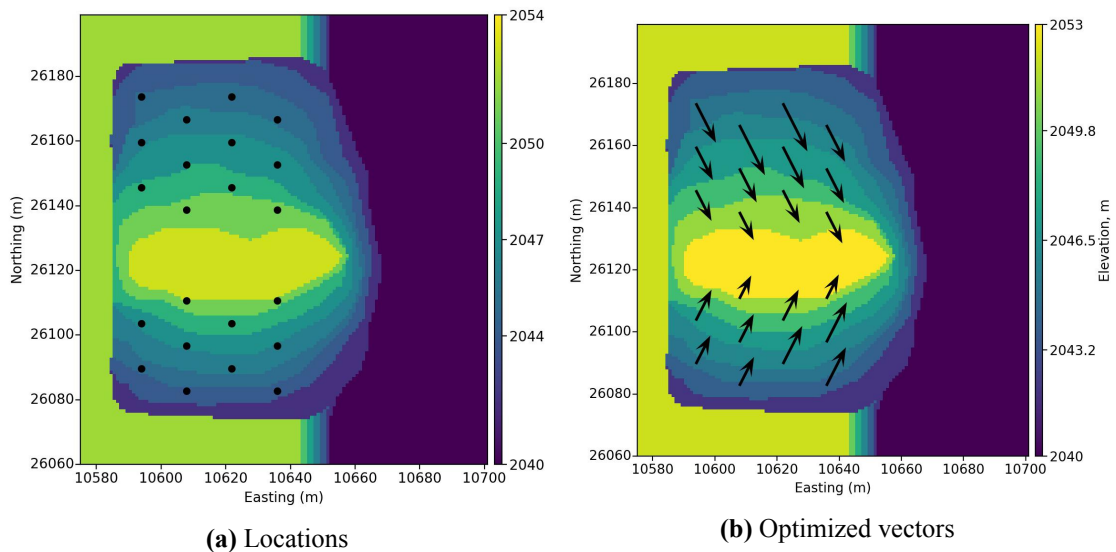
Figure 5.20: Optimized vectors (v-shaped firing pattern)

The locations for optimization are situated at some distance from the centerline to avoid unreliable results. The artificial blast movement vectors are directed at $153°$ from North at the top of the mine bench and at $27°$ from North at the bottom of the mine bench. The optimization algorithm was performed with 1×10^7 iterations. Both tol_{ang} and tol_{magn} were

set to 1×10^{-2}. The algorithm terminated based on tol_{ang} in 0.89 seconds.

Examples provided in this section demonstrate how limited blast movement measurements and firing pattern information can be combined for more reliable blast movement modeling. The optimization algorithm is tested with artificial examples representing simple grade control cases, where the direction of blast movement can be reliably predicted.

5.5.2 Modeling with Approximate Topography

The conditions of each blast in an open pit mine may be different depending on geology and blast design. Within AGC-BM, detailed pre- and post-blast topographic surfaces are used to create 3-D block models of a mine bench before and after blasting and determine an optimal mapping of pre-blast grades or profit onto a post-blast muckpile. Unfortunately, the pre- and post-blast topography is not always available. For simple configurations of mine benches, pre-blast topograpic surfaces can be obtained using blasthole surveys or other related information. However, corresponding post-blast topographic surfaces cannot be inferred from other sources and should be obtained using laser scanners or drone systems.

This section proposes a method to obtain approximate pre- and post-blast topography. The method can be used for simple cases with uniform blast movement. In order to approximately model pre- and post-blast topography of a mine bench, the following information is required: i) bench bottom elevation, ii), bench height, iii) swell factor, iv) the principal direction of blast movement, and v) a pre-blast polygon with a free face indicated.

The approximate pre-blast topography is defined by the pre-blast polygon, bench bottom elevation, and the bench height. Then, it is used to build an approximate 3-D model. The 3-D model is discretized at a high resolution. The pre-blast volume is determined by the summation of the individual volumes of all pre-blast blocks.

The pre-blast polygon is transformed to obtain an approximate post-blast polygon by moving the section of the polygon indicated as a free face in the major direction of blast movement. The free face is moved until the post-blast volume is equal to the pre-blast volume multiplied by the swell factor. The optimal distance at which the free face is moved is determined using the line search algorithm

In order to illustrate the work of AGC-BM with approximate topography, the artificial example from Section 5.4 is used along with the corresponding profit function. The major blast movement direction is set at 90° from North. The bench height of 15 m and the swell factor of 1.25 are used. Figure 5.21 illustrates an initial pre-blast polygon versus an optimized polygon with a free face indicated.

<div align="center">(a) Initial   (b) Optimized</div>
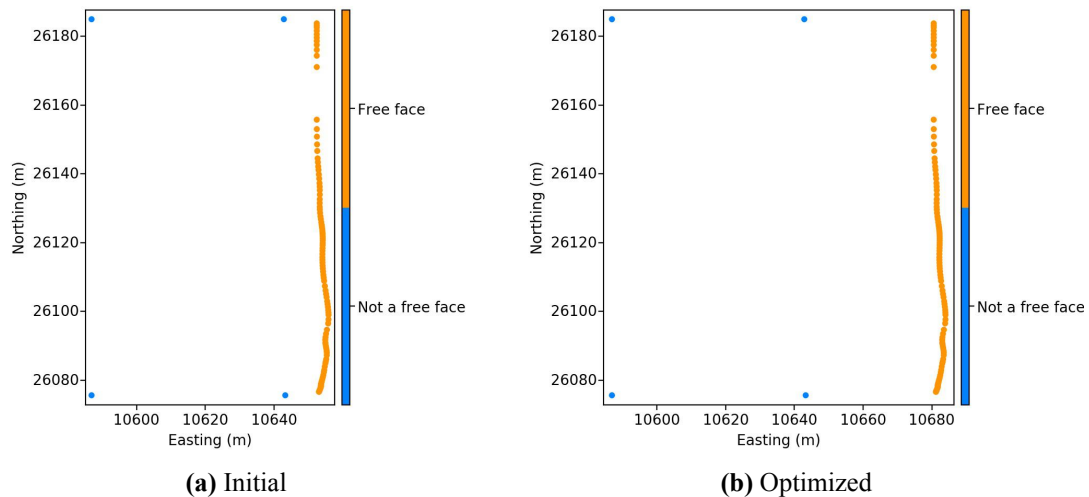
Figure 5.21: Initial and optimized pre-blast polygons with a free face indicated

Since the optimized post-bast polygon expands in the direction of blast movement, the bench height should be reduced. The new bench height is calculated by dividing the initial bench height by the cubic root of the swell factor, which equals to 13.93 m for this example.

AGC-BM was performed with 30 and 60 neighbors for the low resolution and high resolution models, respectively. The tolerance parameter was set to 0.01 % of the cost function improvement. The algorithm performed 23 000 and 196 000 iterations for the LR and HR models, respectively. The total number of blocks being optimized was 12 600. The operation time was 92 minutes 43 seconds. The long operation time may be due to approximate topography, which results in less reliable initial guess models. More research is required.

Figure 5.22 shows pre and post-blast 3-D models of expected profit for the ore, stockpile, and waste destinations for mined material.

<div align="center">134</div>

(a) Ore   **(b)** Stockpile   **(c)** Waste

(d) Ore   **(e)** Stockpile   **(f)** Waste
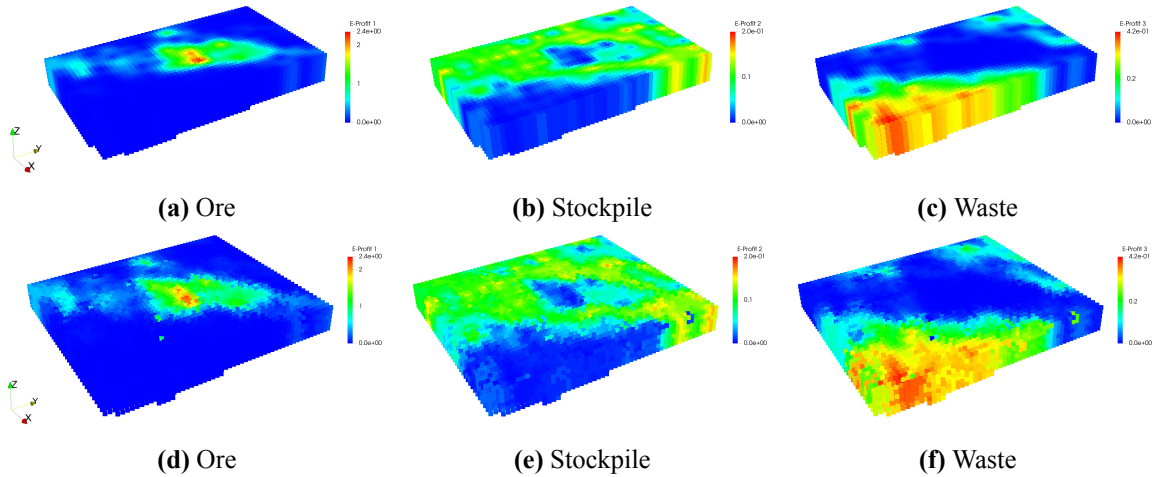
Figure 5.22: Pre-blast 3-D expected profit models versus post-blast 3-D expected profit models obtained with approximate topography

Figure 5.23 shows corresponding pre- and post-blast classification maps at a high resolution.

(a) Pre-blast   **(b)** Post-blast
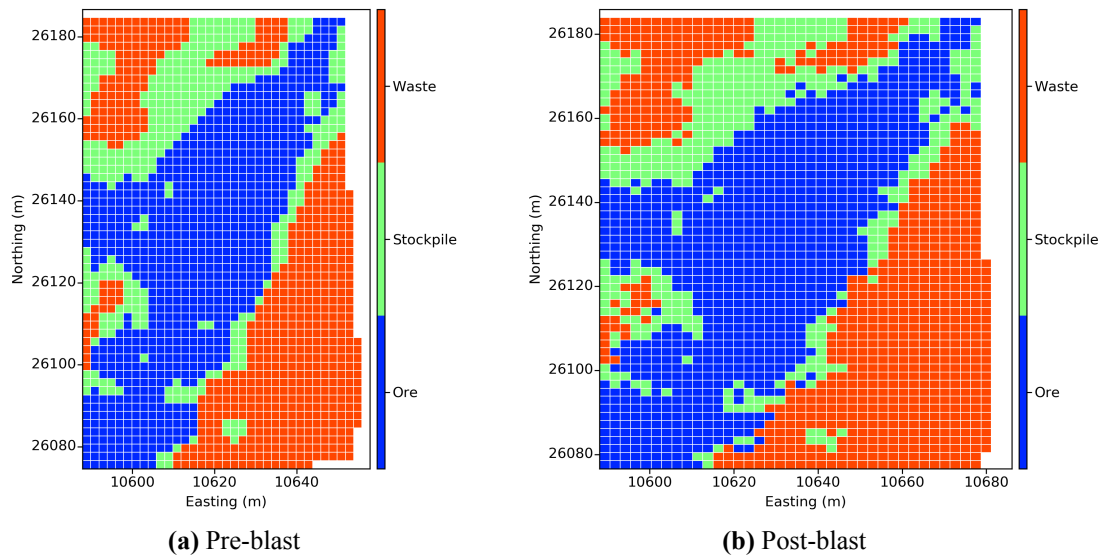
Figure 5.23: Pre-blast classification of mined material versus post-blast classification of mined material (approximate topograpy)

The pre- and post-blast high resolution classification maps in Figure 5.23 have similar spatial structures, which will result in similar dig limit boundaries. Different versions of this algorithm can be used. For example, an approximate magnitude of rock displacement or even a detailed post-blast polygon may be known; this information will allow better estimating approximate topography and obtaining more reliable post-blast dig limits. Also,

some blast movement measurements or firing pattern information can be used to improve mapping. More research is required in this direction

5.6 Summary

An optimization-based algorithm for blast movement modeling called AGC-BM is proposed. Details about objective function and stochastic optimization are described. The algorithm models post-blast grades or expected profit using detailed topography and real blast movement measurements. The blast movement modeling procedure using AGC-BM is explained with an artificial example. Specific cases of blast movement modeling with limited information are discussed

Testing AGC-BM with artificial examples showed the ability of the algorithm to map pre-blast expected profit onto post-blast 3-D models within a reasonable time frame (35 - 90 minutes). Potentially, a more efficient optimization algorithm could be used. However, this is the area of future research.

The practicality of the algorithm would be assessed during an industrial experiment with real data. The 3-D post-blast expected profit generated by AGC-BM could be used to obtain mineable dig limits. An algorithm for dig limits optimization based on the post-blast expected profit and subject to excavating constraints is described in Chapter 6.

CHAPTER 6

DIG LIMITS OPTIMIZATION

The determination of dig limits is the last of four major operations in short-term mine planning or grade control. The first step includes the following prerequisite steps: i) assembly of all relevant data that informs on the rock properties influencing the optimal destination of the mined material, and ii) formulation of a profit calculation for each destination for any combination of input rock properties. The second step is the calculation of the expected profit for each destination on a high resolution (HR) grid using the best possible geostatistical prediction of the multivariate rock properties. Considering expected profit assumes a risk neutral position for short-term planning, which is reasonable given the repeated nature of grade control decisions over relatively short time frames. The third step is to numerically model the blast movement since the dig limits and final selection is performed on the post-blast muck pile. The fourth and final step is the translation of free selection expected profit values at a high resolution to realistic dig lines to be transmitted to mining operations. This chapter addresses this last step.

A heuristic dig limits optimization algorithm called the Advanced Grade Control-Dig Limits (AGC-DL) is described. The algorithm uses high resolution expected profit for optimizing dig limits subject to excavating constraints represented by rectangular selection units. Dig limits optimization with non-rectangular shapes of the selection units is discussed. The work of the algorithm is demonstrated with examples.

6.1   Problem Formulation

The concept of using a floating selection frame for classifying mined material is appealing because of its straightforward implementation with the maximum expected profit approach. It is possible to incorporate equipment constraints through the dimensions of a rectangular floating selection frame. M. Deutsch (2017) proves that this grade control classification

137

problem is NP-hard, which means there is currently no algorithm to solve it in polynomial time. However, it is possible to develop an approximate method for solving this problem since it is well defined. The expected profit at a location $\boldsymbol{u}$ of a domain A over destinations K is defined as follows:

$$EP(\boldsymbol{u}, k), \ k = 1, ..., K, \ \boldsymbol{u} \in A \tag{6.1}$$

The best destination at each location $\boldsymbol{u}$ is:

$$d_{opt}(\boldsymbol{u}) \ = \ \max k \text{ of } (EP(\boldsymbol{u}, k), \ k = 1, ..., K), \ \boldsymbol{u} \in A \tag{6.2}$$

The maximum attainable cumulative expected profit (achieved with free selection) over the domain A is then:

$$CP_{opt} = \sum_{\boldsymbol{u} \in A} EP(\boldsymbol{u}; d_{opt}(\boldsymbol{u})) \tag{6.3}$$

In order to satisfy excavating constraints, each location $\boldsymbol{u}$ may be assigned to a number of larger selection frames $C(\boldsymbol{u}) \subseteq F$, where F represents all the selection frames locations $\boldsymbol{u} \in A$ can be assigned to. For example, a location $\boldsymbol{u}$ (a blue block in Figure 6.1) can possibly be assigned to nine 3×3 block[2] selection frames (Figures 6.1a to 6.1i).

Figure 6.1: Floating selection frame representing excavating constraints; the central blue block must belong to one of the nine selection frames.

All the selection frames that the location $\boldsymbol{u}$ ends up being assigned to comprise a set $S(\boldsymbol{u}) \subseteq C(\boldsymbol{u})$; all locations $\boldsymbol{u} \in A$ also covered by the frames $S(\boldsymbol{u})$ are assigned the same destination, $ds(\boldsymbol{u}') = ds(\boldsymbol{u})$. If all the locations $\boldsymbol{u} \in A$ are assigned $ds(\boldsymbol{u})$, the cumulative mineable profit over the domain A can be written as:

$$CP_{mineable} = \sum_{\boldsymbol{u} \in A} EP(\boldsymbol{u}, ds(\boldsymbol{u})) \tag{6.4}$$

where $CP_{mineable}$ is the total expected profit corresponding to a feasible solution to the classification problem.

If a location $\boldsymbol{u}$ does not belong to at least one of the selection frames $C(\boldsymbol{u}) \subseteq F$, it is not assigned a $ds(\boldsymbol{u})$ and, as such, is called problematic. Some tolerance may be established for the number of problematic locations remaining in an optimized classification map. Setting

the tolerance greater than zero may help to handle the cases with the shapes of selection frames other than rectangular; in such cases, the selection frames may not fit together well in a domain with complex boundaries.

The maximum attainable cumulative expected profit, CP_{opt}, is known. An optimization algorithm should be applied to make $CP_{mineable}$ as close to CP_{opt} as possible. The objective function for the optimization procedure can be expressed as follows:

$$\min_{ds(\boldsymbol{u}) \in K, \forall \boldsymbol{u} \in A} \quad CP_{opt} - \sum_{\boldsymbol{u} \in A} EP(\boldsymbol{u}, ds(\boldsymbol{u})) \tag{6.5}$$

In Equation (6.5), CP_{opt} is constant (since optimal destinations are known at a high resolution), while the cumulative mineable profit changes depending on the destinations $ds(\boldsymbol{u})$ at all locations $\boldsymbol{u} \in A$. Due to the excavating constraints, the objective is always greater or equal to zero. For domains with complex boundaries, it may be necessary to allow some locations $\boldsymbol{u} \in A$ not be assigned a $ds(\boldsymbol{u})$ for optimization to be possible. For convenience, the performance of the optimization algorithm is expressed as the fraction of CP_{opt} in percent throughout this chapter.

6.2   Practical Considerations

The result of blast movement modeling is typically a high resolution 3-D model even though the underlying information supporting the expected profit calculation is from blastholes and inherently 2-D. It is assumed that grades estimated from drill cuttings are averaged along the entire length of the blasthole, and a mine bench is excavated in one lift. If more information is available about the vertical geological variability of a mine bench, grade control modeling should be done in 3-D. The high resolution expected profit block model should be converted to 2-D before starting the dig limits optimization. The total profit in 2-D should be considered.

Assigning each location $\boldsymbol{u}$ a destination $ds(\boldsymbol{u})$ is not a trivial task, especially, with large maps. The number of possible classifications for a map at the resolution of $n_x \times n_y$ block^2 and K destinations is $K^{n_x \times n_y}$; only a few of those classifications are feasible. It is unreasonable to check all possible classifications; therefore, some fast practical algorithm should

be developed to find the feasible solutions. Assigning a block to a selection frame also influences adjacent blocks; doing it in sequence does not guarantee a feasible solution. For example, consider a 6×5 block^2 map that should be classified by a 3×3 block^2 selection frame. The map is discretized by white and green blocks with the expected profit values of 1 and 1.5, respectively; the colors represent two destinations for mined material. If the total expected profit of the green blocks inside a selection frame is higher than the total expected profit of the white blocks inside the frame, all the blocks inside the frame are classified green; all the blocks are classified white otherwise. The selection frame is moved within the map; for this example, the horizontal coordinate of the frame's lower left corner changes first, then the vertical one. All the high resolution HR blocks covered by the floating selection frame are assigned the destination corresponding to a maximum total expected profit value of all the blocks in the frame (Figure 6.2).
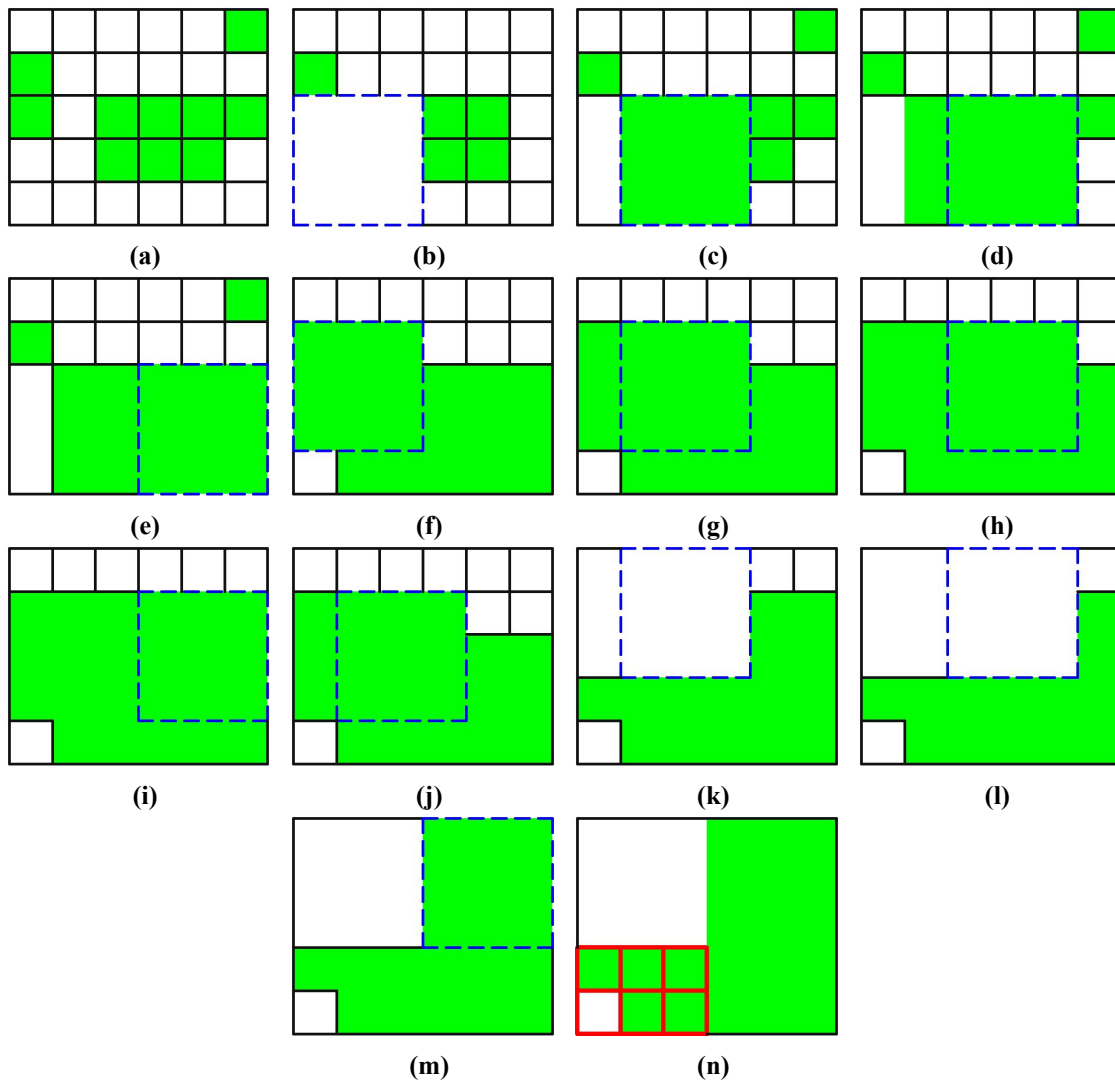
Figure 6.2: Sequential classification with a floating frame

The movement of the selection frame is shown in Figures 6.2b-6.2m. Figure 6.2n illustrates that after all steps are done, 6 problematic locations (red blocks) still remain. Applying the above algorithm on a different path might eventually bring a feasible solution but many iterations might be required for large maps with complex boundaries; the entire process would be slow and not guaranteed to converge.

Using non-overlapping classification frames on a grid of nodes to classify a map guaranties that each block (except for the boundary blocks) will be assigned to a frame; the centers of the classification frames should be on a fixed grid of nodes. Using the fixed grid implies that there are only as many possible positions for a frame's center as the number of

HR blocks that fall inside it; for example, for a 3×3 block^2 frame, there are only 9 possible positions its center can take. This principle is illustrated in Figure 6.3.
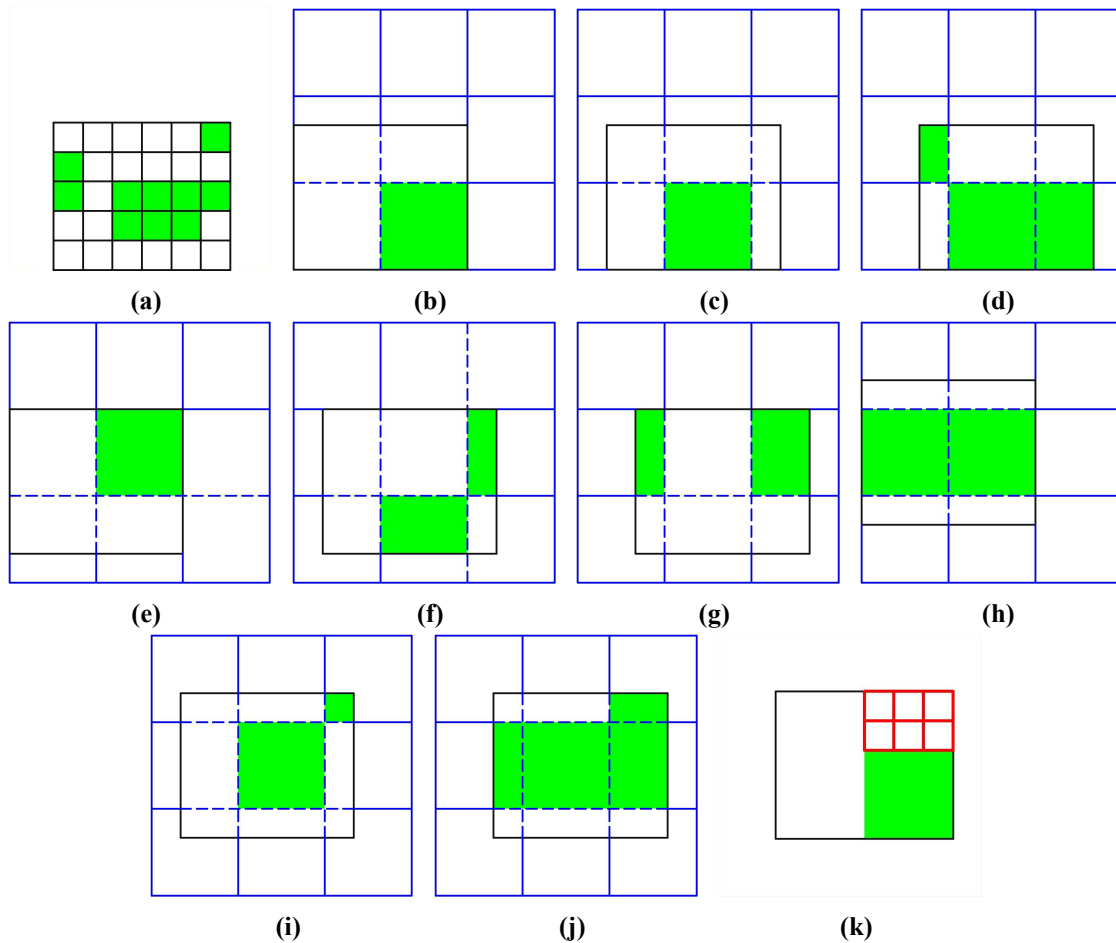
Figure 6.3: Classification by frames on a fixed grid

Different positions of the fixed grid (Figures 6.3b to 6.3j) yield different classifications and thus different cumulative expected profits. All the 9 classifications in Figure 6.3 are infeasible due to the model edges. However, the classifications shown in Figures 6.3b and 6.3e have the fewest problematic locations; the classification in Figure 6.3b is chosen because it brings higher cumulative expected profit (fewer green blocks are misclassified). The example above is just for illustration. For a real life classification, every HR block would have several grade control destinations and an expected profit value associated with each of them. The expected profit of misclassified blocks would reduce the mineable profit.

6.3   Optimization Algorithm

Both approaches described in the previous section cannot be used to optimize dig limit boundaries. In terms of the number of problematic locations, their performances seem similar on such a small example. However, using the fixed grid instead of the floating frame approach for large maps results in fewer problematic locations; thus, less effort is required to fix them and reach a feasible classification.

The main algorithm consists of the following steps:

1. Determine an initial classification with the fixed grid approach. The main purpose of this step of the algorithm is to reduce the number of problematic locations and bring the initial guess classification closer to a feasible solution; the initial classification with the fewest problematic locations and the largest cumulative profit CP is chosen.

$$CP = \sum_{\boldsymbol{u} \, \in \, A} EP(\boldsymbol{u}, dt(\boldsymbol{u})) \tag{6.6}$$

   where $dt(\boldsymbol{u}) \in K$ is a temporary destination assigned to a location $\boldsymbol{u}$.

   If an input model has complex boundaries, the number of problematic locations usually increases. Increasing the spacing of nodes (frame size) of the fixed grid makes the initial guess classification blockier and less precise but generally decreases the number of problematic locations. The 'blockiness' of the initial classification is fixed in later stages of the algorithm. The classification frame of a fixed grid should not be confused with a floating selection frame; the size of the floating selection frame should always be smaller than or equal to the node spacing of the fixed grid.

2. In this step, all remaining problematic locations are visited and eliminated to obtain a feasible solution; the maximum profit feasible solution among all possible fixes is kept (Figure 6.4).
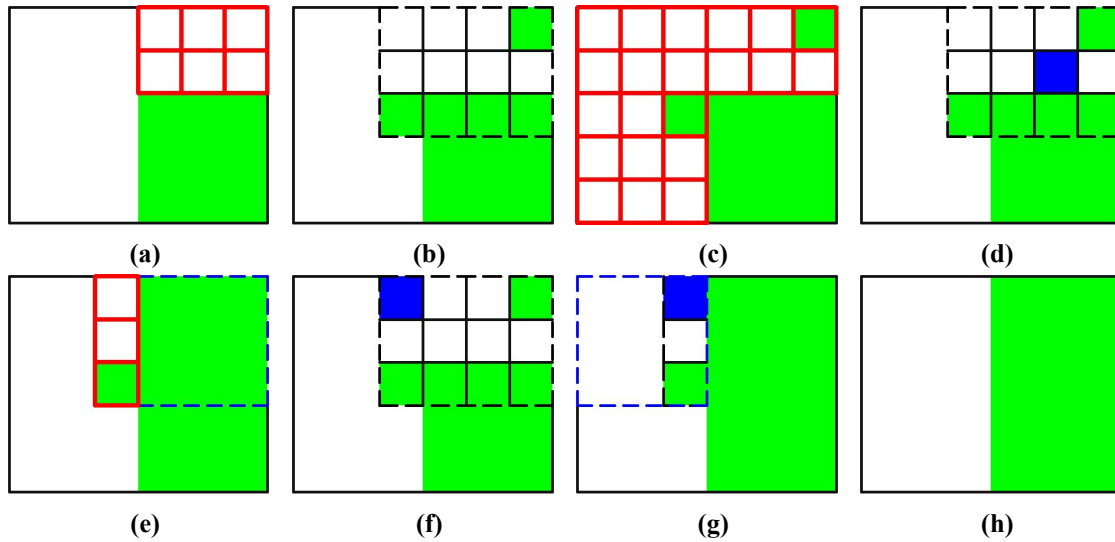
Figure 6.4: Schematic illustration of the fixing algorithm

In this small example, the first step of the algorithm produces a classification with 6 problematic locations illustrated as red squares in Figure 6.4a; each of the 6 blocks is not assigned to at least one 3×3 block^2 frame. The destinations of all the problematic locations and their closest neighbors (one block in each direction) are reverted to their best HR destinations irrespective of excavating constraints; for the current example, the area with replaced HR destinations is indicated by the black dashed line in Figure 6.4b. After the destinations of the blocks are replaced, the number of problematic locations increases to 21 (Figure 6.4c). All the blocks in the replaced area are visited in a random order and assigned to a 3×3 block^2 frame. For example, a randomly chosen block in the replaced area (highlighted in blue) is shown in Figure 6.4d; using the algorithm illustrated in Figure 6.1, all the frames it can be assigned to are checked. Both green and white destinations are checked with the frames that do not go beyond the boundaries of the map. The blue block should be assigned to a frame (blue dashed square in Figure 6.4e) and a destination reducing the number of problematic locations the most and resulting in the highest cumulative expected profit of the map CP (Equation (6.6)). After the block is assigned to its frame and destination, the number of problematic locations is reduced to 3 (Figure 6.4e). The next random location is shown in Figure 6.4f. Again, this location is assigned to a

frame representing the white destination (Figure 6.4g). After a feasible classification is achieved, the algorithm terminates. A fixed map for the current example is in Figure 6.4h. If all the blocks from the problematic area (Figure 6.4b) are visited and assigned to their frames and destinations but a feasible solution is not reached yet, the fixing algorithm is repeated; a new set of problematic locations and their closest neighbors are determined and replaced with their HR best destinations.

Usually, no more than 10 repetitions are required to obtain a feasible solution with a corresponding $CP_{mineable}$ (Equation (6.4)). The user may choose the size of the neighborhood for each problematic location or the number of iterations to be used in this procedure; using more neighbors increases chances of removing all problematic locations but usually takes more time. If after the specified number of iterations all the problematic locations are still not fixed, the first step of the algorithm with an increased node spacing of the fixed grid is repeated. The node spacing of the fixed grid in the horizontal and vertical directions is increased sequentially. If a frame size of 3×3 block^2 is allowed to be increased by one unit in each direction, the following frame dimensions are checked: i) 4×3 block^2, ii) 3×4 block^2, and iii) 4×4 block^2. The best frame dimensions in terms of problematic locations and cumulative expected profit CP are chosen. A tolerance to the number of problematic locations in the second stage classification can be used for some situations to increase cumulative mineable expected profit and/or decrease the operation time; examples are provided later in this chapter.

3. Steps 1 and 2 lead to a solution to the classification problem that satisfies the constraints. In an attempt to increase the cumulative mineable expected profit from a mine bench, $CP_{mineable}$, a final hill climbing step is performed. Every location of the feasible solution is visited in random order; a location is assigned to a new frame (Figure 6.1) and/or a new destination if this change increases $CP_{mineable}$ and does not result in more problematic locations. Within each hill climbing operation, all the locations $\boldsymbol{u} \in A$ can be visited at random several times to increase the current solution $CP_{mineable}$ and minimize the objective function (Equation (6.5). The number

of times this random visiting is repeated is limited by the number of times it is done without an improvement to the objective function; one repetition is used by default to minimize the time required. Each hill climbing operation is repeated several times with a different random path and a solution bringing the largest cumulative mineable expected profit is chosen. At this stage, all the changes to the feasible classification map should ensure it remains feasible. If a tolerance to the number of problematic locations is used in the Stage 2, it is also accounted for during the hill climbing operation.

Selection of Parameters

The main focus of the AGC-DL algorithm is fast optimization; chosen input parameters should ensure achieving reasonable results in the shortest time. The first stage of the algorithm is performed automatically. An initial fixed grid node spacing is equal to the floating frame size specified by the user. No other input parameters are required.

For the second stage of the algorithm, the size of the neighborhood (e.g., 1, 2, 3, etc. blocks in each direction) for each problematic location should be specified. Another important parameter is the number of times the second stage can be repeated without an improvement in the number of problematic locations remaining in a classification map (the second stage tolerance) before repeating the first stage with a new fixed frame size. The size of the neighborhood and the second stage tolerance should be chosen as small as possible to avoid a significant change in the initial guess solution (Stage 1). It is recommended to use 1 block in each direction to define a neighborhood and the second stage tolerance of 1 iteration without a decrease in the number of problematic locations. Different optimization plans with different parameters for the second stage can be used to achieve a higher cumulative mineable profit if the operation time is not of concern.

In the third stage, the number of times the hill climbing operation is performed should be specified. Each hill climbing operation results in a new optimized feasible solution and a new objective function value. The more times this operation is repeated, the more likely the best possible optimized solution for a current initial guess will be reached. The third stage of the optimization algorithm may be terminated based on a number of repetitions without an improvement to the cumulative mineable profit (the third stage tolerance parameter).

For the fastest operation, the third stage tolerance parameter should be as small as possible (e.g., one). For a better exploration of the solution space, it may be set in the range from 5 to 10. The AGC-DL algorithm terminates based on the third stage tolerance parameter or on a specified number of hill climbing operations.

Another practical consideration is isolated blocks at the edges of an expected profit map (artifacts) that cannot be optimized (assigned to a full selection frame). This may happen due to a low resolution and/or sharp edges of the expected profit map. One solution is to set the tolerance to the number of problematic locations remaining in the final solution equal to the number of such blocks. Another solution is to remove all the edge artifacts before optimization.

Remarks

This dig limits optimization algorithm is heuristic and designed to minimize the difference between the profit achieved within the chosen dig limits and the profit achieved with free selection. There is no guarantee of optimality. This is considered a limitation, but also a practical advantage. Results are obtained very fast and it is possible to visually and quantitatively assess how the free selection case is modified to be considered more practical for the mining constraints. The algorithm is implemented as a standalone program written in Fortran according to the GSLIB conventions (C. V. Deutsch & Journel, 1998).

6.4   Examples

Two examples are shown to demonstrate the dig limits optimization for expected profit block models subject to rectangular and non-rectangular excavating constraints. The two examples represent pre-blast domains with realistic boundaries. The first example is artificial. It is used to illustrate some of the steps in the AGC-DL optimization algorithm described in Section 6.3 and specific optimization cases. The second example is based on a real blasthole data set from the Red Dog mine.

148

6.4.1 Artificial Example with Three Destinations

For the first example, a reference realization of a grade is simulated with $sgsim$ (C. V. Deutsch & Journel, 1998) for an area of 100×180 m^2 with a grid size of 2×2 m^2. The variogram model used for simulation has one spherical nested structure with a nugget effect of 0.1 and the major direction of continuity at $60°$ from North. Major and minor ranges of continuity are 75 m and 35 m, respectively. The simulated grades are transformed to be lognormal with a mean and standard deviation of 1. The reference realization is then sampled at a grid size of 6×6 m^2 with a random error in coordinates of up to 1 m. Figure 6.5 illustrates the reference simulated model and samples.

(a) Reference model
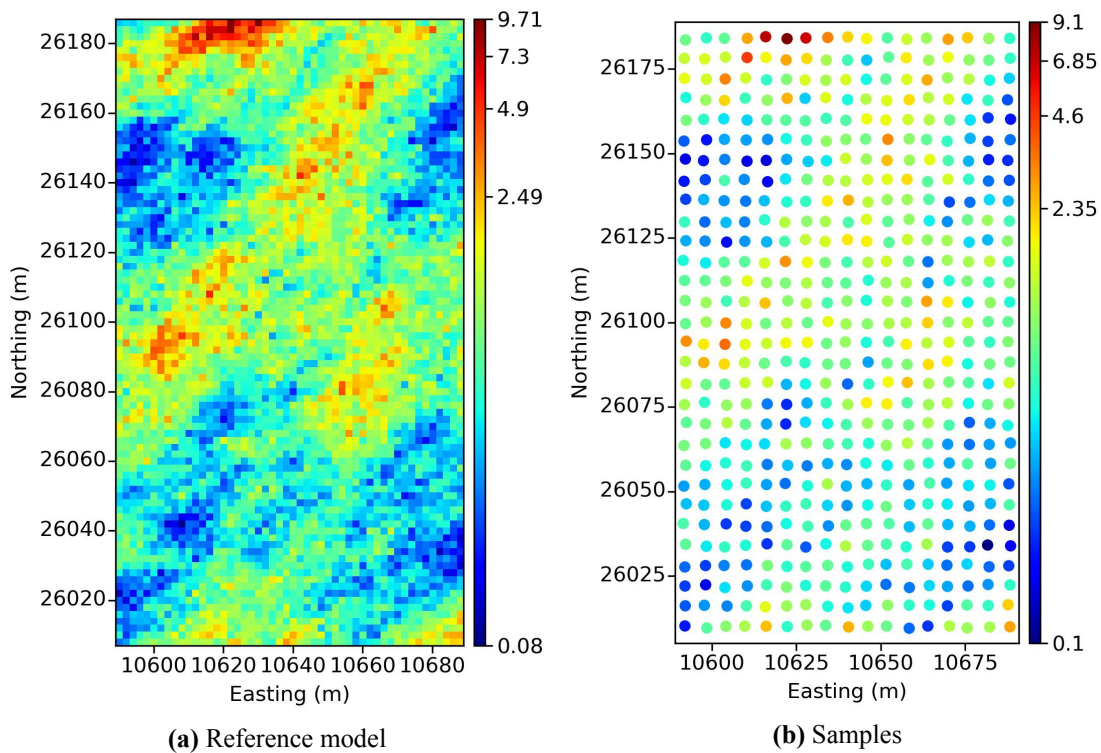
(b) Samples

Figure 6.5: Artificial reference realization and samples

Expected profit is obtained for the area of the reference model using the Advanced Grade Control-Expected Profit (AGC-EP) algorithm. The expected profit modeling was performed using 141 nearby samples. The number of samples used for the modeling was determined using the k-fold cross-validation part of AGC-EP; the node spacing of a super grid used for the k-fold cross-validation procedure was set to 25 % of the average sample

spacing of 5.93 m. Final expected profit maps for all destinations are post-processed with a 3×3 block^2 Gaussian filter. More details about the k-fold cross-validation and main parts of AGC-EP are in Chapters 3 and 4.

Profit Function

Similarly to the profit function from Chapter 5, a profit function for this example uses a single grade variable and two cutoff grades, $z_c^1 = 1.2$ and $z_c^2 = 0.6$, to distinguish between three destinations for mined material: ore, stockpile, and waste. Grade values simulated with AGC-EP, $z^l(\boldsymbol{u}), l = 1, ..., L$, are converted to expected profit at all locations $\boldsymbol{u} \in A$ using the profit function. Recall how expected profit is calculated for the three destinations. If a simulated value $z^l(\boldsymbol{u})$ at a location $\boldsymbol{u}$ is greater than or equal to the cutoff grade z_c^1, the expected profit for the ore decision is calculated as follows:

$$P(z^l(\boldsymbol{u}); \text{ore}) = \begin{cases} z^l(\boldsymbol{u}) - z_c^1, & \text{if } z^l(\boldsymbol{u}) \geq z_c^1; \\ 0, & \text{otherwise.} \end{cases} \tag{6.7}$$

$$EP(\boldsymbol{u}; \text{ore}) = \frac{1}{L} \sum_{l=1}^{L} P(z^l(\boldsymbol{u}); \text{ore})$$

where $P(z^l(\boldsymbol{u}); \text{ore})$ is the profit at the location $\boldsymbol{u}$ given the ore decision; $EP(\boldsymbol{u}; \text{ore})$ is the expected profit at the location $\boldsymbol{u}$ given the ore decision.

If $z^l(\boldsymbol{u})$ is below than z_c^1 and $z^l(\boldsymbol{u})$ is greater than or equal to z_c^2, the expected profit for the stockpile decision is calculated as follows:

$$P(z^l(\boldsymbol{u}); \text{stockpile}) = \begin{cases} z^l(\boldsymbol{u}) - z_c^2, & \text{if } z^l(\boldsymbol{u}) < z_c^1 \text{ and } z^l(\boldsymbol{u}) \geq z_c^2; \\ 0, & \text{otherwise.} \end{cases} \tag{6.8}$$

$$EP(\boldsymbol{u}; \text{stockpile}) = \frac{1}{L} \sum_{l=1}^{L} P(z^l(\boldsymbol{u}); \text{stockpile})$$

where $P(z^l(\boldsymbol{u}); \text{stockpile})$ is the profit at the location $\boldsymbol{u}$ given the stockpile decision; $EP(\boldsymbol{u}; \text{stockpile})$ is the expected profit at the location $\boldsymbol{u}$ given the stockpile decision.

If $z^l(\boldsymbol{u})$ is below than z_c^2, the expected profit for the waste decision is calculated as follows:

$$P(z^l(\boldsymbol{u}); \text{waste}) = \begin{cases} z_c^2 - z^l(\boldsymbol{u}), & \text{if } z^l(\boldsymbol{u}) < z_c^2; \\ 0, & \text{otherwise.} \end{cases} \tag{6.9}$$

$$EP(\boldsymbol{u}; \text{waste}) = \frac{1}{L} \sum_{l=1}^{L} P(z^l(\boldsymbol{u}); \text{waste})$$

where $P(z^l(\boldsymbol{u}); \text{waste})$ is the profit at the location $\boldsymbol{u}$ given the waste decision; $EP(\boldsymbol{u}; \text{waste})$ is the expected profit at the location $\boldsymbol{u}$ given the waste decision.

Figure 6.6 shows the expected profit for the three destinations.

(a) Ore destination   **(b)** Stockpile destination   **(c)** Waste destination

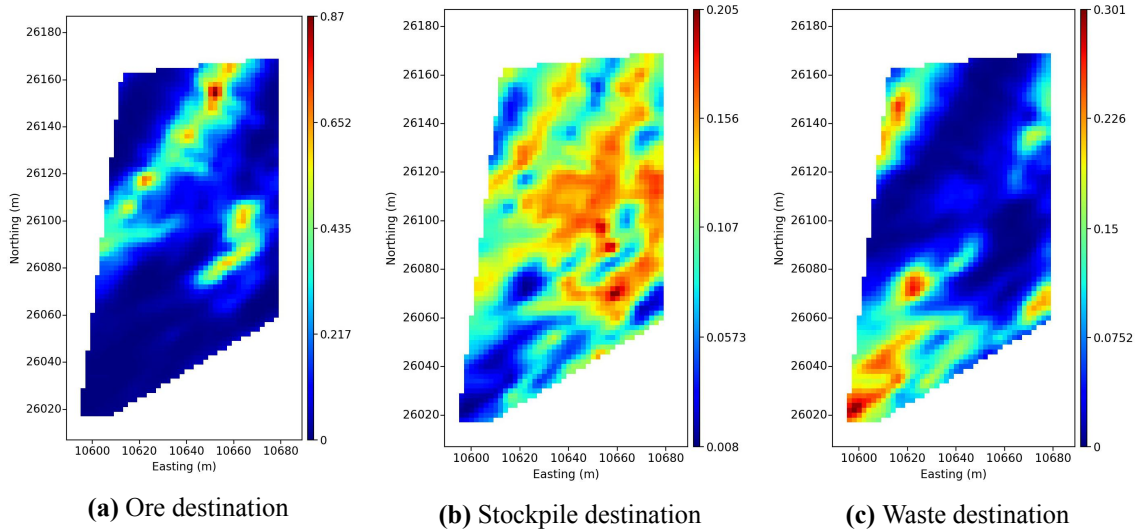**Figure 6.6:** Expected profit for three destinations (example 1)

Optimal destinations at each high resolution location are determined using Equation (6.2). Excavating constraints are represented by a 5×5 block^2 floating selection frame. Figure 6.7 illustrates a high resolution 2-D classification map representing maximum expected profit destinations for the case of free selection (without excavating constraints).
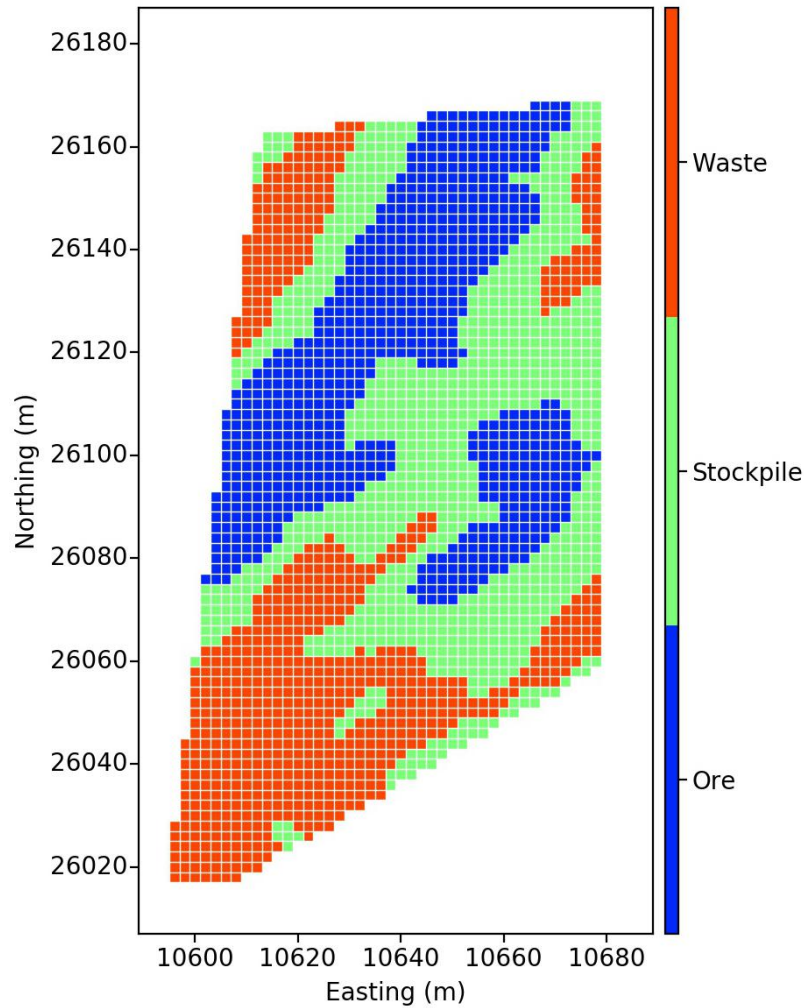
Figure 6.7: A 2-D maximum expected profit destination map at high resolution (example 1)

Cumulative expected profit, CP_{opt}, is calculated using Equation (6.3). It represents a maximum attainable profit achieved with free selection for the current resolution or 100 % selection. In Figure 6.7, each high resolution block represents a 2×2 m^2 area. The expected profit model has complex boundaries both at its edges and between different types of mined material. A failure to follow such precise dig limits would result in a certain amount of dilution and ore loss. The AGC-DL optimization algorithm from Section 6.3 is used to re-assign destination for each high resolution location accounting for excavating constraints represented by rectangular selection frames.

Figure 6.8a illustrates the classification produced in the first stage of the algorithm using a fixed grid with a frame size of 11×9 block^2. It achieves 89.84 % of the maximum total ex-

pected profit and still contains 13 problematic locations (Figure 6.8b). All the problematic locations are then fixed using the second step of the algorithm.

(a) Classification map after Stage 1 **(b)** Problematic locations
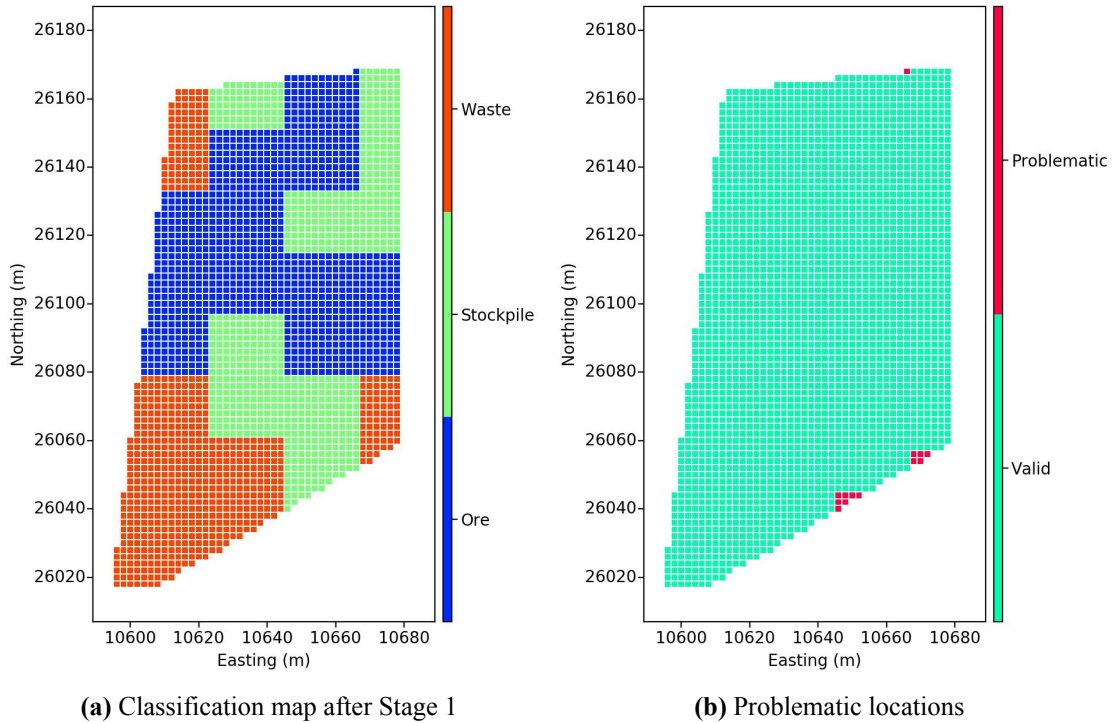
Figure 6.8:   A classification map produced in the first stage of the optimization algorithm and corresponding problematic locations (example 1)

Figure 6.9a shows the classification map for this example after Stage 2 of the optimization algorithm is completed. A changed classification map represents a feasible solution since it does not contain problematic locations and each high resolution block belongs to at least one 5×5 block^2 selection frame. However, this classification is far from optimal and allows selecting only 89.44 % of the cumulative expected profit achieved with free selection. The final hill climbing step (the third stage of the optimization algorithm) was performed to increase a cumulative mineable profit, $CP_{mineable}$. Figure 6.9b demonstrates a final optimized classification map.

(a) Classification map after Stage 2   **(b)** Optimized classification map

Figure 6.9: Classification map after the second stage of the optimization algorithm versus final optimized classification map satisfying the excavating constraints represented by the 5×5 block ^{2} selection frame (example 1)

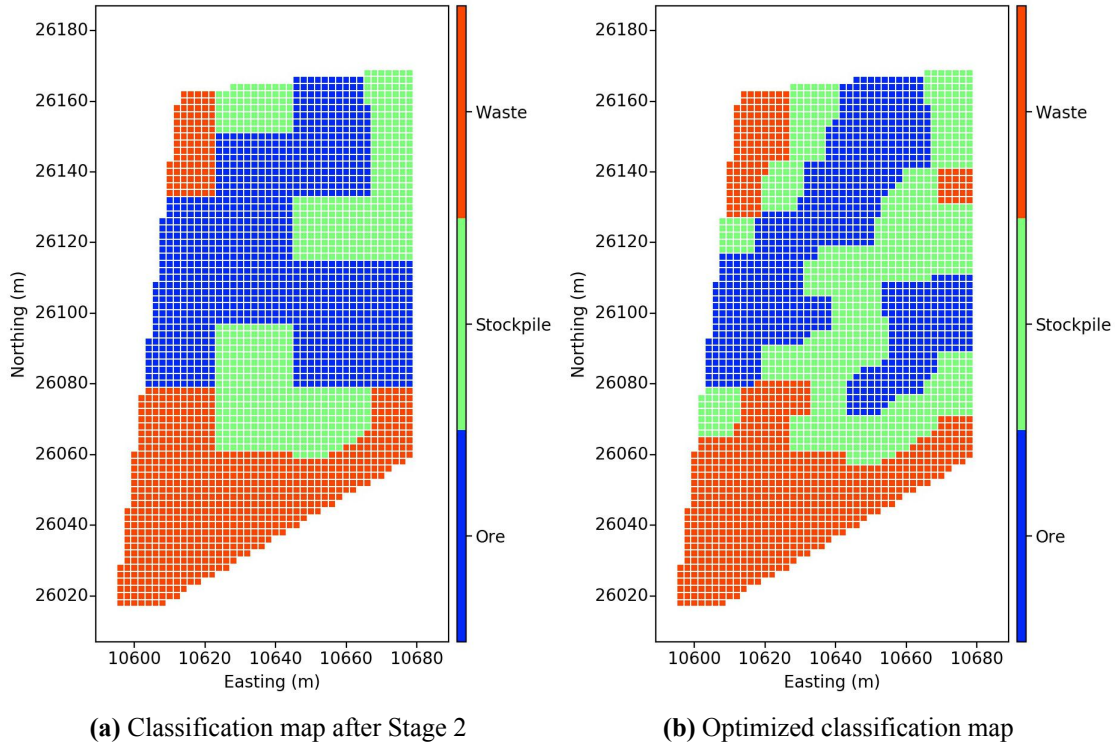It is seen in Figure 6.9b that each location belongs to at least one 5×5 block^2 classification frame (covering an area of 10×10 m^2). The total number of blocks for this example is 2426. The pre-blast optimized classification map achieves 97.18 % of a maximum cumulative expected profit. The second stage of the algorithm was run with the neighborhood size of 1 block in each direction and the tolerance of 1 iteration without a decrease in the number of problematic locations for the fastest operation. The optimization algorithm terminated based on the Stage 3 tolerance of 10 hill climbing operations without an improvement to the objective function. The run-time was 40.96 seconds.

The cumulative mineable expected profit varies depending on the size and dimensions of the selection frame. Since partial frames are not allowed, the complexity of the edges of the expected profit model can greatly influence a final classification. Generally, smaller frame sizes are better fit to the edges of a model, which results in higher $CP_{mineable}$ and shorter operation time. Shapes of the frames other than square can also be considered. Figure 6.10 demonstrates the same domain classified using selection frames sizes of 3×3

block^2 and 7×3 block^2.

(a) 3×3 block^2 frame size   **(b)** 7×3 block^2 frame size
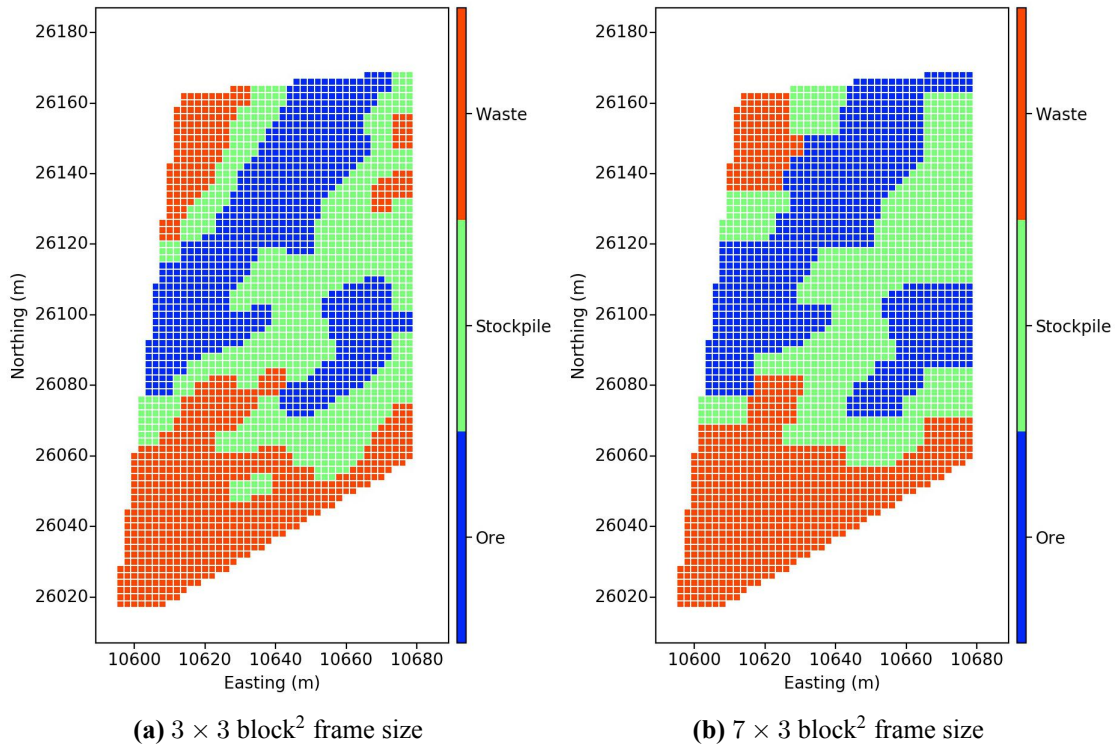
Figure 6.10: Optimized classification maps satisfying excavating constraints represented by different rectangular frames

The same optimization plan as in the previous example was used for obtaining the two classification maps in Figure 6.10. The optimized classification map satisfying the 3×3 block^2 frame size constraint (Figure 6.10a) allows selecting 99.29 % of the cumulative expected profit achieved with free selection. The operation time for this map was 5.64 seconds. The optimized classification map satisfying the 7×3 block^2 frame size constraint (Figure 6.10b) allows selecting 96.62 % of the cumulative expected profit achieved with free selection. The operation time for this map was 18.43 seconds. Overall, the performance of AGC-DL for all the shapes and sizes of rectangular selection frames is reasonable considering the short operation times. Optimality is not guaranteed; better results may be achieved with different optimization plans.

6.4.1.1 Dig Limits Optimization with Non-rectangular Selection Units

Shapes of selection units other than rectangular may be desirable to better account for such factors as the direction of mining, local shapes of geological features, equipment limitations, and the sequence of individual scoops, among others. M. Deutsch (2017) indicates that it is important that the shapes of individual selection units allow them to be fit well to one another inside a domain; otherwise, some unexpected artifacts may be produced at the edges of a classification map, which may drastically decrease corresponding cumulative mineable expected profit. Since individual selection units can overlap, they are often combined into larger units during dig limits optimization to account for large ore/waste zones; many combinations of the individual units may be possible. The geometrical shapes of such combined units should be flexible enough to account for complex edges of a domain. Dig limits optimization with non-rectangular shapes is possible with the AGC-DL algorithm. It may be necessary to allow some number of problematic locations in the final solution to account for complex edges of a domain. Figure 6.11 illustrates an arbitrary-shaped floating selection unit.
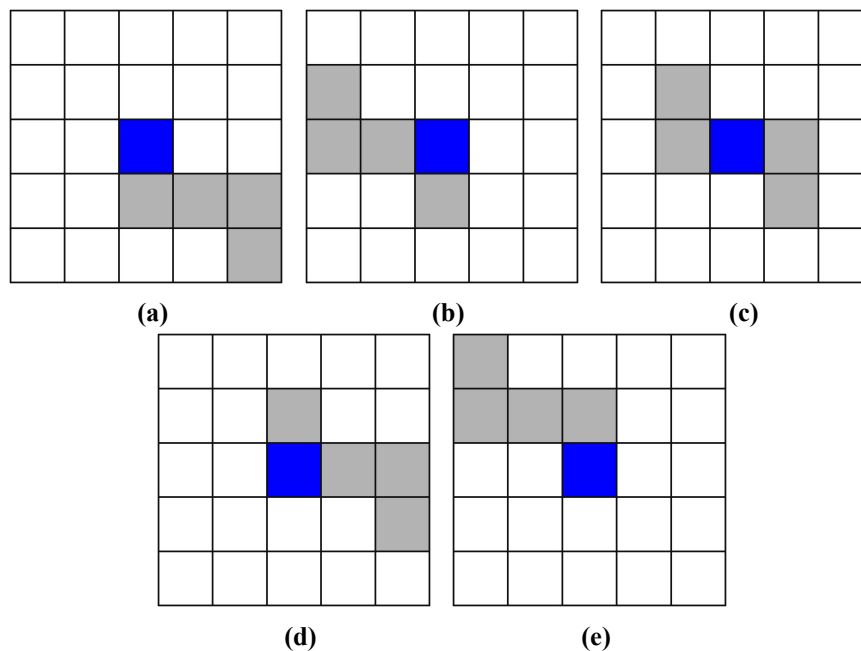

Figure 6.11: Floating selection unit of an arbitrary shape representing excavating constraints; the central blue block must belong to one of the 5 selection units.

Figure 6.11 shows all possible selection units a block can be assigned to within a 5×5

block² area. Expected profit calculated for the first example (Figure 6.6) is used to obtain optimized dig limits accounting for the constraints imposed by the selection unit shown in Figure 6.11. The second stage of AGC-DL is run with the neighborhood size of 1 block in each direction and the tolerance of 1 iteration without a decrease in the number of problematic locations. The optimization algorithm terminated based on the Stage 3 tolerance of 10 hill climbing operations without an improvement to the objective function. Two problematic locations are allowed in the final solution to handle the edges of the domain. Figure 6.12 demonstrates a classification map optimized accounting for the constraints imposed by the arbitrary-shaped floating selection unit.

(a) Optimized classification map   **(b)** Problematic locations
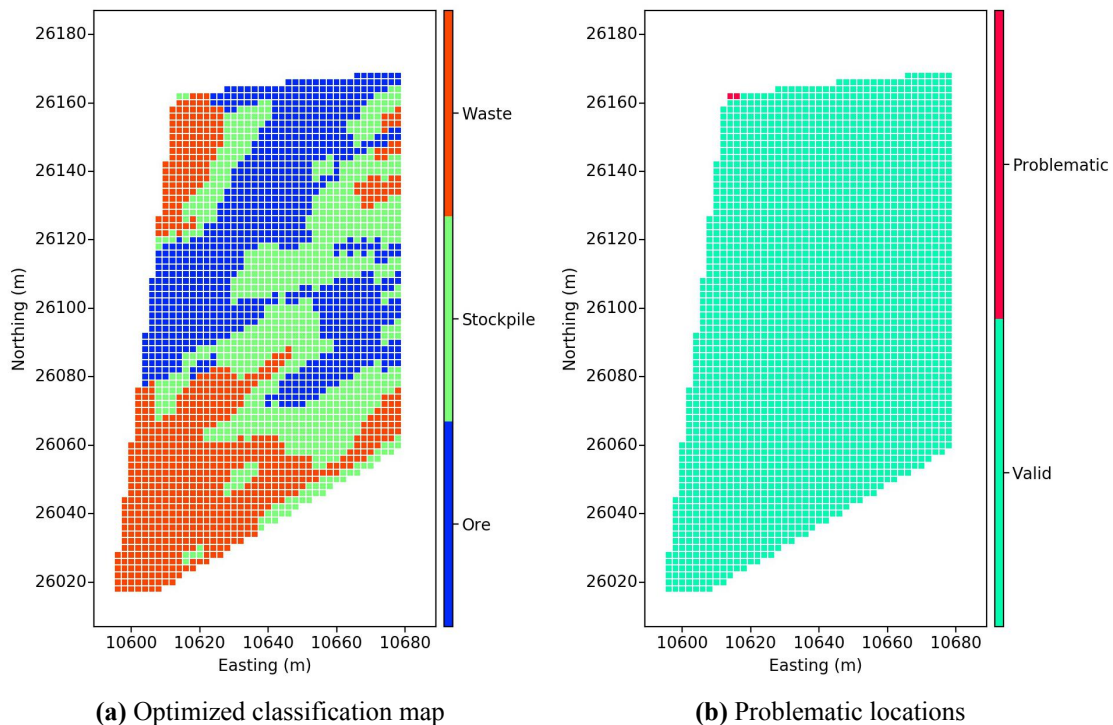
Figure 6.12: An optimized classification satisfying excavating constraints represented by an arbitrary-shaped selection unit (example 1)

The final classification allows selecting 97.3 % of the cumulative expected profit achieved with free selection. The run-time was 10.56 seconds.

Other shapes of the floating selection units may allow accounting for the direction of mining. A floating selection unit directed at 45° from North is illustrated in Figure 6.13.
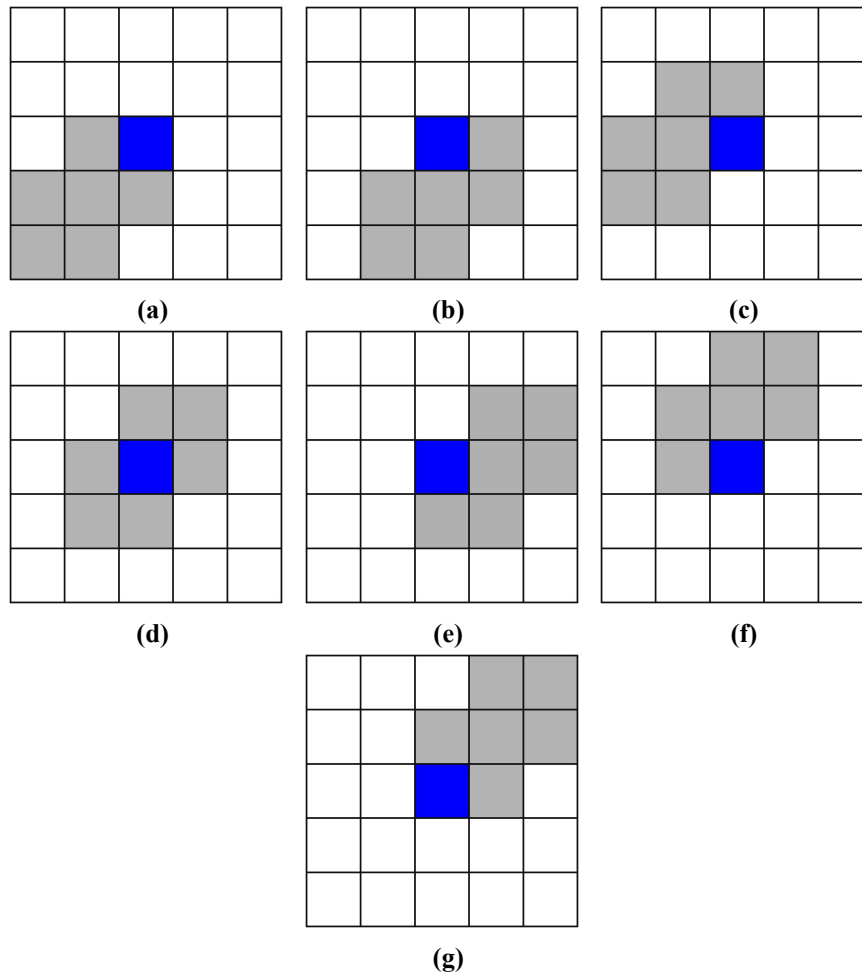
Figure 6.13: A floating selection unit directed at 45° from North representing excavating constraints; the central blue block must belong to one of the 7 selection units.

AGC-DL is run with the same optimization plan as for the previous examples. Cases with different allowances for the number of problematic locations remaining in final classification maps are considered. Figure 6.14a shows an optimized classification map with 2 problematic locations allowed.

(a) Optimized classification map

(b) Problematic locations

Figure 6.14: An optimized classification map satisfying excavating constraints represented by a selection unit directed at 45° from North and two problematic locations allowed (example 1))

The classification map in Figure 6.14a allows selecting 95.03 % of the cumulative expected profit achieved with free selection. The run-time was 18.78 seconds. There are visible artifacts in the right hand side of the classification map caused by a single problematic location at the right hand side edge of the domain (Figure 6.14b). Figure 6.15 shows an optimized classification map for the current domain with 6 problematic locations allowed.

(a) Optimized classification map   **(b)** Problematic locations
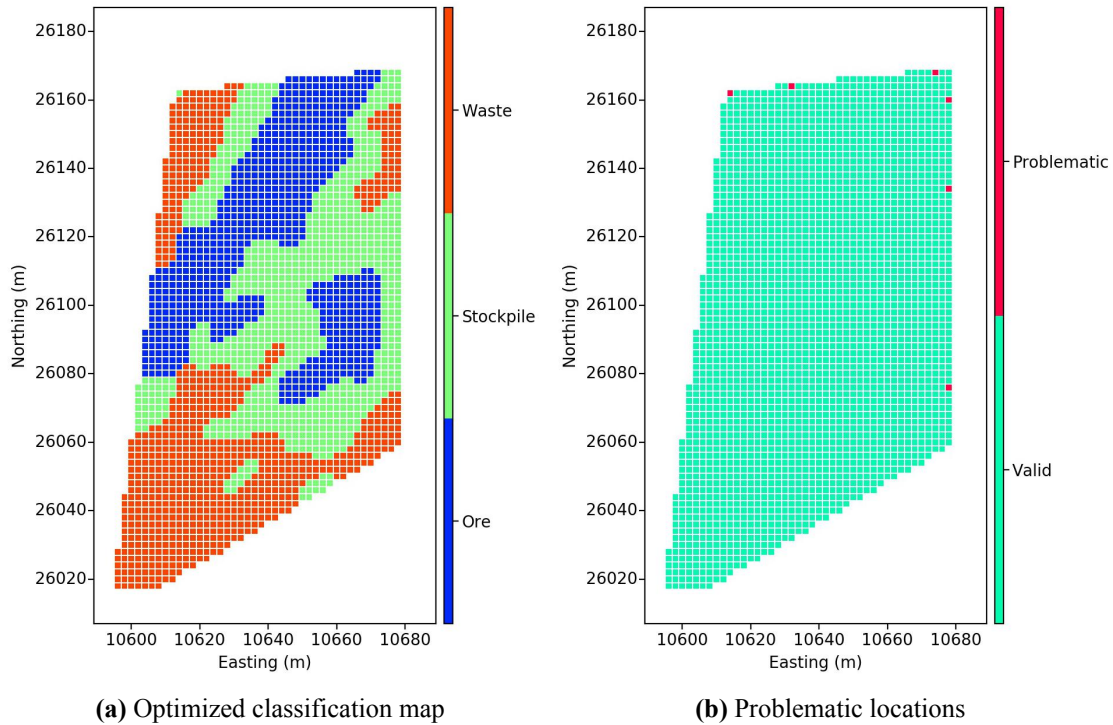
Figure 6.15: An optimized classification map satisfying excavating constraints represented by a selection unit directed at 45° from North and six problematic locations allowed (example 1)
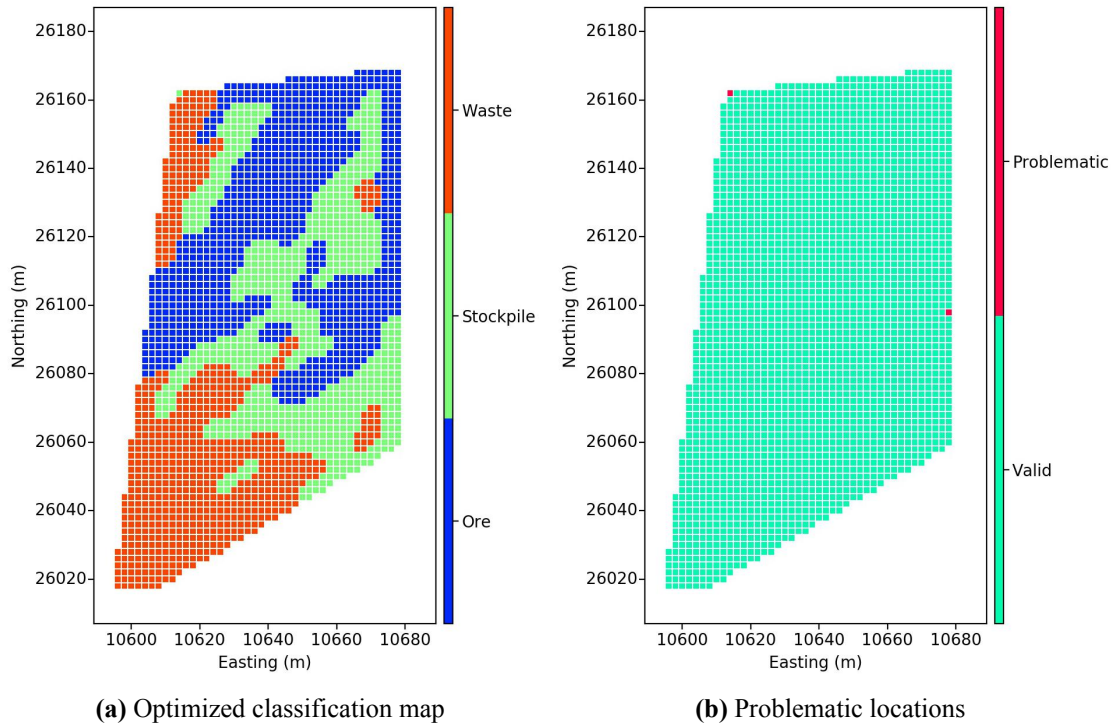
The classification map in Figure 6.15 allows selecting 98.72 % of the cumulative expected profit achieved with free selection. The run-time was 5.85 seconds. Allowing more problematic locations in the classification map resulted in a better handling of the edges of the classification map and a significant increase in the cumulative mineable profit.

6.4.2 Example Based on Real Data

Another example is based on a real blasthole data set from the Red Dog mine in Alaska, USA. The data is released by Teck Resources Limited to the Centre for Computational Geostatistics (CCG) for PhD research. The blasthole samples inform on the content of five collocated grade variables: Zn, Pb, Fe, Ba, and SPb (soluble lead); the first four variables are used for this example. Figure 6.16 illustrates blasthole samples from '19204' mine bench for the four grade variables.
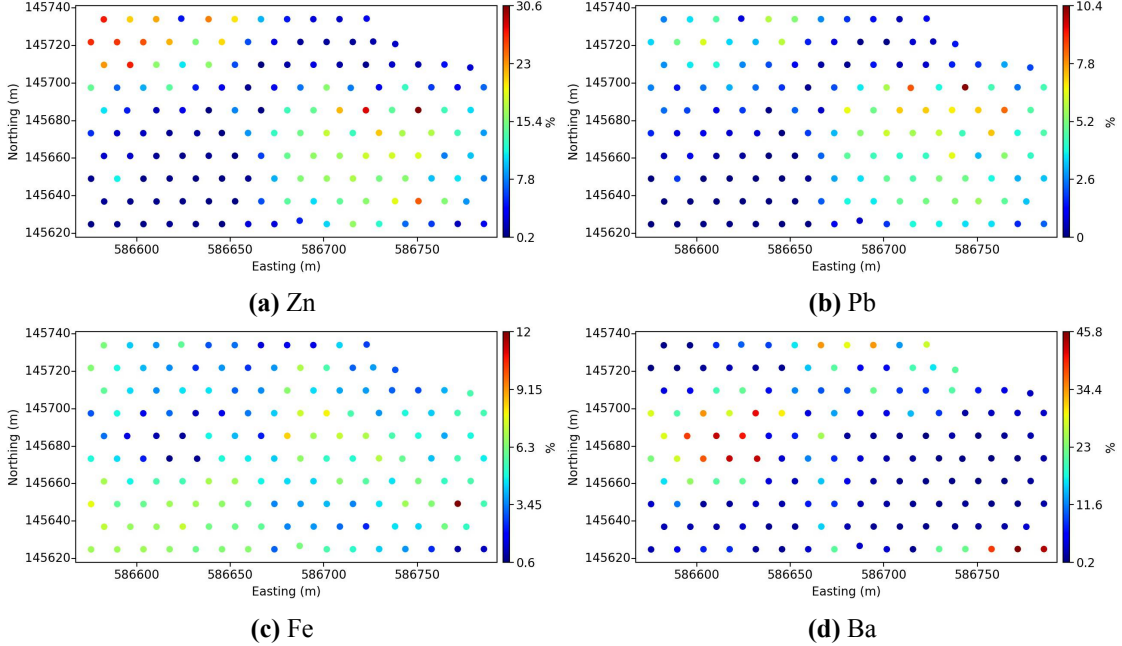
Figure 6.16: Location maps for four grade variables (example 2)

The profit function designed for the case study in Chapter 4 is used for this example. The profit function is partially based on the stockpile blending criteria used at the Red Dog mine. Recall the rules for calculating expected profit for ore and waste decisions. Expected profit for the ore decision is calculated as follows:

$$P(z^l(\boldsymbol{u}; Zn), z^l(\boldsymbol{u}; Pb), z^l(\boldsymbol{u}; Fe), z^l(\boldsymbol{u}; Ba); \text{ore}) =$$

$$\begin{cases} (z^l(\boldsymbol{u}; Zn) - 5) \cdot s(z^l(\boldsymbol{u}; Zn), z^l(\boldsymbol{u}; Pb), z^l(\boldsymbol{u}; Fe), z^l(\boldsymbol{u}; Ba)), & \text{if } z^l(\boldsymbol{u}; Zn) \geq 5; \\ 0, & \text{otherwise.} \end{cases}$$

$$EP(\boldsymbol{u}; \text{ore}) = \frac{1}{L} \sum_{l=1}^{L} P(z^l(\boldsymbol{u}; Zn), z^l(\boldsymbol{u}; Pb), z^l(\boldsymbol{u}; Fe), z^l(\boldsymbol{u}; Ba); \text{ore}) \qquad (6.10)$$

where $z^l(\boldsymbol{u}; Zn)$, $z^l(\boldsymbol{u}; Pb)$, $z^l(\boldsymbol{u}; Fe)$, and $z^l(\boldsymbol{u}; Ba)$ are simulated grade values at a location $\boldsymbol{u}$; $s(z^l(\boldsymbol{u}; Zn), z^l(\boldsymbol{u}; Pb), z^l(\boldsymbol{u}; Fe), z^l(\boldsymbol{u}; Ba))$ is a function depending on the compliance with the stockpile blending criteria at the location $\boldsymbol{u}$; $P(z^l(\boldsymbol{u}; Zn), z^l(\boldsymbol{u}; Pb), z^l(\boldsymbol{u}; Fe), z^l(\boldsymbol{u}; Ba); \text{ore})$ is profit given the ore decision at the location $\boldsymbol{u}$; $EP(\boldsymbol{u}; \text{ore})$ is the expected profit given the ore decision at the location $\boldsymbol{u}$.

Expected profit for the waste decision is calculated as follows:

$$P(z^l(\boldsymbol{u}; Zn); \text{waste}) = \begin{cases} 5 - z^l(\boldsymbol{u}; Zn), & \text{if } z^l(\boldsymbol{u}; Zn) < 5; \\ 0, & \text{otherwise.} \end{cases}$$

$$EP(\boldsymbol{u}; \text{waste}) = \frac{1}{L} \sum_{l=1}^{L} P(z^l(\boldsymbol{u}; Zn); \text{waste}) \tag{6.11}$$

where $P(z^l(\boldsymbol{u}; Zn); \text{waste})$ is profit given the waste decision at the location $\boldsymbol{u}$; $EP(\boldsymbol{u}; \text{waste})$ is the expected profit given the waste decision at the location $\boldsymbol{u}$.

Function $s(z^l(\boldsymbol{u}; Zn), z^l(\boldsymbol{u}; Pb), z^l(\boldsymbol{u}; Fe), z^l(\boldsymbol{u}; Ba))$ in Equation (6.10) is defined by the outcome of three bivariate functions: $s_1(z^l(\boldsymbol{u}; Ba), z^l(\boldsymbol{u}; Fe))$, $s_2(z^l(\boldsymbol{u}; Zn), z^l(\boldsymbol{u}; Fe))$, and $s_3(z^l(\boldsymbol{u}; Zn), z^l(\boldsymbol{u}; Pb))$. The first function is defined as follows:

$$s_1(z^l(\boldsymbol{u}; Ba), z^l(\boldsymbol{u}; Fe)) = \begin{cases} 0.5, & \text{if } z^l(\boldsymbol{u}; Ba) > 7 \text{ and } z^l(\boldsymbol{u}; Fe) < 8; \\ 0.9, & \text{otherwise.} \end{cases} \tag{6.12}$$

The second function is defined as follows:

$$s_2(z^l(\boldsymbol{u}; Zn), z^l(\boldsymbol{u}; Fe)) =$$
$$\begin{cases} \exp(-(2.5 - z^l(\boldsymbol{u}; Zn)/z^l(\boldsymbol{u}; Fe))), & \text{if } z^l(\boldsymbol{u}; Zn)/z^l(\boldsymbol{u}; Fe) < 2.5; \\ 1, & \text{otherwise.} \end{cases} \tag{6.13}$$

The third function is defined as follows:

$$s_3(z^l(\boldsymbol{u}; Zn), z^l(\boldsymbol{u}; Pb)) =$$
$$\begin{cases} \exp(-(3.65 - z^l(\boldsymbol{u}; Zn)/z^l(\boldsymbol{u}; Pb))), & \text{if } z^l(\boldsymbol{u}; Zn)/z^l(\boldsymbol{u}; Pb) < 3.65; \\ 1, & \text{otherwise.} \end{cases}$$
$$\tag{6.14}$$

Function $s(z^l(\boldsymbol{u}; Zn), z^l(\boldsymbol{u}; Pb), z^l(\boldsymbol{u}; Fe), z^l(\boldsymbol{u}; Ba))$ is expressed as follows:

$$s(z^l(\boldsymbol{u}; Zn), z^l(\boldsymbol{u}; Pb), z^l(\boldsymbol{u}; Fe), z^l(\boldsymbol{u}; Ba)) =$$
$$s_1(z^l(\boldsymbol{u}; Ba), z^l(\boldsymbol{u}; Fe)) \cdot s_2(z^l(\boldsymbol{u}; Zn), z^l(\boldsymbol{u}; Fe)) \cdot s_3(z^l(\boldsymbol{u}; Zn), z^l(\boldsymbol{u}; Pb))$$
$$\tag{6.15}$$

More details about the profit function are in Chapter 4. The profit function is used with the AGC-EP algorithm to perform local multivariate simulation and calculate expected profit for the ore and waste destinations for an area of 241.5×136.5 ft^2 with a grid size of 3.5×3.5 ft^2. The simulated expected profit is clipped to a polygon to remove grid locations that are far away from the blasthole samples. AGC-EP is performed with the number of samples (94) determined by cross-validation. The node spacing of a super grid used for the cross-validation procedure was defined as 25 % of the average sample spacing of 13.88 ft. Final expected profit maps for the two destinations are post-processed with a 3×3 block^2 Gaussian filter. Figure 6.17 illustrates high resolution expected profit maps for the ore and waste destinations.

(a) Ore destination   **(b)** Waste destination

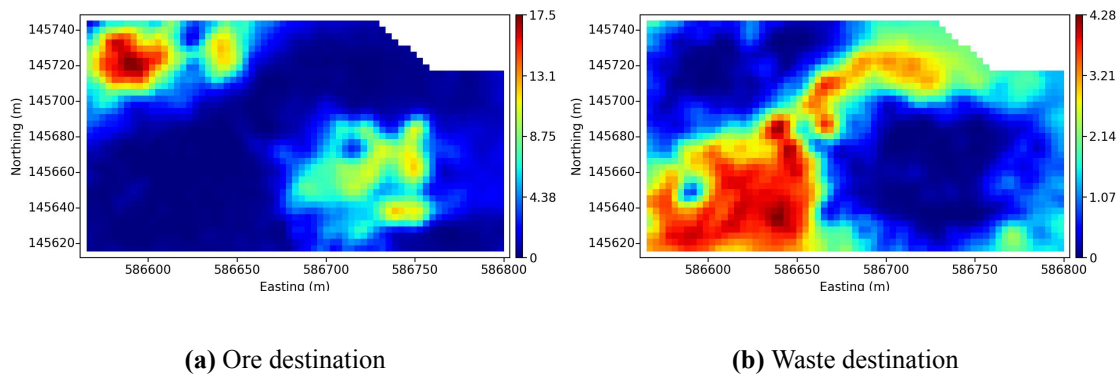**Figure 6.17:** Expected profit for the ore and waste destinations (example 2)

In order to impose excavating constraints on the selection of mined material, a 7×7 block^2 selection frame (covering an area of 24.5×24.5 ft^2) is used. The total number of blocks for this example is 2351. Figure 6.18 compares a classification map for the case of free selection and an optimized classification map for this example.
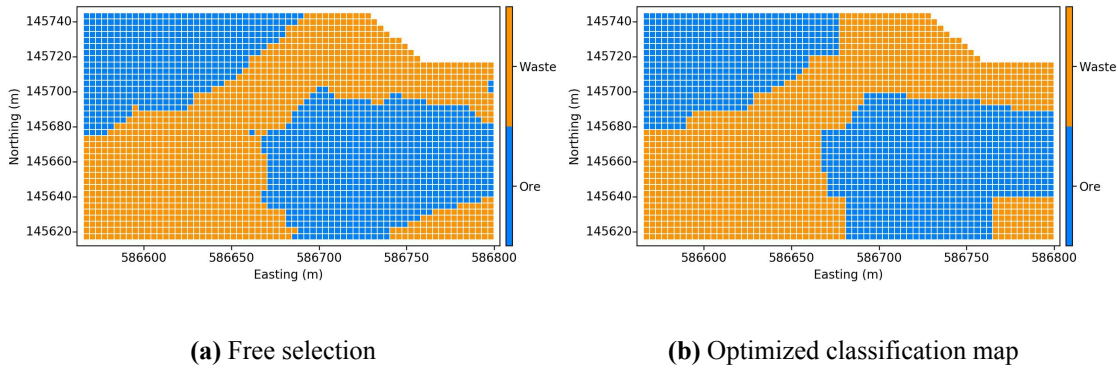
(a) Free selection   **(b)** Optimized classification map

Figure 6.18: A classification map for the case of free selection versus an optimized classification map satisfying the excavating constraints represented by the 7×7 block^2 selection frame

The optimized classification map allows selecting 99.49 % of the cumulative expected profit achieved with free selection. The second stage of the algorithm is run with the neighborhood size of 1 block in each direction and 1 iteration without a decrease in the number of problematic locations. The dig limits optimization algorithm terminated based on the Stage 3 tolerance of 10 hill climbing operations without an improvement to the objective function. The run-time was 24.05 seconds.

The classification maps generated by the AGC-DL optimization algorithm allow selecting areas of mine benches with high expected profit values accounting for excavating constraints. Precise following such classification maps during excavation would bring cumulative expected profit close to the maximum cumulative expected profit achieved with free selection.

6.4.3 Summary

A simple heuristic algorithm for dig limits optimization called AGC-DL is presented. The algorithm works with expected profit for all destinations for rocks to determine mineable dig limits maximizing the cumulative mineable expected profit of a mine bench. Excavating constraints may be represented by rectangular or non-rectangular selection units. The algorithm is new and offers a different approach for optimizing the short-term rock classification. The algorithm is explained in detail and can be modified for solving similar classification problems in a reasonable time.

For the two examples provided in this chapter, the AGC-DL algorithm produced classification maps that allow selecting 96.5-99.5 % of the maximum attainable cumulative expected profit obtained with free selection subject to satisfying constraints represented by rectangular selection frames. The run-time was under 45 seconds for both examples.

While it is convenient to use rectangular selection frames with different dimensions, one might want to use some other arbitrary shapes. Using complex shapes may make it difficult to find a feasible solution to the optimal classification problem; most of the problems are expected at the boundaries of models. Dig limits for this case may be improved by establishing some tolerance to the number of problematic locations allowed in final classification maps.

The presented heuristic algorithm is a part of an integrated grade control system but it can also be used separately or as a part of another grade control system utilizing the maximum expected profit method.

CHAPTER 7

CASE STUDY: GRADE CONTROL AT THE MISIMA MINE

The primary goal of grade control in open pit mines is maximizing profit from mining operations. An open pit mine may have several active mine benches and/or stockpiles that are excavated concurrently to optimize head grades to the mill. The situation with multiple mine benches is not considered in this chapter. It is assumed that increasing the total profit from a mine bench increases the total profit from mining operations. Maximum profit would be possible if: i) grade values relevant for the final selection of mined material are known at a high resolution, and ii) free selection is possible. Unfortunately, it is impossible to satisfy these conditions.

Assuming that sampling preparation and assaying procedures are of sufficient quality, the main reasons for misclassification include the following: i) spatial prediction errors, ii) significant displacement of pre-blast predictions due to blast movement, iii) errors in detecting correct ore/waste contacts, and iv) failure to follow complex dig lines during selection. All these reasons cause the accumulation of misclassification errors, which results in a loss of profit (Isaaks, Treloar, & Elenbaas, 2014).

This chapter compares two grade control methods applied to data from a single mine bench at the Misima mine in Papua New Guinea. The first grade control method is based on the Advanced Grade Control system. The second grade control method is based on ordinary kriging. The total profit is assessed for the two methods. Blast movement is modeled using artificial topography and blast movement measurements. Excavating constraints are represented as rectangular selection frames.

7.1 Background

A blasthole data set for the entire operation period of the Misima mine was released by Placer Dome to the Centre for Computational Geostatistics (CCG) for PhD research. The mine was owned by Placer Dome Incorporated and operated by its subsidiary Misima Mines Pty Ltd from 1988 to 2004. Placer Dome was a large Canadian mining company operating from 1987 to 2006 when it was purchased by another large mining company, Barrick Gold Corporation.

The Misima mine was situated at the eastern side of Misima Island, which is a part of the Louisiade Archipelago in Milne Bay province of Papua New Guinea. The Umuna epithermal gold/silver deposit has a stike length of over 3 km; it is characterized by a complex system of faults (Clarke, Lewis, & Waldron, 1990). The deposit is hosted in metamorphosed Cretaceous-Paleogene rocks of the Sisa Association (Shannon & Stoker, 2013). Mineralization is developed in faults, fractures, stockworks, breccias, skarns, and disseminations (Clarke et al., 1990; Shannon & Stoker, 2013). The Umuna Lode has the most distinctive mineralization. It is characterized by a complex veined system infilled with quartz (Clarke et al., 1990). A detailed review of the geology and mineralization of the Umuna deposit can be found in Clarke et al. (1990) and Shannon and Stoker (2013).

The principal gold deposits of the Misima mine were Umuna (including the Kulumalia area) and Quartz Mountain. The Quartz mountain deposit was mined by Maika, Kobel Creek, and Ewatinona pits. The Kulumalia open pit was developed as a source of soft ore in addition to the hard ore from the main Umuna pit and had higher ore grades than expected (Lyday, 1994). In 1994, the Kulumalia pit was replaced by the Ewatinona pit (Lyday, 1994) operating from 1995 to 1997. Stages 1, 2, and 3 of the main Umuna open pit were mined by 1996; then, the operation in Stages 4, 5, and 6 began (Shannon & Stoker, 2013). In 1999, mining continued in East Umuna Stage 2 and Tonowak pits (Lyday, 1999). Open pit production stopped at the Misima mine in 2001 due to a decline in ore grades and was followed by stockpile processing up to 2004 (McManus, 2017).

7.1.1 Available Data

This case study uses blasthole samples from the Kulumalia open pit. A data set representing a single mine bench at the elevation of 110 m is selected; the mine bench will be further referred to as Bench '110'. The data set has grades of Au and Ag in grams per tonne. The grade values are used in profit calculations to distinguish between ore and waste destinations for mined material.

Blast Movement Data

In order to assess the influence of blasting on total profit from Bench '110', blast movement should be modeled. The Advanced Grade Control-Blast Movement (AGC-BM) algorithm is used for this case study to map pre-blast predictions of profit onto a 3-D post-blast muckpile; details about the algorithm are in Chapter 5. The most accurate modeling results with AGC-BM are obtained with pre- and post-blast topography and blast movement measurements. The blast movement measurements are obtained using specialized transmitters and detecting equipment (e.g., a system like that described in Adam and Thornton (2004)).

Real topography and blast movement measurements are not available for this case study. Artificial topography and blast movement measurements are created instead. It is assumed that the mine bench was confined by the surrounding rock mass during blasting (buffer blasting) to prevent excessive movement in the direction of free faces. This blast configuration represents the most favorable situation for grade control since blast movement is expected inside the area of blasting only.

7.2 Methodology

A grade control method based on ordinary kriging (OK) is compared to a grade control method based on the Advanced Grade Control (AGC) system. Total profit from Bench '110' is compared for the two methods at three main stages of grade control: i) spatial prediction, ii) blast movement modeling, and iii) selection optimization. The comparison is based on a high resolution 'true' model constructed for Bench '110'. A detailed workflow for this case study consists of the following steps:

1. A reference model at a high resolution is obtained. The model contains grade values for Au and Ag at each high resolution location. A multivariate simulation workflow based on the Projection Pursuit Multivariate Transform (PPMT) algorithm (Barnett et al., 2014) is used. The reference model allows calculating the true total profit from Bench '110'.

2. The reference model is validated in terms of reproducing important statistics.

3. A profit function is developed.

4. The reference model is sampled with positioning errors and clipped to a polygon to more realistically represent the shape of the mine bench.

5. The grades of Au and Ag are used to model optimal destinations with OK and the Advanced Grade Control-Expected Profit (AGC-EP) algorithm; the profit function form step 3 is used. Section 7.2.2 describes the profit function in detail.

6. Total pre-blast profit from Bench '110' is calculated for the two methods. Methodology for calculating total profit is explained in Section 7.2.2.

7. Artificial pre- and post-blast topography and artificial blast movement vectors are created for Bench '110'.

8. Blast movement modeling is performed. The high resolution profit predicted by ordinary kriging and AGC-EP is mapped onto a 3-D shape of a muckpile.

9. Optimal post-blast destinations are obtained for the two grade control methods.

10. The pre- and post-blast high resolution profit is used to design optimal pre- and post-blast dig limits for the two grade control methods.

11. Total mineable profit is compared at different stages of grade control. Different grade control scenarios are considered.

The following sections describe the construction of the reference model and provide details about profit calculations. Then, the grade control modeling with AGC and OK is illustrated and results are summarized.

7.2.1 Construction of a Reference Model

In order to calculate a total profit value from Bench '110', a high resolution 'true' reference model is required. The reference model is simulated using a multivariate simulation workflow based on the PPMT algorithm and sequential Gaussian simulation (Isaaks, 1991). Location maps for Au and Ag are provided in Figure 7.1; Figure 7.2 shows corresponding histograms.

(a) Au   **(b)** Ag
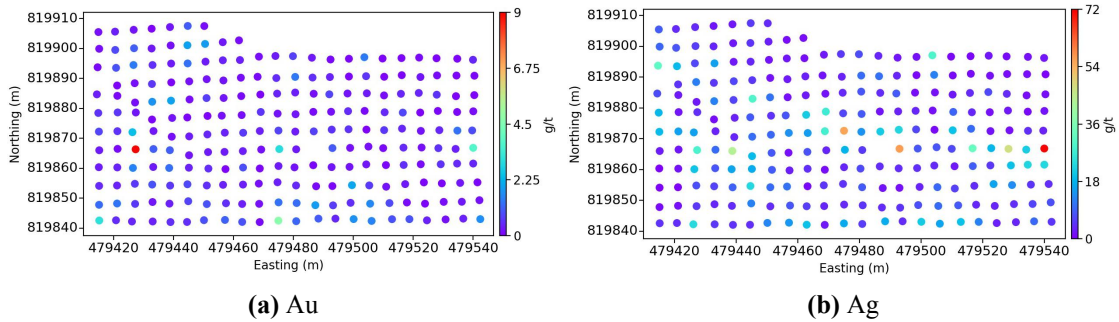
Figure 7.1: Location maps for grade variables sampled at Bench '110'

(a) Au   **(b)** Ag
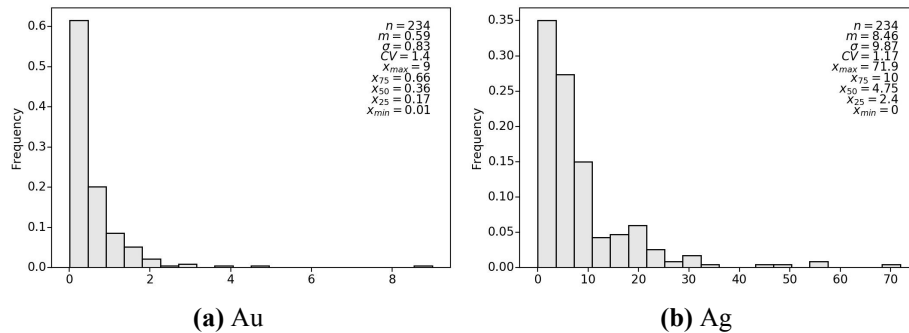
Figure 7.2: Histograms for grade variables sampled at Bench '110'

There are 234 BH samples situated at a square pattern with positioning errors. The average distance between BHs (h_{xy}) is 5.91 m (calculated using Equation (3.11)). The simulation workflow consists of the following steps.

1. Original Au and Ag grade values are normal score transformed (Rossi & Deutsch, 2014, p. 22). Declustering is not performed since the blasthole data are relatively evenly spaced throughout the mine bench.

2. The normal-scored Au and Ag grade values are used to calculate variogram models used for simulation. The variograms of normal scores are used to improve the variogram reproduction according to recommendations from Barnett and Deutsch (2015a). Figure 7.3 demonstrates the modeled variograms.

(a) Au (calculated at 130° from North)   **(b)** Ag (calculated at 110° from North)

Figure 7.3: Variograms of grade variables sampled at Bench '110'
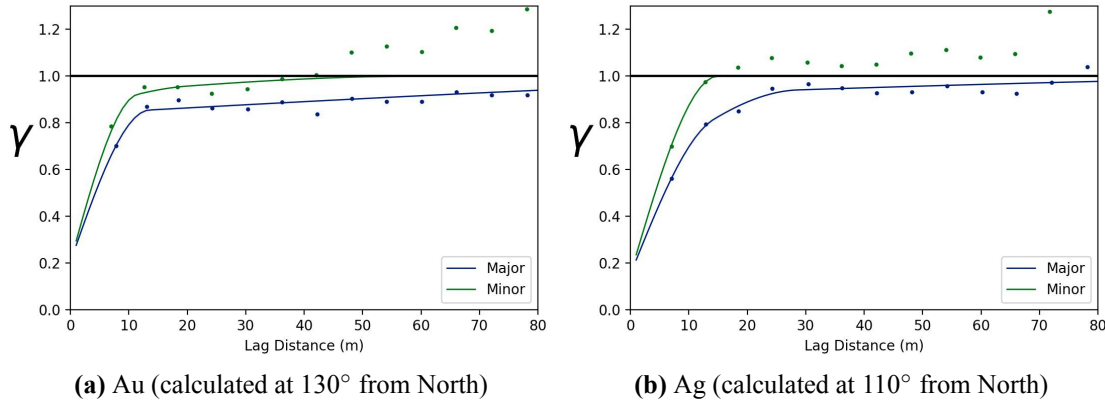
In Figure 7.3, blue and green dots represent experimental variogram points calculated in the major and minor continuity directions, respectively; blue and green lines represent corresponding modeled variograms.

3. The original Au and Ag grades are PPMT forward transformed using $ppmt$ program described in Barnett and Deutsch (2015a). Recommended parameters for the PPMT transformation from Barnett and Deutsch (2015a) are used.

4. The PPMT-transformed Au and Ag grades are used as conditioning data to obtain the reference models for an area of 138×75 m² with a grid size of 1.5×1.5 m² using $sgsim$ (C. V. Deutsch & Journel, 1998).

5. Simulated Au and Ag grades are back-transformed to original units using $ppmt\_b$ program described in Barnett and Deutsch (2015a).

The back-transformed reference models are sampled at a grid size of 6×6 m² with a random error in coordinates of 1 m. The samples are then clipped to a polygon to approximately reproduce the original shape of Bench '110'.

7.2.1.1 Reference Model Validation

Figures 7.4 and 7.5 show simulated Au and Ag grades and corresponding samples.

(a) Au **(b)** Ag
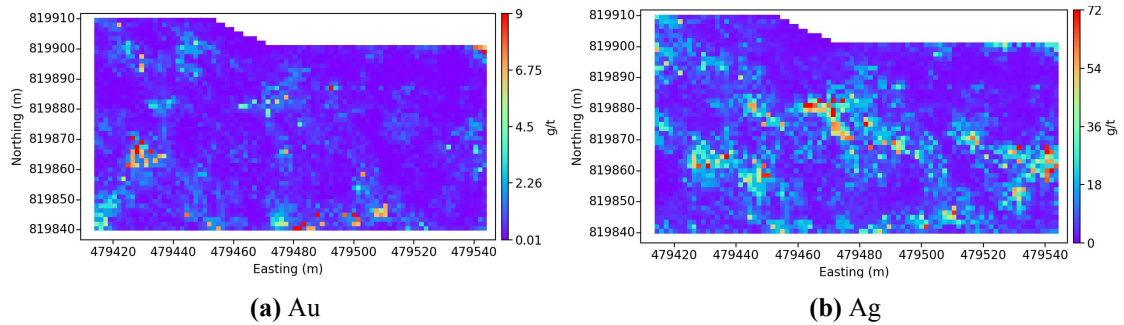
Figure 7.4: Reference models for Au and Ag

(a) Au **(b)** Ag

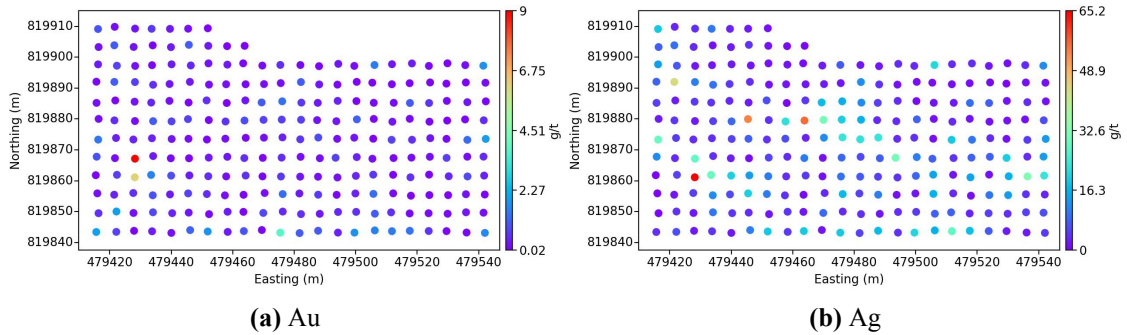**Figure 7.5:** Artificial BH samples for Au and Ag

Histogram Reproduction

Histogram reproduction is an important validation check. It is performed using 20 simulated realizations. The shapes of the original and simulated cumulative distribution functions (CDFs) should be similar as well as corresponding means and standard deviations. Figure 7.6 shows the histogram reproduction for Bench '110'.

(a) Au   **(b)** Ag
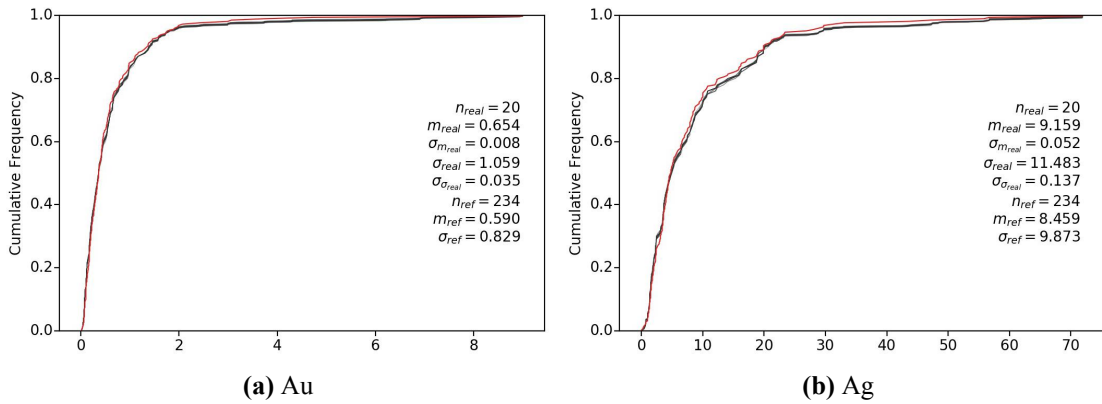
Figure 7.6: Histogram reproduction for the Au and Ag grades sampled at Bench '110'

In Figure 7.6, the shapes of the CDFs of original (red color) and simulated (black color) data are similar. Some fluctuations in the univariate statistics are expected and desired.

Variogram Reproduction

Another important check is the reproduction of original variograms. Since the variogram models of the normal scored Au and Ag grades are used to simulate the reference model, the reproduction is checked for the simulated Au and Ag grades in normal scores (before the PPMT back-transformation). Figure 7.7 demonstrates the reproduction of variograms for Bench '110'.

(a) Au   **(b)** Ag
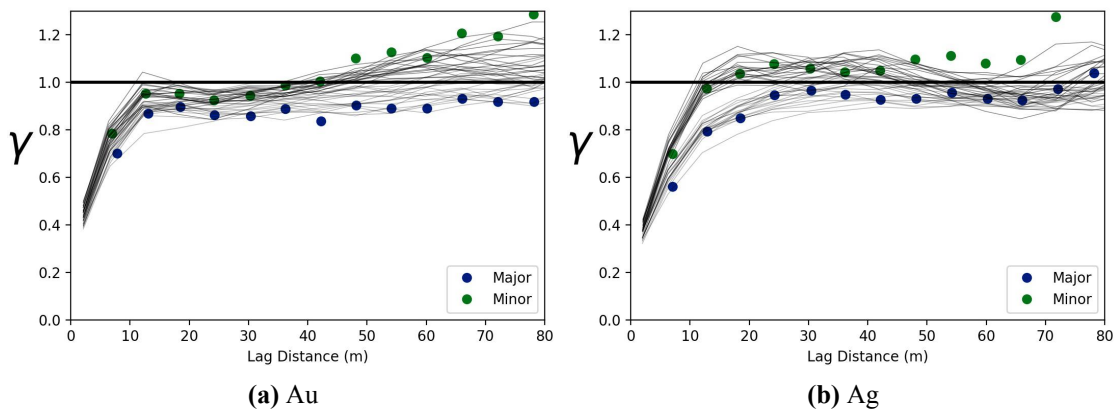
Figure 7.7: Variogram reproduction for the Au and Ag grades sampled at Bench '110'

In Figure 7.7, blue and green dots represent experimental variogram points calculated in the major and minor continuity directions, respectively, while grey lines represent the variograms of simulated models. The variograms of simulated realizations are calculated

in the same directions as the original variograms. Overall, the variogram reproduction is satisfactory for the two grade variables.

Reproduction of Bivariate Relationships between Grade Variables

The total profit of Bench '110' is calculated based on the simulated grade values of Au and Ag. Since the bivariate relationship between Au and Ag may influence profit calculations, it should be reproduced in the simulated models. Figure 7.8 shows the bivariate relationship between the two grade variables before and after the PPMT transformation, respectively.

(a) Before PPMT   (b) After PPMT
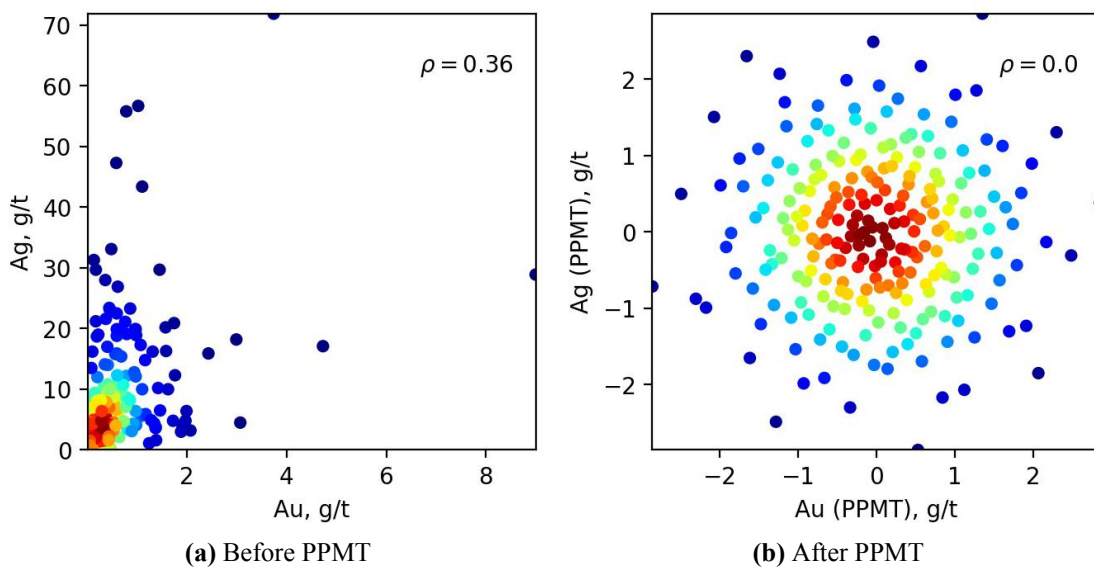
Figure 7.8: Scatter plots between the Au and Ag grade variables before and after the PPMT transformation

Figure 7.9 shows the reproduction of the bivariate relationship between Au and Ag in the simulated reference model.
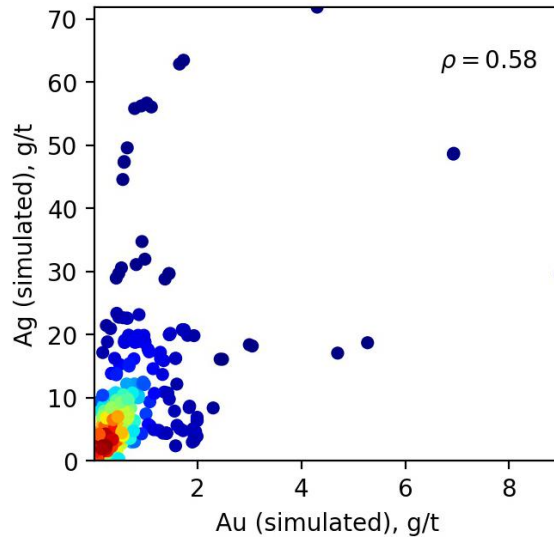
Figure 7.9: Scatter plot between the simulated Au and Ag grade variables after the PPMT back-transformation

Figures 7.8a and 7.9 show that the bivariate relationship between the Au and Ag grade variables is reproduced in the simulated models.

7.2.2 Determining Optimal Destinations with AGC-EP and Ordinary Kriging

The single reference model is used to calculate the true optimal destinations for Bench '110' and a true total profit value. Optimal destinations for OK and AGC-EP are obtained using the following steps:

1. The reference model is sampled at a grid size of 6×6 m^2 with a random error in coordinates of up to 1 m.

2. The sampled grades are modeled with OK for an area of 138×75 m^2 with a grid size of 1.5×1.5 m^2. A profit function P is used to convert ordinary kriging estimates to optimal destinations $d_{opt}^{ok}(\boldsymbol{u})$ at all mine bench locations $\boldsymbol{u} \in A$. OK is performed with variograms of Au and Ag in original units.

3. The sampled grades are used to model expected profit with AGC-EP for the area of 138×75 m^2 with the grid size of 1.5×1.5 m^2. The profit function P is used

175

to calculate high resolution expected profit at all the locations $\boldsymbol{u} \in A$. Then, the expected profit is used to determine the best AGC-EP destinations $d_{opt}(\boldsymbol{u})$ at all the locations $\boldsymbol{u} \in A$.

4. The simulated Au and Ag grades are used to obtain the true profit values at all the locations $\boldsymbol{u} \in A$. Then, the true high resolution profit is used to obtain the true optimal destinations $d_{true}(\boldsymbol{u})$ at all the locations $\boldsymbol{u} \in A$.

5. The optimal OK destinations $d_{opt}^{ok}(\boldsymbol{u})$, the optimal AGC-EP destinations $d_{opt}(\boldsymbol{u})$, and the true simulated grades are used to calculate total profit from Bench '110'. The predicted total profit values for both methods are compared.

Steps 1-5 are relevant to the first stage of grade control. They are used to calculate pre-blast total profit from Bench '110' for the case of free selection. Then, blast movement is modeled to map the true and predicted pre-blast profit on the post-blast shape of a muck-pile. Finally, dig limits are optimized to account for equipment limitations. The post-blast mineable destinations and the post-blast true profit define total mineable profit for OK and AGC-EP; this is the actual profit that can be extracted from Bench '110'.

7.2.3 Profit Function

Sampled grade values are used to predict high resolution profit with OK and AGC-EP for two mined material destinations: ore and waste. The real profit and recovery functions are not available for this case study. A simple profit function is designed accounting for monetary profit obtained from recovered gold and silver. Profit at a location $\boldsymbol{u}$ is calculated as follows:

$$P(z(\boldsymbol{u}; Au), z(\boldsymbol{u}; Ag)) = (z(\boldsymbol{u}; Au) \cdot p_1 \cdot r_1 + z(\boldsymbol{u}; Ag) \cdot p_2 \cdot r_2 - c_m - c_p) \cdot T. \quad (7.1)$$

where $z(\boldsymbol{u}; Au)$ and $z(\boldsymbol{u}; Ag)$ are the grades of gold and silver in grams per tonne, respectively; r_1 and r_2 are the recoveries of gold and silver, respectively; p_1 and p_2 are the prices of gold and silver in US dollars per gram, respectively; c_m is the cost of mining a tonne of mined material; c_p is the cost of processing a tonne of ore; T is the number of tonnes of mined material associated with the location $\boldsymbol{u}$.

The recoveries for Au and Ag are assumed to be 0.9 and 0.7, respectively. The price of Au is chosen to be \$1 305 per troy ounce, while the price of Ag is chosen to be \$16.7 per troy ounce. The prices are based on average prices from the London Metal Exchange in January and February, 2019. The prices are converted to US dollars per gram based on 31.1035 grams per troy ounce. The costs of mining and processing are assumed to be \$2 per tonne and \$17 per tonne, respectively. The density of mined material is assumed to be 2.3 tonnes per m³.

The true destination at the location $\boldsymbol{u}$ is defined as follows:

$$
d_{true}(\boldsymbol{u}) = \begin{cases} ore, & \text{if } P(z_{true}(\boldsymbol{u}; Au), z_{true}(\boldsymbol{u}; Ag)) \geq 0; \\ waste, & \text{otherwise.} \end{cases}
\tag{7.2}
$$

where $z_{true}(\boldsymbol{u}; Au)$ and $z_{true}(\boldsymbol{u}; Ag)$ are the true grades of gold and silver at the location $\boldsymbol{u}$, respectively.

The total profit from Bench '110' is calculated based on the predicted and true destinations at each high resolution location. If a predicted destination $d_{est}(\boldsymbol{u})$ is ore, and the true destination $d_{true}(\boldsymbol{u})$ is ore, profit for correct acceptance at the location $\boldsymbol{u}$ is calculated as follows:

$$
P1(\boldsymbol{u}) = \begin{cases} P(z_{true}(\boldsymbol{u}; Au), z_{true}(\boldsymbol{u}; Ag)), & \text{if } d_{est}(\boldsymbol{u}) \text{ is } \textit{ore} \text{ and } d_{true}(\boldsymbol{u}) \text{ is } \textit{ore}; \\ 0, & \text{otherwise.} \end{cases}
\tag{7.3}
$$

If $d_{est}(\boldsymbol{u})$ is waste, and $d_{true}(\boldsymbol{u})$ is waste, profit for correct rejection at the location $\boldsymbol{u}$ is calculated as follows:

$$
P2(\boldsymbol{u}) = \begin{cases} -c_m \cdot T, & \text{if } d_{est}(\boldsymbol{u}) \text{ is } \textit{waste} \text{ and } d_{true}(\boldsymbol{u}) \text{ is } \textit{waste}; \\ 0, & \text{otherwise.} \end{cases}
\tag{7.4}
$$

If $d_{est}(\boldsymbol{u})$ is ore, and $d_{true}(\boldsymbol{u})$ is waste, loss (negative profit) for false acceptance at the location $\boldsymbol{u}$ is calculated as follows:

$$
P3(\boldsymbol{u}) = \begin{cases} P(z_{true}(\boldsymbol{u}; Au), z_{true}(\boldsymbol{u}; Ag)), & \text{if } d_{est}(\boldsymbol{u}) \text{ is } \textit{ore} \text{ and } d_{true}(\boldsymbol{u}) \text{ is } \textit{waste}; \\ 0, & \text{otherwise.} \end{cases}
\tag{7.5}
$$

If $d_{est}(\boldsymbol{u})$ is waste, and $d_{true}(\boldsymbol{u})$ is ore, profit for false rejection at the location $\boldsymbol{u}$ is calculated as follows:

$$P4(\boldsymbol{u}) = \begin{cases} -c_m \cdot T, & \text{if } d_{est}(\boldsymbol{u}) \text{ is } \textit{waste} \text{ and } d_{true}(\boldsymbol{u}) \text{ is } \textit{ore}; \\ 0, & \text{otherwise.} \end{cases} \tag{7.6}$$

The total profit from Bench '110' is calculated as follows:

$$P_{total} = \sum_{\boldsymbol{u} \in A} (P1(\boldsymbol{u}) + P2(\boldsymbol{u}) + P3(\boldsymbol{u}) + P4(\boldsymbol{u})). \tag{7.7}$$

The profit for the correct rejection and false rejection decisions is negative since the cost of removing mined material should be covered. Lost opportunity cost for false rejection is not considered. The cost of processing waste is negative and linearly increases with the decrease in grade values.

7.3 First Grade Control Stage

OK is performed separately for Au and Ag. The OK estimates are then used with the profit function P to obtain predicted destinations $d_{opt}^{ok}(\boldsymbol{u})$ at all locations $\boldsymbol{u} \in A$. The total OK profit from Bench '110' is calculated using the optimal OK destinations $d_{opt}^{ok}(\boldsymbol{u})$, the true destinations $d_{true}(\boldsymbol{u})$ at all locations $\boldsymbol{u} \in A$, and Equations 7.3-7.7. OK is repeated with numbers of nearby conditioning samples in the range from 15 to 220; the best scenario is chosen for comparing with AGC-EP. An optimal number of nearby samples to use with AGC-EP is predicted by k-fold cross-validation (more details are in Chapter 3). Optimal destinations $d_{opt}(\boldsymbol{u})$, the true destinations $d_{true}(\boldsymbol{u})$ at all locations $\boldsymbol{u} \in A$, and Equations 7.3-7.7 are used to calculate total AGC-EP profit from Bench '110'. The total profit values obtained with OK and AGC-EP are then compared to the true total profit value achieved at free selection with all destinations predicted correctly. Figure 7.10 shows variogram models used for ordinary kriging.

(a) Au

(b) Ag
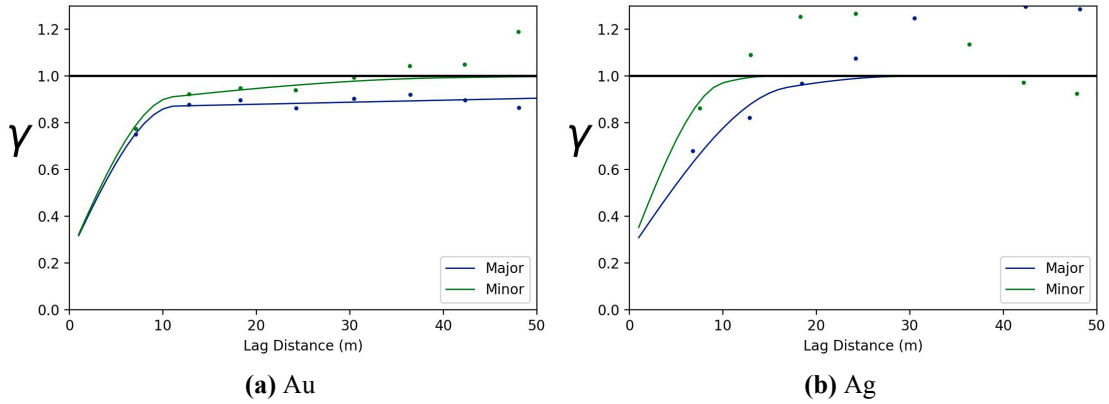
Figure 7.10: Variograms of Au and Ag used for OK

The variograms shown in Figure 7.10 are modeled using the Au and Ag grades in original units. The highest total profit for OK was achieved with 15 nearby samples at each location. Figure 7.11 shows OK estimates corresponding to the best OK classification.

(a) Au

(b) Ag

Figure 7.11: Ordinary kriging estimates for Au and Ag

Figure 7.12 shows the best classification map obtained with kriging versus the classification map showing the true destinations.

(a) OK destinations

(b) True destinations

Figure 7.12: Optimal OK mined material destinations versus the true optimal destinations at Bench '110'

The classification map in Figure 7.12a allows selecting around $170 246 of total profit from Bench '110'.

Figure 7.13 shows optimal ore/waste destinations determined by AGC-EP with 155 nearby samples (predicted by k-fold cross-validation) and the true optimal ore/waste destinations.

(a) AGC-EP destinations   **(b)** True destinations

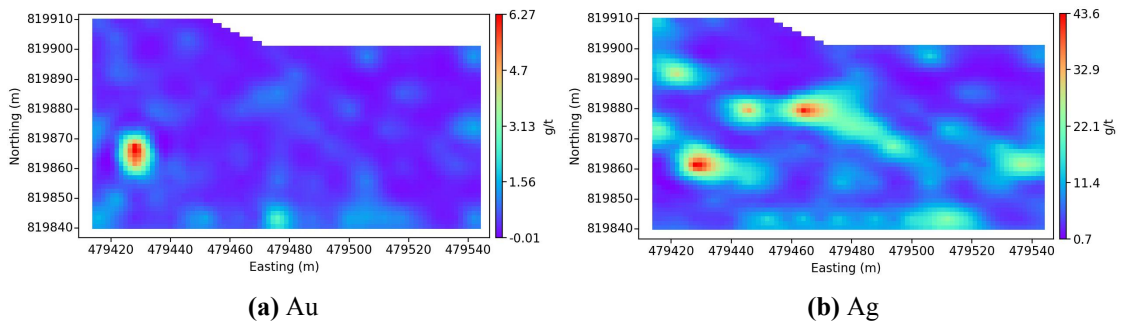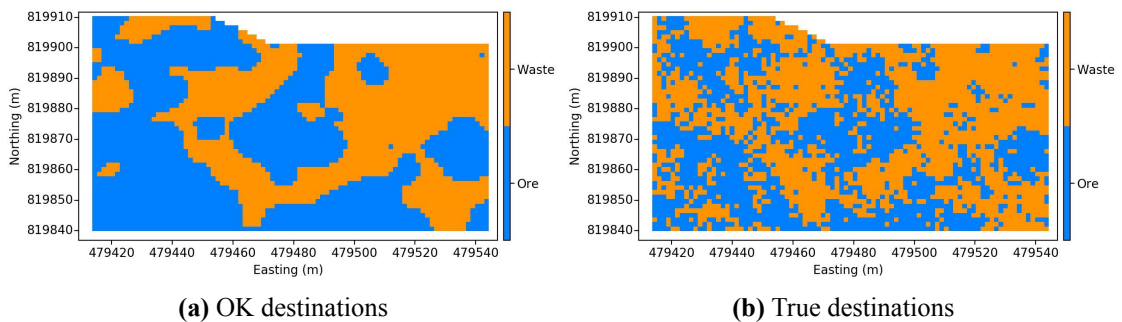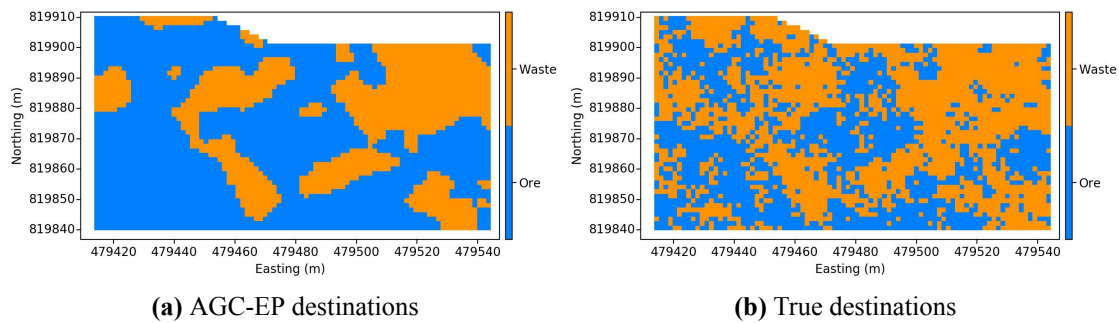**Figure 7.13:** Optimal AGC-EP mined material destinations versus the true optimal destinations at Bench '110'

The classification map in Figure 7.13a allows selecting the total profit of $ 172 118, which is $1 872 or around 1.1 % improvement in profit over ordinary kriging for no additional cost. The tonnes of ore and waste at each location are calculated using pre-blast topography and a 3-D model created for this example; the model is shown later in this chapter. This total profit value is not achievable because it assumes free selection. Total profit from a mine bench should be calculated for a pre-blast mineable classification.

Note that ordinary kriging is performed well. Also, the best possible ordinary kriging estimate is selected based on carefully modeled variograms. An inexperienced junior engineer assigned to the grade control task may not select optimal input parameters for OK, which may result in a more significant loss of profit.

The classification maps produced by OK and AGC-EP allow selecting 80.1 % and 80.9 % of the true total profit value of $212 648, respectively, from Bench '110'. This is possible to assess since the high resolution 'truth' is known. If blasting is performed, the positions of pre-blast profit or grade predictions should be corrected due to blast movement. The following section assesses a possible impact of blast movement on the total mineable profit from Bench '110'.

7.4 Second Grade Control Stage

The pre-blast predictions of profit obtained with OK and AGC-EP are mapped onto a post-blast 3-D model of muckpile. The model is constructed using artificial topography. The post-blast predicted profit is used to determine optimal post-blast destinations for each method. The true post-blast profit defines the total profit from Bench '110' relevant for selection. The workflow of this part of the case study consists of the following steps:

1. Realistic topography for Bench '110' before and after blasting is created.

2. Realistic blast movement vectors are created. The vectors are defined by assuming pre- and post-blast positions of transmitters.

3. Blast movement is modeled with the Advanced Grade Control-Blast movement (AGC-BM) algorithm. A 3-D model of the true post-blast profit is obtained. The true post-blast profit in 3-D is relevant for selection and, therefore, is used for calculating total mineable profit from Bench '110'.

4. Post-blast profit prediction models for OK and AGC-EP are obtained.

After steps 1-4 are performed, the post-blast profit in 3-D is used for designing optimal dig limits in the next grade control stage.

7.4.1 Modeling Results

Artificial pre-blast topography is approximated based on blasthole surveys. Inverse distance is used to interpolate sparse elevation measurements. Post-blast topography is constructed based on two assumptions: i) Bench '110' is confined during blasting, and ii) blasting is performed using a v-shaped firing pattern. Both pre- and post-blast topographic surfaces are obtained for the area of the reference model of 138×75 m^2 with a grid size of 1.5×1.5 m^2. Figure 7.14 demonstrates the pre- and post-blast topographic surfaces.

(a) Pre-blast **(b)** Post-blast
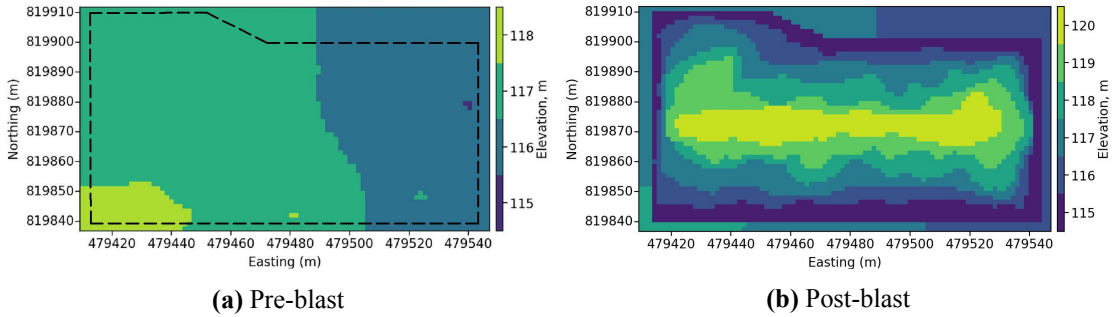
Figure 7.14: Pre- and post-blast artificial topography for Bench '110'

In Figure 7.14a, the black dashed line illustrates the outline of the mine bench. In Figure 7.14b, there is a distinctive ridge formed along the centerline of the blast initiation. It is assumed that the rock mass moves towards the centerline perpendicular to timing contours. Figure 7.15 shows the artificial blast movement vectors created for Bench '110'; the vectors are plotted as arrows on the top of the post-blast topographic surface.

Figure 7.15: Artificial blast movement vectors for Bench '110'

In Figure 7.15, the blast movement vectors are plotted in 2-D, which illustrates horizontal displacement only. However, the pre- and post-blast positions of transmitters in 3-D are used for this case study. The pre- and post-blast positions of each transmitter are summarized in Table 7.1.

182

Table 7.1: Pre- and post-blast coordinates of 9 transmitters

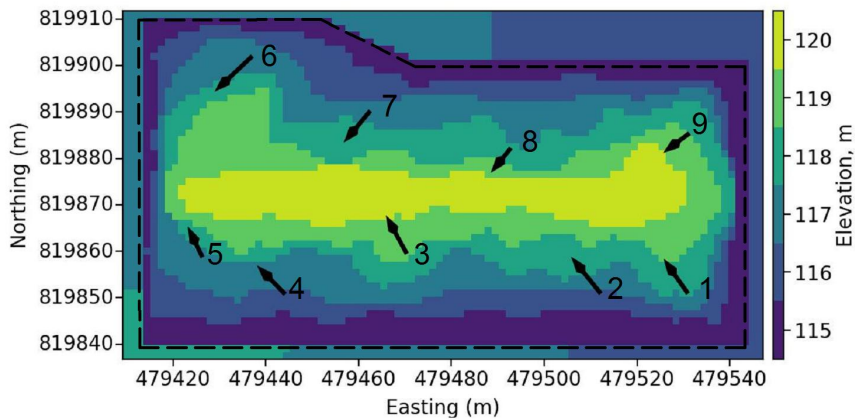| Transmitter ID	East (pre-blast)	North (pre-blast)	Elevation (pre-blast)	East (post-blast)	North (post-blast)	Elevation (post-blast)
Transmitter 1	479,531.0	819,850.9	114.0	479,525.7	819,858.4	115.0
Transmitter 2	479,512.2	819,850.9	113.0	479,505.8	819,858.8	114.0
Transmitter 3	479,470.4	819,859.5	116.0	479,465.9	819,867.8	118.0
Transmitter 4	479,444.2	819,850.7	113.0	479,438.1	819,856.9	114.0
Transmitter 5	479,426.4	819,858.7	114.0	479,423.2	819,865.3	115.0
Transmitter 6	479,437.1	819,902.0	114.0	479,428.9	819,894.3	115.0
Transmitter 7	479,462.5	819,890.2	114.0	479,456.8	819,883.4	115.0
Transmitter 8	479,492.8	819,882.2	115.0	479,488.5	819,876.8	118.0
Transmitter 9	479,531.3	819,885.4	116.0	479,525.6	819,881.2	118.0

The artificial pre- and post-blast topography and blast movement vectors are used to construct pre- and post-blast 3-D models approximately representing blast movement for Bench '110'. Figure 7.16 shows pre-blast 3-D profit and corresponding 3-D classification map.

(a) Ore profit

(b) Waste profit
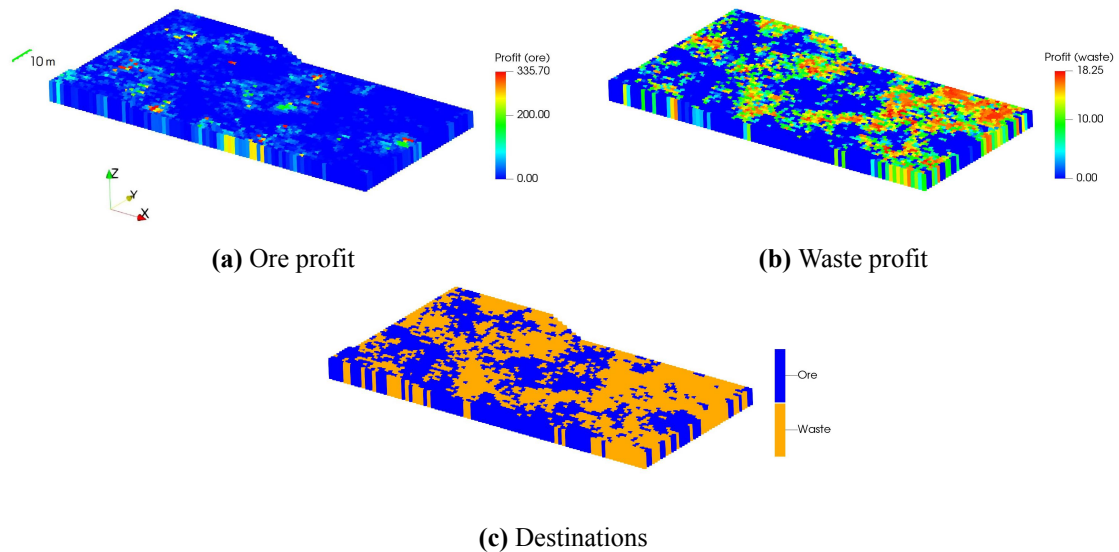
(c) Destinations

Figure 7.16: True pre-blast profit for the ore and waste destinations and the corresponding true optimal destinations for Bench '110'

In Figure 7.16, profit is defined by Equation 7.1. Profit for the waste destination is shown positive although it represents the loss of profit. Figure 7.17, shows pre-blast high resolution profit mapped to a 3-D muckpile using AGC-BM.

(a) Ore profit

(b) Waste profit
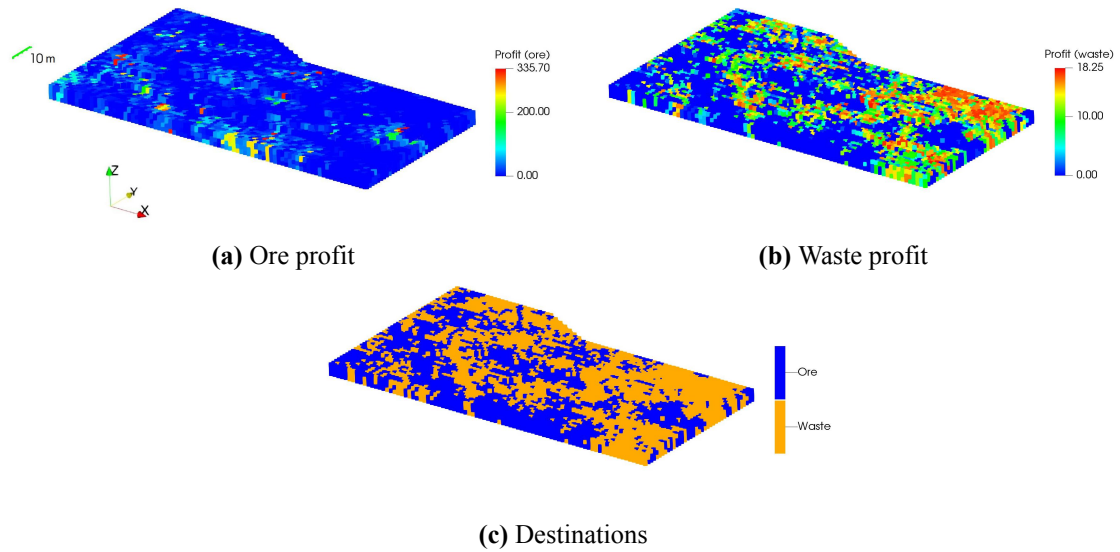
(c) Destinations

Figure 7.17: Post-blast true profit for the ore and waste destinations and the corresponding true optimal destinations for Bench '110'

Figures 7.18 and 7.19 show pre- and post-blast expected profit for the ore and waste destinations (calculated with AGC-EP), respectively; also, the corresponding pre- and post-blast classification maps in 3-D are shown.

(a) Ore expected profit

(b) Waste expected profit

(c) Destinations

Figure 7.18: Pre-blast expected profit for the ore and waste destinations calculated with AGC-EP and the corresponding optimal destinations for Bench '110'

(a) Ore expected profit

(b) Waste expected profit

(c) Destinations

Figure 7.19: Post-blast expected profit for the ore and waste destinations calculated with AGC-EP and the corresponding optimal destinations for Bench '110'

Figures 7.20 and 7.21 show pre- and post-blast profit for the ore and waste destinations (calculated with OK), respectively; also, the corresponding pre- and post-blast classification maps in 3-D are shown.

(a) Ore profit

(b) Waste profit

(c) Destinations

Figure 7.20: Pre-blast profit for the ore and waste destinations calculated with OK and the corresponding optimal destinations for Bench '110'

(a) Ore profit

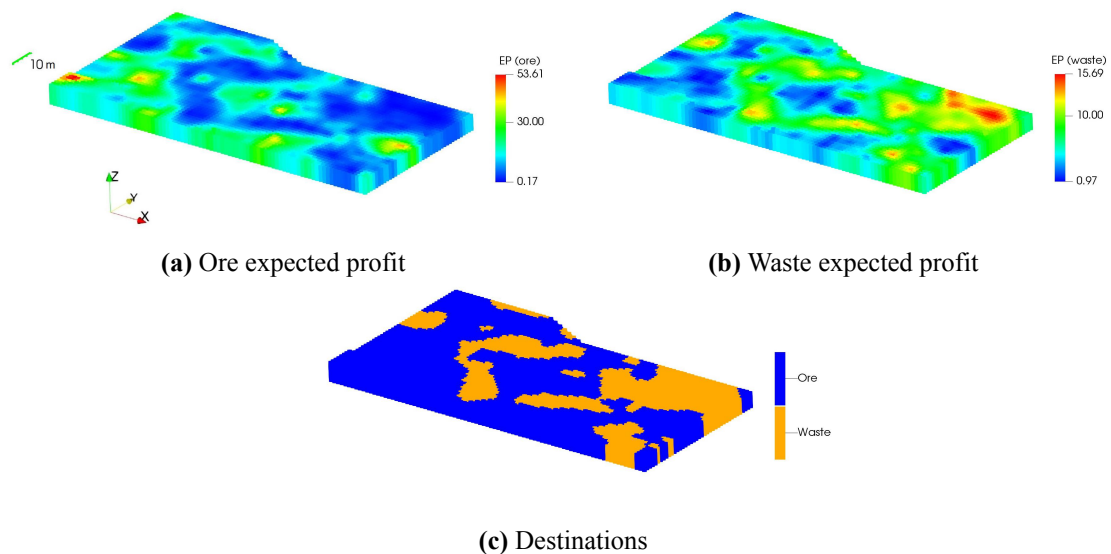
(b) Waste profit
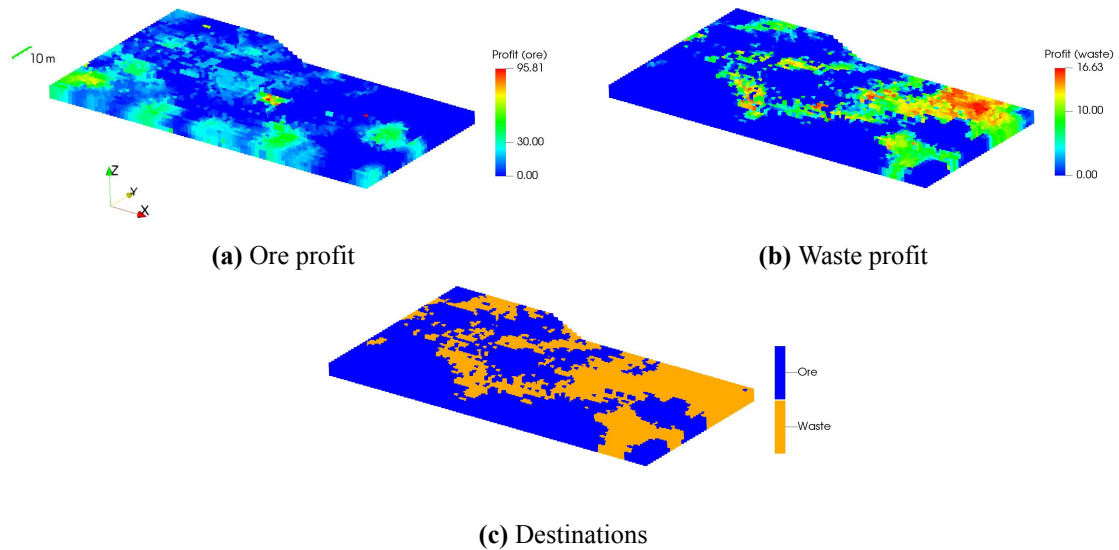
(c) Destinations

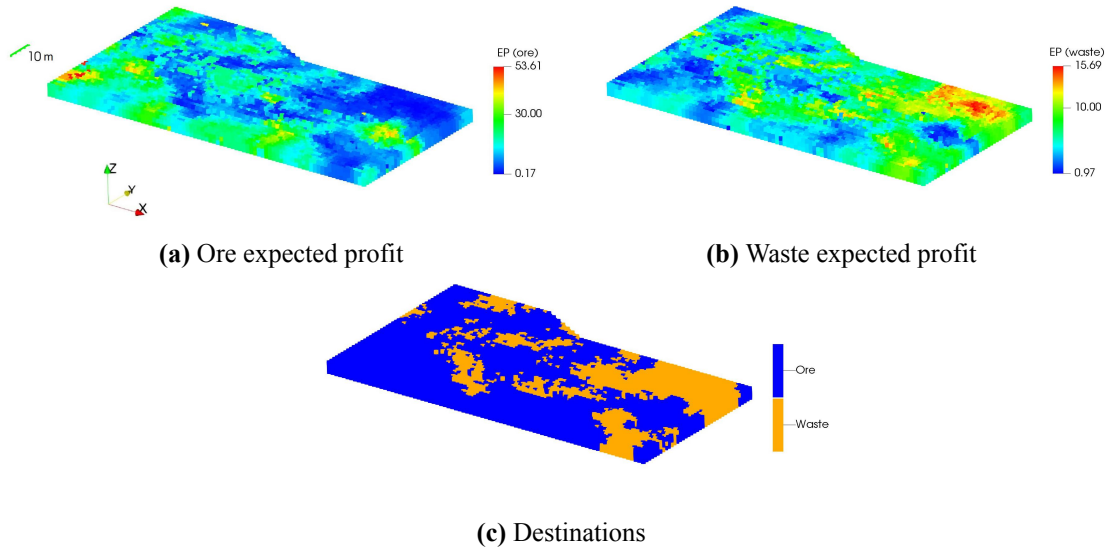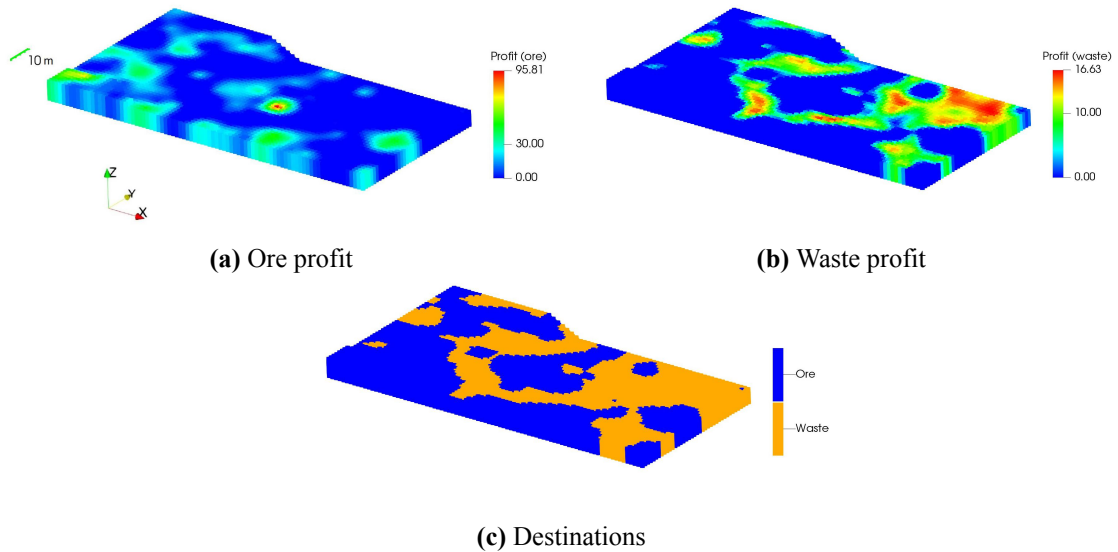**Figure 7.21:** Post-blast profit for the ore and waste destinations calculated with OK and the corresponding optimal destinations for Bench '110'

The AGC-BM algorithm was run with all the elements of the cost function weighted equally. The algorithm was run with 20 and 40 nearest neighbors for the low resolution (LR) and high resolution (HR) models, respectively. The algorithm performed 61 000 and 137 000 iterations for the LR and HR model, respectively. The cost function tolerance parameter was set to 0.05 %. The total number of blocks to optimize was 15 000. The swell factor was estimated to be around 1.15. The operation time was 88 minutes 40 seconds. Details about the optimization algorithm are in Chapter 5. The post-blast model shows some minor artifacts due to the artificial topography and blast movement measurements.

It is assumed that the blast movement model generated by AGC-BM represents the true blast movement; this implies that the true post-blast profit at high resolution is known. Since the true and predicted high resolution profit is modeled during the same optimization procedure, the total post-blast monetary profit of Bench '110' (calculated with Equations (7.3)-(7.7)) is the same as the total pre-blast monetary profit. The 3-D models of the true and predicted profit are used with the Advanced Grade Control-Dig Limits (AGC-DL) optimization algorithm to define optimal dig limits in 2-D for each method.

7.5 Third Grade Control Stage

The first two stages of grade control described in the previous sections determine true and predicted post-blast profit from Bench '110'. The high resolution optimal destinations in Figures 7.19c and 7.21c may not be possible to mine selectively due to equipment limitations. Ideally, the 3-D post-blast predicted profit should be used to define mineable dig limits in 3-D. However, the information used to predict profit is from blastholes and inherently 2-D. Unless there is additional information that informs on the vertical geological variability of the mine bench (from multiple samples along the blastholes or dedicated drillholes), dig limits should be optimized in 2-D accounting for the 3-D shape of a muckpile.

The most straightforward approach is to average the predicted profit in the vertical direction at each modeled location over the mine bench. A more correct approach is to give different locations different weights during optimization based on local bench heights; this is done by using the cumulative profit calculated along the vertical direction for each location at the bottom elevation of the mine bench. After a location in 2-D is assigned a mineable destination during the dig limits optimization, all the corresponding locations along the vertical direction are also assigned this destination. Conversion of the 3-D post-blast expected profit obtained with AGC-EP in 2-D is illustrated in Figure 7.22.

(a) Ore expected profit

(b) Waste expected profit

(c) Destinations
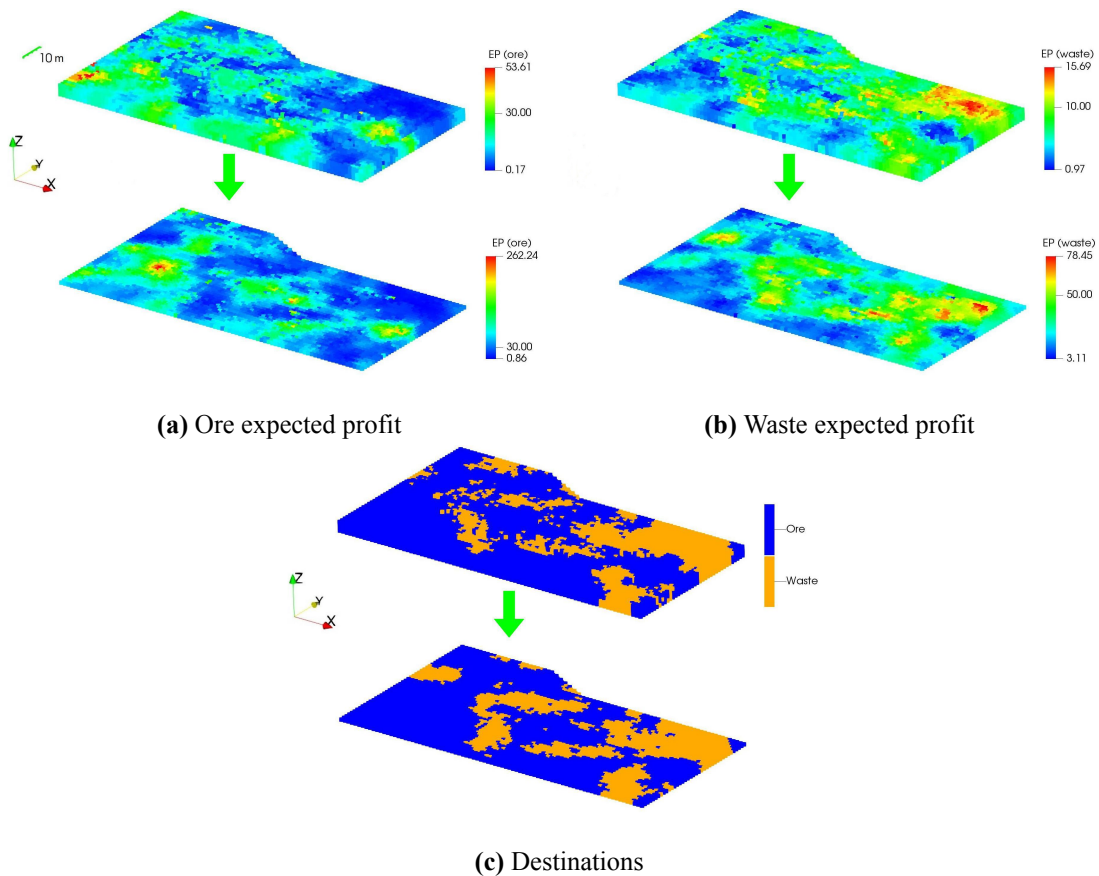
Figure 7.22: Conversion of the post-blast expected profit obtained with AGC-EP from 3-D to 2-D

After the pre-and post-blast 3-D models of profit are converted to 2-D, the AGC-DL algorithm is run to obtain optimal dig limits. Pre- and post-blast optimal dig limits are obtained for both AGC-EP and OK. This final classification is used to calculate total mineable monetary profit for both grade control methods. A detailed workflow of the third stage of grade control for Bench '110' consists of the following steps:

1. The pre- and post-blast 3-D profit predicted by AGC-EP and OK is converted to 2-D; this procedure is schematically illustrated in Figure 7.22.

2. Pre-blast dig limits are optimized for AGC-EP and OK using the pre-blast profit predictions converted to 2-D.

3. Post-blast dig limits are optimized for AGC-EP and OK using the post-blast profit predictions converted to 2-D.

4. The optimized dig limits are used to classify the pre- and post-blast 3-D models and obtain pre- and post-blast 3-D dig limits. This reverse conversion from 2-D to 3-D is illustrated below.

5. Total mineable profit is calculated for AGC-EP and OK using the pre-blast 3-D dig limits, the true high resolution pre-blast profit in 3-D, and Equations (7.3)-(7.7).

6. Total mineable profit is calculated for AGC-EP and OK using the post-blast 3-D dig limits, the true high resolution post-blast profit in 3-D, and Equations (7.3)-(7.7).

7. Total mineable profit is calculated for AGC-EP and OK using the pre-blast 3-D dig limits, the true high resolution post-blast profit in 3-D, and Equations (7.3)-(7.7). This step allows assessing the consequence of not accounting for blast movement while optimizing dig limits.

8. Results are summarized.

7.5.1 Modeling Results

The dig limits optimization is performed using a rectangular frame with the size of 5×5 block^2 (7.5×7.5 m^2). The frame covers the areas of 56.25 m^2 and 59.48 m^2 for the pre- and post-blast models, respectively. The difference in the size of the areas covered by the frame is due to a slight increase in the post-blast grid size during blast movement modeling; the post-blast grid size is $1.54 \times 1.54 \times 1.62$ m^3. Figure 7.23 demonstrates a pre-blast optimized classification map based on the AGC-EP profit prediction; a classification map for the case of free selection is also shown.

(a) Optimized classification map

(b) Free selection

Figure 7.23: Optimized pre-blast classification map (5×5 block^2 frame size) and a corresponding high resolution classification map (free selection) based on the expected profit obtained with AGC-EP

The pre-blast optimized classification map in Figure 7.23a allows selecting 99.03 % of a maximum attainable cumulative expected profit value. This measure indicates the total estimated profit (Equation (6.3)) as opposed to total true profit (Equation (7.7)). The second stage of the algorithm was run with the neighborhood size of 1 block in each direction and the tolerance of 1 iteration without a decrease in the number of problematic locations. The optimization algorithm terminated based on the stage 3 tolerance of 10 hill climbing operations without an improvement to the objective function. The run-time was 13.72 seconds. More details about the AGC-DL optimization algorithm are in Chapter 6.

Figure 7.24 demonstrates a pre-blast optimized classification map based on the OK profit predictions; a classification map for the case of free selection is also shown.
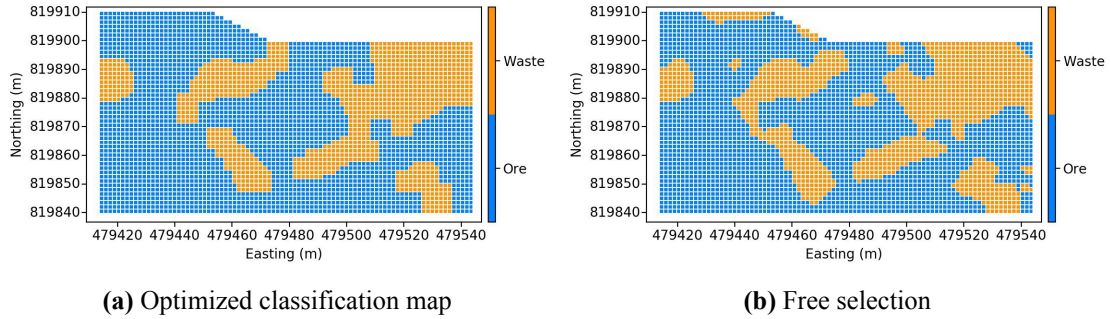

(a) Optimized classification map

(b) Free selection

Figure 7.24: Optimized pre-blast classification map (5×5 block^2 frame size) and a corresponding high resolution classification map (free selection) based on the profit predictions obtained with OK

The pre-blast optimized classification map in Figure 7.24a allows selecting 98.85 % of a maximum attainable cumulative profit value. AGC-DL was run with the same input parameters as in the previous case. The run-time was 8.87 seconds.

Figure 7.25 demonstrates a post-blast optimized classification map based on the post-blast AGC-EP expected profit; a post-blast classification map for the case of free selection is also shown.

(a) Optimized classification map
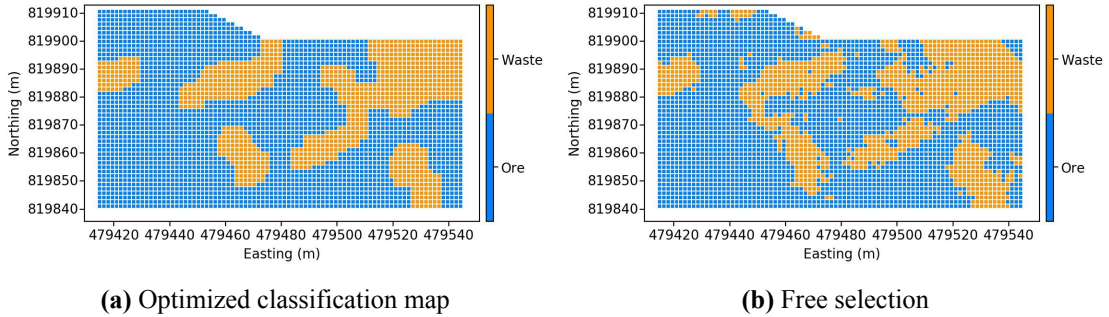
(b) Free selection

Figure 7.25: Optimized post-blast classification map (5×5 block^2 frame size) and a corresponding high resolution classification map (free selection) based on the expected profit obtained with AGC-EP

The post-blast optimized classification map in Figure 7.25a allows selecting 98.34 % of a maximum attainable cumulative expected profit value. AGC-DL was run with the same optimization plan as for the pre-blast optimization. The run-time was 6.62 seconds.

Figure 7.26 demonstrates a post-blast optimized classification map based on the post-blast OK profit predictions; a post-blast classification map for the case of free selection is also shown.

(a) Optimized classification map
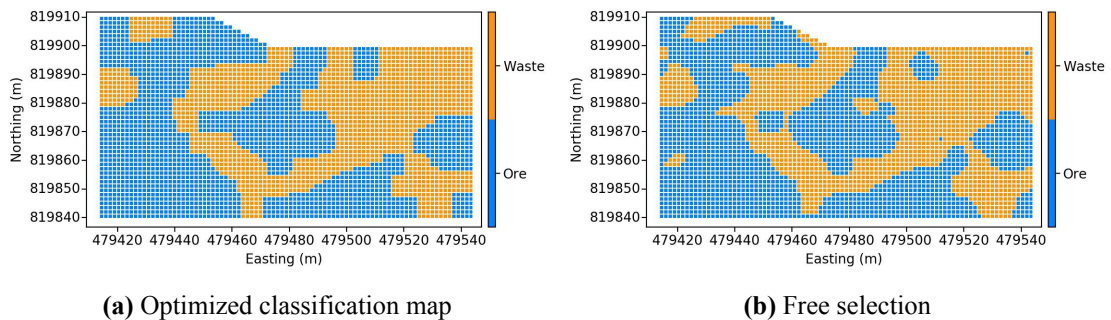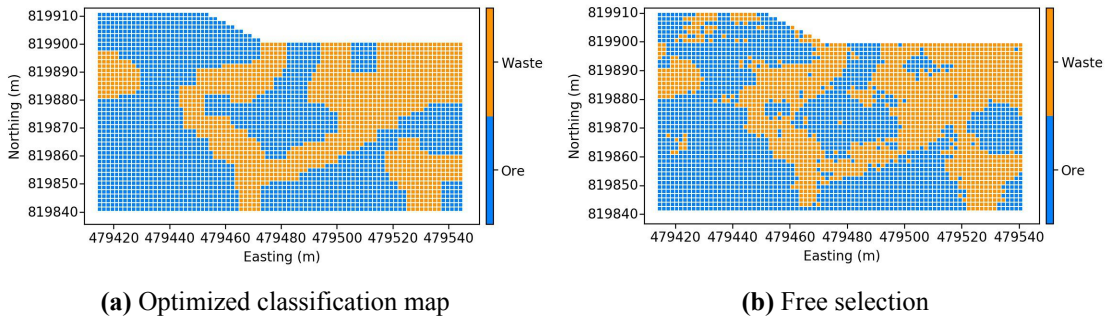
(b) Free selection

Figure 7.26: Optimized post-blast classification map (5×5 block^2 frame size) and a corresponding high resolution classification map (free selection) based on the profit obtained with OK

The post-blast optimized classification map allows selecting 97.17 % of a maximum attainable cumulative profit value. AGC-DL was run with the same optimization plan as for the pre-blast optimization. The run-time was 6.26 seconds.

The optimized classification maps in Figures 7.23-7.26 are obtained based on predicted profit. In real life, maximizing the selection of this predicted profit is the only performance measure available since the true pre- and post-blast profit is unknown. For this case study, the true pre- and post-blast profit is known. Therefore, the performance of the kriging-based grade control method and AGC should be compared with respect to the true profit. Optimized dig limits in 2-D are applied to corresponding 3-D volume to compare the true and estimated destinations. Figure 7.27 schematically illustrates how a 2-D optimized classification map is used to classify the corresponding post-blast 3-D volume; the classification map based on the post-blast AGC-EP expected profit is used as an example.
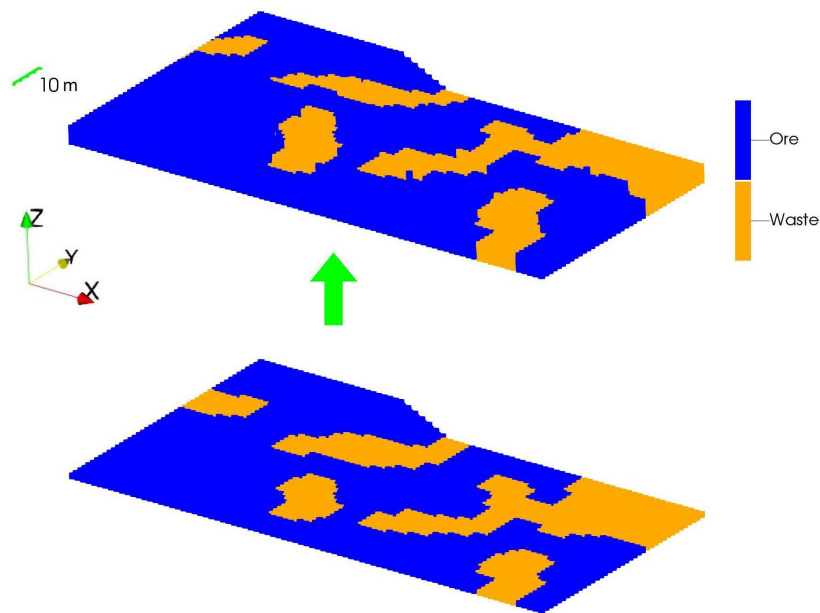
Figure 7.27: Optimized 2-D dig limits (based on the AGC-EP expected profit) applied to the corresponding post-blast 3-D volume

An optimal destination at a location of the 2-D classification map is applied to all the locations of the 3-D post-blast model that have the same coordinates in the horizontal plane; a 3-D dig limits model is obtained. The 3-D dig limits in Figure 7.27 are then used to calculate a total mineable profit value from Bench '110' using Equations (7.3)-(7.7). Figure 7.28 shows 3-D dig limit models for the AGC-EP and OK cases obtained using the optimized pre-blast 2-D dig limits (Figures 7.23-7.24) and the pre-blast 3-D volume.

(a) AGC-EP dig limits   **(b)** OK dig limits
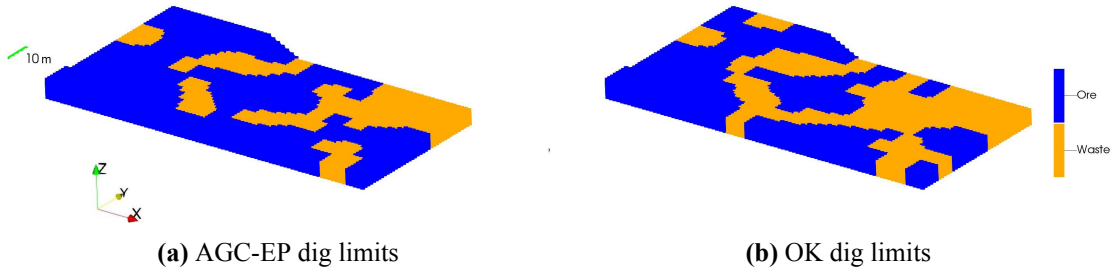
Figure 7.28: Pre-blast dig limits in 3-D obtained based on the AGC-EP and OK profit predictions

The 3-D dig limits for the AGC-EP case allow selecting $ 169 338, which is 79.6 % of the true total profit value of $ 212 648. The 3-D dig limits for the OK case allow selecting $ 167 493, which is 78.8 % of the true total profit value. These total profit values are the actual monetary profits that would be selected from Bench '110' if blasting was not performed. The total mineable profit values for both OK and AGC-EP are close to the total profit values calculated for the case of free selection in Section 7.3. AGC-EP outperforms OK by $1 845, which is around 1.1 %.

Figure 7.29 shows 3-D dig limits for the AGC-EP and OK cases obtained using opti-mized post-blast 2-D dig limits (Figures 7.25-7.26) and the post-blast 3-D volume.

(a) AGC-EP dig limits   **(b)** OK dig limits
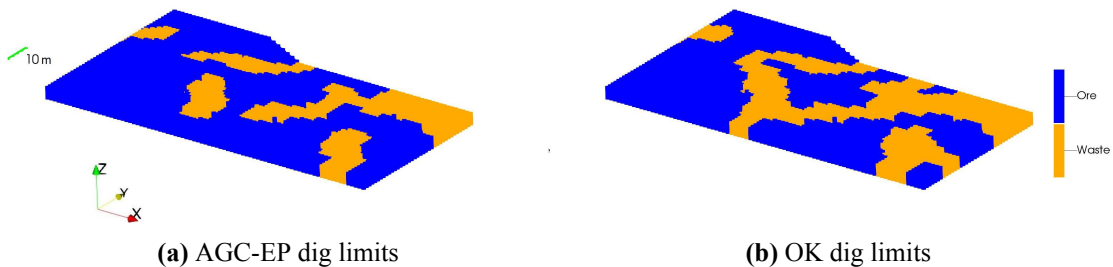
Figure 7.29: Post-blast dig limits in 3-D obtained based on the AGC-EP and OK profit predictions

The 3-D dig limits for the AGC-EP case allow selecting $ 160 194, which is 75.3 % of the true total profit value. The 3-D dig limits for the OK case allow selecting $ 154 913, which is 72.8 % of the true total profit value. These total profit values are the actual monetary profits that would be selected from Bench '110' if blasting was performed. The post-blast optimized dig limits in both the AGC-EP and OK cases allow selecting signifi-cantly less true profit than the pre-blast optimized dig limits. The difference between the

total mineable profit values for OK and AGC-EP are higher in this case. AGC-EP outperforms OK by \$5 282, which is a 3.4 % improvement.

It is interesting to analyze how using pre-blast dig limits impacts the total post-blast mineable profit from Bench '110'. This comparison is valid since the pre- and post-blast shapes of the mine bench have the same boundaries for this cases study. Therefore, the pre-blast optimized dig limits are relevant for the post-blast 3-D volume. Figure 7.30 shows 3-D dig limits for the AGC-EP and OK cases obtained using optimized pre-blast 2-D dig limits (Figures 7.23- 7.24) and the post-blast 3-D volume.

**(a)** AGC-EP dig limits   **(b)** OK dig limits
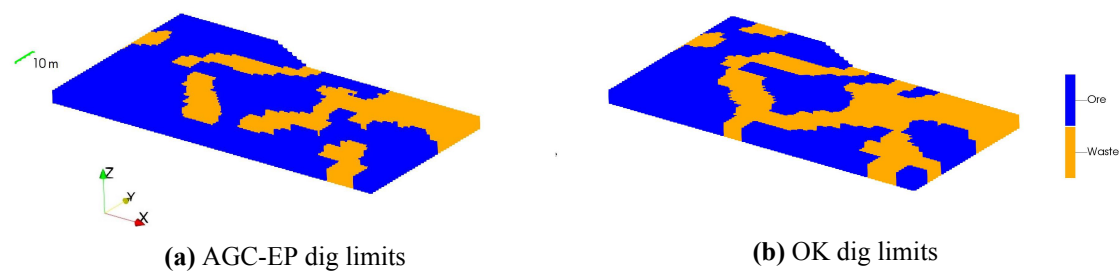
Figure 7.30: Post-blast dig limits in 3-D obtained based on the AGC-EP and OK pre-blast profit predictions and corresponding pre-bast 2-D dig limits

The 3-D dig limits for the AGC-EP case allow selecting \$ 156 689, which is 73.7 % of the true total profit value. The 3-D dig limits for the OK case allow selecting \$ 148 016, which is 69.6 % of the true total profit value. These total profit values are the actual monetary profits that would be selected from Bench '110' if blasting was performed but was not accounted for during dig limits optimization. AGC-EP outperforms OK by \$8 673, which is a 5.9 % improvement.

The 3-D dig limit models should be precisely followed by excavating equipment to maximize the true total profit from Bench '110'. Positioning errors during excavation may increase misclassification and reduce the total profit value.

7.6 Summary

A case study partially based on a real blasthole data set from the Misima mine in Papua New Guinea is presented. The case study shows the importance of a careful grade control modeling at three stages of short-term mine planning: i) spatial prediction of grades or

profit, ii) blast movement modeling (if blasting is performed), and iii) selection optimization. The misclassification errors may accumulate during the three stages, which may result in a significant loss of profit.

The AGC system is compared to a conventional grade control method based on OK estimation. A real blasthole data set is used to construct a high resolution reference model and compare the two methods in terms of total monetary profit achieved from a mine bench.

Spatial prediction of profit was performed using OK and the AGC-EP algorithm (Chapters 3 and 4). AGC-EP was run fully automatically while OK required manual implementation. Blast movement modeling was performed using the AGC-BM algorithm (Chapter 5). Artificial topography and blast movement vectors were used. Dig limits optimization was performed with the AGC-DL algorithm (Chapter 6) using the pre- and post-blast profit predictions.

Optimized pre-blast dig limits based on the AGC-EP profit predictions outperform the optimized pre-blast dig limits based on the OK profit predictions by around 1.1 % in terms of the total mineable profit from the mine bench. The AGC-EP and OK pre-blast dig limits allow selecting 79.6 % and 78.8 % of the total true profit of the mine bench, respectively. Optimized post-blast dig limits based on the AGC-EP profit predictions outperform the optimized post-blast dig limits based on the OK profit predictions by around 3.4 % in terms of the total mineable profit from the post-blast mine bench. The AGC and OK post-blast dig limits allow selecting 75.3 % and 72.8 % of the total true profit of the post-blast mine bench, respectively.

The impact of using the pre-blast optimized dig limits for post-blast selection of mined material is assessed. The AGC and OK pre-blast dig limits allow selecting 73.7 % and 69.6 % of the total true profit of the post-blast mine bench, respectively; AGC outperforms OK by 5.9 % in terms of the total mineable profit from the post-blast mine bench.

The case study represents a possible grade control scenario. The cumulative loss of profit may be higher or lower for other scenarios with more significant blast movement, more complex bench boundaries, and/or significant modeling errors.

CHAPTER 8

CONCLUSIONS

Grade control in open pit mines is a procedure that aims at optimizing the extraction of mineral resources. Profit from mining operations is maximized when material is sent to the correct destination. Grade control is performed in several stages summarized by three main unit operations: i) spatial prediction of grades or profit, ii) modeling the blast-induced displacement of pre-blast spatial predictions (if blasting is performed), and iii) selection optimization. The focus of this dissertation research is improving each grade control unit operation via developing an integrated system called the Advanced Grade Control (AGC) system. Figure 8.1 schematically illustrates the main elements of the system.
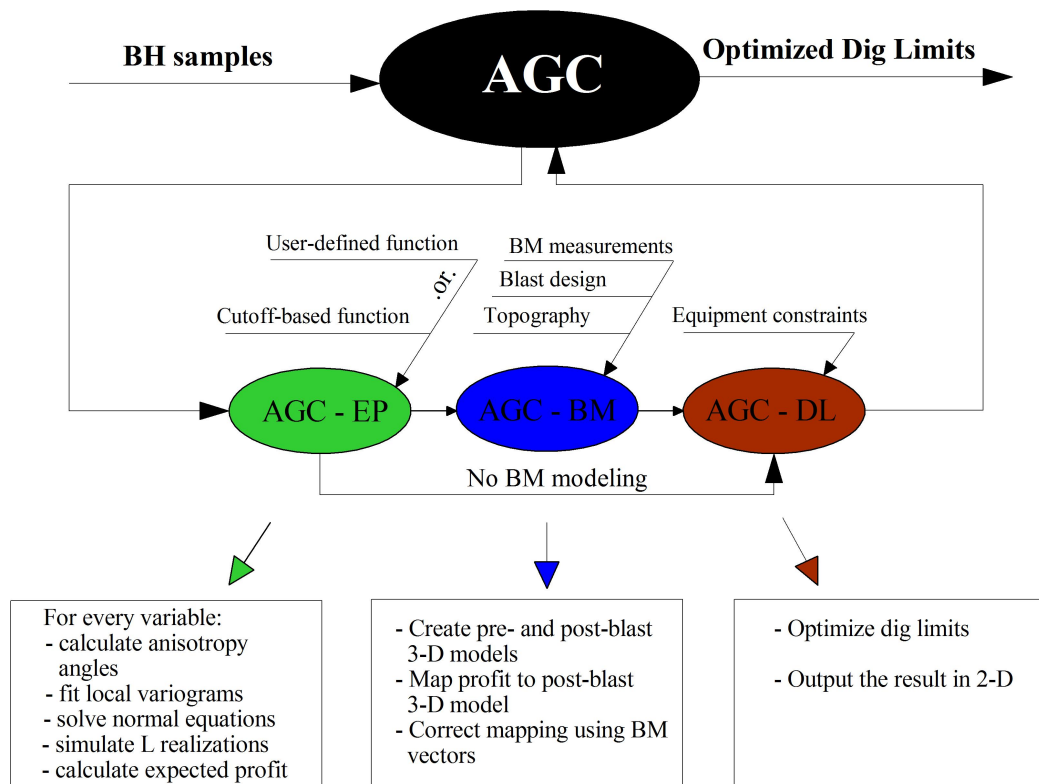

Figure 8.1: Schematic illustration of the Advanced Grade Control system

Spatial prediction for grade control is performed using a local multivariate simulation algorithm called the Advanced Grade Control-Expected Profit (AGC-EP). The algorithm is

196

used to generate high resolution expected profit for any number of destinations for mined material. The expected profit is then used to determine optimal destinations subject to excavating constraints.

Blast movement modeling is formulated as an optimization assignment problem. A heuristic optimization algorithm called the Advanced Grade Control-Blast Movement (AGC-BM) is developed. The algorithm is used to approximately solve the optimization problem based on detailed topography and blast movement measurements.

Optimal classification of mined material is formulated as an optimization problem. Optimization constraints imposed by such factors as parameters and characteristics of excavating and hauling equipment and/or the direction of mining are represented by the shape and size (rectangular or non-rectangular) of a floating selection unit. A fast heuristic algorithm called the Advanced Grade Control-Dig Limits (AGC-DL) is developed to solve the optimization problem and obtain mineable dig limits.

All the elements of AGC may operate in a chained fashion automatically or nearly automatically. This may allow integrating the system as a part of a mine's short-term planning workflow.

8.1 Key Research Contributions

The main contributions of this dissertation are related to improving and standardizing grade control practice in open pit mines and developing practical tools for solving grade control problems. Some of the developed tools like the improved mass moment of inertia tensor (MOI) method for determining directions of geological anisotropy or the AGC-DL algorithm may potentially be applied in other areas of geostatistical modeling and mine planning.

8.1.1 Local Multivariate Simulation Algorithm

The benefits of using geostatistical simulation in a combination with economic functions over estimation methods like kriging or inverse distance in grade control were previously discussed (Dimitrakopoulos & Godoy, 2014; Verly, 2005). Assuming global stationarity

for a modeling domain may be unrealistic. Performing simulation with locally varying anisotropy (LVA) requires special modeling tools such as described in Leuangthong et al. (2006) and Boisvert and Deutsch (2011). Multiple grade variables may be involved in profit calculations; in such case, it may be beneficial to model the multivariate relationships between grades to improve the final classification of mined material. Using a simulation-based grade control method may require a certain level of expertise in geostatistical modeling even for relatively simple grade control cases with only one grade variable and two grade control destinations, ore and waste. Manual implementation of the local multivariate simulation may be challenging and prone to errors. In addition, it may require significant time to complete all modeling operations. Therefore, industry practitioners often choose simple estimation methods, which may result in a loss of profit in some cases.

The AGC-EP algorithm addresses the issues described above. It performs a full local multivariate simulation workflow nearly or fully automatically. The simulation procedure is approached partially as an optimization problem. The main goal is minimizing the mean squared error between the true and predicted expected profit using a k-fold cross-validation procedure. The decision of stationarity is reassessed locally. Main modeling operations at each location include: i) normal score transformation (multivariate for more than one grade variable), ii) anisotropy determination, iii) simulation, and iv) expected profit calculation. Internal validation checks are included to ensure reasonable modeling results. AGC-EP may be run on a coarse grid to increase the speed of operation. Expected profit estimates generated by AGC-EP may be post-processed by a smoothing filter to achieve better modeling results. It has been demonstrated with two multivariate grade control cases studies that the AGC-EP algorithm run fully automatically outperforms carefully applied kriging estimation in terms of profit achieved from a mine bench.

The AGC-EP modeling algorithm supports automatic grade control modeling. It may be used separately or as a part of another grade control system based on the expected profit approach for grade control decision making.

8.1.1.1   Improved MOI Method

The MOI method implemented for determining local directions of geological anisotropy is described by Hassanpour (2007). The method relies on the calculation of local correlation maps. The accuracy of the method may be decreased when the correlation maps contain artifacts.

An algorithm for fixing correlation maps with artifacts is described. It is demonstrated that using the MOI method with the fixing algorithm significantly improves the accuracy of the method and, as a result, the quality of local predictions. The MOI algorithm is incorporated within the AGC-EP local multivariate simulation algorithm.

The method is implemented both on a grid and at arbitrary locations. It is fast and straightforward to automate. The only required input information is correlation maps.

8.1.2   Optimization Approach for Blast Movement Modeling

The are two main approaches for modeling blast movement in grade control: i) modeling based on the physics of rock breakage, and ii) modeling based on direct blast movement measurements. Due to the complexity of the blasting process and the uncertainty in input information and boundary conditions, using the fully theoretical approach may result in a significant error and the loss of profit (La Rosa & Thornton, 2011). Specialized systems such as the one described by Adam and Thornton (2004) may be used to obtain pre-and post-blast positions of specialized transmitters defining blast movement vectors. The main disadvantage of this approach is that only a limited number of the transmitters is used due to their high costs. Also, there is currently a lack of methods to use these limited measurements for reliable blast movement modeling. Pre- and post-blast topography provides another important source of information about blast movement. It can be obtained using mine laser scanners or drones.

The AGC-BM optimization algorithm is developed to model blast movement in 3-D using gridded pre- and post-blast topography and direct measurements. The blast movement problem is expressed as an optimization assignment problem approximately solved by the heuristic algorithm. Details about the objective function and optimization are described.

The AGC-BM algorithm is suitable for mapping pre-blast grades, categories, expected profit, or other information onto the post-blast configuration of a muckpile in 3-D. It can be used separately or within another grade control system.

8.1.2.1 Blast Movement Modeling with Limited Information

There are situations in open pit mines when only limited information is available about blast movement. Pre- and post-blast topography may be unavailable. Blast movement measurements may be limited or deemed unreliable.

A method to perform blast movement modeling with approximate topography is proposed. Approximate pre- and post-blast topographic surfaces are inferred within AGC-BM using the following information: i) bench bottom elevation, ii), bench height, iii) swell factor, iv) the principal direction of blast movement, and v) a pre-blast polygon with a free face indicated.

A method to infer approximate blast movement vectors based on the firing sequence of a blast and limited blast movement vectors is proposed. Firing sequence is used to obtain the direction of blast movement while the sparse blast movement vectors inform on the magnitude of displacement. An optimization algorithm to perform this operation is proposed.

8.1.3 Dig Limits Optimization Algorithm

Profit predictions obtained in the first grade control stage and corrected for blast movement (if blasting is performed) should be used with a cutoff grade or a profit function to classify mined material for further selection. Using the high resolution profit predictions for classifying mined material may result in complex ore/waste contacts. It may be impossible for excavating equipment to follow such complex dig lines, which results in misclassification errors and a loss of profit. Methods described by Isaaks, Treloar, and Elenbaas (2014) and M. Deutsch (2017) are similar to the method proposed in this thesis; however, it is not clear how to implement them due to a lack of details. The AGC-DL algorithm proposed in this thesis is based on a new heuristic algorithm for dig limit optimization. The algo-

rithm is simple, fast, and easily modified; it is described in detail and is demonstrated with examples.

The AGC-DL algorithm uses high resolution expected profit models to optimize classification maps subject to site specific rectangular or non-rectangular excavating constraints. This optimization problem defies traditional closed form analytical solutions; a practical heuristic algorithm has been developed to quickly determine the optimum final destination for material subject to realistic constraints. The optimization is fast and generates results that achieve up to 98-99 % of the total expected profit achieved with free selection. This algorithm provides a fast viable option for practical application in short-term grade control and in managing multiple realizations in long-term resource estimation.

8.2   Limitations and Future Work

There are limitations related to the application of the AGC system. Most of the limitations are due to the heuristic nature of the main optimization algorithms and the limited testing with real data. Another important limitation is considering grade control on a single mine bench basis, whereas blending ore from several mine benches and/or stockpiles may be utilized. Main areas of future work are discussed below.

8.2.1   Local Multivariate Simulation

AGC-EP is a complex algorithm consisting of several elements performing modeling operations automatically. Some of its elements are complex algorithms themselves and may require several input parameters specified. Ideally, k-fold cross-validation should be used to optimize all the input parameters. The operation time of AGC-EP would grow significantly in this case. Therefore, many input parameters are fixed within the algorithm. Using fixed parameters may lead to sub-optimal modeling results for some deposits. It may be required to tune the AGC-EP algorithm to site specific conditions.

AGC-EP usually performs better with many local conditioning samples (100 and more). The number of local samples should be sufficient for local normal score transformation (es-

pecially, multivariate), determination of local anisotropy, and variogram modeling. Using AGC-EP for small domains having less than 50 samples may result in poor performance.

Multivariate simulation requires collocated samples (homotopic observations). Before using AGC-EP, a multivariate imputation procedure should be performed and homotopic observations obtained. The current version of AGC-EP does not have tools for multivariate imputation of missing data.

The current version of AGC-EP assumes 2-D conditioning data from blastholes. Data from a bench above or dedicated grade control drilling cannot be incorporated for modeling expected profit in 3-D with the current version of the program.

8.2.2   Blast Movement Modeling

The AGC-BM algorithm proposed for blast movement is tested with artificial data only. Additional validation and comparison to existing alternatives and industrial experiment are required.

The modeling algorithm is based on the assumption that there is no mixing and collision of particles during blasting. It is assumed that sparse blast movement vectors allow avoiding modeling the complex physics of rock breakage and directly link the blocks of pre- and post-blast models.

The size of 3-D models is an important factor for blast movement modeling. The blast movement optimization problem is approximately solved by a heuristic optimization algorithm based on random perturbations. Having more than 15 000 blocks significantly increases the operation time. Due to the stochastic nature of the optimization algorithm, there is a possibility of being trapped in a local minimum during optimization. A better optimization strategy may result in improved performance of AGC-BM.

8.2.3   Dig Limits Optimization

The AGC-DL algorithm for dig limits optimization is heuristic. Results are obtained fast, but optimality is not guaranteed.

The main focus of the algorithm is selection optimization subject to rectangular selection frames. While using non-rectangular selection frames is possible, it is not thoroughly tested.

The AGC-DL optimizes the classification of mined material. This is different from dig limit polygon optimization, which may provide more flexible and suitable dig lines.

8.2.4 Future Work

Conventional grade control is based on available information on the pre-blast geological composition of a deposit, limited information about blast movement, and characteristics of available excavating and hauling equipment. Obtaining additional grade control information may be expensive. The benefit of adding new information from dedicated drillholes or other sources of information for grade control should be studied. A way to determine a reasonable number of transmitters for blast movement modeling should be proposed.

Future research should focus on ways to account for ore blending from several mine benches and/or stockpiles. The benefit of using a dynamic profit function to distinguish between different types of mined material should be investigated.

Grade control modeling may be integrated into a mining complex that may include several mineral deposits, waste dumps, stockpiles, and final products (Goodfellow & Dimitrakopoulos, 2017). Grade control could be used as one of the aspects influencing the net present value of the entire mining complex in the face of geological uncertainty.

Multivariate imputation should be considered to be a part of AGC-EP. A profit function used to define expected profit for different mined material destinations may include categorical variables. Some tools for modeling categorical variables may be incorporated into AGC-EP if the values of the categorical variables are not provided at a high resolution. An option to optimize more of the input parameters to the algorithm using cross-validation should be added.

Alternative sources of information about blast movement should be considered. Video obtained with ultra high speed cameras is one such source. More details about the blast design such as explosive properties and blasthole parameters could also be used for modeling.

The heuristic optimization algorithms for blast movement modeling and dig limits optimization should be improved or replaced with more efficient optimization techniques. Overall, the current implementation of the described optimization algorithms in computer codes should be improved.

It is becoming popular in the mining industry to use precise sensors for tracking the bucket position of an excavator using GPS (Trimble Inc., n.d.) or even measure and report the characteristics of ore while it is being excavated or conveyed (MineSense Technologies Ltd, n.d.). Such a level of control over the mined material should enable a real-time updating of the dig limit maps. In an ideal situation, the operator of an excavator should receive real-time updated information on where to make each subsequent scoop. The use of augmented reality for displaying the real-time grade control information should be considered.

References

Adam, M., & Thornton, D. (2004). A new technology for measuring blast movement. In C. Sabin (Ed.), *Innovative Mineral Developments - Achievements in a Changing World.* Sydney, Australia: The Australasian Institute of Mining and Metallurgy: Sydney Branch.

Almeida, A. S., & Journel, A. G. (1994). Joint simulation of multiple variables with a Markov-type coregionalization model. *Mathematical Geology*, *26*(5), 565–588.

Barnett, R. M., & Deutsch, C. V. (2015a). Guide to multivariate modeling with PPMT. In *Centre for Computational Geostatistics (CCG) guidebook series* (Vol. 20). Edmonton, AB, Canada: Centre for Computational Geostatistics.

Barnett, R. M., & Deutsch, C. V. (2015b). Multivariate imputation of unequally sampled geological variables. *Mathematical Geosciences*, *47*(7), 791–817.

Barnett, R. M., Manchuk, J. G., & Deutsch, C. V. (2014). Projection pursuit multivariate transform. *Mathematical Geosciences*, *46*(3), 337–359.

Beer, F. P., Johnston, E. R., Jr., Mazurek, D. F., Cornwell, P. J., & Self, B. P. (2015). *Vector mechanics for engineers: Statics and dynamics (11th edition)*. New York: McGraw-Hill Education.

Boisvert, J. B., & Deutsch, C. V. (2011). Programs for kriging and sequential Gaussian simulation with locally varying anisotropy using non-Euclidean distances. *Computers & Geosciences*, *37*(4), 495–510.

Boisvert, J. B., Manchuk, J. G., & Deutsch, C. V. (2009). Kriging in the presence of locally varying anisotropy using non-Euclidean distances. *Mathematical Geosciences*, *41*(5), 585–601.

Brachetti, P., Ciccoli, M. D. F., Di Pillo, G., & Lucidi, S. (1997). A new version of the Price's algorithm for global optimization. *Journal of Global Optimization*, *10*(2), 165–184.

Brunell, R. M. (1992). *An automatic procedure for fitting variograms by Cressie's approximate weighted least squares criterion* (Technical Report No. SMU/DS/TR). Dallas,

TX, USA: Southern Methodist University.

Burkard, R. E., & Derigs, U. (2013). *Assignment and matching problems: Solution methods with fortran-programs* (Vol. 184). Berlin, Germany: Springer Science & Business Media.

Cirio, L., Lucidi, S., Parasiliti, F., & Villani, M. (2002). A global optimization approach for the synchronous motors design by finite element analysis. *International Journal of Applied Electromagnetics and Mechanics*, *16*(1-2), 13–27.

Clarke, D. S., Lewis, R. W., & Waldron, H. M. (1990). Geology and trace-element geochemistry of the Umuna gold-silver deposit, Misima Island, Papua New Guinea. *Journal of Geochemical Exploration*, *35*(1-3), 201–223.

Cressie, N. (1985). Fitting variogram models by weighted least squares. *Journal of the International Association for Mathematical Geology*, *17*(5), 563–586.

Cressie, N. (1992). Statistics for spatial data. *Terra Nova*, *4*(5), 613–617.

Cundall, P. A. (1980). *UDEC-A generalised distinct element program for modelling jointed rock* (Technical Report No. PCAR-1-80). Retrieved from `http://www.dtic.mil/get-tr-doc/pdf?AD=ADA087610`

David, M. (1977). The practice of variogram modelling. In *Geostatistical Ore Reserve Estimation (Developments in Geomathematics 2)* (1st ed., p. 115-174). Elsevier Scientific Publishing Company.

Davis, B. M., & Greenes, K. A. (1983). Estimation using spatially distributed multivariate data: an example with coal quality. *Journal of the International Association for Mathematical Geology*, *15*(2), 287–300.

Davis, J. G. (1992). Grade control for australian open pit gold mines. *Geological Society, London, Special Publications*, *63*(1), 219-232.

Dempster, A. P., Laird, N. M., & Rubin, D. B. (1977). Maximum likelihood from incomplete data via the em algorithm. *Journal of the Royal Statistical Society: Series B (Methodological)*, *39*(1), 1–22. Retrieved from `http://www.jstor.org/stable/2984875`

Desassis, N., & Renard, D. (2013). Automatic variogram modeling by iterative least squares: univariate and multivariate cases. *Mathematical Geosciences*, *45*(4), 453–

470.

Desbarats, A. J., & Dimitrakopoulos, R. (2000). Geostatistical simulation of regionalized pore-size distributions using min/max autocorrelation factors. *Mathematical Geology*, *32*(8), 919–942.

Deutsch, C. V., & Journel, A. G. (1998). *GSLIB: Geostatistical software library and user's guide* (2nd ed.). New York: Oxford University Press.

Deutsch, C. V., Magri, V. E., & Norrena, K. P. (2000). Optimal grade control using geostatistics and economics: methodology and examples. *Transactions-Society for Mining Metallurgy and Exploration Incorporated*, *308*, 43–52.

Deutsch, J. L. (2015). Variogram model refresh. In *Proceedings of the 17th CCG Annual Meeting* (Paper 410). Edmonton, AB, Canada: Centre for Computational Geostatistics.

Deutsch, M. (2017). A branch and bound algorithm for open pit grade control polygon optimization. In *Proceedings of the 38th International Symposium on the Application of Computers and Operations Research in the Mineral Industry (APCOM 2017)*. Golden, CO, USA.

Dimitrakopoulos, R., & Godoy, M. (2014). Grade control based on economic ore/waste classification functions and stochastic simulations: examples, comparisons and applications. *Mining Technology*, *123*(2), 90–106.

Feng, X., & Milanfar, P. (2002). Multiscale principal components analysis for image local orientation estimation. In *Conference Record of the Thirty-Sixth Asilomar Conference on Signals, Systems and Computers, 2002* (Vol. 1, pp. 478–482). IEEE.

Friedman, J. H. (1987). Exploratory projection pursuit. *Journal of the American statistical association*, *82*(397), 249–266.

Furtney, J. K., Andrieux, P., & Hall, A. K. (2016). Applications for numerical modeling of blast induced rock fracture. In *50th US Rock Mechanics/Geomechanics Symposium*. American Rock Mechanics Association.

Geman, S., & Geman, D. (1984). Stochastic relaxation, gibbs distributions, and the bayesian restoration of images. *IEEE Transactions on Pattern Analysis and Machine Intelligence*, *6*(6), 721–741.

Gershon, M. E. (1983). Optimal mine production scheduling: evaluation of large scale mathematical programming approaches. *International Journal of Mining Engineering*, *1*(4), 315–329.

Gilbride, L. J. (1995). *Blast induced rock movement modelling for bench blasting in Nevada open-pit mines* (Master's thesis, University of Nevada, Reno, NV, USA). Retrieved from `https://scholarworks.unr.edu/handle/11714/1314`

Glacken, I. M. (1996). *Change of support by direct conditional block simulation* (Master's thesis, Stanford University, Stanford, CA, USA). Retrieved from `http://pangea.stanford.edu/departments/ere/dropbox/scrf/documents/Theses/SCRF-Theses/1990-1999/1996_MS_Glacken.pdf`

Godoy, M., Dimitrakopoulos, R., & Costa, J. F. (2001). A new technology for measuring blast movement. In A. Edwards (Ed.), *Mineral Resource and Ore Reserve Estimation - The AusIMM Guide to Good Practice*. Melbourne, Australia: The Australasian Institute of Mining and Metallurgy.

Goodfellow, R., & Dimitrakopoulos, R. (2017). Simultaneous stochastic optimization of mining complexes and mineral value chains. *Mathematical Geosciences*, *49*(3), 341–360.

Hart, R., Cundall, P. A., & Lemos, J. (1988). Formulation of a three-dimensional distinct element model. Part II. Mechanical calculations for motion and interaction of a system composed of many polyhedral blocks. *International Journal of Rock Mechanics and Mining Sciences & Geomechanics Abstracts*, *25*(3), 117–125.

Hassanpour, R. M. (2007). *Tools for multivariate modeling of permeability tensors and geometric parameters for unstructured grids* (Master's thesis). University of Alberta, Edmonton, AB, Canada.

Hotelling, H. (1933). Analysis of a complex of statistical variables into principal components. *Journal of Educational Psychology*, *24*(6), 417-441.

Isaaks, E. H. (1991). *The application of Monte Carlo methods to the analysis of spatially correlated data* (Doctoral dissertation). Stanford University, Stanford, CA, USA.

Isaaks, E. H., Barr, R., & Handayani, O. (2014). Modeling blast movement for grade control. In *Proceedings of the 9th international mining geology conference 2014*

(p. 433-439). Australian Institute of Mining and Metallurgy.

Isaaks, E. H., & Srivastava, R. M. (1989). *Applied geostatistics*. New York: Academic Press.

Isaaks, E. H., Treloar, I., & Elenbaas, T. (2014). Optimum dig lines for open pit grade control. In *Proceedings of the 9th international mining geology conference 2014* (pp. 425–432). Australian Institute of Mining and Metallurgy.

Jensen, J. (2016). *Introductory digital image processing : a remote sensing perspective*. Glenview, IL: Pearson Education, Inc.

Journel, A. G. (1984). MAD and conditional quantile estimators. In *Geostatistics for natural resources characterization* (pp. 261–270). Springer.

Journel, A. G. (1989). *Fundamentals of geostatistics in five lessons* (Vol. 8). Washington, DC: American Geophysical Union.

Journel, A. G., & Huijbregts, C. J. (1978). *Mining geostatistics*. New York: Academic Press.

Kalman, R. E. (1960). A new approach to linear filtering and prediction problems. *Journal of Basic Engineering*, *82*(1), 35–45.

Kelley, K. D., & Jennings, S. (2004). A special issue devoted to barite and Zn-Pb-Ag deposits in the Red Dog district, western Brooks Range, northern Alaska. *Economic Geology*, *99*(7), 1267–1280.

Kirkpatrick, S., Gelatt, C. D., & Vecchi, M. P. (1983). Optimization by simulated annealing. *Science*, *220*(4598), 671–680.

Krige, D. G. (1951). A statistical approach to some basic mine valuation problems on the Witwatersrand. *Journal of the Chemical, Metallurgical and Mining Society of South Africa*, *52*, 119-139.

Krolak, T., Palmer, K., Lacouture, B., & Paley, N. (2017). *NI 43-101 Technical Report for the Red Dog Mine* (Tech. Rep.). Retrieved from `https://www.miningdataonline.com/reports/Red%20Dog%20Mine_TR12312016.pdf`

Kuhn, H. W. (1955). The Hungarian method for the assignment problem. *Naval Research Logistics Quarterly*, *2*(1-2), 83–97.

Land, A. H., & Doig, A. G. (1960). An automatic method of solving discrete programming

problems. *Econometrica*, *28*(3), 497-520. Retrieved from `http://www.jstor.org/stable/1910129`

La Rosa, D., & Thornton, D. (2011). Blast movement modelling and measurement. In *Proceedings of the 35th APCOM Symposium* (p. 244-247). Wollongong, NSW, Australia.

Larrondo, P. F., Neufeld, C. T., & Deutsch, C. V. (2003). Varfit: a program for semi-automatic variogram modelling. In *Proceedings of the 5th CCG Annual Meeting* (Paper 122). Edmonton, AB, Canada: University of Alberta.

Leuangthong, O. (2003). Multivariate geostatistical simulation at Red Dog Mine, Alaska, USA. In *Proceedings of the 5th CCG Annual Meeting* (Paper 113). Edmonton, AB, Canada: University of Alberta.

Leuangthong, O., & Deutsch, C. V. (2003). Stepwise conditional transformation for simulation of multiple variables. *Mathematical Geology*, *35*(2), 155–173.

Leuangthong, O., Neufeld, C. T., & Deutsch, C. V. (2003). Optimal selection of selective mining unit (SMU) size. In *Proceedings of the 5th CCG Annual Meeting* (Paper 116). Edmonton, AB, Canada: University of Alberta.

Leuangthong, O., Prins, C., & Deutsch, C. V. (2006). SGSIM_LVA: Gaussian simulation with locally varying angles. In *Proceedings of the 8th CCG Annual Meeting* (Paper 408). Edmonton, AB, Canada: University of Alberta.

Lillah, M., & Boisvert, J. B. (2015). Inference of locally varying anisotropy fields from diverse data sources. *Computers & Geosciences*, *82*, 170–182.

Little, J. D. C., Murty, K. G., Sweeney, D. W., & Karel, C. (1963). An algorithm for the traveling salesman problem. *Operations Research*, *11*(6), 972–989.

Little, R. J. A., & Rubin, D. B. (2014). *Statistical analysis with missing data* (Vol. 333). John Wiley & Sons.

Liuzzi, G., & Lucidi, S. (n.d.). *DFL-A Derivatife-Free Library*. Retrieved 2019-03-09, from `http://www.iasi.cnr.it/~liuzzi/DFL/index.php/list3/11-global-optimization/7-acrs`

Liuzzi, G., Lucidi, S., Parasiliti, F., & Villani, M. (2003). Multiobjective optimization techniques for the design of induction motors. *IEEE Transactions on Magnetics*,

39(3), 1261–1264.

Lusk, B., Silva, J., & Eltschlager, K. K. (2013). *Field testing and analysis of blasts utilizing short delays with electronic detonators* (Final Report No. S09AP15632). Lexington, KY: University of Kentucky.

Luster, G. R. (1986). *Raw materials for portland cement: Applications of conditional simulation of coregionalization* (Doctoral dissertation). University Microfilms.

Lyday, T. Q. (1994). The Mineral Industry of Papua New Guinea. In *1994 Minerals Yearbook (Volume III. – Area Reports: International).* Retrieved from `https://minerals.usgs.gov/minerals/pubs/country/1994/9325094.pdf`

Lyday, T. Q. (1999). The Mineral Industry of Papua New Guinea. In *1999 Minerals Yearbook (Volume III. – Area Reports: International).* Retrieved from `https://minerals.usgs.gov/minerals/pubs/country/1999/9325099.pdf`

Machuca-Mory, D. F., & Deutsch, C. V. (2013). Non-stationary geostatistical modeling based on distance weighted statistics and distributions. *Mathematical Geosciences*, *45*(1), 31–48.

Magneron, C., Jeannee, N., Le Moine, O., & Bourillet, J.-F. (2010). Integrating prior knowledge and locally varying parameters with moving-geostatistics: methodology and application to bathymetric mapping. In P. Atkinson & C. Lloyd (Eds.), *GeoENV VII–Geostatistics for Environmental Applications. Quantitative Geology and Geostatistics* (Vol. 16, pp. 405–415). Dordrecht, Netherlands: Springer, Dordrecht.

Manchuk, J. G., & Deutsch, C. V. (2017). Isotropic covariance functions and fitting with newton method. In *Proceedings of the 19th CCG Annual Meeting* (Paper 115)*.* Edmonton, AB, Canada: University of Alberta.

Martin, R. (2017). Automatic LVA field generation. In *Proceedings of the 17th CCG Annual Meeting* (Paper 111)*.* Edmonton, AB, Canada: University of Alberta.

Matheron, G. (1963). Principles of geostatistics. *Economic Geology*, *58*(8), 1246–1266.

Matheron, G. (1973). The intrinsic random functions and their applications. *Advances in Applied Probability*, *5*(3), 439–468.

McManus, S. (2017). *Misima gold-copper project, milne bay, papua new guinea* (Technical Report). Port Macquarie, Australia: Skandus Pty Ltd. Re-

trieved from `http://www.kingstonresources.com.au/wp-content/uploads/2018/10/WCB-2017-NI43-101-Technical-Report-Website-version.pdf`

Metropolis, N., Rosenbluth, A. W., Rosenbluth, M. N., Teller, A. H., & Teller, E. (1953). Equation of state calculations by fast computing machines. *The Journal of Chemical Physics*, *21*(6), 1087–1092.

MineSense Technologies Ltd. (n.d.). *Our technology*. Retrieved 2019-03-09, from `http://minesense.com/our-technology/`

Moore, D. W., Young, L. E., Modene, J. S., & Plahuta, J. T. (1986). Geologic setting and genesis of the Red Dog zinc-lead-silver deposit, western Brooks Range, Alaska. *Economic Geology*, *81*(7), 1696–1727.

Neufeld, C. T., Norrena, K. P., & Deutsch, C. V. (2003). Semi-automatic dig limit generation. In *Proceedings of the 5th CCG Annual Meeting* (Paper 115). Edmonton, AB, Canada: University of Alberta.

Neufeld, C. T., Norrena, K. P., & Deutsch, C. V. (2005). Guide to geostatistical grade control and dig limit determination. In *Centre for Computational Geostatistics (CCG) guidebook series* (Vol. 1). Edmonton, AB, Canada: Centre for Computational Geostatistics.

Norrena, K. P. (2007). *Decision making using geostatistical models of uncertainty* (Doctoral dissertation). University of Alberta, Edmonton, AB, Canada.

Norrena, K. P., & Deutsch, C. V. (2001). Automatic determination of dig limits subject to geostatistical, economic and equipment constraints. In *Proceedings of the 3rd CCG Annual Meeting* (Paper 114). Edmonton, AB, Canada: University of Alberta.

Onederra, I. A., Furtney, J. K., Sellers, E., & Iverson, S. (2013). Modelling blast induced damage from a fully coupled explosive charge. *International Journal of Rock Mechanics and Mining Sciences*, *58*, 73–84.

Persson, P.-A., Holmberg, R., & Lee, J. (1993). *Rock blasting and explosives engineering*. CRC press.

Preece, D. S., & Silling, S. A. (2016). *Ore loss and dilution studies of surface mineral blasting with 3d distinct element heave models*. (Technical Report No. SAND2016-1317C). Albuquerque, NM, USA: Sandia National Laboratories. Retrieved from

`https://www.osti.gov/scitech/servlets/purl/1344685`

Preece, D. S., & Taylor, L. M. (1989). *Complete computer simulation of crater blasting including fragmentation and rock motion* (Technical Report No. SAND-88-2108C). Albuquerque, NM, USA: Sandia National Labs.

Price, W. L. (1977). A controlled random search procedure for global optimisation. *The Computer Journal*, *20*(4), 367–370.

Pyrcz, M. J., & Deutsch, C. V. (2014). *Geostatistical reservoir modeling*. Oxford university press.

Richmond, A. J. (2003). Financially efficient ore selections incorporating grade uncertainty. *Mathematical Geology*, *35*(2), 195–215. Retrieved from `https://doi.org/10.1023/A:1023239606028` doi: 10.1023/A:1023239606028

Richmond, A. J., & Beasley, J. E. (2004a). Financially efficient dig-line delineation incorporating equipment constraints and grade uncertainty. *International Journal of Surface Mining*, *18*(2), 99–121.

Richmond, A. J., & Beasley, J. E. (2004b). An iterative construction heuristic for the ore selection problem. *Journal of Heuristics*, *10*(2), 153–167.

Rosenblatt, M. (1952). Remarks on a multivariate transformation. *The Annals of Mathematical Statistics*, *23*(3), 470–472.

Rossi, M. E., & Deutsch, C. V. (2014). *Mineral resource estimation*. Springer Science & Business Media.

Rubin, D. B. (1978). Multiple imputations in sample surveys-a phenomenological Bayesian approach to nonresponse. In *Proceedings of the survey research methods section of the American Statistical Association* (Vol. 1, pp. 20–34). American Statistical Association. Retrieved from `http://www.asasrms.org/Proceedings/papers/1978_004.pdf`

Ruiseco, J. R. (2016). *Dig-limit optimization in open pit mines through genetic algorithms* (Master's thesis). McGill University, Montreal, Quebec , Canada.

Russ, J. C. (2016). *The image processing handbook*. Boca Raton, FL: CRC press.

Sari, Y. A., & Kumral, M. (2018). Dig-limits optimization through mixed-integer linear programming in open-pit mines. *Journal of the Operational Research Society*, *69*(2),

171–182.

Schamaun, J. T. (1984). Methods for predicting rubble motion during blasting. In *Proceedings of the 25th US Symposium on Rock Mechanics (USRMS)*. American Rock Mechanics Association.

Shannon, J. M., & Stoker, P. T. (2013). *Misima Gold-Copper Project, Milne Bay, Papua New Guinea* (Technical Report No. AMC713006). Vancouver, BC: AMC Mining Consultants (Canada) Limited.

Shepard, D. (1968). A two-dimensional interpolation function for irregularly-spaced data. In *Proceedings of the 1968 23rd ACM national conference* (pp. 517–524). New York: ACM.

Sheskin, D. J. (2003). *Handbook of parametric and nonparametric statistical procedures*. CRC Press.

Silva, D. S. F., & Deutsch, C. V. (2016). Multivariate data imputation using Gaussian mixture models. *Spatial Statistics*, *27*, 74-90.

Srivastava, R. M. (1987). Minimum variance or maximum profitability?. *CIM Bulletin*, *80*(901), 63–68.

Switzer, P. (1985). *Min/max autocorrelation factors for multivariate spatial imagery* (Technical Report No. 6). Stanford, CA: Stanford University.

Tabesh, M., & Askari-Nasab, H. (2011). Two-stage clustering algorithm for block aggregation in open pit mines. *Mining Technology*, *120*(3), 158–169.

Tabesh, M., & Askari-Nasab, H. (2013). Automatic creation of mining polygons using hierarchical clustering techniques. *Journal of Mining Science*, *49*(3), 426–440.

Taylor, D. L., & Firth, I. R. (2003). Utilization of blast movement measurements in grade control. In *Proceedings of the 31th APCOM Symposium on Application of Computers and Operations Research in the Minerals Industries*. Johannesburg, South Africa: South African Institute of Mining and Metallurgy.

Taylor, S. L. (1995). *Blast induced movement and its effect on grade dilution at the Coeur Rochester Mine* (Master's thesis). University of Nevada, Reno, NV, USA.

Teck Cominco Alaska Inc. (2009). *Red Dog Mine closure and reclamation plan. Supporting document B. Plan of operations.* Retrieved from `http://dnr.alaska.gov/mlw/`

mining/largemine/reddog/publicnotice/pdf/sdb1.pdf

Te Stroet, C. B. M., & Snepvangers, J. J. J. C. (2005). Mapping curvilinear structures with local anisotropy kriging. *Mathematical Geology*, *37*(6), 635–649.

Thornton, D. (2009a). The application of electronic monitors to understand blast movement dynamics and improve blast designs. In J. A. Sanchidrian (Ed.), *Proceedings of the 9th International Symposium on Rock Fragmentation by Blasting,* Fragblast (pp. 287–300). CRC Press.

Thornton, D. (2009b). The implications of blast-induced movement to grade control. In *Proceedings of the 7th International Mining Geology Conference* (pp. 147–154). Perth, WA, Australia.

Thornton, D., Sprott, D., & Brunton, I. (2005). Measuring blast movement to reduce ore loss and dilution. In *Proceedings of the 31st Annual Conference on Explosives and Blasting Technique* (p. 1-11). Cleveland, OH: International Society of Explosives Engineers.

Tordoir, A., Weatherley, D., Onederra, I., & Bye, A. (2009). A new 3D simulation framework to model blast induced rock mass displacement using physics engines. In J. A. Sanchidrian (Ed.), *Proceedings of the 9th International Symposium on Rock Fragmentation by Blasting,* Fragblast (pp. 381–388). CRC Press/Balkema.

Torgerson, W. S. (1952). Multidimensional scaling: I. Theory and method. *Psychometrika*, *17*(4), 401–419.

Trimble Inc. (n.d.). *Grade control for excavators.* Retrieved 2019-03-09, from https://construction.trimble.com/products-and-solutions/grade-control-excavators

Vasylchuk, Y. V. (2016). *Integrated system for improved grade control in open pit mines* (Master's thesis). University of Alberta, Edmonton, AB, Canada.

Vasylchuk, Y. V., & Deutsch, C. V. (2016). Non-linear estimation for grade control. In *Proceedings of the 18th CCG Annual Meeting* (Paper 132). Edmonton, AB, Canada: University of Alberta.

Vasylchuk, Y. V., & Deutsch, C. V. (2017). Improved grade control in open pit mines. *Mining Technology*, *14*, 1-8. Retrieved from http://dx.doi.org/10.1080/14749009

`.2017.1363991` doi: 10.1080/14749009.2017.1363991

Verly, G. (1993). Sequential Gaussian cosimulation: a simulation method integrating several types of information. In *Geostatistics Troia 92* (pp. 543–554). Springer.

Verly, G. (2005). Grade control classification of ore and waste: A critical review of estimation and simulation based procedures. *Mathematical Geology*, *37*(5), 451–475.

Wierzbicki, T. (2013). *2.080J Structural Mechanics. Fall 2013* [PDF file]. Retrieved from `https://ocw.mit.edu/courses/mechanical-engineering/2-080j-structural-mechanics-fall-2013/recitations/MIT2_080JF13_Recitation2.pdf`

Wilde, B. J., & Deutsch, C. V. (2007). Feasibility grade control (FGC):simulation of grade control on geostatistical realizations. In *Proceedings of the 9th CCG Annual Meeting* (Paper 301). Edmonton, AB, Canada: University of Alberta.

Yang, P., Xiang, J., Chen, M., Fang, F., Pavlidis, D., Latham, J.-P., & Pain, C. C. (2017). The immersed-body gas-solid interaction model for blast analysis in fractured solid media. *International Journal of Rock Mechanics and Mining Sciences*, *91*, 119–132.

Yang, R. L., & Kavetsky, A. (1990). A three dimensional model of muckpile formation and grade boundary movement in open pit blasting. *International Journal of Mining and Geological Engineering*, *8*(1), 13–34.

Yang, R. L., Kavetsky, A., & McKenzie, C. K. (1989). A two-dimensional kinematic model for predicting muckpile shape in bench blasting. *International Journal of Mining and Geological Engineering*, *7*(3), 209–226.

Yennamani, A. L. (2010). *Blast induced rock movement measurement for grade control at the Phoenix mine* (Master's thesis). University of Nevada, Reno, NV, USA.

Zhang, S. (1994). *Rock movemnt due to blasting and its impact on ore grade control in Nevada open pit gold mines* (Master's thesis). University of Nevada, Reno, NV, USA.